به نام خدا

مرکز دانلود رایگان
مهندسی متالورژی و مواد

www.Iran-mavad.com

ADVANCES IN MATERIALS RESEARCH

The series Advances in Materials Research reports in a systematic and comprehensive way on the latest progress in basic materials sciences. It contains both theoretically and experimentally oriented texts written by leading experts in the field. Advances in Materials Research is a continuation of the series Research Institute of Tohoku University (RITU).

1 **Mesoscopic Dynamics of Fracture**
Computational Materials Design
Editors: H. Kitagawa, T. Aihara, Jr., and Y. Kawazoe

2 **Advances in Scanning Probe Microscopy**
Editors: T. Sakurai and Y. Watanabe

3 **Amorphous and Nanocrystalline Materials**
Preparation, Properties, and Applications
Editors: A. Inoue and K. Hashimoto

4 **Materials Science in Static High Magnetic Fields**
Editors: K. Watanabe and M. Motokawa

5 **Structure and Properties of Aperiodic Materials**
Editors: Y. Kawazoe and Y. Waseda

6 **Fiber Crystal Growth from the Melt**
Editors: T. Fukuda, P. Rudolph, and S. Uda

7 **Characterization of Corrosion Products on Steel Surfaces**
Editors: Y. Waseda and S. Suzuki

Y. Waseda S. Suzuki (Eds.)

Characterization of Corrosion Products on Steel Surfaces

With 205 Figures, 2 in color and 16 Tables

Springer

Professor Yoshio Waseda
Professor Shigeru Suzuki
Institute of Multidisciplinary
Research for Advanced Materials
Tohoku University
2-1-1 Katahira, Aoba-ku
Sendai 980-8577, Japan
E-Mail: waseda@tagen.tohoku.ac.jp, ssuzuki@tagen.tohoku.ac.jp

ISSN 1435-1889
ISBN-10 3-540-35177-9 Springer Berlin Heidelberg New York
ISBN-13 978-3-540-35177-1 Springer Berlin Heidelberg New York

Library of Congress Control Number: 2006927188

Typesetting by the Authors and SPi using a Springer LaTeX macro package
Cover concept by eStudio Calmar Steinen using a background picture from Photo Studio "SONO".
Cover design: *design & production* GmbH, Heidelberg

Printed on acid-free paper SPIN: 11365617 57/3100/SPi - 5 4 3 2 1 0

Preface of Series by the Editor-in-Chief

This book entitled "Characterization of Corrosion Products on Steel Surfaces" is published as the seventh volume in the series of "Advances in Materials Research" edited by Professors Yoshio Waseda and Shigeru Suzuki. The book is composed of twelve chapters, the contents of which together try both to solve the currently important basic problems in corrosion and to contribute to the steel making industries in the realization of substantially better process engineering. It will contribute to society worldwide "for preventing environmental degradation" which the editors stressed as the subtitle of the book. The book contains recent high level research results starting from the fundamental mechanism of corrosion to various measurement tools which are used for characterization to reveal the structures of corrosion products both statically and dynamically. As series editor, I would like to thank Dr. Claus Aschelon of Springer-Verlag, who has always had interest in and kindly taken care of our research activity by encouraging publication in this series of books.

Sendai, December 2005 *Yoshiyuki Kawazoe*

Preface

The structure of corrosion products, also referred to as rust, formed on the steel surface is of great interest, because the corrosion rate of steel is known to depend strongly on the condition of such corrosion products covering the surface as a protective film. For example, the corrosion rate of weathering steel in the atmosphere is found to be considerably suppressed when an amorphous-like rust layer is formed. This enables us to reduce maintenance costs and also contributes to the beneficial utilization of iron natural resources.

On the other hand, corrosion products of iron and steel are formed by reaction of iron and its alloying elements with reactive species, such as oxygen and water, which originate from the atmosphere. Corrosion products are frequently not describable by the typical structure of iron oxides. This indicates that the structure of corrosion products is considered to be very complicated, and some parts of such iron oxides are assigned to the amorphous state for this reason. Thus, a method for characterizing the atomic-scale structure of corrosion products is strongly required, because it is likely to be related to a corrosion mechanism of metallic materials. Lifetime of steel is sometimes dominated by environmental degradation, so that the structure of corrosion products formed on the surface of steel during exposure to air for a prolonged period is of great importance. For example, the Delhi iron pillar, which was made in India about 1600 years ago, still stands without serious degradation, whereas steel structures produced by modern manufacturing methods are sometimes replaced after use for a few tens years.

Analytical techniques, such as X-ray diffraction, Fourier-transform infrared spectroscopy, electron probe microanalysis and Mössbauer spectroscopy, have been used for obtaining the structure and chemical composition of corrosion products formed on the surface of iron and steel under various atmospheric conditions. By applying these methods, for example, the corrosion product formed on the surface of the ancient Delhi iron pillar has been found to consist of α-FeOOH, γ-FeOOH, δ-FeOOH, Fe_3O_4 and iron hydrogen phosphate hydrates. Mössbauer spectroscopy also provides superparamagnetism data on oxyhydroxides, being types of FeOOH, suggesting that particles of these oxyhydroxides in corrosion products are very fine. Results from the extended X-ray absorption fine structure (EXAFS) method indicate that the fundamental local ordering structure of corrosion products

is represented mainly by FeO_6 octahedral units and hydrogen atoms are quite likely to be intercalated in these structural units of ferric oxyhydroxides. By applying these methods, characterization including structure of rust formed on the surface of weathering steel has been carried out, in order to make clear the corrosion protective property of this particular steel. Nevertheless, our present understanding of the atomic-scale structure of rust is far from complete for several reasons; the component phases in rust formed on the surface of weathering steel show imperfection of their structures and their realistic structures of components appear to deviate from an ideal crystallographic structure of typical iron oxides such as α-FeOOH and γ-FeOOH. The structure of a very thin passive film formed on the stainless steel, which plays an important role in its corrosion resistance, may be similar to that of such oxides to some extent. Although the structure of the passive film is still controversial, optical or semiconductor properties of the passive film have been extensively studied coupled with electrochemical properties.

This book provides a critical, up-to-date evaluation starting with an extended introductory treatise on the fundamentals, followed by a description of relatively new results, several advanced methods and techniques for materials characterization of corrosion products formed on the steel surface and ends with their characterization. New information is given with respect to corrosion products formed on the surface of iron-based alloys, containing chromium, nickel or copper, and weathering steel in salt water, because a few percent of these alloying elements are known to be added to iron-based alloys in order to improve corrosion protection of steel. It has also been the focusing point of this book to reveal the network structure consisting of FeO_6 octahedral units and its distortion from the ideal iron oxide case such as α-FeOOH and γ-FeOOH. This includes how the alloying elements affect the structure of rust formed on the surface of various iron-based alloys and steel.

The subject is approached from both the basic science and the applied engineering points of view. The many references, illustrations and tables provide adequate help and guidance for specialists and non-specialists who wish to become acquainted with the processing, controlling and characterization of corrosion products formed on the steel surface.

Sendai *Yoshio Waseda*
December 2005 *Shigeru Suzuki*

Contents

List of Contributors

Professor Katsuhisa Sugimoto
Educational Counseling Office
Graduate School of Engineering,
Tohoku University
Aramaki, Aoba, Aoba-ku
Sendai 980-8579, Japan
ksugimot@bureau.tohoku.ac.jp

Professor Toshiaki Ohtsuka
Graduate School of Engineering,
Hokkaido University
Kita-ku, Sapporo 060-8628 Japan
ohtsuka@elechem1-mc.eng.
hokudai.ac.jp

Professor Shinji Fujimoto
Department of Materials and
Manufacturing Science,
Graduate School of Engineering,
Osaka University
Yamada-oka 2-1, Suita, Osaka
565-0871, Japan
fujimoto@mat.eng.osaka-u.ac.jp

Doctor Hiroaki Tsuchiya
Department of Materials and
Manufacturing Science,
Graduate School of Engineering,
Osaka University
Yamada-oka 2-1, Suita, Osaka
565-0871, Japan
tsuchiya@mat.eng.osaka-u.ac.jp

Professor Atsushi Muramatsu
Institute of Multidisciplinary
Research for Advanced Materials,
Tohoku University
Katahira 2-1-1, Aoba-ku
Sendai 980-8577, Japan
mura@tagen.tohoku.ac.jp

Doctor Kiyoshi Kanie
Institute of Multidisciplinary
Research for Advanced Materials,
Tohoku University
Katahira 2-1-1, Aoba-ku
Sendai 980-8577, Japan
kanie@tagen.tohoku.ac.jp

Professor Yoshio Waseda
Institute of Multidisciplinary
Research for Advanced Materials,
Tohoku University
Katahira 2-1-1, Aoba-ku
Sendai 980-8577, Japan
waseda@tagen.tohoku.ac.jp

Professor Shigeru Suzuki
Institute of Multidisciplinary
Research for Advanced Materials,
Tohoku University
Katahira 2-1-1, Aoba-ku
Sendai 980-8577, Japan
ssuzuki@tagen.tohoku.ac.jp

Professor Masatoshi Saito
School of Health Sciences, Faculty of Medicine,
Niigata University
Asahimachi-dori 2-746,
Niigata 951-8518, Japan
masaito@clg.niigata-u.ac.jp

Professor Eiichiro Matsubara
Department of Materials Science and Engineering, Kyoto University Yoshida Honmachi,
Sakyo-ku, Kyoto, 606-8501, Japan
e.matsubara@materials.mbox.media.kyoto-u.ac.jp

Professor Katsuhiko Asami
Institute for Materials Research,
Tohoku University
Katahira 2-1-1, Aoba-ku
Sendai 980-8577, Japan
cats@imr.tohoku.ac.jp

Doctor Hiroyuki Konishi
Quantum Beam Science Directorate,
Japan Atomic Energy Agency
Kouto 1-1-1, Sayo-cho, Sayo-gun
Hyogo 679-5143, Japan
konishi@spring8.or.jp

Professor Masato Yamashita
Division of Mechanical Engineering,
Graduate School of Engineering,
University of Hyogo
Shosha 2167, Himeji
Hyogo 671-2201, Japan
yamasita@eng.u-hyogo.ac.jp

Doctor Jun′ichiro Mizuki
Quantum Beam Science Directorate,
Japan Atomic Energy Agency
Kouto 1-1-1, Sayo-cho, Sayo-gun
Hyogo 679-5143, Japan
mizuki@spring8.or.jp

Professor Hitoshi Uchida
Division of Mechanical Engineering,
Graduate School of Engineering,
University of Hyogo
Shosha 2167, Himeji
Hyogo 671-2201, Japan
uchida@eng.u-hyogo.ac.jp

Doctor Takenori Nakayama
Materials Research Laboratory,
Kobe Steel, Ltd.,
Takatukadai 1-5-5, Nishi-ku
Kobe, 615-2271, Japan
ta-nakayama@kobelco.jp

Professor Tatsuo Ishikawa
School of Chemistry, Osaka University of Education
Asahigaoka 4-698-1, Kashiwara
Osaka 582-8582, Japan
ishikawa@cc.osaka-kyoiku.ac.jp

Doctor Masao Kimura
Advanced Technology Research Laboratories,
Nippon Steel Corp.,
Shintomi 20-1, Futtsu
Chiba, 293-8511, Japan
kimura@re.nsc.co.jp

Professor Tadashi Mizoguchi
Faculty of Science, Gakushuin University,
Mejiro 1-5-1, Toshima-ku
Tokyo, 171-8588, Japan
19710113@gakushuin.ac.jp

Doctor Hiroshi Kihira
Steel Research Laboratories,
Nippon Steel Corp.,
Shintomi 20-1, Futtsu
Chiba, 293-8511, Japan
kihiras@d1.dion.ne.jp

Doctor Michio Kaneko
Steel Research Laboratories,
Nippon Steel Corp.,
Shintomi 20-1, Futtsu
Chiba, 293-8511, Japan
kaneko@re.nsc.co.jp

Professor Saburo Nasu
Department of Materials
Engineering Science
Graduate School of Engineering
Science
Osaka University
Machikaneyama-cho 1-3,
Toyonaka-city
Osaka 560-8531, Japan
nasu@mp.es.osaka-u.ac.jp

Doctor Takayuki Kamimura
Corporate Research and
Development Laboratories,
Sumitomo Metal Industries, Ltd.
Fuso-cho 1-8, Amagasaki
Hyogo 660-0891, Japan
kamimura-tky@sumitomometals.co.jp

1 Corrosion Protection Function and Breakdown Mechanism of Passive Films on Stainless Steels

Katsuhisa Sugimoto

1.1 Introduction

Stainless steels are Fe-Cr-based alloys containing more than 12% Cr (%: mass percent). The corrosion resistance of the steels depends on passive films mainly composed of Cr-oxyhydroxide. In order to understand the properties of passive films, many studies concerning the structure and composition of the films have been extensively performed [1]. Since these steels are usually used in aqueous environments, much effort has been directed towards in-situ analysis of the passive films formed in these environments [2]. As a result, the relationship between the corrosion resistance and the properties of passive films has been revealed, at least in fundamental corrosive environments [1–3].

Passive films on stainless steels are, however, heterogeneous and they have many compositional and structural defects. Therefore, it is difficult to obtain a definitive answer to corrosion problems when the corrosion results from microscopic defects in the films because analytical techniques usually measure only average composition over a relatively wide analytical area. In order to cope with such situations, an experimental technique that analyzes electrochemical properties of artificially synthesized films with various compositions in a composition range close to real passive films was begun [4,5]. Artificially synthesized passive films are called artificial passivation films. Studies using artificial passivation films have been very effective in revealing the relationship between film composition and electrochemical property [5].

Among the many types of corrosion on stainless steels, pitting is very dangerous because it arises easily in chloride-containing aqueous environments and penetrates the wall of stainless steel containers or pipes. Pitting is believed to arise at microscopic defects in a passive film. The substance of the defects and the breakdown mechanism of passive films at the defects are, however, still unclear. In this chapter, concerning pitting on Fe-Cr alloys in acidic chloride solutions, conditions for the exhibition of corrosion protection function and, in contrast, for the occurrence of breakdown will be explained for passive films on the alloys based on the results of recent studies using artificial passivation films.

1.2 Origin of Pit Initiation

In pit initiation on commercial stainless steels in neutral chloride solutions, it is well known that non-metallic inclusions in the steels, such as MnS, play an important role [6–10]. However, this chapter covers pitting on high purity stainless steels and does not consider the effect of non-metallic inclusions. Pitting occurs on stainless steel thin films formed by sputtering deposition [11, 12]. This suggests that the breakdown of passivity is one of origins of pit initiation. On the other hand, whether the passive film can exist stably in acidic chloride solutions determines whether a pit, i.e. a corrosion cavity caused by pitting, can be repassivated. Therefore, this chapter focuses on the suppression mechanism of passive film breakdown by Cr in Fe-Cr alloys.

1.3 Suppression Mechanism of Passive Film Breakdown by Alloyed Cr

The threshold Cr content above which high purity Fe-Cr alloys become immune against pitting in acidic chloride solutions can be determined by the anodic polarization curve of the alloys with a series of Cr content in 1 M HCl. Figure 1.1 shows one of examples of such polarization curves [13]. Similar measurements have been reported in the literature [14, 15]. The results reported indicate that steels become immune against pitting in 1 M HCl when their Cr content exceeds 30% [13–15].

Concerning the role of Cr in the inhibition of passive film breakdown on Fe-Cr alloys in acid chloride and other electrolyte solutions, many theories

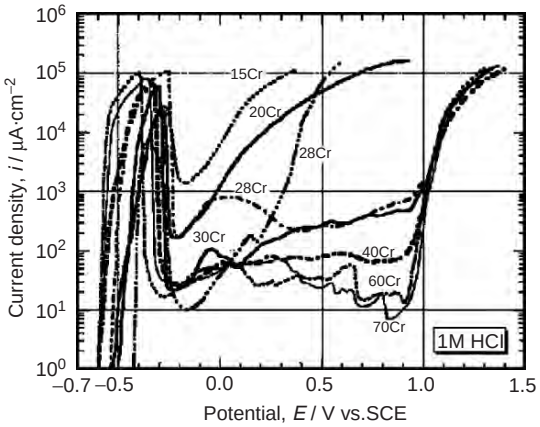

Fig. 1.1. Aodic polarization curves of Fe-Cr alloys in 1 M HCl [13]

have been proposed:

(1) Micro-pore repassivation model [16]: Cr interferes with the development of micro-pores in passive films due to rapid repassivation by the formation of passive Cr-oxyhydroxide film.
(2) Bipolar model [17]: CrO_4^{2-} enriched at the interface between an Fe-rich outer layer and a Cr-rich inner layer bipolarizes the passive film and impedes the ingress of Cl^- ions.
(3) Percolation model [11, 12, 18–20]: Cr forms a passive oxide that is a completely connected structure via first and second nearest neighbor Cr atoms in the original bcc lattice.
(4) Repassivation enhancement model [21, 22]: Cr enhances repassivation through the formation of Fe-Cr oxychloride salt films at the interface of the alloy under which passive films are formed.
(5) Cr-oxide enriched barrier layer model [23]: Cr-oxide increases in the oxide layer near the film/alloy interface, forming a more protective barrier layer.
(6) Fe_2O_3-component reduction suppression model [24, 25]: Cr suppresses the reductive dissolution of the Fe_2O_3-component in passive films which leads to passive film breakdown.

The basic ideas of the suppression of the chloride pitting by the Cr addition in models (1), (3), (4) and (5) are based on the formation of a Cr-like passive film which is immune against chloride pitting. That is, these models assume that, when an alloy is covered by such a film, the alloy becomes immune against pitting. However, the reason why the Cr-like passive film is immune against pitting should be explained from a functional viewpoint of film. Models (2) and (6) are explanations based on the function of film. However, model (2) is hard to apply to pitting in acid chloride solutions that originates at lower potentials than the transpassive dissolution potential of Cr. The last model (6) was first proposed by the authors to explain the suppression of chloride pitting by Mo on Fe-Cr-Mo alloys based on simulation experiments using artificial passivation films [24]. The model was later proved to be applicable to the suppression of pitting by Cr on Fe-Cr alloys [25]. The suppression of pitting will be explained using this model in the following sections.

1.4 Composition of Passive Films Formed in Acid Chloride Solutions

It is important at first to clarify what kind of passive film is immune against pitting in acid chloride solutions. As stated above, Fe-Cr alloys containing more than 30% Cr suffer from no pitting in 1 M HCl. Results of X-ray photoelectron spectroscopic (XPS) analysis of passive films formed on Fe-19Cr [16] and Fe-30Cr [14] alloys at various potentials in 1 M HCl have been reported. Figure 1.2 shows cationic fraction as a function of potential for the passive

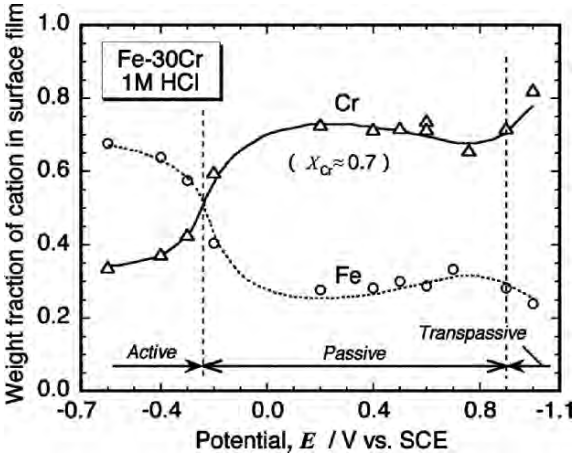

Fig. 1.2. Cationic mass fraction of elements as a function of potential for passive films formed on Fe-30Cr alloy in 1 M HCl [14]

film on the Fe-30Cr alloy reorganized from the original figure of Hashimoto et al. [14]. The cationic fraction of Cr, X_{Cr}, for passive films on Fe-30Cr alloy, which is immune against pitting, is approximately 0.7. On the other hand, that for passive films on the Fe-19Cr alloy, which is susceptible to pitting, is approximately 0.57 [16]. That is, the immunity against pitting in 1 M HCl can be attained at X_{Cr} = ca. 0.7. An explanation should be found for the question why the immunity against pitting is attained at X_{Cr} = ca. 0.7. The application of artificial passivation films, which are the analogue of passive films, is very convenient for examining the quantitative relationship between the composition and the function of films.

1.5 Fabrication of Artificial Passivation Films

Metallorganic chemical vapor deposition (MOCVD) [26, 27] and ion-beam sputter deposition (IBSD) [24, 25] have been employed for film formation. The former provides amorphous oxide films with higher OH^- content [5, 27]. However, it needs complicated control in order to obtain given composition and thickness. The latter gives amorphous oxide films with lower OH^- content but the control of composition and thickness is easy. Although the former is preferable from the viewpoint of the OH^- content, the latter has been commonly employed for ease in the control of composition and thickness.

In the formation of Fe_2O_3-Cr_2O_3 artificial passivation films by IBSD, high purity Ar is used for the ion source. A complex target is composed of a Cr_2O_3 plate and small Fe_2O_3 tablets. The maximum and the working degree of vacuum are 2.39×10^{-5} Pa and 1.46×10^{-2} Pa, respectively. The

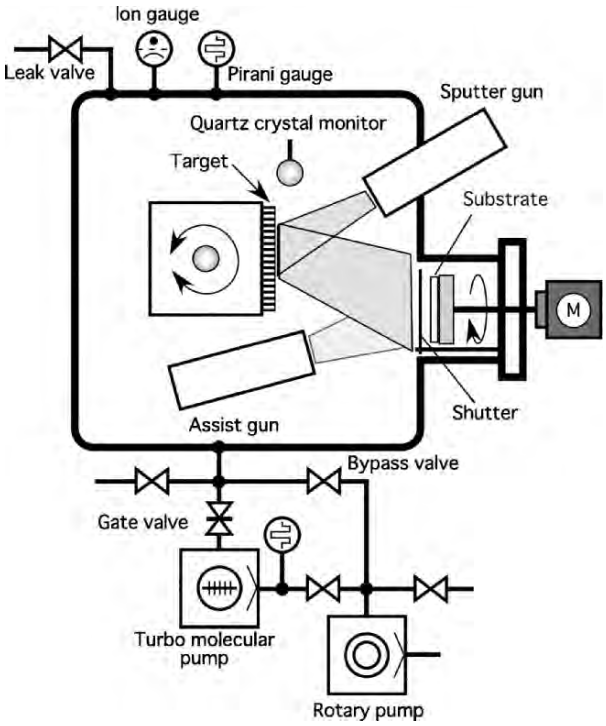

Fig. 1.3. Schematic diagram of ion-beam sputter deposition apparatus [28]

thickness of films formed is usually about 50 nm. The schematic diagram of the ion-beam sputtering system is given in Fig. 1.3 [28].

The chemical state of constituent elements in the film was analyzed by XPS. Figure 1.4 shows measured Fe 2p, Cr 2p and O 1s XPS spectra for Fe_2O_3-Cr_2O_3 films with X_{Cr} = 0.00–1.00 [28]. The films are composed of Fe^{3+} ions, Cr^{3+} ions, and O^{2-} ions with MO_x and $M(OH)_y$ type bonds (M: metal element). The deconvolution of Fe 2p and Cr 2p spectra revealed that Fe^{3+} ions exist as Fe_2O_3 and FeOOH type bonds and Cr^{3+} ions as Cr_2O_3 and $Cr(OH)_3$ type bonds [27, 28]. These chemical states of elements are just the same as those in real passive films [1].

AES depth profiles of elements in an Fe_2O_3-Cr_2O_3 film with X_{Cr} = 0.36 are shown in Fig. 1.5 [28]. The distribution of Fe, Cr and O content in the film is uniform from the top to the bottom of the film. Consequently, homogeneous films with given composition in the depth direction can be formed by IBSD.

From electron diffraction patterns and transmission electron micrographs, Fe_2O_3-Cr_2O_3 films with X_{Cr} larger than 0.35 are amorphous [28]. These films are not a mixture but a solid solution of Fe_2O_3 and Cr_2O_3.

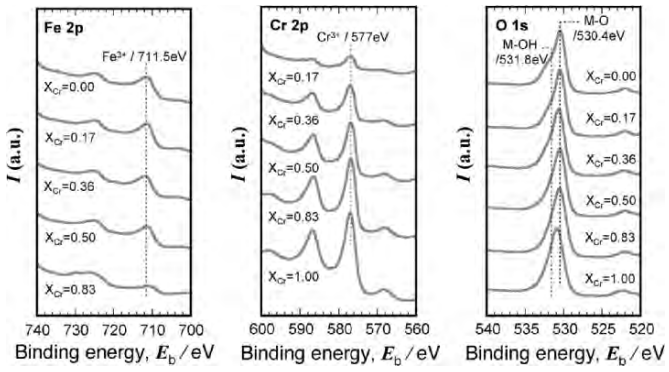

Fig. 1.4. XPS spectra for Fe_2O_3-Cr_2O_3 films with various X_{Cr} values [28]

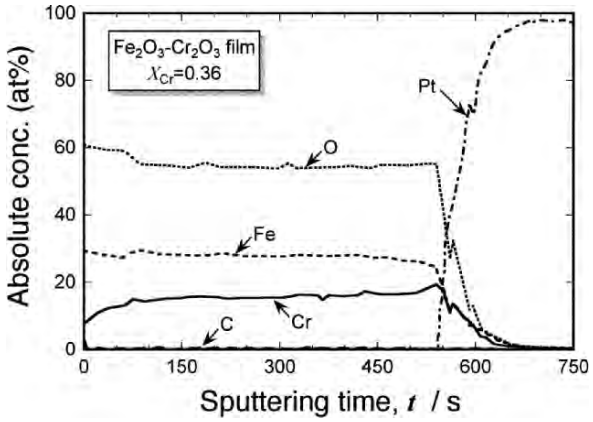

Fig. 1.5. AES in-depth profile of Fe_2O_3-Cr_2O_3 film with $X_{Cr} = 0.36$ [28]

1.6 Evaluation of Corrosion Resistance of Artificial Passivation Films

The electrochemical properties and corrosion resistance of Fe_2O_3-Cr_2O_3 films were examined by measuring the change in film thickness at various potentials in corrosive aqueous solutions using ellipsometry [4, 5]. This measurement technique is the same as that used for the measurement of thickness of passive films on stainless steels in solutions [1–3]. Figure 1.6 shows the schematic diagram of the apparatus used for the measurements [29]. The potential of specimens was controlled by a potentiostat in deaerated 1M HCl. The ellipsometric change in the surface of specimen was measured by a rotating analyzer type automatic ellipsometer. In the measurement and analysis, the three-parameter method was employed. That is, the relative phase retardation, Δ, the relative amplitude reduction, tanΨ, and the relative reflectivity, ΔR/R, were measured and the thickness, d, and the optical constant,

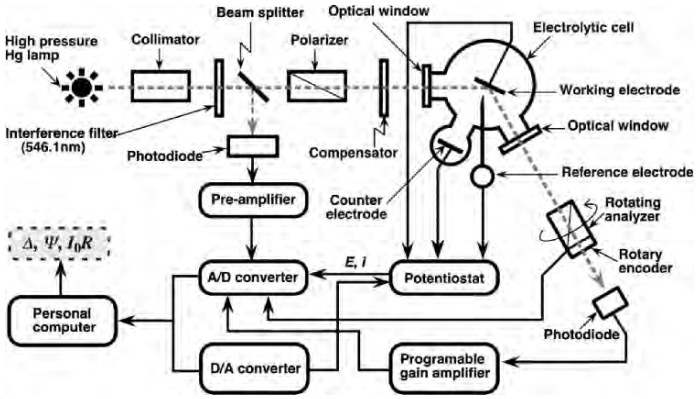

Fig. 1.6. Schematic diagram of electrochemical ellipsometric apparatus [29]

$N_2 = n_2 - k_2 i$, were calculated by Drude's optical equations using the three parameters measured. The thinning rate of film thickness was obtained from the gradient of decrease in film thickness vs time curve.

1.7 Dissolution Behavior of Fe_2O_3-Cr_2O_3 Films

Anodic and cathodic polarization curves of Fe_2O_3-Cr_2O_3 films with a series of X_{Cr} values in 1 M HCl at 298 K are shown in Fig. 1.7 [28]. The potential region under 0.5 V (vs Ag/AgCl, 3.33 M KCl) is the cathodic region. In this region, the films with X_{Cr} values of 0.00–0.50 show reductive currents at potentials from −0.2 V to 0.5 V. The increase in cathodic currents under −0.2 V is due to H_2 evolution. The potential region above 0.5 V is the anodic region. In the region of 0.5–1.0 V below the transpassive dissolution potential of Cr_2O_3-component, all films show very small currents corresponding to the passive current. That is, the Fe_2O_3-Cr_2O_3 films suffer from no pitting. Above 1.0 V, the films with X_{Cr} values of 0.17–1.00 show increases in anodic currents by the transpassive dissolution of the Cr_2O_3-component. The films with X_{Cr} values of 0.00–0.17 show Cl_2 evolution above 1.1 V and O_2 evolution above 1.5 V.

Figure 1.8 shows film thinning rate as a function of potential for the films in 1 M HCl [25]. Decreases in film thickness occur on the films with X_{Cr} values of 0.00–0.50 owing to the reductive dissolution of the Fe_2O_3-component ($Fe_2O_3 + 6H^+ + 2e^- \rightarrow 2Fe^{2+} + 3H_2O$) below 0.6 V. They also occur on the films with X_{Cr} values of 0.30–1.00 owing to the transpassive dissolution of the Cr_2O_3-component ($Cr_2O_3 + 4H_2O \rightarrow {Cr_2O_7}^{2-} + 8H^+ + 6e^-$) above 0.9 V. In the potential region between 0.6 V and 0.9 V there is no dissolution of any component of the films. Based on such a relationship between the thinning rate of film thickness and potential, the reductive dissolution region of the Fe_2O_3-component was designated as Region I, the region without dissolution

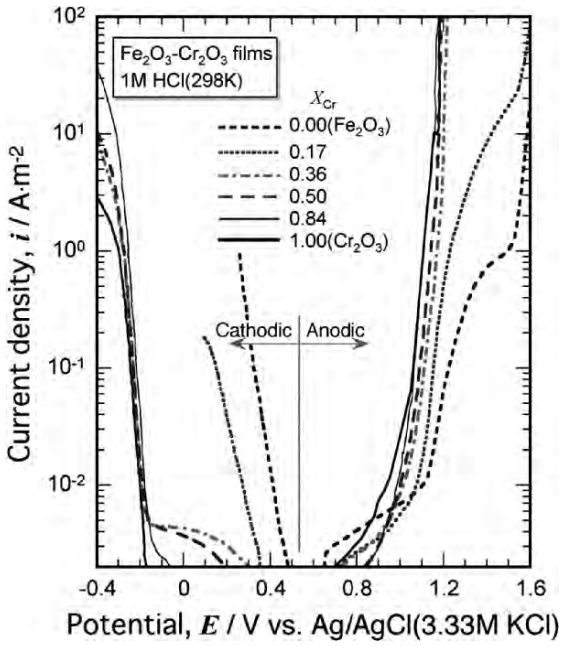

Fig. 1.7. Anodic and cathodic polarization curves of Fe_2O_3-Cr_2O_3 films in 1 M HCl [28]

as Region II, and the transpassive dissolution region of the Cr_2O_3-component as Region III. Region II is the intrinsic passivity region of Fe_2O_3-Cr_2O_3 films [30]. It is important that no pitting occurs on Fe_2O_3-Cr_2O_3 films in the anodic region.

In order to get the X_{Cr} value at which the reductive dissolution of the Fe_2O_3-component is suppressed, the relationship between the thinning rate of film thickness and the X_{Cr} value at -0.3 V in 1 M HCl is shown in Fig. 1.9. The thinning rate reached the analytical limit of ellipsometry at $X_{Cr} = 0.72$. That is, the Fe_2O_3-Cr_2O_3 films with X_{Cr} values larger than 0.72 cause no breakdown by reductive dissolution in 1 M HCl.

1.8 Anodic Polarization Behavior of Fe-Cr Alloys

Anodic polarization curves of high purity Fe-Cr alloys containing 10–30% Cr in 1 M HCl are shown in Fig. 1.10 [25]. This figure is similar to Fig. 1.1 but the purity of alloys used is much higher than those used for Fig. 1.1. As shown in Fig. 1.10, the alloys containing 10–25% Cr undergo pitting but the alloy containing 30% Cr does not suffer from pitting in this solution. This coincides well with the description of Fig. 1.1 [13–15]. The current density in the passive state of Fe-30Cr alloy is, however, unstable, showing that the

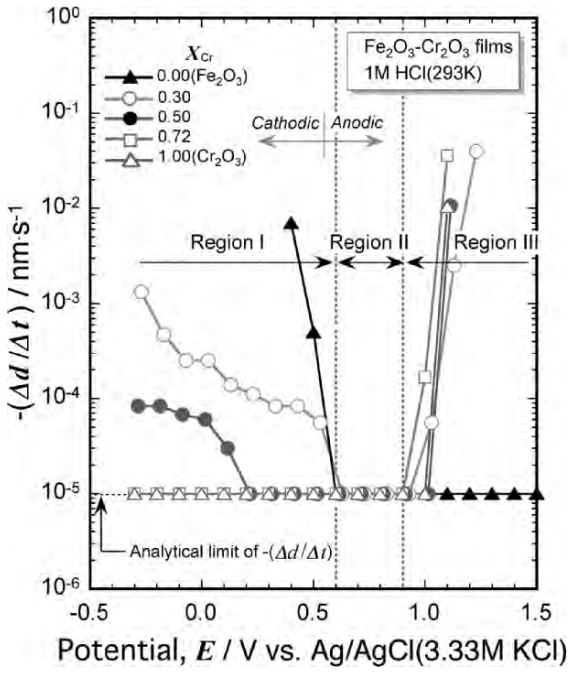

Fig. 1.8. Thinning rate of film thickness as a function of potential for Fe_2O_3-Cr_2O_3 films in 1M HCl [25]

passive film on the alloy has threshold composition for passivation in this solution. The three regions observed on the dissolution behavior of Fe_2O_3-Cr_2O_3 films were also present in Fig. 1.10. It should be noted that pitting occurs on low Cr alloys in Region I. That is, if part of a passive film has composition which is susceptible to reductive dissolution, that part should be broken down by reductive dissolution in the potential range of Region I.

1.9 Composition of Passive Films on Fe-Cr Alloys

In order to examine the change in the composition of passive films with potential, the surfaces of Fe-30Cr alloy treated at various potentials in 1M HCl for 3.6 ks were analyzed by Auger electron spectroscopy (AES) using Ar^+ ion sputtering at the same time. Figure 1.11 shows in-depth profiles of cationic mole fraction of elements in passive films [25]. It was found that the films formed at 0.3 V and 0.7 V have X_{Cr} values of about 0.6. This value is very close to the threshold value of 0.72, which is needed to suppress the reductive dissolution of the Fe_2O_3-component in Fe_2O_3-Cr_2O_3 films. The X_{Cr} values of the passive films on Fe-30Cr alloy are slightly lower than the threshold value. However, their real X_{Cr} values should be close to or higher than the threshold value because the AES signals of Fe and Cr from passive

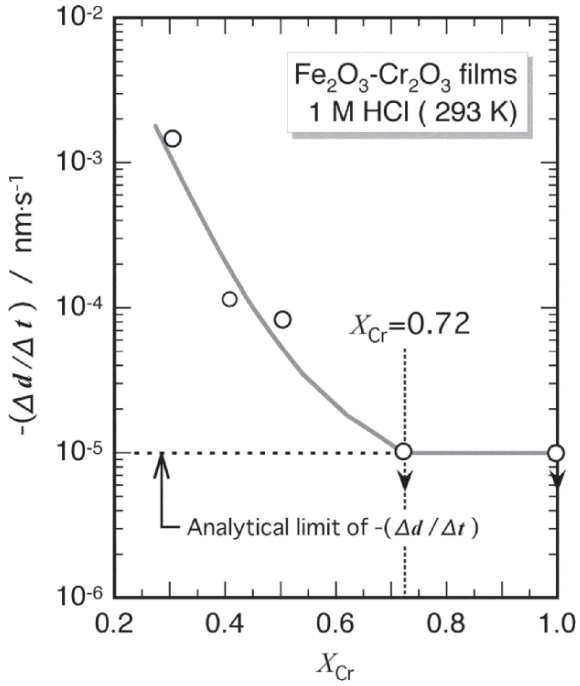

Fig. 1.9. Thinning rate of film thickness as a function of X_{Cr} value for Fe_2O_3-Cr_2O_3 films at −0.3 V in 1M HCl

films of about 2.7 nm thickness [14] under sputtering inevitably contain the signals from the alloy matrix and this sometimes makes the analytical values of Cr lower. Weight fractions of 0.6–0.7 have been reported for Cr cations in passive films on Fe-30Cr alloy at potentials between –0.16 V and 0.92 V in 1M HCl by quantitative XPS analysis without sputtering [14].

1.10 Comparison of Dissolution Behavior Between Fe_2O_3-Cr_2O_3 Artificial Passivation Film and Real Passive Film on Fe-Cr Alloy

Based on the dissolution behavior of Fe_2O_3-Cr_2O_3 film with potential, the passivation behavior of Fe-Cr alloy can be examined. Figure 1.12 compares the anodic polarization curve of Fe-30Cr alloy with the thinning rate vs potential curve of Fe_2O_3-Cr_2O_3 film with X_{Cr} = 0.72 in 1M HCl [25]. The composition of Fe_2O_3-Cr_2O_3 film simulates the threshold value which is needed to suppress the reductive dissolution of the Fe_2O_3-component in Fe_2O_3-Cr_2O_3 films in 1M HCl. It can be seen that the film with X_{Cr} = 0.72 hardly dissolves in the potential range between –0.3 V and 0.9 V, and this potential range corresponds well to the passivity region of Fe-30Cr alloy. From this fact, it

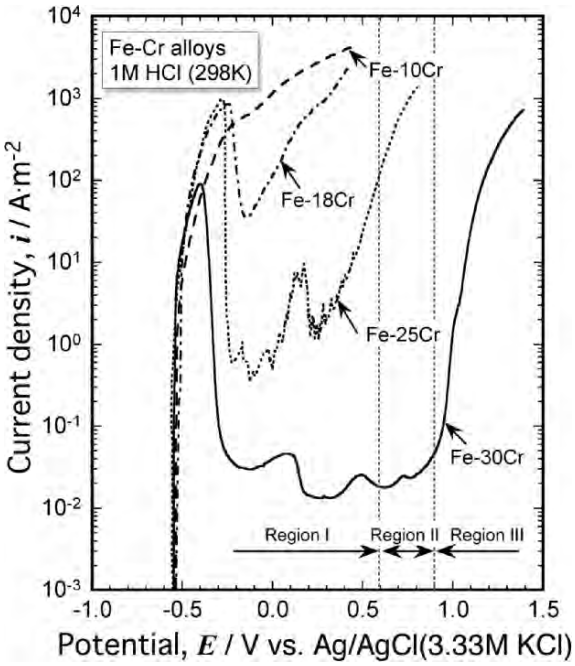

Fig. 1.10. Anodic polarization curves of high purity Fe-Cr alloys containing 10–30% Cr in 1 M HCl [25]

is thought that if the passive films contain an adequate amount of Cr_2O_3, which can suppress the dissolution in Region I, no pitting occurs on Fe-Cr alloys as Fe-30Cr alloy is stable up to 0.9 V in HCl.

1.11 Induction Period of Pitting on Fe-Cr Alloys

Since no dissolution occurs on Fe_2O_3-Cr_2O_3 films in Region II, there is a possibility that no pitting occurs on Fe-Cr alloys in this potential region. To substantiate this, induction periods for pitting were measured on Fe-20Cr alloy. In this measurement, the alloy was first passivated at given potentials in 1 M H_2SO_4 at 298 K for 18 ks and then the solution was switched over to 0.8 M H_2SO_4 + 0.4 M HCl + 0.6 M NaCl at 298 K while retaining the potentials. The induction time was defined as the time for the initiation of a continuous increase in current by pitting. Figure 1.13 shows the induction period for pitting as a function of potential [25]. Pitting started after a short time in the potential region between –0.1V and 0.3V. No initiation of pitting was observed up to 18 ks in the region between 0.5V and 0.7V. Pitting was observed at 0.9V due to the slight transpassive dissolution of passive film.

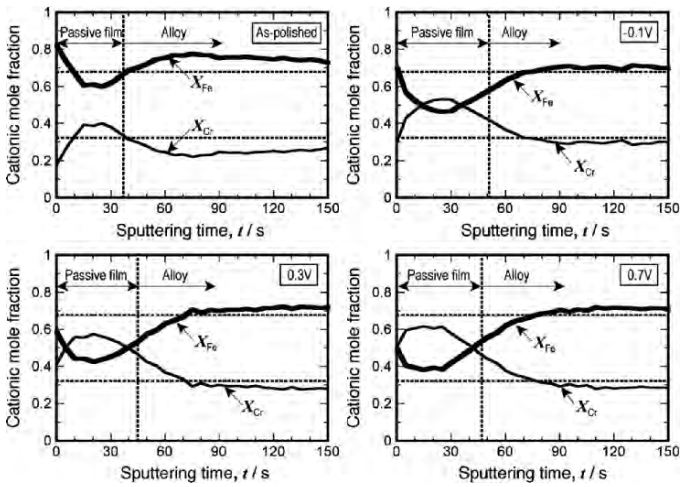

Fig. 1.11. AES in-depth profiles of cationic mole fraction of elements in passive films formed on Fe-30Cr alloy at various potentials in 1M HCl for 3.6 ks [25]

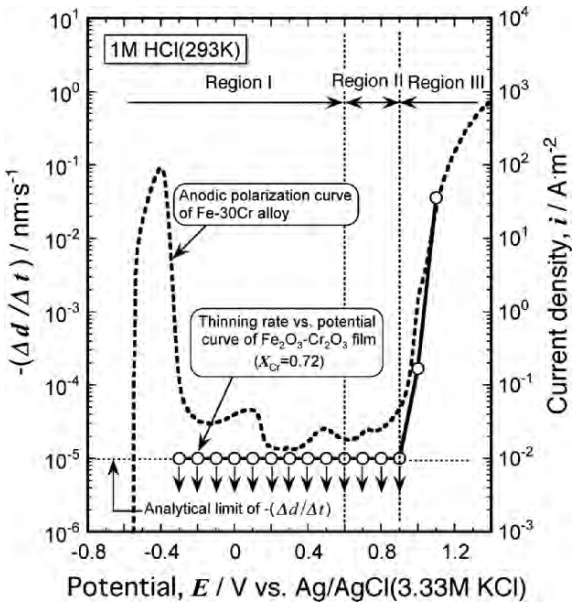

Fig. 1.12. Anodic polarization curve of Fe-30Cr alloy and thinning rate vs potential curve of Fe_2O_3-Cr_2O_3 film with $X_{Cr} = 0.72$ in 1M HCl [25]

That is, if a passive film is formed at a potential in Region II and then exposed to the Cl^--containing solution at the same potential, no pitting occurs [25].

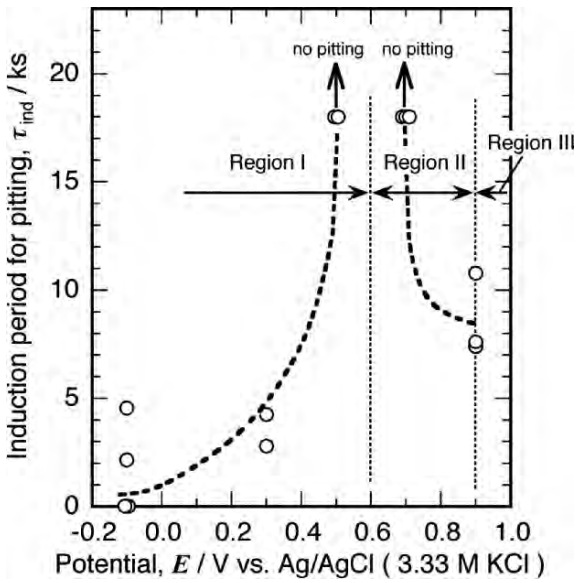

Fig. 1.13. Induction period for pitting as a function of potential for Fe-20Cr alloy first passivated in 1M H_2SO_4 and then kept in 0.8 M H_2SO_4 + 0.4 M HCl + 0.6 M NaCl [25]

1.12 Pitting Potentials of Fe-Cr Alloys in 1M HCl

In order to determine empirically the potential where pitting starts, pitting potentials of Fe-Cr alloys in 1M HCl reported in literatures [13, 14, 16, 24, 31, 32] were reviewed. Figure 1.14 shows pitting potential as a function of Cr content of alloys [25]. Almost all pitting potentials for Fe-Cr alloys containing 14–25% Cr exist between –0.23 V and 0.32 V, that is, in Region I. The pitting potentials for alloys containing 28–30% Cr jump up to over 0.98 V. Pitting potential is not the breakdown potential of passive film but the start potential of stable pitting. However, the breakdown potential should be very close to the pitting potential in a low pH and high Cl^- concentration environment such as 1 M HCl. The fact that pitting occurs in Region I suggests that, if the reductive dissolution of Fe_2O_3-component in passive films is suppressed, the breakdown of passive films, which leads to pitting, can be avoided [25].

1.13 Dissolution of Locally Heterogeneous Fe_2O_3-Cr_2O_3 Film

Since the reductive dissolution of low Cr_2O_3 concentration parts in passive films is thought to be responsible for pit initiation, an Fe_2O_3-Cr_2O_3 film with a low Cr_2O_3 concentration part was made and the dissolution behavior of the

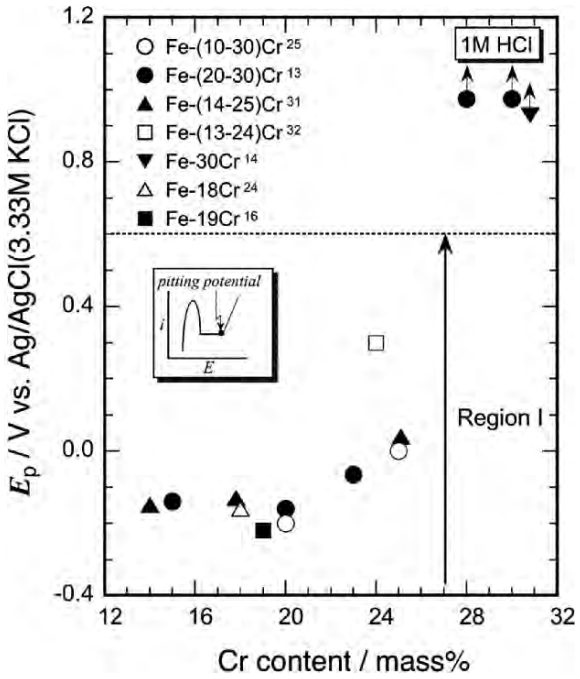

Fig. 1.14. Pitting potential as a function of Cr content for Fe-Cr alloys in 1M HCl reported in the literature [25]

film was examined at potentials in Regions I and II. Figure 1.15 shows optical micrographs of an Fe_2O_3-Cr_2O_3 film with a local part having $X_{Cr} = 0.24$ in a main part having $X_{Cr} = 0.76$ on a Type 304 substrate before and after potentiostatic polarization testing at –0.1V in Region I in 1 M HCl for 1.8 ks [25]. The diameter of the local part was 0.5 mm. The film of the local part was dissolved away after the polarization and the Type 304 substrate under the local part was severely pitted. An Fe_2O_3-Cr_2O_3 film with a local part having $X_{Cr} = 0.24$ in a main part having $X_{Cr} = 0.76$ was also made and tested at 0.7V in Region II in 1M HCl. The film of the local part was not dissolved at this potential [25].

1.14 Mechanism of pit Initiation on Fe-Cr Alloy

Based on the above discussion, the mechanism of pit initiation in an HCl solution can be presumed to be as shown in Fig. 1.16 [25].

In the case of low Cr alloys, the X_{Cr} value of passive films is not so high. Therefore, if the passive films have a localized Cr-depleted part, the X_{Cr} value of the part should be lower than the threshold X_{Cr} value that suppresses the reductive dissolution of Fe_2O_3-component in the films. Consequently, the Cr-depleted part causes the reductive dissolution at potentials in Region I. Since

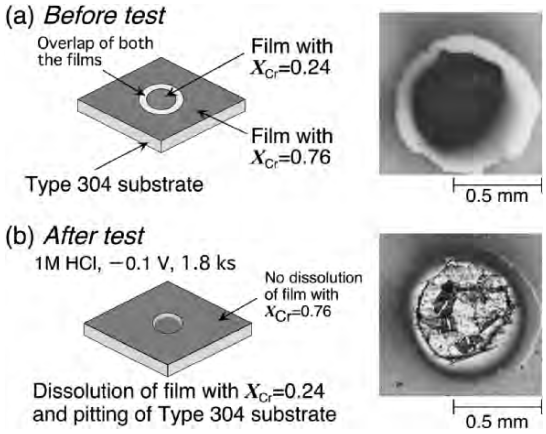

Fig. 1.15. Micrographs of Fe_2O_3-Cr_2O_3 film with locally low Cr_2O_3 concentration part on Type 304 substrate before and after polarization at −0.1 V in 1M HCl for 1.8ks [25]

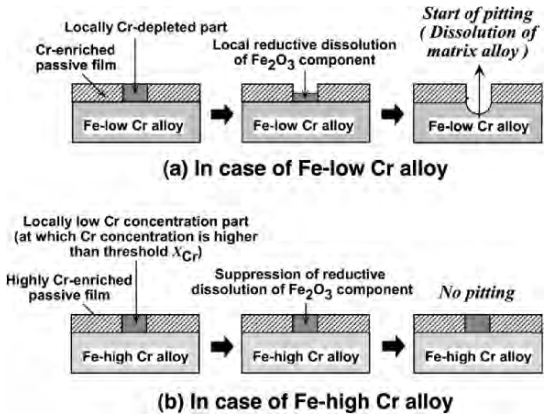

Fig. 1.16. Conceptional drawing of pit initiation mechanism on high purity Fe-Cr alloys in HCl solutions

the potentials in Region I for Fe-Cr alloys are anodic potentials (see Fig. 1.10), the alloy matrix exposed to an HCl solution by the local breakdown of passive film causes anodic dissolution. The anodic dissolution at the exposed part of the matrix continues because repassivation is impossible in this solution.

On the other hand, in case of high Cr alloys, the X_{Cr} value of passive films is high in general. Therefore, even if there is a localized Cr-depleted part in passive films, the X_{Cr} value of the part should be higher than the threshold X_{Cr} value. Consequently, the part causes no reductive dissolution at potentials in Region I and no pitting occurs at the part.

As stated before, pits are considered to initiate through the dissolution of sulfide inclusions in low purity Fe-Cr alloys [6–10]. Whether a pit repassivates or not in this case is dependent on the X_{Cr} value of passive film formed inside a pit. That is, if the X_{Cr} value exceeds the threshold value that is needed to suppress the reductive dissolution of the film in a solution with low pH and high Cl^- concentration inside a grown pit, the pit should be repassivated.

1.15 Summary

Film thinning rate as a function of potential for Fe_2O_3-Cr_2O_3 films in 1 M HCl shows the reductive dissolution region of the Fe_2O_3-component, no dissolution region of both the components, and the transpassive dissolution region of the Cr_2O_3-component. The reductive dissolution of the Fe_2O_3-component of the films can be suppressed by increasing Cr_2O_3 content.

Fe-30Cr alloy with a passive film having the threshold X_{Cr} value for suppression of the reductive dissolution of the Fe_2O_3-component suffers from no pitting in 1 M HCl. Fe-Cr alloys containing 14–25% Cr are susceptible to pitting in 1 M HCl and their pitting potentials exist in the reductive dissolution region of the Fe_2O_3-component in passive films. No initiation of pitting was observed on Fe-20Cr alloy in an acid solution containing 1 M Cl^- in the no dissolution region of both the components between 0.6V and 0.7V.

Potentiostatic polarization tests of Type 304 coated with a heterogeneous film with a localized small part of low Cr_2O_3 content in a wide matrix of high Cr_2O_3 content showed the initiation of pitting on the substrate Type 304 by the reductive dissolution of the small part in 1M HCl.

For the above reasons, the suppression of the reductive dissolution of the Fe_2O_3-component in passive films is presumed to be effective on the suppression of pitting in 1M HCl.

References

1. K. Sugimoto: Tetsu-to-Hagane, **70**, 637 (1984).
2. K. Sugimoto: Hyomen Kagaku, **9**, 61 (1988).
3. K. Sugimoto: Materia, **36**, 900 (1997).
4. K. Sugimoto: Materia, **34**, 1042 (1995).
5. K. Sugimoto: Zairyo-to-Kankyo, **47**, 616 (1998).
6. G. S. Eklund: J. Electrochem. Soc., **121**, 457 (1974).
7. S. E. Lott and R. C. Alkire: J. Electrochem. Soc., **136**, 973 (1989).
8. M. A. Baker and J. E. Castle: Corros. Sci., **34**, 667 (1993).
9. H. Böhni, T. Suter, and A. Schreyer: Electrochim. Acta, **40**, 1361 (1995).
10. D. E. Williams, T. F. Mohiuddin, and Y. Y. Zhu: J. Electrochem. Soc., **145**, 2664 (1998).
11. D. E. Williams, R. C. Newman, Q. Song, and R. G. Kelly: Nature, **350**, 216 (1991).

12. M. P. Ryan, N. J. Laycock, R. C. Newman, and H. S. Isaacs: J. Electrochem. Soc., **145**, 1566 (1998).
13. K. Sugimoto and Y. Sawada: Corros. Sci., **17**, 425 (1977).
14. K. Hashimoto, K. Asami, and K. Teramoto: Corros. Sci., **19**, 3 (1979).
15. K. Sugimoto, N. Hara, M. Isshiki, T. Ejima, and K. Igaki: J. Jpn. Inst. Metals, **46**, 703 (1982).
16. K. Hashimoto and K. Asami: Corros. Sci., **19**, 251 (1979).
17. A. R. Brooks, C. R. Clayton, K. Doss, and Y. C. Lu: J. Electrochem. Soc., **133**, 2459 (1986).
18. R. C. Newman, T. -M. Foong, and K. Sieradzki: Corros. Sci., **28**, 523 (1988).
19. S. Fujimoto, R. C. Newman, G. S. Smith, S. P. Kaye, H. Kheyrandish, and J. S. Colligon: Corros. Sci., **35**, 51 (1993).
20. A. J. Davenport, M. P. Ryan, M. C. Simmonds, P. Ermst, R. C. Newman, S. R. Sutton, and J. S. Colligon: J. Electrochem. Soc., **148**, B217 (2001).
21. U. Steinsmo and H. S. Isaacs: Corros. Sci., **35**, 83 (1993).
22. U. Steinsmo and H. S. Isaacs: J. Electrochem. Soc., **140**, 643 (1993).
23. W. P. Yang, D. Costa, and P. Marcus: J. Electrochem. Soc., **141**, 2669 (1994).
24. M. Son, N. Akao, N. Hara, and K. Sugimoto: J. Electrochem. Soc., **148**, B43 (2001).
25. K. Sugimoto, M. Son, Y. Ohya, N. Akao, and N. Hara: Corrosion Science – A Retrospective and Current Status in Honor of Robert P. Frankenthal, Electrochemical Society Proceedings Volume 2002-13, G. S. Frankel, H. S. Isaacs, J. R. Scully and J. D. Sinclair, Editors, p. 289, The Electrochemical Society, Pennington, (2002).
26. K. Sugimoto, M. Seto, S. Tanaka, and N. Hara: J. Electrochem. Soc. **140**, 1586 (1993).
27. H. Kim, N. Hara, and K. Sugimoto: J. Electrochem. Soc. **146**, 3679 (1999).
28. M. Son: Ph. D. Thesis, Tohoku University (2000).
29. K. Sugimoto: Electrochemistry, **62**, 212 (1994).
30. S. Tanaka, N. Hara, and K. Sugimoto: Mater. Sci. Eng. A, **198**, 63 (1995).
31. H. Chujo: Bachelor Thesis, Tohoku University (1998).
32. R. Goetz, J. Larrent, and D. Landolt: Corros. Sci., **25**, 1115 (1985).

2 Passivation Oxide Films and Rust Layers on Iron

Toshiaki Ohtsuka

2.1 Introduction

In inhibiting the against corrosion of iron and steel, hydrated or dehydrated surface oxide films which are formed in the oxidative environment play a major role. The passivation film consisting of thin oxide film a few nm thick can move down the dissolution current by several orders due to a slight potential ennhancement from active potential to passive potential. The passive films formed on pure iron are not so stable and consequently the passivation state of iron is not maintained for prolonged time periods. However, chromium alloys like stainless steels exhibit stable passivation which is maintained for long time periods even under non-oxidative environments.

Under an oxidative environment, relatively thick oxide rusts are also formed on iron and steels. Although the presence of the passivation film with nm order thickness is impossible to see by the naked eye, the rust layer can grow with time to a few hundreds μm and is easily visible by the naked eye. The rust layers of steels occasionally play a role as a barrier against corrosion, and their growth rate is decreased to a rate similar to that of the passive films, when suitable elements are added to the steel.

The composition of passivation film has not been made clear. It is assumed that the film consists of γ-Fe_2O_3 which may be hydrated, or γ-FeOOH. In contrast, the rust layers on iron and steel are claimed to consist of various types of FeOOH and Fe_3O_4. Although both oxide layers are not considered to be very different from each other, the passive film with nm order thickness allows the substrate iron and steels to be adequately protected, while the rust layers are able to grow to several hundred μm.

In this chapter, the passivation film on pure iron and rust layers on iron and steels are reviewed, and the difference between the passivation film and rust layers is discussed.

2.2 Passivation Oxide Films on Iron

Passivation films on iron have been studied with regard to thickness and physical properties under electrochemical potential control. Passivation films on iron are also formed by action of strong oxidants such as chromate and

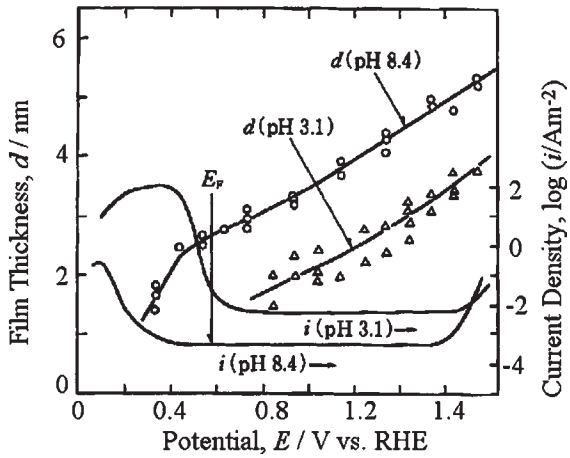

Fig. 2.1. Film thickness-potential and current density (cd)-potential relations under the stationary state. Since a long time period was required to reach the stationary state in neutral solution, the thickness and cd were taken after 1 h polarization at a constant potential. The potential scale was with reference to a reversible hydrogen electrode in the same solution (RHE)

nitrite ions [1]. Passivation under potential control (electrochemical passivation) and passivation by oxidant (chemical passivation) are basically assumed to be the same. The essential factor for passivation is an oxidative condition induced by high anodic electrode potential or a strongly oxidative agency.

The thickness of the passivation film on iron has been estimated by optical techniques such as ellipsometry. Figure 2.1 shows the thickness-anodic potential relation of the passivation film measured by ellipsometry [2,3]. The film was formed by 1 h constant potential oxidation in borate solution at pH 8.4 and phosphate solution at pH 3.1. The current density (cd) taken after 1 h oxidation is also plotted in Fig. 2.1. The potential scale is with reference to a reversible hydrogen electrode in the same solution (RHE). The thickness of the passivation film increases linearly with increase of potential and the cd is kept almost constant in the passive potential region, depending on the solution pH. The logarithm of the stationary passive cd is linearly proportional to the solution pH in acidic solutions [4, 5].

Dependence of the thickness and cd of the passivation film on potential and solution pH under stationary conditions is considered in the following way [6, 7]. When one assumes a stationary condition under which the film thickness is constant and independent of time, the rate of ionic transfer of Fe^{3+} across the substrate/oxide film interface is the same as that across the oxide film/solution interface. A schematic model of the passivation film under the stationary condition is shown in Fig. 2.2. The rate is also similar to the ionic migration rate through the oxide film. Since the amount of anions, O^{2-} or OH^{-} comprising the oxide matrix is constant under the stationary

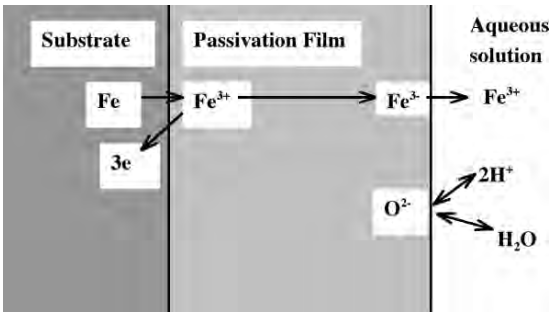

Fig. 2.2. Model of ionic migration of iron electrode passivated under the stationary state. Under the stationary state, since the film mass is assumed to be constant, the amount of O^{2-} and/or OH^- comprising the matrix of the film should be constant and be in equilibrium with H_2O in aqueous phase

condition, the anions are assumed to be in equilibrium with the water molecules in aqueous phase:

$$O^{2-}_{(ox)} + 2H^{+}_{(soln)} = H_2O_{(soln)}$$

$$OH^{-}_{(ox)} + H^{+}_{(soln)} = H_2O_{(soln)}$$

The interfacial potential deference between the oxide film and aqueous solution is estimated from an electrochemical equilibrium of the above reactions:

$$\phi_{(ox/soln)} = \phi_0 - 2.303(RT/F)pH \tag{2.1}$$

where ϕ_0 is an equilibrium potential at pH = 0. Since the charge transfer rate of ferric ions across the interface between the oxide film and aqueous solution is accelerated by the interfacial potential difference, the cd, $i_{(ox/soln)}$, under the stationary condition is determined by the interfacial potential difference or the solution pH.

$$\begin{aligned} \ln i_{(ox/soln)} &= \ln i_0 + (\beta F/RT)\phi_{(ox/soln)} \\ &= \ln i_0 + (\beta F/RT)\{\phi_0 - 2.303(RT/F)pH\} \\ &= \ln i_0 + (\beta F/RT)\phi_0 - 2.303\beta pH \end{aligned} \tag{2.2}$$

where i_0 is a stationary cd at pH = 0 and β is a value of (transfer coefficient of the cationic transfer) × (valence of transfer cations).

The ionic migration of Fe^{3+} through the oxide film is followed by a high-field assisted ionic migration mechanism [8, 9]:

$$\ln i_{(ox)} = \ln i_0^* + (zaF/RT)(d\phi/dx) \tag{2.3}$$

where $i_{(ox)}$ is migration current of Fe(III) ions through the oxide film, $d\phi/dx$ electric field intensity in the film, i_0^* an exchange migration current at

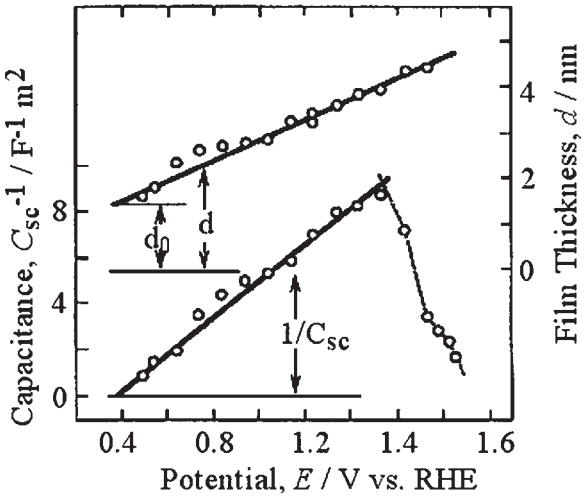

Fig. 2.3. Inverse of capacitance of the filmed iron electrode and thickness of passivation film on iron in neutral borate solution at pH 6.4 as a function of potential formed

$(\mathrm{d}\phi/\mathrm{d}x) = 0$, z valency of the migration ion, and a half-jump distance or activation distance. If one assumes for $(\mathrm{d}\phi/\mathrm{d}x)$ the average electric field, $\Delta\phi/d$ where d is the film thickness, the ionic current can be related to the film thickness:

$$\ln i_{(\mathrm{ox})} = \ln i_0^* + (z a \mathrm{F}/\mathrm{R}T)(\Delta\phi/d) \tag{2.4}$$

Since the ionic migration current is equal to the ionic transfer currents at the interfaces between substrate iron and oxide film and between the oxide film and solution under the stationary condition, the thickness measured can be related to the potential difference, $\Delta\phi$ and solution pH from Eqs. (2.2) and (2.4):

$$d = \Delta\phi(z a \mathrm{F}/\mathrm{R}T)\{\ln(i_0/i_0^*) - 2.3\beta pH + \beta \mathrm{F}\phi_0/\mathrm{R}T\}^{-1} \tag{2.5}$$

Equation (2.5) indicates that the film thickness increases linearly with $\Delta\phi$ at constant pH. Under the condition of constant $\Delta\phi, d^{-1}$ increases with increase of solution pH, i.e., the thickness decreases with increasing solution pH. The experimental results are in agreement with those expected from the equation [4].

In the derivation of $\mathrm{d}\phi/\mathrm{d}x = \Delta\phi/d$, the potential drop in the passivation oxide film was assumed to be homogeneously distributed over the whole film. For estimating the potential distribution in the oxide film, the AC capacitance of the filmed iron electrode has been measured. Figure 2.3 shows details of capacitance of iron covered by the passivation film in borate solution at pH 6.4 [10]. In Fig. 2.3, the thickness of the passive film measured by ellipsometry was also plotted. The individual capacitance values were estimated by AC

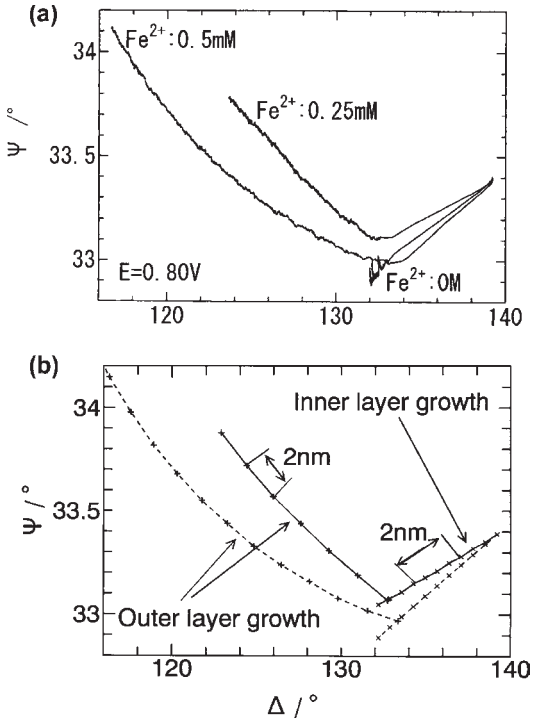

Fig. 2.4. (**a**) Ellipsometric loci of $\Psi - \Delta$ during the growth of passivation film on iron in neutral borate solution at pH 8.4 containing Fe(II) ions at various concentrations. (**b**) Simulation plot of $\Psi - \Delta$ loci during the film growth. The complex refractive index was assumed to be N = 2.3 – j(0.4-0.5) for the inner passivation layer and to be N = 1.8 – j(0.05-0.1) for the outer hydrous layer

impedance technique at the potentials after 1 h passivation at the same potentials. The inverse of capacitance, $(1/C)$, increases linearly with potential; however, at the potential about 0.4 V vs RHE which is obtained from extrapolation to $(1/C) = 0$, the film thickness does not reach zero. At potentials higher than the potential, both the inverse of capacitance and thickness increased linearly. The capacitance is that of a dielectric part of the passivation oxide film and may correspond to that of a space charge layer of the n-type semiconductive oxide film under the anodic bias. The n-type semiconductive property was estimated from a plot of the Mott-Schottky relation between the capacitance and potential for the passivation film formed at relatively high potentials [11]. From the relation between $(1/C)$ and thickness (d) in Fig. 2.4, it is supposed that there is in the passivation film a layer which does not sustain the potential drop. The thickness of this layer may correspond to 1.3 nm denoted by d_0 in Fig. 2.4 in the pH 6.4 solution. In pH 8.4 borate solution a similar relation was obtained between the inverse of capacitance

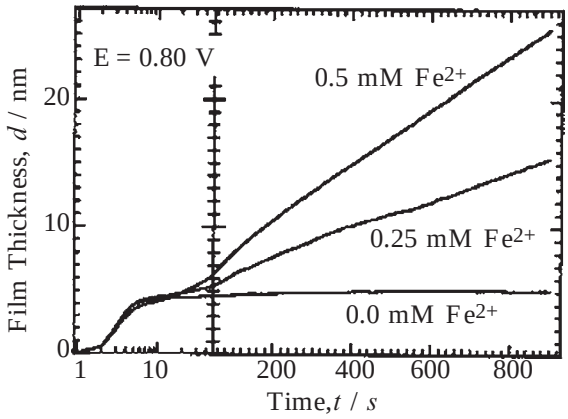

Fig. 2.5. Film thickness during the growth of passivation film on iron. The thickness was estimated from the results and simulation in Fig. 2.4

and thickness. At the potential at which $(1/C)$ was extrapolated to zero, the thickness is about $d_0 = 2.2$ nm in pH 8.4 borate solution. In acidic solution, however, the inverse capacitance, $(1/C)$, is linearly related to the thickness and at the potential at which $(1/C)$ was extrapolated to zero, the thickness was almost zero. In the acidic solution, the potential drop is thus assumed to be distributed over the whole passivation oxide film.

The outer hydrous layer was occasionally formed on the passivation film in neutral pH solution [12, 13]. When the passivation film formed at a relatively high potential in neutral pH solution containing Fe(II) ions, the thick hydrous outer layer was also observed. Figure 2.4 indicates the ellipsometric plots during growth of the passivation film of iron at 0.80 V vs Ag/ AgCl/ sat. KCl in neutral pH 8.4 borate solution containing Fe(II) ions at various concentrations [14]. In Fig. 2.4, Ψ is arctan(relative amplitude ratio of p- to s-polarized light) and Δ relative phase retardation between p- and s-polarized light. In plot (b), theoretically simulated curves were plotted for film growth. The film grows in two steps where the film corresponding to the ordinal passivation film with complex refractive index of $N = 2.3 - \mathrm{j}(0.3 - 0.5)$ appears in the initial step and then the hydrous layer with smaller refractive index of $N = 1.8 - \mathrm{j}(0.05 - 0.10)$ grows in the second step. From the simulation, the growth of the passivation layer with the outer hydrous layer is estimated. The results are shown in Fig. 2.5 [14]. In the initial 10 s, the inner passivation film is formed to 3 nm thickness, followed by the growth of the hydrous layer, the growth rate of which is proportional to the concentration of Fe(II) ions in the solution. The thickness of the hydrous layer reaches 20 nm in 900 s in the solution containing Fe(II) ions at 0.5 mM concentration. Since the growth rate of the outer hydrous layer is proportional to the concentration of Fe(II) ions in the solution, the hydrous layer is found to be formed by an oxidative

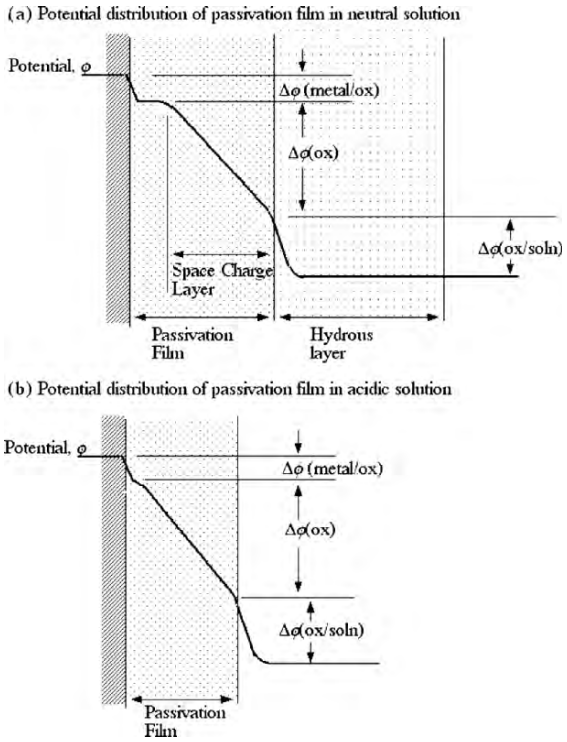

Fig. 2.6. Scheme of potential distribution in the passivation film on iron (**a**) in neutral solution and (**b**) in acidic solution

precipitation from Fe(II) ions in aqueous solution:

$$Fe^{2+} + 3H_2O = FeOOH \cdot H_2O + 3H^+ + e$$

where the composition of $FeOOH \cdot H_2O$ was estimated from the measurement of QCM and ellipsometry [15].

From the above finding, the layer construction and potential distribution of the passivation film on iron is illustrated in Fig. 2.6. In neutral solution, the passivation film is divided into two layer; the inner layer does not sustain any potential drop and the potential drop is distributed in the outer part of the passivation film, which behaves as the space charge layer of n-type semiconductive oxide film. When the aqueous solution surrounding the passive film includes Fe(II) ions, the passivation film is covered with a hydrous layer of $FeOOH \cdot H_2O$. In acidic solution, the outer hydrous layer disappears and the inner part of the passivation film also diminishes. The potential drop may be distributed over the whole passivation film.

The composition of the passivation film on iron was not made clear; however, many diffraction and spectroscopic examinations indicate the presense of a spinel type of oxide. From the fact that the ferric oxide or oxyhydroxide

is stable in the passive potential region, $\gamma - Fe_2O_3$ is the most probable oxide for the passivation film [16–19].

2.3 Rust Formation on Iron and Steels

Since rust layers on iron and steel grow to several hundred μm thickness, a high electric field is not expected in the layer. The growth of the layer, therefore, may not follow ionic migration. For the growth of the rust layer, the oxidation-reduction cycles with which cycles of dry and wet conditions were accompanied have been proposed to play an important role.

According to the Evans Model, the growth mechanism of the rust formation is described in Fig. 2.7 [20, 21]. The rust layer consists of various types of FeOOH under dry conditions. When the rust layer is placed under wet conditions, it works as an oxidant to the substrate steel, and thus metallic iron is oxidized to ferrous ion in the oxide layer:

$$3\mathrm{FeOOH(rust)} + \mathrm{H^+} + \mathrm{e} = \mathrm{Fe_3O_4(rust)} + 2\mathrm{H_2O}$$

$$\mathrm{Fe(metal)} = \mathrm{Fe^{2+}(rust)} + 2\mathrm{e}$$

The ferrous ion reacts with FeOOH in the rust to form Fe_3O_4:

$$2\mathrm{FeOOH(rust)} + \mathrm{Fe^{2+}(rust)} = \mathrm{Fe_3O_4(rust)} + 2\mathrm{H^+}$$

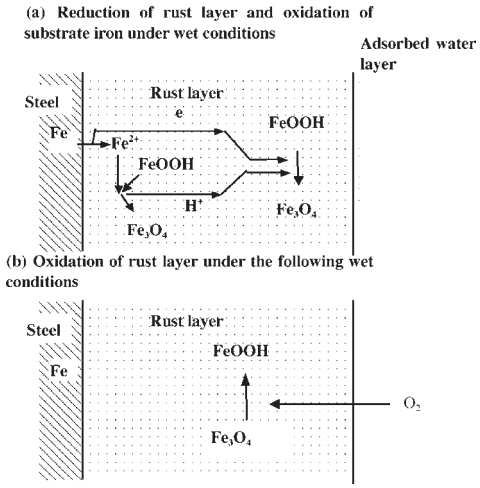

Fig. 2.7. Growth of rust layer on steels during wet and dry cycles. (**a**) During wet conditions, reduction of FeOOH of the rust and oxidation of substrate steels take place due to oxidative action of the rust. (**b**) During the following dry conditions, the rust layer partially reduced is re-oxidized by O_2 in air

The total reaction is described as

$$8\mathrm{FeOOH(rust)} + \mathrm{Fe(metal)} = 3\mathrm{Fe_3O_4(rust)} + 4\mathrm{H_2O}$$

From the reduction of 8 mol of FeOOH, one mol of metallic iron is oxidized. When the condition changes from wet to dry, the rust layer reduced in the wet condition is re-oxidized by a reaction with oxygen in air:

$$4\mathrm{Fe_3O_4(rust)} + \mathrm{O_2(air)} + 6\mathrm{H_2O} = 12\mathrm{FeOOH(rust)}$$

From combination of the above reactions, the reaction scheme during a cycle of wet and dry is summed up in the following reaction:

$$8\mathrm{FeOOH(rust)} + \mathrm{Fe(metal)} + (3/4)\mathrm{O_2(air)} + (1/2)\mathrm{H_2O} = 9\mathrm{FeOOH(rust)}$$

From the above reaction it is seen that 8mol FeOOH in the rust generate new FeOOH of 1mol during a cycle of wet to dry.

The reduction of the rust layer during the wet conditions was confirmed by measurement of electrochemical corrosion potential by Nishikata et al. [22] and by non-contact measurement of corrosion potential using a Kelvin probe by Stratmann et al. [23–25]. The oxidation of the rust by oxygen gas during the following dry condition was found from the measurement of decrease in oxygen pressure by Stratmann et al. [24]. The corrosion potential during the wet-dry cycle changes between an active potential region in the wet and a passive potential region in the dry conditions. The potential during the dry conditions is not high enough, but is slightly higher than the transient region from active to passive. The increase and decrease of corrosion potential are repeated in the relatively small potential range in the neighborhood of the transient region from the active to passive.

For rust growth, the reactions including the low valence Fe ion in wet conditions play an important role. In the presence of the Fe(II) ions in aqueous solution, the thick hydrous layer was seen to be easily formed, as shown in Fig. 2.5. The hydrous layer is also formed when one repeats the potential of an iron electrode between the active and passive potentials. Figure 2.8 shows results measured by Buchler et al., who measured reflectance of an iron electrode as well as current during the repeated potential cycles between the potentials in the hydrogen evolution region and in the passive potential region [26, 27]. The reflectance change may be directly related to the film thickness. From the reflectance, the oxidation film was found to increase with repeated reduction-oxidation cycles. It was proposed that the reduction of the oxidized passive film produced a low valence iron hydroxide which changes to hydrous Fe(III) layer during the following re-oxidation. Simultaneously the new passive film was formed underneath the hydrous layer during the re-oxidation. This indicates that the thick layer is easily formed when the iron electrode undergoes the repeated cycles of oxidation-reduction. The hydrous Fe(III) layer may be amorphous and will change to a rust layer when the layer dries.

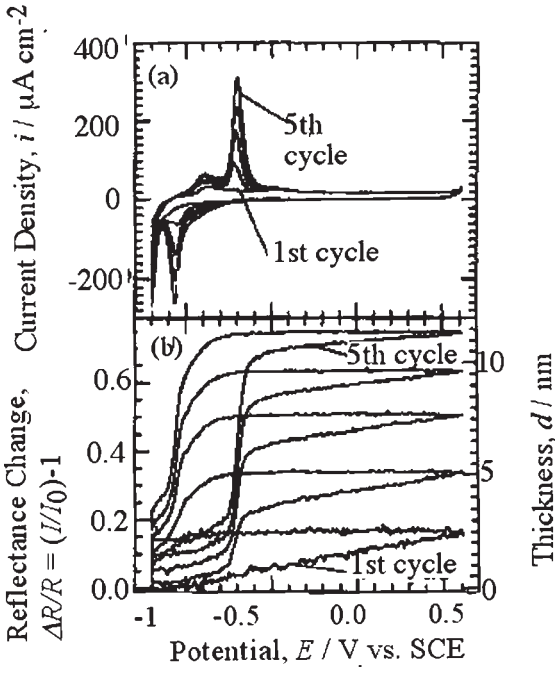

Fig. 2.8. Current density-potential and reflectance-potential relations of an iron electrode during oxidation-reduction cycles by a potential sweep between the active and passive potentials in neutral borate solution. The film thickness was assumed to be linearly proportional to the reflectance change

2.4 Potential Distribution and Ionic Transport

The main difference between the passivation and rust films on iron may be potential distribution in the films. The potential distribution of the film was estimated from capacitance, calculated from AC impedance, and its dependence on potential. Figure 2.9 shows an impedance response of an iron electrode anodically passivated at $E = 0.63$ V vs RHE in pH 6.4 borate solution. The simulation with an equivalent circuit is not discussed for this response at present. In the response, one finds a dielectric response at a frequency region between 10^{-1} and 10 Hz, and thus the dielectric layer which sustain the potential drop is present in the passivation film. The capacitance data plotted in Fig. 2.3 was estimated from this frequency region. The potential drop appears in the dielectric layer in the passivation film and induces the ionic migration through the film.

In the rust layer, field-assisted ionic migration may not take place because the low electric field in the rust layer. In the impedance diagram of the rust layer on weathering steel, as shown in Fig. 2.10, definite dielectric response cannot be seen, and the phase angle reveals relatively small values in the

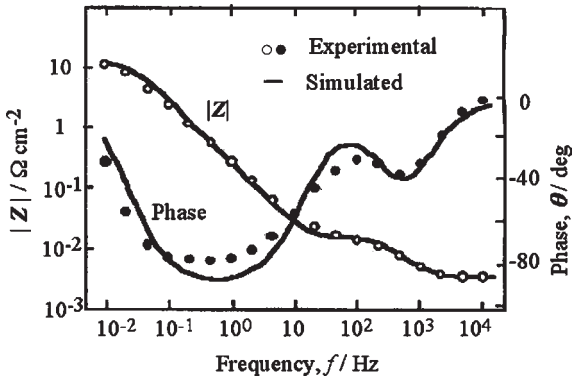

Fig. 2.9. Bode plot of impedance of a passivated iron electrode at E = 0.63 V vs RHE in neutral borate solution at pH 6.4. The *circles* in the figure indicate plots experimentally measured and the *solid lines* simulated results

frequencies smaller than 100 Hz [28]. The dielectric layer does not exist in the rust layer, but a resistance against ionic transport has been assumed to play a large part. It has been assumed that the ionic transport in the rust is caused by ionic diffusion in the rust layer which behaves as a membrane with fixed charges. The potential drop in this case arises as a result of membrane potential, i.e. diffusion potential through the layer with ionic perm-selectivity.

Sakashita et al. estimated the diffusion potential of the membrane comprising of Fe-oxyhydroxide which was imitated as a rust layer and the protectiveness of the rust layer against corrosion of the substrate steel was discussed. They measured membrane potential (diffusion potential) arising across the isolated membrane inserted between two electrolyte compartments filled by aqueous KCl solutions of different concentration:

$$\Delta\phi = (\mathrm{RT/F})\{(t_+/z_+)\ln(a_+^{\mathrm{II}}/a_+^{\mathrm{I}}) + (t_-/z_-)\ln(a_-^{\mathrm{II}}/a_-^{\mathrm{I}})$$

where $t_+(t_-)$ is transport number of cation (anion), $a_+(a_-)$ activity of cation (anion). I and II are aqueous phases at the both sides of Fe-oxyhydroxide membrane. The membrane potential is determined by an ionic perm-selectivity (ratio of transport numbers between cation and anion) of the Fe-oxyhydroxide and the perm-selectivity is dependent on positive or negative fixed charges in the membrane. The ionic perm-selectivity, therefore, can be evaluated from the membrane potential. Sakashita et al. concluded that the rust layer of Fe-oxyhydroxide is a membrane with positive fixed charges and has a property of anionic (Cl^-) perm-selectivity. Thus, if Cl^- ions are present in the aqueous phase, Cl^- can penetrate into the rust layer and corrode the substrate steel. Further, they suggested that adsorption of oxo-anions like molybdate or tungstate to Fe-oxyhydroxide changed the perm-selectivity to cationic and inhibited the Cl^- attack on the substrate steel, because Cl^- cannot penetrate into the cationic perm-selective rust layer [30]. This idea, that ionic

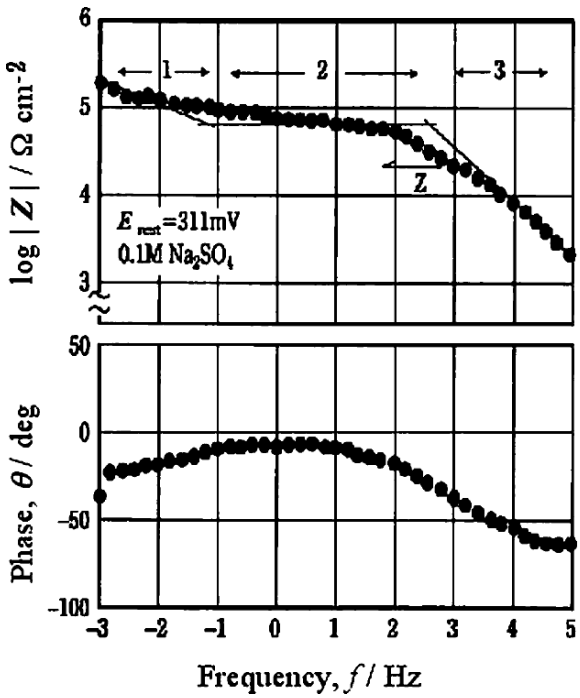

Fig. 2.10. Bode plot of impedance of a rusted weathering steel. The impedance was measured at rest potential of the weathering steel in 0.1 mol dm^{-3} Na_2SO_4 solution [28]

perm-selectivity determines the protectiveness of layer coated on steels, may be available for designing the more protective weathering steels or coating layers. Now the protectiveness of the rust layers on various weathering steels has been examined from membrane potential measurement.

2.5 Summary

The passivation film and the rust layer on iron and steels were compared, both of which are considered not to be very different in composition from each other.

(1) The passivation film on iron is formed in a strongly oxidative environment, i.e., under highly anodic potential, while the rust layers on iron and steels are formed by mild oxidation-reduction cycles. On the formation of the rust layer, reduction of iron oxide or hydroxide to low valence below three may be an important step in wet conditions. In the passivation film, the film thickness is limited to a few nm, because the ionic transport through the film follows the high-field assisted ionic migration

mechanism, while the rust layer growing with oxidation-reduction cycles reaches several hundred μm thickness.

(2) For the passivation film, the anodic potential applied to an iron electrode is sustained by the dielectric layer of space charge, and the impedance response reveals the definite presence of a dielectric layer. The potential drop is distributed in the whole passivation film. For the rust layer, impedance response reveals a resistive property in enough small frequencies. The resistance may be a resistance against ionic diffusion. For protectiveness of the rust layer, an ionic perm-selectivity may be one of the key factors, particularly under exposure to marine environments, where the rust layer exhibiting a cationic perm-selectivity may be more protective.

References

1. T. Ohtsuka: Zairyo-to-Kankyo, **37**, 228 (1988).
2. K. Azumi, T. Ohtsuka, and N. Sato: Denki Kagaku, **29**, 700 (1985).
3. K. Azumi, T. Ohtsuka, and N. Sato: Denki Kagaku, **29**, 700 (1985).
4. N. Sato and T. Noda: Electrochim. Acta, **22**, 839 (1977).
5. N. Sato, T. Noda, and K. Kudo: Electrochim. Acta, **19**, 471 (1974).
6. K. J. Vetter and F. Gorn: Electrochim. Acta, **18**, (1973), 321: Werkst. u. Korrosion, **21**, 703 (1973).
7. K. E. Heusler: Ber. Bunsenges. Phys. Chem., **72**, 1197 (1968).
8. N. F. Mott: Trans. Faraday Soc., **36**, 1197 (1960).
9. H. Cabrera and N. F. Mott: Rep. Progr. Phys., **12**, 163 (1949).
10. K. Azumi, T. Ohtsuka, and N. Sato: Tranasct. Jpn Inst. Metals, **27**, 382 (1986).
11. K. Azumi, T. Ohtsuka, and N. Sato: J. Electrochem. Soc., **45**, 1352 (1987).
12. N. Sato, T. Noda, and K. Kudo: Z. fur Phys. Chem. N. F., **98**, 271 (1975).
13. N. Sato, T. Noda, and K. Kudo: Corrosion Sci., **16**, 1909 (1971).
14. T. Ohtsuka and H. Yamada: Corrosion Sci., **40**, 1131 (1998).
15. T. Ohtsuka, J.-C. Ju, S. Ito, and H. Einaga: Corrosion Sci., **36**, 1257 (1994).
16. H. Konno and M. Nagayama: *Passivity of Metals*, Ed. By R. P. Frankenthal and J. Kruger: The Electrochemical Soc. Inc, Princeton, 585 (1978).
17. W. E. OfGrady: J. Electrochem. Soc., **127**, 555 (1980).
18. J. Kruger: Corrosion Sci., **29**, 149 (1989).
19. K. Kuroda, B. D. Cahan, Gh. Nazri, E. Yeager, and T. E. Mitchell: J. Electrochem. Soc., **129**, 2163 (1982).
20. U. R. Evans: Nature, **206**, 980 (1965).
21. U. R. Evans: Trans. Inst. Metal Finishing, **37**, 1 (1960).
22. A. Nishikata, Y. Yamashita, H. Katayama, T. Tsuru, A. Usami, K. Tanabe, and H. Mabuchi: Corrosion Sci., **37**, 2059 (1995).
23. M. Stratmann and H. Streckel: Corrosion Sci., **30**, 681 (1990).
24. M. Stratmann and H. Streckel: Corrosion Sci., **30**, 697 (1990).
25. M. Stratmann, H. Streckel, K. T. Kim, and S. Crocket: Corrosion Sci., **30**, 715 (1990).
26. M. Buchler, P. Schmuki, and H. Bohni: J. Electrochem. Soc., **144**, 2307 (1997).
27. M. Buchler, P. Schmuki, and H. Bohni: J. Electrochem. Soc., **145**, 609 (1998).
28. H. Kihira, S. Ito and T. Murata: Corrosion, **45**, 347 (1989).
29. M. Sakashita, Y. Yomura, and N. Sato: Denki Kagaku, **45**, 165 (1977).
30. M. Sakashita and N. Sato: Corrosion Sci., **17**, 473 (1977).

3 Semiconductor Property of Passive Films and Corrosion Behavior of Fe-Cr Alloys

Shinji Fujimoto, Hiroaki Tsuchiya

3.1 Introduction

Knowledge of the structure and properties of oxide films of metals and alloys is important for understanding corrosion behaviour, because the protective action of most highly corrosion resistant metals and alloys essentially derives from passivity which is caused by an extremely thin oxide and/or hydroxide surface layer. Passivity of Fe-Cr alloys is one of the most important topics in corrosion science, because alloyed Cr is enriched in the passive film to act in a very important role regarding protection. Therefore, passive films on Fe-Cr alloys have been characterized by various ultrahigh vacuum (UHV) analytical techniques such as Auger electron spectroscopy (AES) and X-ray photoelectron spectroscopy (XPS). Such UHV surface characterization techniques cause specimens to be modified under quite different environmental conditions compared with those in which passive films are formed. Therefore, in situ electrochemical surface characterization techniques have been tried. The author of this work reported the photoelectrochemical response and electrochemical impedance spectroscopy of passive films on Fe-Cr alloys to reveal differences in electronic structure of passive films formed in a sulphuric acid and a borate buffer solution [1–3]. In the present chapter, the author summarizes the photoelectrochemical response of passive films on Fe-18Cr alloy comparing with the Mott-Schottky relation, which is correlated to corrosion behaviour.

3.2 The Photoelectrochemical Response

3.2.1 A Brief History of Photoresponse in Electrochemistry

The first report on the light effect on electrochemistry is known as the Becquerel effect [4]. In 1839, Alexandre Edmond Becquerel (father of the Nobel Laureate in physics) discovered that when one of an electrode couple was exposed to sunlight, voltage difference or current flow was generated. This was also the origin of energy conversion of sunlight into electricity, which has been developed into the solar cell, and also photocatalysis. The first attempt to find the effect of light irradiation on the corrosion behaviour of metals and alloys was reported by Kruger for Cu in a neutral solution [5]. It was

suggested that the semiconductor property of the oxide film was correlated with corrosion behaviour, which was affected by light irradiation. In the 1950s and 1960s, early reports on photoelectrochemical response appeared for compound semiconductors and oxide semiconductors in aqueous solution [6–11]. Such research advanced into many works on the photoelectrochemistry of semiconductors [12–15], including a large number of publications by Allen J. Bard [16–19]. On the other hand, the application of photoeffect into characterisation of the surface of passive metals and alloys had been attempted since the early 1960s. The first report on the application of photoelectrochemical response into passivity study might be the research by Oshe et al. [20]. Photovoltage of Fe electrode was observed in relation to electrochemical condition. In this work the authors clearly recognised the existence of a semiconductor layer on the Fe electrode. After a while, later in the 1970s, many authors had tried to apply photoelectrochemical response to passivity studies [21–23]. Semiconductor properties of Fe and Ni were analysed in detail by Hackerman et al. They determined band gap energy, flat band potential, and type of conduction [24]. Stimming et al. discussed correlation between the photoelectrochemical response and the electrochemical impedance spectroscopy for passive film on Fe [25]. On the other hand, transient behaviour which is often observed in photocurrent was analysed by Peter et al. for passive film on Fe [26]. Such transient phenomena were also discussed by Hara et al. [27] and Azumi et al. [28]. Excellent reviews on the semiconductor property of passive film are available in the literature by Gerischer [29–32].

3.2.2 Measurement of Photocurrent and Spectrum Separation

Assuming that a passive film is composed of an n-type semiconductor thin layer, and is polarized at the potential more noble than the flat band potential, a space charge layer in an electron depleted state is generated at the surface of the semiconductor layer, as shown in Fig. 3.1. If a light with photon energy larger than the band gap is irradiated onto the semiconductor electrode, the photogenerated electron and hole pair are separated along the potential gradient in the space charge layer, and then a positive photocurrent is generated. The photo-quantum effect could be described by the following equation assuming that the phototransition process occurs as indirect transition as usually observed for passive film on Fe-Cr alloys [29]:

$$i_{\mathrm{ph}} h\nu / I_0 = const.(h\nu - E_{\mathrm{g}})^2 \tag{3.1}$$

therefore,

$$(i_{\mathrm{ph}} h\nu / I_0)^{1/2} = C(h\nu - E_{\mathrm{g}}), \tag{3.2}$$

where i_{ph} is photocurrent, $h\nu$ the energy of the incident photons, E_{g} an optical band gap energy of the passive film, I_{o} the power of the incident current, and C constant. Figure 3.2 (a),(b) shows a typical photocurrent spectrum

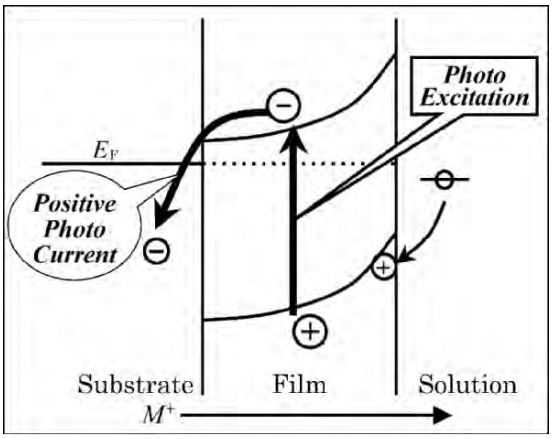

Fig. 3.1. Model of n-type semiconductor thin film electrode and process of photo current generation

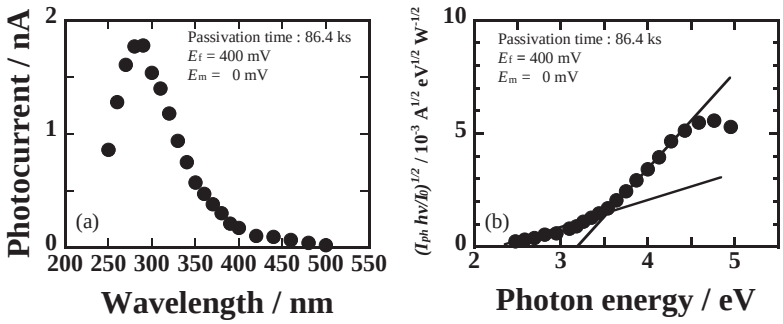

Fig. 3.2. (**a**) A typical photocurrent spectrum, and (**b**) photocurrent action spectrum as indirect transition

as a function of wavelength and the photocurrent action spectrum plotted following Eq. (3.2), respectively. As shown in this figure, the spectrum might fit with a straight line. The line, however, is attained with a tail in the lower photon energy region, which is always observed for photoaction spectra of passive films on Fe, Ni, Fe-Cr and Ni-Cr alloys. In most literature, spectra in this low energy region could be not detected or ignored because of uncertainty in the mobility gap of thin amorphous semiconductors. On the other hand, as well known, the passive film consists not of a single phase, but of multicomponents that form a layer structure. The author tried to separate this spectra curve, supposing that the passive film was composed of multi layers. Assuming that the observed photocurrent is a sum of responses from n components, the photocurrent spectrum is described as follows:

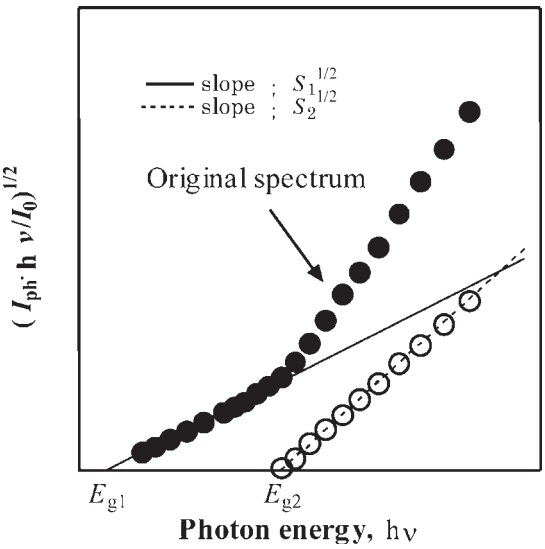

Fig. 3.3. Illustration showing the procedure of photoelectrochemical action spectra separation

$$\left(\frac{i_{ph} \cdot h\nu}{I_0}\right)^{1/2} = \left\{\sum_{k=1}^{n} C_k \cdot (h\nu - E_{\mathrm{gk}})^2\right\}^{1/2} \tag{3.3}$$

The process of spectrum separation is schematically described in Fig. 3.3. The original spectrum shown in solid circles fitted with a straight line in the low energy region to obtain the solid line with band gap of E_{g1}. The reminder spectrum shown as open circles was obtained by subtracting the solid line from the original spectra. Similarly, the open circled spectrum was fitted with a dotted line giving E_{g2}. The reminder line similarly obtained shows a straight line with E_{g3}. Therefore, the spectrum shown in Fig. 3.3 was divided into three spectra. Most of the spectrum observed for passive films on Fe-Cr alloys is divided into two components.

3.3 Passive Films on Cr and Fe-Cr Alloys in Sulphuric Acid

3.3.1 Photocurrent

Typical photocurrent spectrum and the photo action spectrum plotted following Eq. (3.2) for pure Cr and Fe-18Cr alloys are shown in Fig. 3.4 (a) and (b), respectively. It is noticeable that most of the photocurrent appears in the negative direction. Therefore, mainly p-type semiconductor is expected to be formed. As shown in Fig. 3.4(b), photocurrent spectrum could fit with a

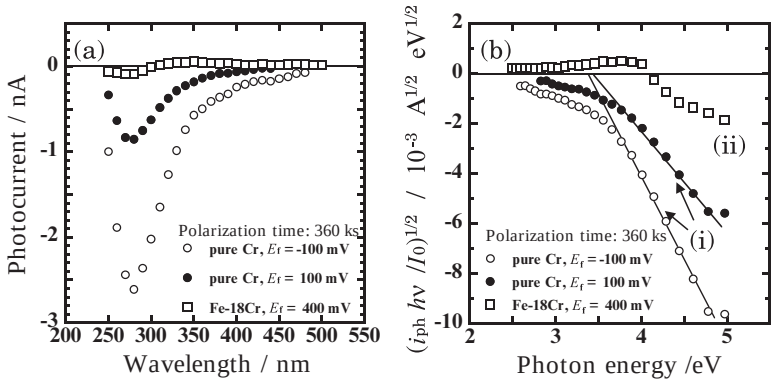

Fig. 3.4. (**a**) Examples of photocurrent responses for pure Cr and Fe-18Cr passivated at various potentials for about 100 h, and (**b**) photoelectrochemical action spectra of the steady photocurrent shown in Fig. 3.4(a)

straight line with E_g about 3.4 eV. The spectrum (i), however, was accompanied by a tail in the low photon energy region. It is noticeable that spectrum (ii) contains both positive and negative values depending on photon energy. Photocurrent which is generated from a single phase should not change its direction at a fixed potential, even if the wavelength of illuminated light is changed. It is highly possible that the photoelectrochemical response arises in more than two layers individually. Therefore, the observed spectra were separated following the procedure introduced above. Most of the photoelectrochemical action spectrum observed for Cr and Fe-Cr alloys in sulphuric acid was separated into two components. E_g of approximately 2.5 eV and 3.6 eV are identified and are almost constant for any material, applied potential and polarization period examined. Referring to E_g for Cr reported by Sunseri et al. [33,34], passive films on pure Cr and Fe-Cr alloys are composed of hydroxide layer, $Cr(OH)_3$, with E_g of 2.5 eV and an inner oxide layer, Cr_2O_3, with 3.6 eV, respectively.

The slopes of photocurrent spectrum, S, for passive film formed on pure Cr and Fe-Cr alloys at 600 $mV_{Ag/AgCl}$ for about 100 h are shown in Fig. 3.5 (a) and (b), respectively. The responses of oxide layer for Fe-Cr alloys are smaller compared with that of Cr, but are similar to each other. The response of the component with E_g = 3.6 eV, that is attributed to an inner oxide layer, shows negative values at most of potentials and decreases with increasing potential. Thus, photoelectrochemical response of the inner oxide layer shows typical p-type semiconductive property with flat band potential, E_{fb}, about 400 mV and 650 $mV_{Ag/AgCl}$ for Fe-Cr alloys and Cr, respectively, at which the photocurrent changes its direction from negative to positive with increasing potential. On the other hand, photocurrent response for the hydroxide, E_g = 2.5 eV, varied from negative to positive with increasing potential with E_{fb}, about 250 $mV_{Ag/AgCl}$, although the photocurrent is very

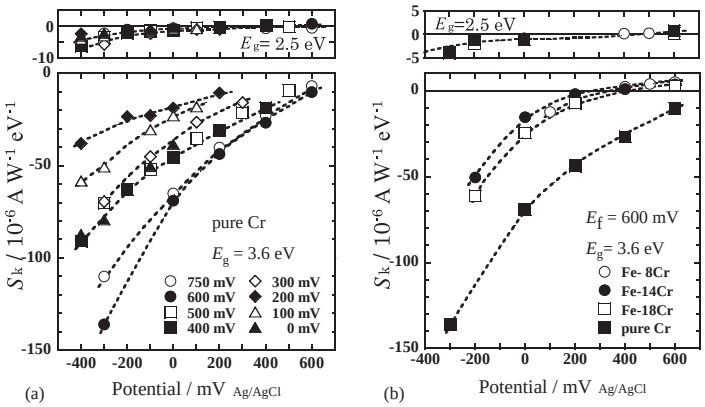

Fig. 3.5. Variation of the slope of the action spectrum, S_k, of passive film for (**a**) Cr and (**b**) Fe-Cr alloys formed in sulphuric acid solution at several potentials as a function of the potential at which the photocurrent was measured

small compared with that of the oxide layer. The type of semiconductor, however, could not be determined because of small and ambiguous current change with potential. As mentioned above, E_{fb} for oxide layer is about 400 mV or 650 $\mathrm{mV_{Ag/AgCl}}$ and that for hydroxide about 250 $\mathrm{mV_{Ag/AgCl}}$. Therefore, it is quite interesting that, between 250 $\mathrm{mV_{Ag/AgCl}}$ and 400 or 675 $\mathrm{mV_{Ag/AgCl}}$, both negative photocurrent for $h\nu > 3.6$ eV and positive photocurrent for $2.5 < h\nu < 3.6$ eV are observed depending on the photon energy as already illustrated in Fig. 3.4.

3.3.2 Capacitance

The space charge layer in the semiconductor electrode is also characterised by capacitance. Electrochemical impedance spectroscopy measurements at a series of potentials in passive region provide capacitance of space charge layer. Capacitance of semiconductor thin film which is polarized as a the depleted state can be expressed as a linear relation between $1/C^2$ and polarised potential, E, that is, Mott-Schottky plot, assuming that the capacitance of the Helmholtz layer is fairly larger than that of space charge region:

$$\frac{1}{C^2} = \frac{2}{\varepsilon\varepsilon_0 qN}\left(E - E_{\mathrm{fb}} - \frac{kT}{q}\right) \tag{3.4}$$

where N is the carrier concentration, ε the dielectric constant, ε_0 the vacuum permittivity, q the elementary charge, k the Boltzman constant, T the absolute temperature and E_{fb} the flat band potential. The term kT/q can usually be ignored. The Mott-Schottky plots for passive films on Fe-18Cr alloy formed at various formation potentials are shown in Fig. 3.6, which reveals two straight lines with positive slope for potentials more noble than 0 $\mathrm{mV_{Ag/AgCl}}$ and with negative slope for potentials less noble than

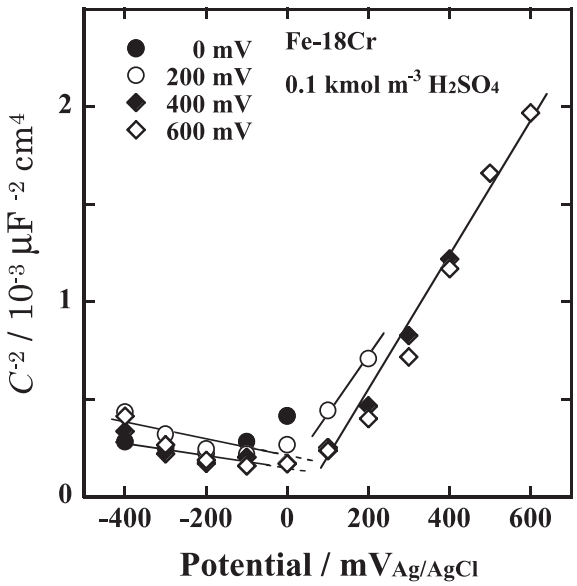

Fig. 3.6. Mott-Schottky plots for passive films formed on Fe-18Cr at several potentials in 0.1 kmol m^{-3} H_2SO_4

0 $mV_{Ag/AgCl}$. If a space charge region of semiconductor electrode varied from accumulation, depletion and then inversion states with a series of applied potentials, capacitance, C, should decrease and then increase showing a minimum at the transition from the depleted to the inversion state [35]. The $1/C^2$ plots in Fig. 3.6, however, exhibit a minimum. Therefore, the capacitance measured should not be derived from a single space charge region, but from at least two regions. As mentioned before, passive film might be composed of inner oxide and covering hydroxide layers, and there are some interfaces in the passive film. Therefore, more than two space charge regions might develop in the film, which will be discussed later. If two space charge layers exist as depleted state and their capacitance is smaller than that at other interfaces including Helmholz layer, passive films formed on Cr and Fe-18Cr should behave as n-type semiconductor in the noble potential region and p-type in the less noble potential region.

3.3.3 Electronic Structure of Passive Films on Cr and Fe-Cr Alloys formed in Acid Solution

As described above, passive film consists of two layers of semiconductor with connection as p-n junction. Similar models are also proposed by some authors [36–40]. A proposed electronic energy band model for Cr and Fe-Cr alloys in sulphuric acid is roughly illustrated in Fig. 3.7. This electrode system has

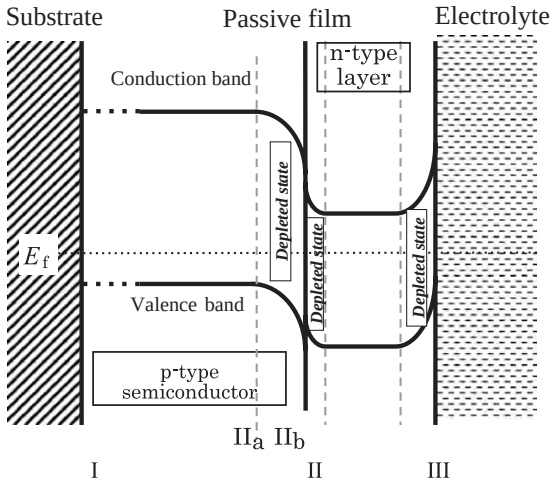

Fig. 3.7. Schematic illustration showing electronic structure of duplex passive films formed on Fe-Cr alloys formed in sulphuric acid solution

three interfaces: (I) substrate metal or alloy / inner oxide, (II) inner oxide / outer hydroxide, and (III) outer hydroxide / electrolyte, respectively. At the interface (III) in hydroxide layer, a space charge region is formed with its state depending on the applied potential. Since hydroxide layer behaves as an n-type semiconductor as mentioned above, this space charge region is basically depleted state. At the interface (II), two semiconductor layers are connected as p-n hetero-junction because of different band gap energies. The space charge region inside the oxide layer (denoted as II_a) should usually be depleted state, because negative photocurrent always generates for the higher photon energy ($3.5\ \text{eV} < h\nu$) at any applied potential except for that more noble than E_{fb}, and increases with decreasing potential as mentioned before; that is typical p-type semiconductor behaviour. On the other hand, the space charge region at the interface inside the hydroxide layer (II_b) might also be depleted state, because p-n junction usually forms depleted regions for both sides. The electronic structure of the interface at the substrate (I) is unknown at the moment. In the following, behaviour of photocurrent and capacitance for various potentials is described.

The change in electron energy state band for Fe-18Cr alloy for various applied potentials is described in Fig. 3.8 with a diagram showing the sign of photocurrent generated in the hydroxide and oxide layers, respectively. With low energy photoirradiation ($2.5 < h\nu < 3.6$ eV), photoexcitation occurs only in the outer hydroxide layer which includes two space charge regions, (II_b) and (III). The photogenerated hole moves both into the inner layer, and into the electrolyte to be consumed by some oxidation, whereas the excited electron

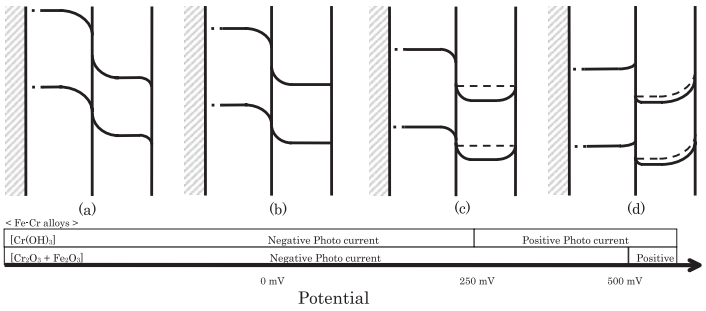

Fig. 3.8. Schematic presentations of the electronic structures of passive films formed on Fe-Cr alloys, and diagram showing the potential region of the photocurrent direction for $Cr(OH)_3$ and Cr_2O_3 on Fe-Cr alloys

might accumulate in the conduction band of the outer hydroxide layer, because both ends of the conduction band are potential barriers (Fig. 3.8 (b), (c)). Then, most of the photoexcited electrons might disappear by recombination with holes. The net photocurrent is determined by the balance of hole migration inward and outward, because the depleted region at (III) grows with increasing potential and that at (II_b) grows with decreasing potential. Therefore, it is noticeable that the potential at which photocurrent becomes zero with increasing potential is not flat band potential, but the potentials at which the photocurrent generates at the space charge region (II_b) and (III) are equivalent. A similar photo current behaviour was discussed by Goossens et al. for zirconium oxide [41].

Photoirradiation of the higher photon energy ($h\nu > 3.6$ eV) generates electron-hole pairs in both inner oxide and outer hydroxide layers. Holes generated in the space charge region (II_a) in the oxide layer easily migrate toward the substrate alloy along ascending potential slope in the oxide layer. On the other hand, photo excited electron migrates outward into conduction band of hydroxide layer. In order to generate continuous negative photo current, it is necessary that the excited electrons reach the hydroxide / electrolyte interface to be consumed by some cathodic reaction, such as hydrogen evolution. When applied potential is around the flat band potential of depleted region (III) as shown in Fig. 3.8 (a), electrons can easily move to electrolyte passing the small space charge region (III). With increasing applied potential, space charge region (III) develops as a depleted region to form an energy barrier for outward migration of photoelectrons. It is highly likely that photoelectrons migrating from oxide layer into the hydroxide layer and photoelectrons generated in the hydroxide accumulate in the conduction band of hydroxide layer to flatten the energy band of hydroxide, as shown in dashed line in Fig. 3.8 (c). Therefore, photoelectrons generated in the oxide layer can

migrate to electrolyte passing the outer hydroxide layer, accompanying some transient phenomena just after illumination starts, which is actually observed as photocurrent transient. Consequently, although the number of photoelectrons generated in the oxide layer decreases with increasing potential, the photo-excitation in oxide layer can generate negative photocurrent at any potential in the passive region below E_{fb}.

It is interesting that the oxide layers of both Cr and Fe-Cr alloys exhibit a similar photoelectrochemical response with almost the same E_{b}s, that is 3.6 and 2.5 eV. This means that the semiconductor property of the oxide layer of Fe-Cr alloys is derived from Cr oxide and not from Fe oxide, because E_{b} of passive films on Fe is approximately 2.5 eV. It has been proposed that Cr oxide in the passive film on Fe-Cr alloys may form some sort of three-dimensional networked structure across the whole oxide layer, for example, like the percolation model proposed by Newman and Sieradzki [42, 43]. It is suggested that a continuously connected domain of Cr oxide might be formed to introduce a channel for photoexcited electrons and holes to pass through the oxide layer. The Fe oxide domain may retard the formation and conduction of photoexcited electrons and holes, resulting in a reduced photocurrent, as observed in Fig. 3.3. The reason why the photocurrent response of Fe was not detected is unknown at the moment. The differences in some microstructure might change flat band potential for the higher band gap layer, that is, the inner oxide.

3.4 Passive Film on Fe-18Cr Alloy formed in Borate Buffer Solution

3.4.1 Photocurrent and Capacitance

Figure 3.9 shows the photocurrent spectrum plotted from Eq. (3.2), which does not show a straight line, but exhibits a line with two regions of different slopes. This spectrum was also separated into two components. E_{g}s were recognized as approximately 2.4 eV and 3.4–3.5 eV, which were nearly constant for all the examined polarization periods and film formation potentials, and were attributed to $Cr(OH)_3$ and Cr_2O_3, respectively. Analysis using XPS revealed that the passive films on Fe-18Cr alloys are usually composed of an inner oxide layer and an outer hydroxide layer [44]. Therefore, it was determined that passive films on Fe-18Cr alloys are composed of an inner oxide layer and a covering hydroxide layer. Figure 3.10 shows the slopes of the photocurrent spectrum, S, for passive films formed at various potentials. Positive photocurrents were generated at most of the applied potentials in the hydroxide and the oxide layers. The positive photoresponse increased as the applied potential increased. Therefore, both the hydroxide and oxide layers of passive films formed on Fe-18Cr alloys in a borate buffer solution exhibit the typical n-type semiconductive behaviour. The observed flat band potential, E_{fb}, was approximately $-300\ \mathrm{mV_{Ag/AgCl}}$ for both layers.

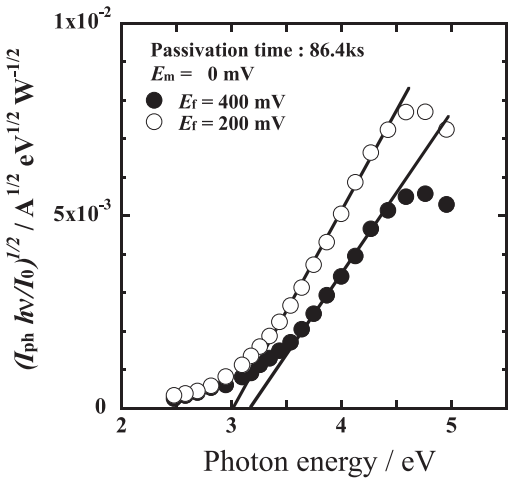

Fig. 3.9. Photoelectrochemical action spectra of the steady photocurrent for passive films formed at various potentials

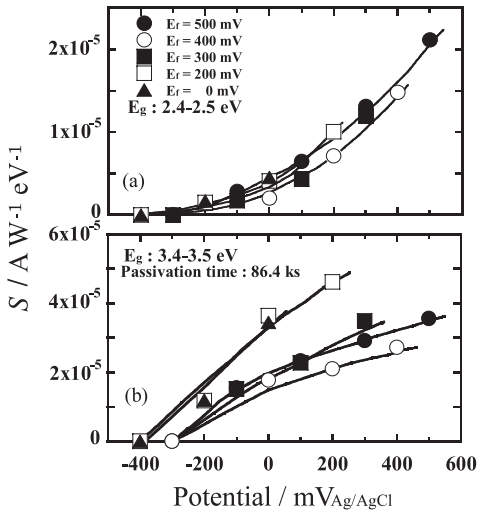

Fig. 3.10. Variation of the slopes of the action spectrum, S, for (**a**) hydroxide layer with E_g of 2.4-2.5 eV and (**b**) oxide layer with E_g of 3.4-3.5 eV as a function of measuring potential

The space charge region of the semiconductive passive films were characterized by evaluating the capacitance. Using a similar procedure to that for photocurrent measurements, the specimen was polarized at various potentials and then the applied potential was sequentially shifted in the less noble direction at intervals of 100 $mV_{Ag/AgCl}$. Figure 3.11 exhibits the Mott-Schottky plots for the passive films formed on Fe-18Cr at various applied potentials for 24 h. The straight lines with positive slopes reveal an n-type semiconductive

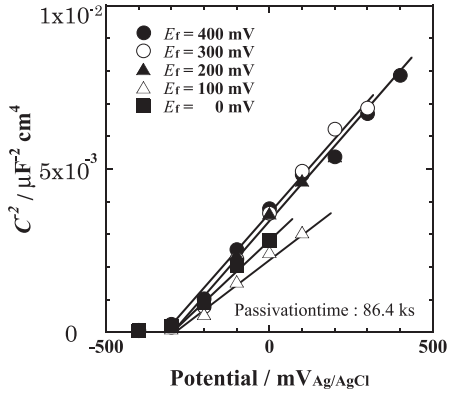

Fig. 3.11. Mott-Schottky plots for passive films formed on Fe-18Cr alloy at several potentials in a neutral borate buffer solution

behaviour and the presumed flat band potential, E_{fb}, is -300 $\mathrm{mV_{Ag/AgCl}}$, which was derived from the intercept of the straight line to the x-axis. This capacitance might arise in the space charge region developed in the outer hydroxide layer for reasons discussed later. Figure 3.12 (a) and (b) shows the variations in the donor density obtained from the slope of the Mott-Schottky plot as a function of the film formation potential and passivation time, respectively. The carrier densities of the passive films decrease as the potential and passivation time increase. It is also observed that a low film formation potential like 0 $\mathrm{mV_{Ag/AgCl}}$ causes the carrier densities to decrease abruptly with time in the early stages of passivation.

3.4.2 Electronic Structure of Passive Films on Fe-18Cr Alloy formed in Borate Buffer Solution

As described above, passive films formed on a Fe-18Cr alloy in a borate buffer solution consist of an outer n-type hydroxide layer with an E_{g} of 2.4 eV and an inner n-type oxide layer with an E_{g} of 3.4–3.5 eV. Therefore, the two n-type semiconductor layers are simultaneously polarized at more noble potentials than their flat band potentials to generate depleted space charge regions in each layer. Figure 3.13 describes the electronic energy band model for a passive film formed on Fe-18Cr alloy in a borate buffer solution. The proposed model has three interfaces: (I) substrate alloy/inner oxide, (II) inner oxide/outer hydroxide, and (III) outer hydroxide/electrolyte. At interface (III), the space charge region developed inside hydroxide is a depleted state. Therefore, the width of the depleted region increases with the applied potential, which results in a larger positive photocurrent. At interface (II), the two n-type semiconductor layers with different optical band gap energies are connected as an isotype heterojunction. The space charge region in the oxide layer ($\mathrm{II_a}$) is also depleted since the positive photocurrent is always generated and increases as the applied potential increases as shown in Fig. 3.10. On the

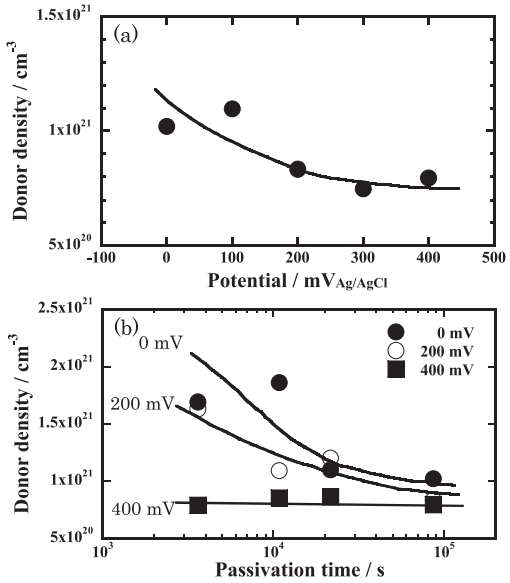

Fig. 3.12. Changes in the donor densities of passive films on Fe-18Cr alloy (**a**) with the film formation potential and (**b**) with passivation time

other hand, the space charge region inside the hydroxide layer (II_b) may be the accumulated region because an n-n junction usually forms the depleted region in one side of the interface and the accumulated region in the other. Typically, the width of the accumulated region, which is very thin compared to the depleted region, is nearly constant regardless of the applied potential. Therefore, the accumulated region should not affect the photocurrent behaviour.

3.5 Correlation between Electronic Structure of Passive Films and Corrosion Behaviour for Fe-Cr Alloys

The potential gradient in the film controls the transportation of the charged species including ions and electrons. Therefore, the electron energy band structure is related to the film growth kinetics and also corrosion behaviour.

As described above, passive films formed on Cr and Fe-Cr alloys in a sulphuric acid solution and passive films on Fe-18Cr alloy formed in a borate buffer solution are composed of an inner oxide and covering hydroxide layer, that are of duplex layered structure. However, there are differences in electronic structure between these passive films. Passive films formed in a borate buffer solution have n-type semiconductor properties for both inner and outer layers, and are polarized to be in depleted state at most potentials in the passive region. Therefore, the energy band slopes both in the inner oxide and outer hydroxide layer are ascending towards the film/electrolyte

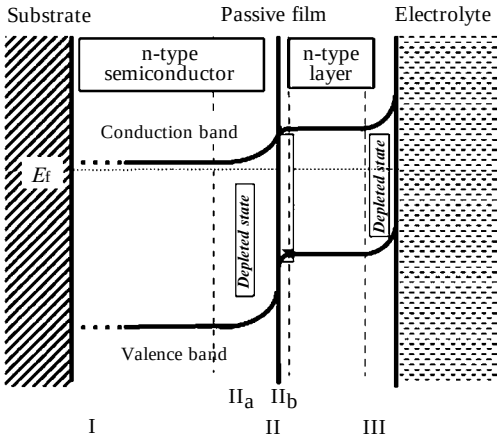

Fig. 3.13. Schematic illustration showing electronic structure of duplex passive films formed on Fe-Cr alloys formed in borate buffer solution

interface. Under such energy states, the outward migration of cations and inward migration of anions and electrons are both possible. Consequently, a passive film may continue to grow under high electric fields, which results in a more protective film with time. Localized corrosion, however, may be initiated by harmful anions, such as Cl^- and $SO_4{}^{2-}$ that are able to penetrate into the passive film from the electrolyte following the electron energy band slope in the passive film. Therefore, passive films do not necessarily suppress corrosion.

On the other hand, passive films on Cr and Fe-Cr alloys formed in a sulphuric acid solution consist of a p-type inner oxide layer, which is in the depleted state in most of the passive potential region, and an n-type outer hydroxide layer, as described in Fig. 3.7. The energy band slope in the inner oxide layer descends towards the surface. Therefore, film growth is not promoted by the potential gradient. The outer hydroxide layer exhibits the n-type semiconductor properties, but the electric field in the outer layer may be small because photocurrent generated in the hydroxide was insignificant. On the other hand, inward penetration of harmful anions is effectively inhibited.

Kirchheim reported that in a neutral solution a passive film can continuously grow for long periods following the Cabrera-Mott mechanism, whereas in an acidic solution, the growth of the passive film is terminated in a few minutes [45]. Thus, in an acidic solution the passivity is completed in a very short period. Fujimoto et al. reported that n-type semiconductor properties are observed in the initial period of passivation for Fe-18Cr in a sulphuric acid solution [46], which means that a passive film grows as a positive potential gradient is established in a short period. These differences in the film growth kinetics may be correlated to the electronic structure in the passive

films formed in a borate buffer and a sulphuric acid solution. The author also reported the photoinduced modification of a passive film. Irradiating by uv light enhances the Cr enrichment in the passive film on Fe-Cr alloys [46]. A photomodification occurred during the very initial stage of passivation in a sulphuric acid solution, but lasted for a longer time in a neutral solution. Since uv irradiation enhances the migration of ions along the potential gradient in a passive film, the difference in photomodification behaviour between an acidic and a neutral solution is quite reasonable [47].

3.6 Summary

The semiconductor structure of passive films formed in a borate buffer solution and in a sulphuric acid solution are discussed in terms of their electronic structure and growth and corrosion behaviour. A passive film formed in a borate buffer solution is composed of an inner oxide layer and a covering hydroxide layer, and both are n-type semiconductors with optical band gap energy, E_g, of 3.4–3.5 eV and 2.4 eV, respectively. The two n-type semiconductor layers, which consist of a passive film formed in a borate buffer solution, are both in depleted states. These conditions allow the migration of ionic species and electrons, which results in the continuous growth of the film. On the other hand, passive films on Cr and Fe-Cr alloys formed in a sulphuric acid solution consist of a p-type semiconductor inner oxide layer and n-type semiconductor outer hydroxide layer. The field assisted growth for a film grown in an acidic solution is difficult in the steady state and the inner oxide layer grows in the initial stage of passivation when the inner layer exhibits n-type semiconductor properties. This difference in semiconductor properties coincides with passive film growth kinetics reported in the literature.

Acknowledgements

The author is grateful for the support by "Priority Assistance of the Formation of Worldwide Renowned Centers of Research. The 21st Century COE Program (*Project: Center of Excellence for Advanced Structural and Functional Materials Designs, Osaka University*)" from the Ministry of Education, Sports, Culture, Science and Technology of Japan.

References

1. S. Fujimoto, O. Chihara and T. Shibata: Materials Science Forum, **289-292**, 989 (1998).
2. H. Tsuchiya, S. Fujimoto, O Chihara and T. Shibata: Electrochimica Acta, **47**, 4357 (2002).
3. H. Tsuchiya, S. Fujimoto and T. Shibata: J. Electrochem. Soc., **151**, B39 (2004).
4. E. Becquerel: C. R. Hebd. Séan. Acad. Sci., **9**, 58, 561, 711 (1839).

5. J. Kruger: J. Electrochem. Soc., **106**, 847 (1959).
6. W. H. Brattain and C. G. B. Garrett: Bell System Tech. J., **34**, 129 (1955).
7. W. W. Gärtner: Physical Rev., **116**, 84 (1959).
8. H. U. Harten: J. Phys. Chem. Solids, **14**, 220 (1960).
9. H. R. Schöppel and H. Gerischer: Ber. Bunsenges. Phys. Chem., **69**, 578 (1965).
10. H. Gerischer: J. Electrochem. Sci., **113**, 1174 (1966).
11. W. C. Tennant: J. Phys. Chem., **72**, 1078 (1968).
12. A. Fujishima, K. Honda and S. Kikuchi: J. Chem. Soc. Jpn., **72**, 108 (1969), *Nature*, **238**, 37 (1972).
13. M. A. Butler: J. Appl. Phys., **48**, 1914 (1977).
14. R. Memming: J. Electrochem. Soc., **125**, 117 (1978).
15. H. Tributsch: J. Electrochem. Soc., **125**, 1086 (1978).
16. K. L. Hardee and A. J. Bard: J. Electrochem. Soc., **122**, 739 (1975).
17. K. L. Hardee and A. J. Bard: J. Electrochem. Soc., **124**, 215 (1977).
18. K. Hiranoand A. J. Bard: J. Electrochem. Soc., **127**, 1056 (1980).
19. B. L. Wheeler, J. K. Leland and A. J. Bard: J. Electrochem. Soc., **133**, 358 (1986).
20. K. E. Oshe and I. L. Rosenfeld: Electrokhimiya, **4**, 1200 (1968).
21. E. Angelini, M. Maja and P. Spinelli: J. Physique, **38**, C5-261 (1977).
22. W. Paatsch: *Proc. 7th Int.Cong. Met. Corr.*, Rio de Haneiro, Vol. 1, 213 (1978).
23. S. M. Wilhelm, K. S. Yun, L. W. Ballenger and N. Hackerman: J. Electrochem. Soc., **126**, 419 (1979).
24. S. M. Wilhelm and N. Hackerma: J. Electrochem. Soc., **128**, 1668 (1981).
25. U. Stimming: *Proc. of Int. Conf. on Passivity of Metals and Semiconductors*, Ed. by M. Froment, p. 477 (1983).
26. L. M. Peter, J. Li and R. Peat: J. Electroanal. Chem., **165**, 29 (1984).
27. N. Hara and K. Sugimoto: J. Japan Inst. Metals, **52**, 189, (1988).
28. K. Azumi, T. Ohtsuka and N. Sato: J. Japan Inst. Metals, **53**, 479, (1989).
29. H. Gerischer: Corros. Sci., **29**, 191 (1989).
30. H. Gerischer: Corros. Sci., **29**, 257 (1989).
31. H. Gerischer: Corros. Sci., **31**, 88 (1990).
32. H. Gerischer: Electrochim. Acta, **35**, 1677 (1990).
33. F. Di Quarto, S. Piazza, and C. Sunseri: Corros. Sci. **31**, 721 (1990).
34. C. Sunseri, S. Piazza, and F. Di Quarto: J. Electrochem. Soc. **137**, 2411 (1990).
35. N. Sato: *Electrochemistry at Metal and Semiconductor Electrodes*, Elsevier (1998), pp.180.
36. G. Lorang, M. Da Cunha Belo, A. M. P. Simoes and M. G. S. Ferreira: J. Electrochem. Soc. **141**, 3347 (1994).
37. N. E. Hakiki, S. Boudin, B. Rondot and M. Da Cunha Belo: Corros. Sci. **37**, 1809 (1995).
38. N. E. Hakiki and M. Da Cunha Belo: J. Electrochem. Soc. **143**, 3088 (1996).
39. N. E. Hakiki, M. Da Cunha, A. M. P. Simões, and M. G. S. Ferreira: J. Electrochem. Soc. **145**, 3821 (1998).
40. M. G. S. Ferreira, N. E. Hakiki, G. Goodlet: S. Faty, A. M. P. Simões and M. Da Cunha Belo: Electrochimica Acta **46**, 3767 (2001).
41. A. Goossens, M. Vazquez and D. D. Macdonald: Electrochimica Acta **41**, 47 (1996).
42. K. Sieradzki and R. C. Newman: J. Electrochem. Soc. **133**, 1979 (1986).

43. S. Fujimoto, R. C. Newman, G. S. Smith, S. P. Kaye, H. Kheyrandish and J. S. Colligon: Corros. Sci. **35**, 51 (1993).
44. W. P. Yang, D. Costa, and P. Marcus: J. Electrochem. Soc. **141**, 111 (1994).
45. R. Kirchheim: *"Modification of Passive Films"* edited by P. Marcus, B. Baroux, and M. Keddam, p. 17, (The Institute of Materials, London, 1994).
46. S. Fujimoto, S. Kawachi and T. Shibata: *Proc.* 8th *Int. Sym. Passivity and Metals and Semiconductors*, edited by M. B. Ives, J. L. Luo and J. R. Rodda, PV99-42, p. 260, The Electrochemical Society Proceedings Series, Pennington, NJ (2001).
47. S. Fujimoto: *Proc. Asian Pacific Corrosion Control Conference*, Osaka, Nov. 2003, F-08 (2003).

4 Mechanistic Study on Formation of Iron Hydroxides and Oxides with FT-IR and UV Photospectroscopy

Atsushi Muramatsu, Kiyoshi Kanie

4.1 Introduction

Iron oxides are generally stable as a solid in solution phase, because they are barely soluble in water. However, they are formed by a precipitation reaction from a solution including precursor complexes of iron. This precipitation is thermodynamically treated using solubility products, such as $a_{Fe^{3+}} \cdot (a_{OH^-})^3$ (a is an activity). We must pay attention to this treatment, since this description is as a result of an ideal system. Apparently, so many complexes, including ones expressed in solubility products, are in equilibrium in the solution, from which the specific solid is precipitated.

Precipitation reaction is regarded as a phase transformation like the freezing of water. In particular, for solidification of ionic crystal, a precursory complex is very important. Namely, the choice of a specific complex is a key step for the synthesis of a desired solid. For example, we cannot obtain the desired Fe_2O_3 particles if we just mix Fe^{3+} and OH^- ions stochiometrically in a solution, obeying $2Fe^{3+} + 6OH^- \rightarrow Fe_2O_3 + 3H_2O$, because the solidification reaction includes the nucleation and the growth via supersaturation of precursor complexes. In other words, the identification of the precursor and the precise control of precursor concentration are very important. We can understand the mechanism of particle formation only when we discuss the precursory complexes. In the present chapter, iron complexes will be exemplified as a precursor for solidification of iron oxides. We will discuss the influence of coexistent ions on the formation of specific complexes and precipitation by way of UV-vis absorption spectrophotometry, and will also discuss the characterization of as-prepared solids by FT-IR spectroscopy.

4.2 Utilization of UV-vis and FT-IR

Figure 4.1 shows the outline of spectroscopy in terms of wavelength [1]. Among them, absorbance and transmittance data are obtained as a function of time, pH, and so on by a computer system. In this case, we estimate the identification and quantitative treatment by utilization of the remarkable difference in molar absorptivity of specific complexes due to their structure. For example, there is low-order difference in molar absorptivity between

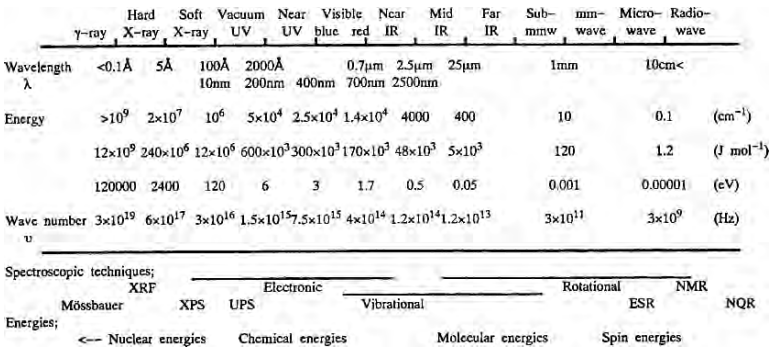

Fig. 4.1. Spectrum of electromagnetic radiation: relationship between representative spectroscopic techniques and the energy and wavelength of the radiation

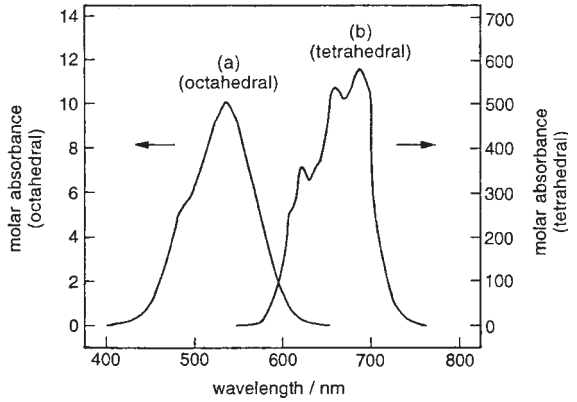

Fig. 4.2. Molar absorbance on visible spectra of (a) octahedral $[Co(H_2O)_6]^{2+}$ and (b) tetrahedral $[CoCl_4]^{2-}$ structures

$[CoCl_4]^{2-}$, regular tetrahedron, and $[Co(H_2O)_6]^{2+}$, regular octahedron, as shown in Fig. 4.2. For the latter, the molar absorptivity is quite low, since electron d-transition is forbidden because of its center of symmetry [2]. Figure 4.3 illustrates some typical molar extinction coefficients for d-d and charge-transfer transitions of transition metal complexes at the UV region of the spectra, where Laporte selection means that the transition in the same orbital is generally forbidden.

Infrared spectroscopy is not usually used for aqueous solutions except for the use of ATR. Generally, dried precipitates are evaluated by transmission and diffuse reflection methods. Metal oxides and halides can be analyzed among inorganic compounds, since IR activity results from vibration with change in dipole moment. The dependence of ligand frequency on its bonding form with metal atoms is also utilized for the characterization of metal complexes. For example, symmetric bending vibration of NH_3 is shifted from

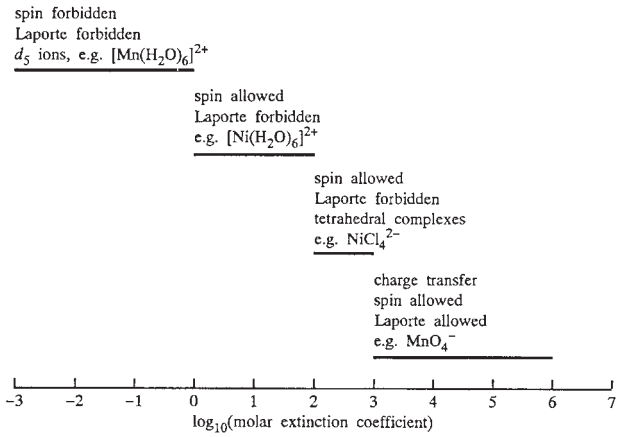

Fig. 4.3. Some typical molar extinction coefficients for d-d and charge-transfer transitions of transition metal complexes on the UV region of the spectra

950 to 1350 cm^{-1} by the formation of ammine complexes [3]. An IR spectrum of an inorganic compound is considerably affected by impurities [4]. Identification of peaks in IR spectra of inorganic compounds is generally difficult because of overlapping absorbance due to the symmetry of vibration and polarization effect due to the shape difference of the primary crystal [5]. For example, 10 vibration modes, in the wavenumber range from 350 to 1400 cm^{-1}, are identified for a single crystal of SiO_2 but 9 modes can be found for SiO_2 powders, in spite of 12 modes theoretically [6]. Hence, for further characterization of inorganic compounds, the detailed theoretical development is indispensable [7].

UV-vis spectrophotometry informs us of useful information such as the concentration ratio of specific complexes in aqueous solutions. TiO_2, well known as a photocatalyst, is always characterized through UV-vis spectroscopy. For example, photo-excitation of O_2 and H_2O was directly observed through spectroscopy with wavelength-changeable laser [8]. However, the most serous defect in UV-vis photoscopy is the low transmission of light for concentrated solutions including target complexes. Figure 4.4 shows UV-vis spectra of $FeCl_3$ solution with different concentrations, using a 1-cm light-pass cell. As shown in Fig. 4.4, light cannot be transmitted by a 1×10^{-3} mol dm^{-3} $FeCl_3$ solutions. In addition, high temperatures such as 100°C are generally required for particle precipitation in homogeneous solution systems. As a result, in situ analysis of particle formation with UV-vis spectrometry cannot be carried out in general. Sapiezko et al. reported the formation mechanism of monodispersed hematite particles with UV spectroscopy [9]. Figure 4.5 shows the relationship of inverse number of absorption at 340 nm with $[H^+]$ (proton concentration) in 5.0×10^{-4} mol dm^{-3} $Fe(ClO_4)_3$ solution at 25°C, giving an excellent linearity. However, these analysis conditions were far from those for particle formation. Desesa and Rogers reported that absorbance of $FeCl_3$ solution was considerably affected by pH [10]. Heistand

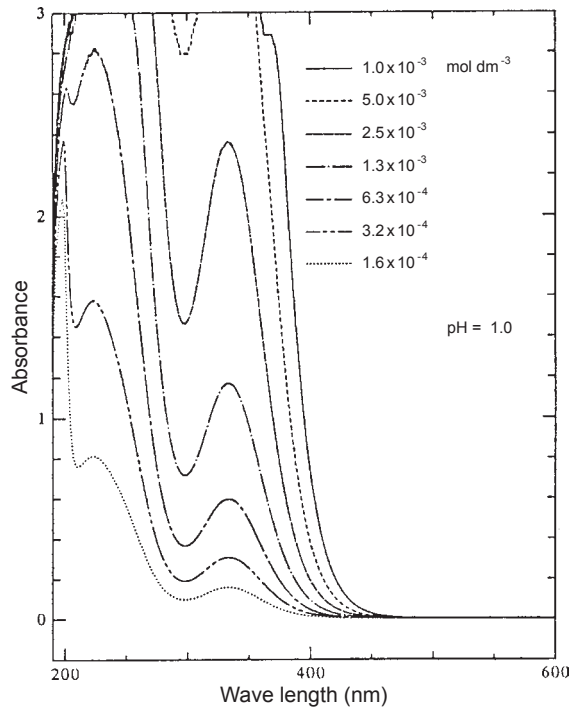

Fig. 4.4. UV absorption spectra of ferric chloride aqueous solutions (cell length: 1 cm; pH = 1.0; 25°C)

and Clearfield clarified the formation rate constant of $FeCl^{2+}$ as a function of electrolyte concentration by UV analysis [11]. Since the UV spectrum is virtually altered with changing Fe^{3+} complexes in solution, UV spectroscopy is an excellent technique to study the formation mechanism of Fe-based particles in aqueous solutions. Henglein et al. evaluated UV spectra change due to the formation of fine Pb particles from dilute $Pb(ClO_4)_2$ solution by the introduction of an electrical pulse, as shown in Fig. 4.6 [12]. They calculated the formation rate constant of Pb from these spectra by theoretical treatment. They also studied the formation mechanism on Ag [13], Au [14], and Cu [15]. We cannot find any report on the mechanistic study with UV spectroscopy other than these reports, though it has been used as the identification method for metal complexes [16].

4.3 Precipitation from Aqueous Solutions

Generally speaking, the precipitation obeys the following steps:

(1) Reservation of monomers
(2) Supersaturation

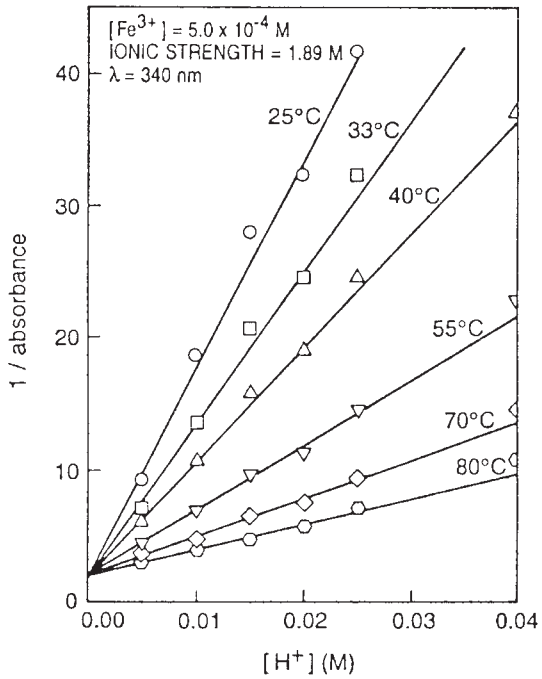

Fig. 4.5. Plots of reciprocal absorbance (λ = 340 nm) vs total added acid concentration at various temperatures. The ionic strength was 1.89 M and $[Fe^{3+}]_{tot}$ = 5.0×10^{-4} M

(3) Nucleation
(4) Particle growth
(5) Termination

What is the monomer? For example, is $Fe(OH)_3$ a monomer for ferric hydroxide as a precipitate? How about hematite? Is the Fe_2O_3 molecule that of a monomer? It already includes the Fe-O-Fe bond! Consider the solubility, also. One molecule, $Fe(OH)_3$ can be dissolved. How about two, three, four, five, etc.? How many $Fe(OH)_3$ complexes can be dissolved in an aqueous solution? $Fe(OH)_3$ is nucleated via supersaturation, or the formation of oligomers.

In general, the embryo initially formed is unstable, but it is gradually stabilized by increasing its size to form nucleus. Specifically, when nucleation has started, numerous molecules have already been precipitated from solution-phase. What is the complex formed prior to this precipitation? It is called a precursor complex. Consider the pH effect. For example, below pH 1, ferric solution is rather stable, but it is remarkably different over pH 6. Precipitation occurs at such pH, in particular with increasing temperature. What phenomenon occurs in solution-phase? It is the most important step for particle formation.

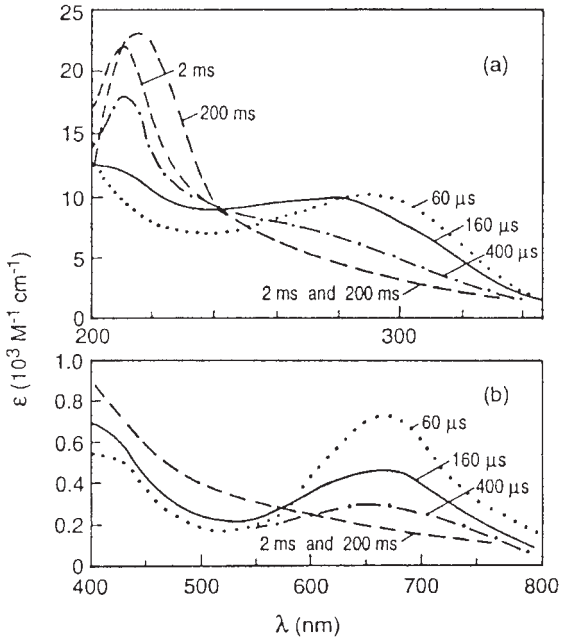

Fig. 4.6. UV absorption spectra (**a**) and spectra in the visible (**b**) at various times after the pulse. Solution: 2×10^{-4}M $Pb(ClO_4)_2$; 2×10^{-3} M $NaClO_4$; pH = 5.4. Radical concentration produced by the pulse: 1.1×10^{-5} M. The solution was deaerated by bubbling with argon

4.4 Simplest Complex of Iron

To simplify the discussion, consider ferric perchlorate solution, because perchlorate is not complexing with ferric ion, ascertained by our investigation. On the other hand, chloride and sulfate are easily coordinated along it. Measuring pH of this ferric perchlorate solution, pH was 1.64 for the 0.10 mol dm^{-3} $Fe(ClO_4)_3$ solution. Why was it so low? It can be explained by the formation of ferric hydroxide complexes. When transition metal salt is dissolved in water, it always shows a low pH, because it is formed as $M(OH)_x$ by coordination with hydroxide ion. Now, consider this pH, 1.64. pH is concerned with activity of H^+. Since activity product of H^+ and OH^- is an ion-product of water, we can discuss the following equations [17]. Namely, assuming that $FeOH^{2+}$ is the primary complex of the 0.10 mol dm^{-3} $Fe(ClO_4)_3$ solution, where the primary complex is defined as the most stable one in the respective solution, pH should be below 1 because there is more than 0.10 mol dm^{-3} $[H^+]$ supplied from the ionic equilibrium:

$$Fe^{3+} + H_2O \Leftrightarrow FeOH^{2+} + H^+ \tag{4.1}$$

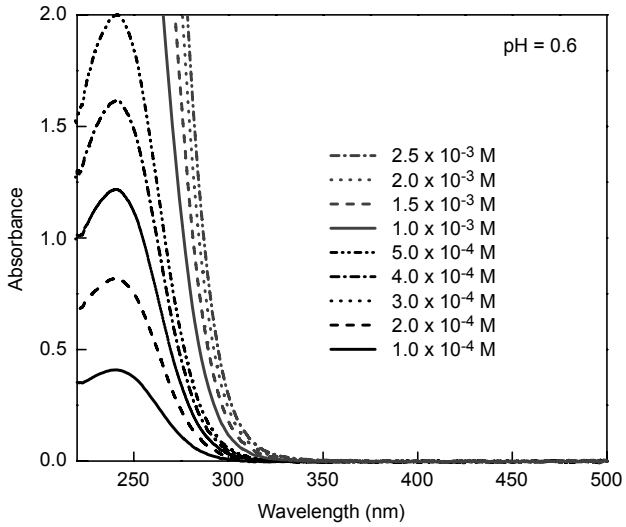

Fig. 4.7. UV absorption spectra of $Fe(ClO_4)_3$ aqueous solutions; effect of concentration (pH=1.0, 5°C)

Moreover, when more than two OH^- ligands are coordinated along Fe^{3+} to form $Fe(OH)_n{}^{(3-n)+}$ obeying Eq. (4.2), pH is below 0.7 because of the formation of more than 0.20 mol dm^{-3} $[H^+]$:

$$Fe^{3+} + nH_2O \Leftrightarrow Fe(OH)_n{}^{(3-n)+} + nH^+ \qquad n = 2, 3, 4, \cdots \qquad (4.2)$$

As a result, free Fe^{3+} ion is surely present in the respective $Fe(ClO_4)_3$ solution with $Fe(OH)^{2+}$ because of the pH of 1.64. We hence conclude that the primary complex is Fe^{3+} [17].

For UV spectra of the $Fe(ClO_4)_3$ solutions below pH 1, a peak appeared around 240 nm. If pH is decreased even more below pH 1, the UV profiles are unchanged by the changing of the concentrations as shown in Fig. 4.7. Furthermore, the UV absorbance is directly proportional to the concentrations of the $Fe(ClO_4)_3$ solutions (Fig. 4.8). So, we conclude that a peak around 240 nm corresponds with free Fe^{3+}, or $Fe(H_2O)_6{}^{3+}$, as the primary complex. Since this peak appears in any other ferric salt solution, Fe^{3+} is thought to be the simplest complex among Fe-based ones.

In the course of precipitation, including nucleation and particle growth, we want to identify the specific complex concerned with the formation of particles. Here, for the precipitation of ferric oxide, olation and oxolation are included. Olation is based on the simple polymerization, such as $Fe_n(OH)_{3n}$, but oxolation is dehydrated condensation to form Fe-O-Fe bonding. The latter gives a pH change because of the release of protons. Also, the former is reversible, but the latter irreversible. It is well known that the former is a rather fast reaction, but the latter slower [18]. For both reactions, the precise

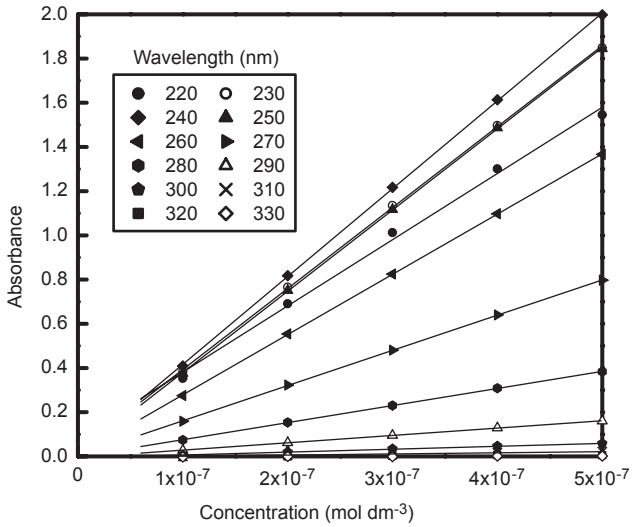

Fig. 4.8. Linear relationships of ferric ion concentrations in $Fe(ClO_4)_3$ aqueous solutions vs the absorbance

evaluation is generally difficult because so many complexes are concerned in the solution phase.

4.5 Change in Ferric Complexes with pH

As mentioned above, $Fe(H_2O)_6{}^{3+}$ is the predominant species below pH 1. With increasing pH, the ligand is changed from H_2O to OH^- step by step. If Cl^- and/or $SO_4{}^{2-}$ is co-present, the ferric ions are complexed with them [19]. Here, we consider $Fe(ClO_4)_3$ solution as the simplest solution system.

So many investigations have been reported on the identification of structure, composition, stability constants, and reaction mechanism of ferric hydroxide complexes [18, 19]. Hedstrom identified Fe^{3+}, $FeOH^{2+}$, $Fe(OH)_2{}^{+}$, and $Fe_2(OH)_2{}^{4+}$ from the difference in potential vs pH in $Fe(ClO_4)_3$ solutions and then calculated their stability constants [20]. Vosburgh et al. reported UV spectroscopy of $Fe(ClO_4)_3$ solutions as a function of pH [21]. Here, they showed that Fe^{3+} and $FeOH^{2+}$ were predominant in the 10^{-4} mol dm^{-3} solution, but $Fe_2(OH)_4{}^{2+}$ became the major species in the 10^{-3} and 10^{-2} mol dm^{-3} solutions, and also that their stability constants and molar absorbance coefficient could be calculated. They also pointed out that mononuculear complexes decreased with increasing ionic strength [22].

Mulay and Selwood investigated the UV spectra in combination with magnetic susceptibility for ferric perchlorate solution [23]. They evaluated the stability constants of $Fe_2(OH)_4{}^{2+}$ independently and their values were agreed. They also claimed that $Fe_2(OH)_4{}^{2+}$ was diamagnetism and then that

ferric oxides had low magnetic moment because this complex was structured in it. Similar to Vosburgh's report, they pointed out that binuclear complexes were rather stable at higher temperatures.

Hsu et al. analyzed $Fe(ClO_4)_3$ solution for more than eight months by pH, XRD, turbidity, colorimetry, and so on [24]. They concluded that $Fe(OH)_3$ initial concentration was in a reverse relationship with the stabilized periods before precipitation by adopting Lamb's model [25] that $Fe_n(OH)_{3n}$ played a role of nucleus and that $Fe(OH)_3$ was condensed on them. They also claimed that $Fe(OH)_3$, a neutral complex, was identified as the precursor complex to direct condensation, because $Fe_n(OH)_{3n}$ was positively charged by proton coordination with terminal OH base.

In these studies, Fe^{3+}, $FeOH^{2+}$, $Fe(OH)_2{}^{+}$, $Fe(OH)_3$, $Fe(OH)_4{}^{-}$, $Fe_2(OH)_4{}^{2+}$, and $Fe_3(OH)_4{}^{5+}$ were reported, in particular, Fe^{3+}, $FeOH^{2+}$, $Fe(OH)_2{}^{+}$, and $Fe_2(OH)_4{}^{2+}$ were commonly used for the analysis. However, they were identified only by Hedstrom with potentiometric titration. The other research took Hedstrom's model for use in further analysis. Flynn's review [19], cited by recent researchers on ferric complexes in waste fluid treatment, was based on reports by Hsu et al. [24], Spiro et al. [26], and Sapiezko et al. [27] in which discussion was started from pioneering researches of Hedstrom [20] and Vosburg [21,22]. Namely, study on ferric complexes was started only by them. What was the problem with the study of Hedstrom [20]? Without any evidence, he identified $Fe(H_2O)_6{}^{3+}$ as the primary complex but he did not prove it. The potentiometric titration itself was a relative evaluation technique but not an absolute one. Hence, strictly speaking, the precursory complex of hematite formation has never been identified, possibly because its identification and estimation of the stability constants is quite difficult under the conditions of particle formation. Also, based on the potentiometric and pH analysis, the primary complex of Fe must be assumed.

4.6 UV Spectroscopy for the Direct Identification of Ferric Complexes

For the first time, Sugimoto et al. tried to identify the precursory complex of nucleation of hematite directly by using a UV spectrometric technique combined with the mathematical analysis established by them [17]. The ferric solution for analysis was chosen to be mainly a dilute system because it is easy to observe its change with pH or time through a UV spectrophotometer. Also, perchlorate solution was used in order to avoid the formation of ferric complexes other than ferric hydroxide ones. Virtually, since monodispersed hematite particles were directly precipitated by aging 5.0×10^{-4} mol dm^{-3} $Fe(ClO_4)_3$ with 0.013 mol dm^{-3} ionic strength at 25 or 60°C and pH = ca. 3.0 without an intermediate such as β-FeOOH, the absence of such an intermediate is advantageous in the kinetic analysis of precursory complex.

Figure 4.9 shows a schematic diagram of the system used in the respective study, consisting of a thermostated bath, a cooler, a pH meter with a pH electrode, a UV spectrophotometer, and a computer for data processing. The UV spectrophotometer was composed of an external light source unit, optical fibers, and a detector (Otsuka Electronics, MCPD-1000), where a measuring cell was immersed in a target solution with a light pass of 6 mm. The light generated by the light source passed through optical fibers to the cell, then finally reached the photodiode allay detector, detecting them and dividing 512 points of the wave simultaneously. Hence, a UV spectrum was obtained in 16 ms at minimum time interval, convenient for pursuing rapid reaction in kinetics. $K_2Cr_2O_7$ solutions at different concentration were measured with MCPD-1000 at light pass = 6 mm. Since the excellent linearity between the concentration and absorbance was obtained in the absorbance range of 0 to 1.5, the measurement was carried out within these limits so that the total concentration of Fe^{3+} was limited to 5×10^{-4} mol dm^{-3} for use of the ordinary cell. For the concentrated solution of $Fe(ClO_4)_3$, however, the special thin cell was used, whose light pass was 25 mm.

Figure 4.10 shows a typical change in UV spectra with altering pH in the solution of $[Fe^{3+}]_{tot} = 5 \times 10^{-4}$ mol dm^{-3} and an ionic strength = 0.013 mol dm^{-3}. The first complex of Fe^{3+}, free Fe^{3+} ion, gave a characteristic peak at ca. 240 nm. With increasing pH, the shoulder peak appeared at ca. 300 nm and then became higher. In this process, they found the isosbestic point at ca. 270 nm. When the isosbestic point was concerned, two kinds of complexes of Fe mainly contributed to the UV absorption, even if the other complex was inactive in the UV region. As a result, they considered only two kinds of complexes as far as the isosbestic point was concerned. With increasing pH, the second complex of Fe^{3+} increased at the expense of the first complex, free Fe^{3+} ion. As pH was increased further, the absorbance at the wavelength, ca. 270 nm, of the isosbestic point was shifted to its upper level (see a curve at

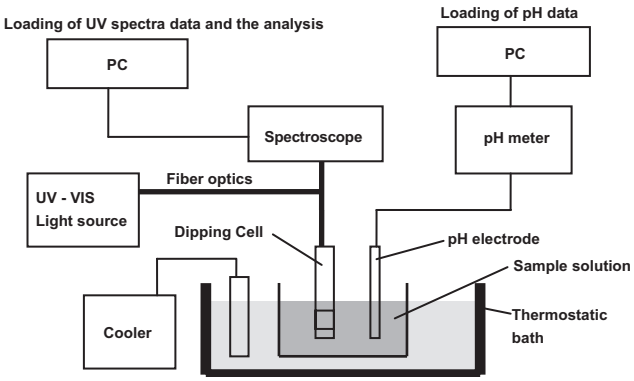

Fig. 4.9. A schematic illustration of UV absorption spectroscopy using a multi channel photodetector

pH = 3.01 in Fig. 4.10), indicating the considerable formation of new complex, called the third complex of Fe^{3+}. In this pH range, the contribution of the third complex cannot be negligible. Hence, we could classify the UV spectra into two groups; those with and without the isosbestic point. For the former (solid lines in Fig. 4.10), by using the molar extinction coefficient, ε_1, of the first complex of Fe^{3+} (free Fe^{3+} ion), estimated by the separate experiments, the second complex of Fe^{3+} can be identified and its stability constant and the molar extinction coefficient also calculated with the mathematical treatment they established. For the latter (broken lines in Fig. 4.10), by using data of the first and second complexes of Fe^{3+} obtained through the above-mentioned analysis, the third and the other complexes of Fe^{3+} could be identified by the mathematical treatment established.

Peaks in the UV spectra of the solution of $[Fe^{3+}]_{tot} = 5.0 \times 10^{-4}$ mol dm^{-3} and an ionic strength = 0.013 mol dm^{-3} at 5, 25, and 60°C, were located in almost the same wavelength but the isosbestic point was a little shifted to the higher wavelength. The second complex of Fe^{3+} was identified by using UV spectra in the pH ranges 2.01–3.41, 1.99–3.30, and 1.03–2.46, respectively, where the isosbestic point was concerned. $FeOH^{2+}$ was identified as the second complex of Fe^{3+}. Also, for 25 and 60°C, the same complex, $FeOH^{2+}$, was suggested through the analysis plot. Since the stability

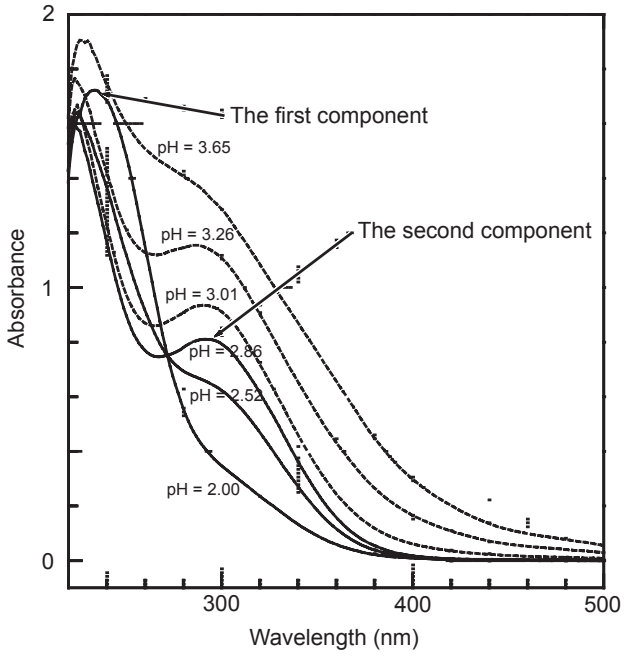

Fig. 4.10. UV absorption spectra of $Fe(ClO_4)_3$ aqueous solutions: effect of pH (ionic strength: 0.013 mol dm^{-3}, 25°C)

Table 4.1. Stability constant (β_1') and molar absorbance coefficient (ε_2) of the second component at various temperatures (330 nm)

Temperature(°C)	Assigned complex	β_1'(mol . dm^{-3})	ε_2(cm^2 · mol^{-1})
5	$FeOH^{2+}$	1.12×10^{-3}	1.35×10^6
25	$FeOH^{2+}$	3.83×10^{-3}	1.31×10^6
60	$FeOH^{2+}$	2.01×10^{-2}	1.34×10^6

Table 4.2. Stability constant (β_1') at 25°C and molar absorbance coefficient (ε_2) of the second component at various ionic strengths (330 nm)

Ionic strength(M)	Assigned complexes	β_1'(mol · dm^{-3})	ε_2(cm^2 · mol^{-1})
0.013	$FeOH^{2+}$	3.83×10^{-3}	1.31×10^6
1.003	$FeOH^{2+}$	1.21×10^{-3}	1.88×10^6
2.003	$FeOH^{2+}$	1.05×10^{-3}	1.96×10^6
4.003	$Fe_2(OH)_2{}^{4+}$	1.12×10^{-2}	2.67×10^6

constant, β_1', gradually increased with increasing temperature, as shown in Table 4.1, the formation of $FeOH^{2+}$ complex is advantageous in the rather high temperature. The molar extinction coefficient, ε_2, is virtually unchanged with changes in temperature.

Since UV spectra of the solution of $[Fe^{3+}]_{tot} = 5.0 \times 10^{-4}$ mol dm^{-3} at 25°C and an ionic strength = 1.003, 2.003, and 4.003 mol dm^{-3}, were compared, with increasing ionic strength, the shoulder peak at ca. 300 nm was shifted to ca. 320 nm while the peak at 240 nm was not shifted. From the linearity of the analysis plot for the ionic strength = 1.003 and 2.003 mol dm^{-3}, $FeOH^{2+}$ was identified as the second complex of Fe^{3+} while, for 4.003 mol dm^{-3}, $Fe_2(OH)_2{}^{4+}$ was identified. In Table 4.2, the stability constants β_1', and the molar extinction coefficients, ε_1, at 330 nm of identified complex at 25°C with different ionic strengths are summarized. The stability constant, β_1', of $FeOH^{2+}$ decreased with increasing ionic strength. As a result, $FeOH^{2+}$ complex was changed to $Fe_2(OH)_2{}^{4+}$ at the higher ionic strength, 4.003 mol dm^{-3}, as pointed out by Milburn and Vosburgh, who mentioned that $FeOH^{2+}$ could be dimerized as a result of suppression of ionic circumstance due to the higher ionic strength. The molar extinction coefficients, ε_1 and ε_2, of the respective first and second complex of Fe^{3+} are summarized in Fig. 4.11. The ε_1 was almost the same but ε_2 was virtually affected by the electrolyte concentration. Table 4.3 shows the results of the analysis of the third and fourth complexes of Fe^{3+}.

Figure 4.12 shows the summary of identification of the first, second, third, and fourth complexes of Fe^{3+}. The precursory species for hematite particles must be the Fe complexes that appeared at the specific pH in which the absorbance became distant from the isosbestic point. From this point of view,

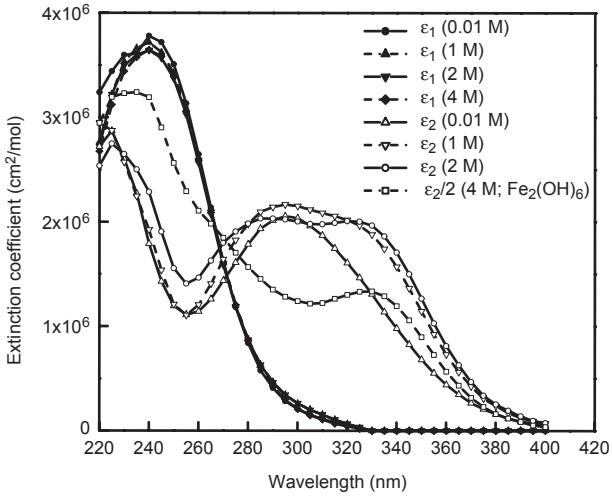

Fig. 4.11. Change of molar absorbance of each components by the changing of ionic strength (5.0×10^{-4} mol dm^{-3} $Fe(ClO_4)_3$, 25°C)

Table 4.3. Analysis results of the third and fourth components of complexes and the stability constants (β_2' and β_3') for the system of 5.0×10^{-4} mol dm^{-3} ferric ions at the ionic strength of 0.013 M

Temperature(°C)	Third component	Fourth component	β_2'	β_3'
5	$Fe_2(OH)_6$	$Fe_2O(OH)_4$	$6.41\ 10^{-18}$	$1.80\ 10^{-19}$
25	$Fe_4(OH)_{18}{}^{6-}$	-	$4.14\ 10^{-50}$	-
60	$Fe_4(OH)_{18}{}^{6-}$	-	$8.32\ 10^{-40}$	-

Units of β_2' for $Fe_2(OH)_6$ and $Fe_4(OH)_{18}{}^{6-}$ components are mol^5 · dm^{-15} and mol^5 · dm^{-45}, respectively

the third complex at 5°C was $Fe_2(OH)_6$ but it cannot be called the minimum unit of Fe because of binuclear Fe species. It is possible to consider that the precursory complex is unstable, that is very active, so that it is easily converted into the other complex. Hence, the precursory complex must be intermediate between the second complex, $FeOH^{2+}$, and the third complex, $Fe_2(OH)_6$. Namely, it must be $Fe(OH)_3$, which may be stabilized as a dimer, $Fe_2(OH)_6$, early in its formation. As pointed out by Hsu et al., $Fe(OH)_3$ was advantageous to gain access to electrically charged surfaces of hematite particle. The polymerization of $Fe(OH)_3$ proceeded to form a complex consisting more than four Fe atoms, such as $Fe_4(OH)_{18}{}^{6-}$. Finally, insoluble Fe clusters were formed and then a stable nucleus was shaped.

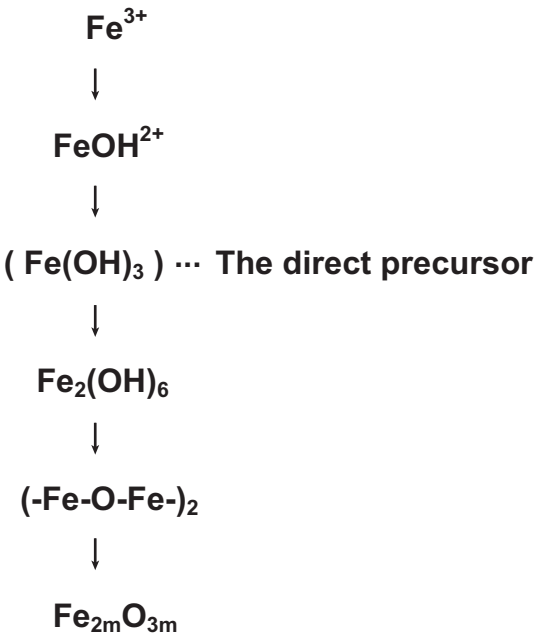

Fig. 4.12. Change of ferric ion complexes in an aqueous $Fe(ClO_4)_3$ solution

It can be concluded that whether in a dilute or concentrated solution of ferric perchlorate, with increasing pH, ferric complexes and hematite particles are formed via the following pass:

$$\begin{aligned} & Fe^{3+} \rightarrow FeOH^{2+}({Fe_2(OH)_2}^{4+}) \rightarrow Fe(OH)_3 \rightarrow (\text{olation}) \rightarrow Fe_2(OH)_6 \\ \rightarrow\ & (\text{oxolation}) \rightarrow (HO)_2{-}Fe - O - Fe{-}(OH)_2 \\ \rightarrow\ & \text{ferric cluster (ex. } {Fe_4(OH)_{18}}^{6-}) \rightarrow \text{nucleus of hematite.} \end{aligned}$$

Dousma and de Bruyn reported that the titration curve of $Fe(NO_3)_3$ solution by NaOH gave three regions, namely, with increasing pH the first region with OH/Fe mole ratio $= 0 - 1$, the second one with $1 - 2.5$, and the third with > 2.5 where the solid formation started. This tendency was consistent with their results but they jumped to the conclusion that Fe complex with OH/Fe > 2.5 mole was unlikely because of not obtaining species without precipitation. A similar discussion was reported by other researchers. Unfortunately, even by their detailed analysis, ${Fe(OH)_2}^{+}$ species could not be found. However, $Fe(OH)_3$ was identified as a stable complex and it was converted to dimer through oxolation by elimination of H_2O. Although Flynn [19] pointed out that whether hematite forms via a process involving polymer complex or forms from low-molecular-weight species, was not clear, from their results, clearly, hematite particles were formed via polymerization of monomeric and/or dimeric species, namely, via polymeric species (ex. ${Fe_4(OH_{18}}^{6-}$).

Formation mechanism of hematite particles involves consideration of monomeric species to form polymeric Fe complexes, their conversion into insoluble Fe cluster, and then finally shaping nuclei. Since the oxolation has been reported to be much slower than the oxolation, the reaction, $Fe(OH)_3 \rightarrow Fe_2(OH)_6$, is considered to be quickly in equilibrium but the reaction, $Fe_2(OH)_6 \rightarrow (HO)_2$-Fe-O-Fe-$(OH)_2$ is rather slow, compared with the further growth of $(HO)_2$-Fe-O-Fe-$(OH)_2$ via the oxolation by monomeric Fe species. Hence, the process of the initial oxolation, $Fe_2(OH)_6$ $(HO)_2$-Fe-O-Fe-$(OH)_2$, must be the rate-determining step. On the other hand, since the equilibrium, $FeOH^{2+} \leftrightarrow {Fe_2(OH)_2}^{4+}$, was rapidly established, reported by Wendt, the formation process of hematite must be the same for dilute or concentrated Fe solutions, even if ${Fe_2(OH)_2}^{4+}$ was formed in place of $FeOH^{2+}$.

The nucleation of hematite follows the polymerization of Fe complexes to form clusters via polymeric species, viz. ${Fe_4(OH)_{18}}^{6-}$. Hematite particles may be grown by the direct adsorption and oxolation of precursory complex, $Fe(OH)_3$, onto their surface, namely, edge-linked dehydration of $Fe(OH)_3$ and surface Fe-O-H, since the initial pH drop reduces the concentration of polymeric species because of low pH, advantageous to the formation of monomeric species. Also, this pH effect must be the definitive role of the formation mechanism of monodispersed hematite particles, pointed out by Sugimoto et al. in concentrated solution.

4.7 IR Spectroscopy for the Formation Mechanism of Particles

Next, we introduce the researches on IR spectroscopy for the particle synthesis mechanism of oxide or hydroxides, because the behavior of OH in bulk and/or on surface can be clarified more easily than XRD, which cannot be applied to amorphous materials. Since it is readily used as a characterization, many inorganic compounds have been evaluated and the attribution of absorption peaks was identified [28]. However, theoretical treatment is rather difficult, compared with that of the actual organic compounds. Several investigations on α-FeOOH transformation to α-Fe_2O_3 have been reported. Rendon et al. [29] discussed structural change of α-Fe_2O_3 through IR spectra of α-Fe_2O_3 calcined in air, in comparison with the results of Onari et al. [30]. Kustova et al. reported that α-Fe_2O_3 crystallinity was lowered by surface OH group, as a result of structural change of α-Fe_2O_3 from α-FeOOH, monitored through IR spectroscopy [31]. A similar study was reported on AlOOH transformation to Al_2O_3 by heat treatment [32]. Although these studies were solid-solid transformation, the information on attribution of IR peaks is also very important for the synthesis of inorganic materials in solution phase. The study of Yates [33] on surface OH group of TiO_2 is very famous. He clearly identified that the phase transformation of anatase and rutile was due to the difference of surface OH properties between them, by the comparison of OH

characteristics between Al_2O_3 and TiO_2 with IR and adsorption of CO and CO_2. In addition, IR spectroscopy was used as the structural and mechanistic study on SiO_2 gel, Al_2O_3, and $AlPO_4$ [34, 35].

IR measurement is also important for the characterization of zeolite and silica-alumina crystalline compounds by hydrothermal synthesis. Ward investigated the surface acidity of OH by IR intensities and shift [36]. He also clarified the difference between Brønsted and Lewis acid sites by the detailed investigation of IR [37]. Refer to Kieslev's book on the relationship of the acid structure and OH base [38]. We don't have an accepted theory on the crystallization mechanism of zeolite, [39] but two mechanisms have been proposed, that is, direct synthesis from amorphous solid [40, 41] and precipitation via its dissolution [42–46]. These studies, spectroscopy of UV, IR, and Raman gave supporting evidence.

Let us survey the mechanistic studies on monodispersed particles of inorganic colloids. Scott and Matijević used the IR spectra of monodispersed boemite colloid as an identification method [47]. Van der Woude and de Bruyn reported the kinetic analysis of the phase transformation of amorphous $Fe(OH)_3$ into crystalline α-FeOOH on the basis of Fe complexes in solution phase through IR measurement of $Fe(OH)_3$ formed in homogenous solution [48]. In coutrast, IR spectroscopy was used as an evaluation method for the coating technique of hydroxides on α-Fe_2O_3. The structural change of Zn hydroxides coated on hematite, due to thermal treatment, was characterized by IR spectra [49], but unfortunately the information of surface could not be identified from the bulk because of the transmission analysis method. A similar investigation has been reported on hydroxides of chromium [50] and aluminum [51]. We also investigated the phase transformation of amorphous $Fe(OH)_3$ via β-FeOOH to α-Fe_2O_3 [52], monitored through IR measurements [53]. Thus, IR spectroscopy is one of the most important techniques for the characterization of inorganic compounds.

Recently, a challenging attempt for IR measurement has been reported on the evaluation of structure and shape of fine particles synthesized. Genzel and Martin proposed the average dielectric constant theory to give the IR spectra of ionic-crystalline particles and then showed good agreement with the spectra actually analyzed [54]. Hayashi also claimed the application of this theory to crystals other than ionic, exemplifying ZnO particles [55]. It was generalized. Ocaña et al. explained the polarization effect of α-quartz and α-cristobalite due to this theory and then anticipated the IR spectra. Moreover, they carried out theoretical analysis on fine crystals of α-Fe_2O_3 [56] and TiO_2 [57] and then applied it to the structural and shape analysis of ZnO colloids obtained by hydrolysis of zinc nitrate and zinc chloride solutions. They correctly estimated the change in shape owing to the aging the solution. Figure 4.13 shows these IR spectra as a function of shape, calculated by the average dielectric constant theory, where the absorption constant K is given by the following equation:

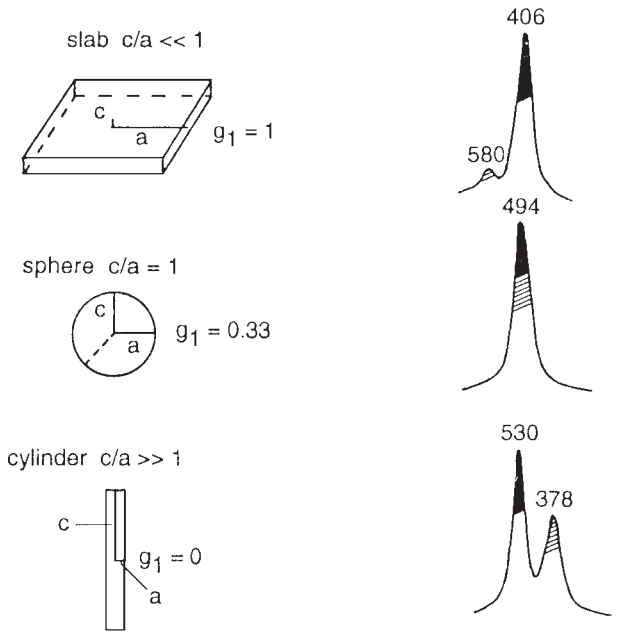

Fig. 4.13. Calculated IR spectra of ZnO microcrystals corresponding to different axial ratios (c/a)

$$\varepsilon_{\mathrm{av}} = 1 + \frac{3(1-f)(\varepsilon_{\mathrm{m}}-1) + \sum\limits_{k} f_k(\tilde{\varepsilon}_1^k + \tilde{\varepsilon}_2^k + \tilde{\varepsilon}_3^k)}{3(1-f) + \sum\limits_{k} f_k(\hat{\varepsilon}_1^k + \hat{\varepsilon}_2^k + \hat{\varepsilon}_3^k)} \tag{4.3}$$

$$\hat{\varepsilon}_1^k = \frac{\varepsilon_{\mathrm{m}}}{\varepsilon_{\mathrm{m}} + g_i^k(\varepsilon_i - \varepsilon_{\mathrm{m}})} \tag{4.4}$$

$$\tilde{\varepsilon}_i^k = (\varepsilon_i - 1)\hat{\varepsilon}_i^k \tag{4.5}$$

$$K = \frac{\omega I(\varepsilon_{\mathrm{av}})}{c_{(\varepsilon_{\mathrm{av}})^{\frac{1}{2}}}} \tag{4.6}$$

where $\varepsilon_{\mathrm{av}}$ is the average dielectric constant; f: filling factor; f_k: k-order ellipsoid; ε_{m}: the average dielectric constant of matrix (viz. KBr); i: basic axis of dielectric constant tensor ($i = 1$ to 3); g: shape factor ($g = 0$ to 1), sum of $g_{\mathrm{i}} = 1$. Andes-Vergas et al. reported [58] that f was out of consideration and matrix effect was negligible for KBr-diluted specimen (<10 wt%) and

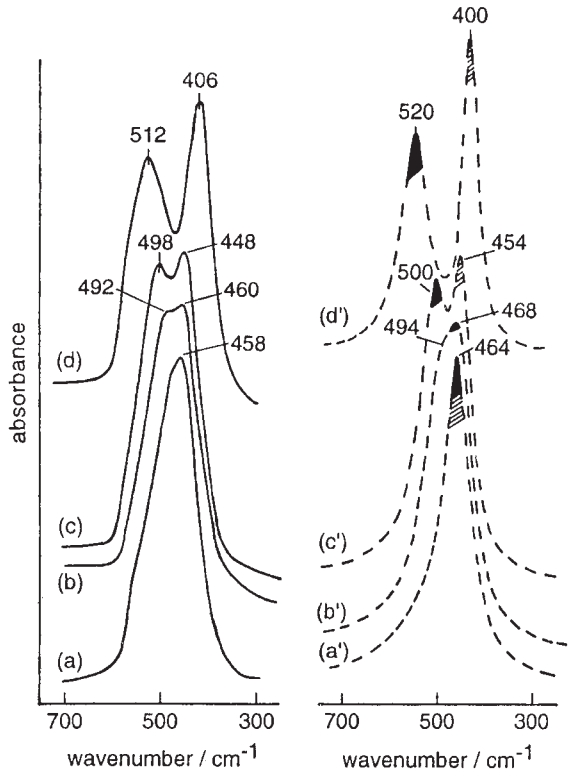

Fig. 4.14. IR spectra corresponding to different formation steps of the prismatic ZnO particles from $Zn(NO_3)_2$ (0.05 mol dm^{-3}) and hexamethylemne imine (0.05 mol dm^{-3}) at 100°C. Experimental spectra (*solid lines*): (a) 0 min; (b) after 3 min; (c) after 7 min; (d) after 30 min. Calculated IR spectra (*dashed lines*): (a′) $g_1 = 0.3$; (*b*′) $g_1 = 0.26$; (c′) $g_1 = 0.22$; (d′) $g_1 = 0.06$, $g_2 = g_3$, $g_1 + g_2 + g_3 = 1$

then that the above equation became only the function of shape factor, g. Accordingly, we can simplify the theory; for platelet particles, $g_1 = 1$, and $g_1 = g_2 = g_3 = 0.33$ for spherical particles. Figure 4.14 shows theoretical and actual IR spectra of ZnO obtained by aging 0.05 mol dm^{-3} $Zn(NO_3)_2$ and 0.05 mol dm^{-3} hexamethylenetetramine. The shape of ZnO was changed during the aging. From SEM observation, it was spherical after 3 min from the start of aging, and the changed to rod-like shape at 30 min, via their mixture at 7 min.

Wang et al. applied the theory to hematite particles and then concluded that the shape effect was confirmed by FT-IR [59]. They also clarified the shape effect of primary crystalline particles and then showed that the characterization of internal structure was possible by FT-IR. Note, however, that the specimen is well dispersed in matrix and that filling factor is below 0.1 [60].

4.8 Characterization of Iron Oxides by FT-IR

Shape control of polycrystalline monodispersed α-Fe_2O_3 particles [52, 53, 62–64] are readily achieved by the Gel-Sol method [61] in the presence of ${SO_4}^{2-}$ or ${PO_4}^{3-}$ ions. Figure 4.15 shows SEM images of the α-Fe_2O_3 particles

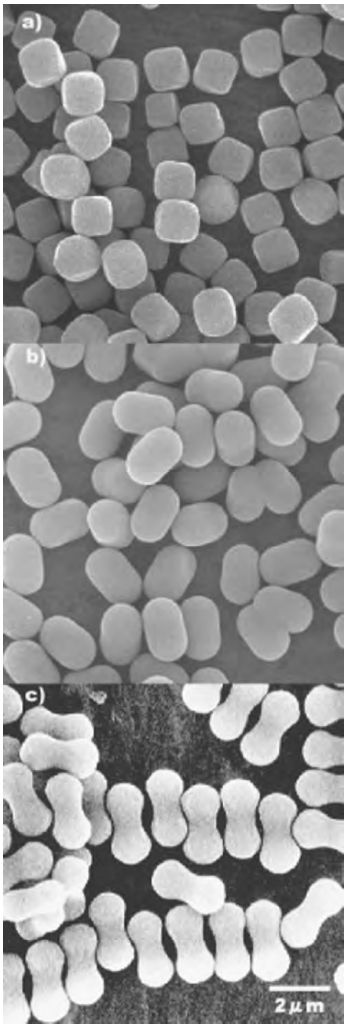

Fig. 4.15. Scanning electron micrographs of monodispersed hematite particles prepared by the Gel-Sol method: (**a**) pseudocubic particles obtained by aging a suspension consisting of 1.0 mol dm^{-3} $FeCl_3$ and 2.7 mol dm^{-3} NaOH at 100°C for eight days; (**b**) ellipsoidal particles formed by the same condition for sample a but in the presence of 1.0×10^{-2} mol dm^{-3} of Na_2SO_4; (**c**) peanut-type particles obtained by the same condition for sample a but in the presence of 3.0×10^{-2} mol dm^{-3} of Na_2SO_4

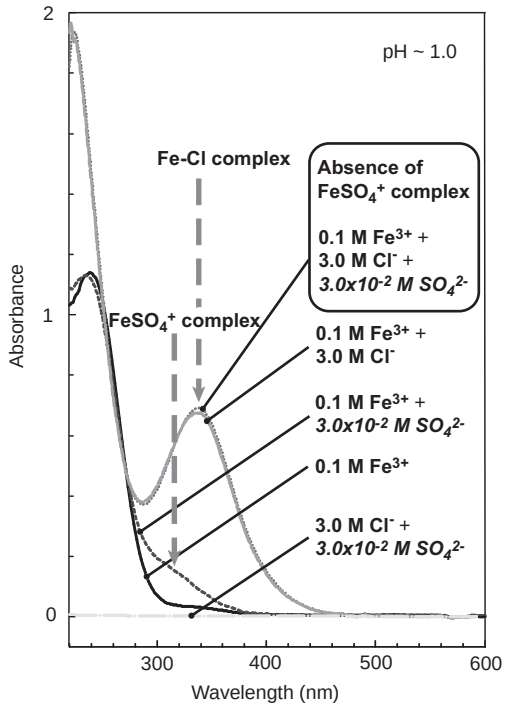

Fig. 4.16. Influence of sulfate ions on the formation of ferric chloride complexes determined by UV spectra

obtained (a) in the absence and in the presence of (b) 1.0×10^{-2} mol dm^{-3} and (c) 3.0×10^{-2} mol dm^{-3} of Na_2SO_4. Since the concentration of Na_2SO_4 to control the shape was only 1.0×10^{-2} and 3.0×10^{-2} mol dm^{-3} in comparison with the total iron concentration (1.0 mol dm^{-3}), a slight amount of shape controller may form the particle shape. We considered that the shape evolution was brought about by the anisotropic crystal growth in the direction of the *c*-axis of the particles by the specific adsorption of the sulfate ions on a plane parallel to the *c*-axis of hexagonal crystal of α-Fe_2O_3. FT-IR is a useful technique for the observation of such specific adsorption behavior of the sulfate ions on a plane parallel to the *c*-axis [65]. Figure 4.16 exhibits the effect of SO_4^{2-} ion on formation of ferric chloride (Fe-Cl) complexes, which is characterized by UV spectroscopy. Although formation of the Fe-Cl complexes is not affected by the coexisting SO_4^{2-} ions, ferric ions form ferric sulfate complexes in the absence of chloride ions. It indicates that the sulfate ions show less affinity for ferric ions than the chloride ions; however, it is enough to adsorb on the specific planes of α-Fe_2O_3 growing particles to form anisotropic shapes. In addition, the sulfate ions show no adsorption ability toward α-Fe_2O_3 over pH 4. It might be brought about by competitive

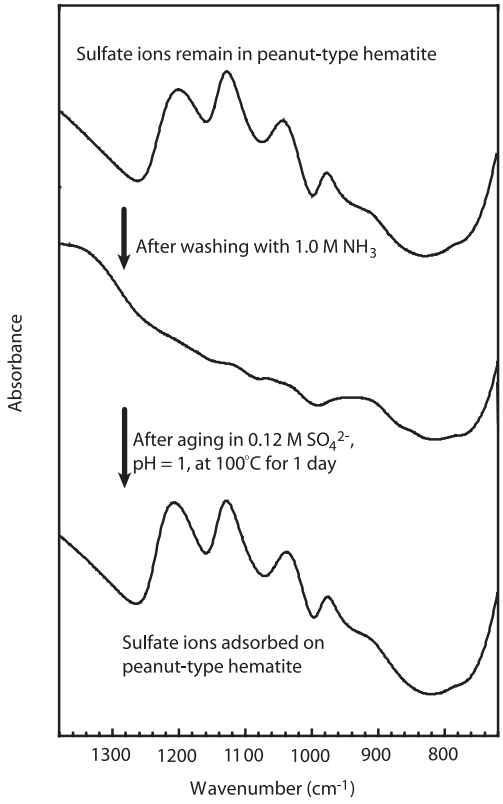

Fig. 4.17. IR spectra of peanut-type α-Fe_2O_3 particles: (a) washed three times with H_2O after their preparation; (b) washed twice with 1 mol dm^{-3} NH_3 and three times with H_2O; (c) washed three times with H_2O after readsorption of sulfate to sample b by aging 0.12 mol dm^{-3} Na_2SO_4 with 0.45 mol dm^{-3} α-Fe_2O_3 for 24 h at pH 1 and 100°C

adsorption of OH^- ions. Furthermore, the isoelectric point of α-Fe_2O_3 particles is normally observed ca. pH 7–8, and the surfaces are negatively charged above this pH by the adsorption of OH^- ions. The sulfate ions exhibit no adsorption ability at such negatively charged surfaces. Elemental analysis of intraparticle structure of the peanuts-type polycrystalline α-Fe_2O_3 particles shown in Fig. 4.15 (c), which was prepared by the Gel-Sol procedure in the presence of sulfate ions, revealed that about 90% of the added amount of sulfate ions were incorporated in the interior of the particles. The sulfate ions were uniformly distributed on the surface and in the interior of the particles. Almost all the sulfate ions were desorbed by treatment with ammonia, and re-adsorbed by treatment with 0.12 mol dm^{-3} Na_2SO_4 at pH 1 with HNO_3 at 100°C for 24 h. Figure 4.17 exhibits the FT-IR spectra of adsorbed, desorbed, and re-adsorbed sulfate ions on the peanut-type α-Fe_2O_3

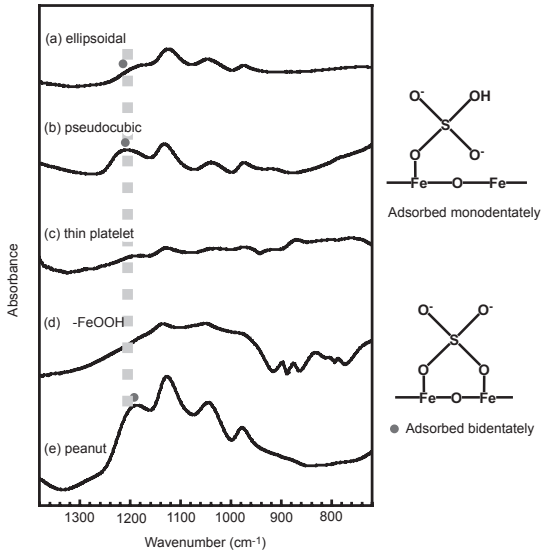

Fig. 4.18. FT-IR spectra of sulfate adsorbed on α-Fe_2O_3 with different shapes

particles. The result shows that the sulfate ions are not incorporated in the α-Fe_2O_3 crystal structure and adsorbed on the surfaces of the polycrystalline α-Fe_2O_3 particles. Furthermore, those adsorption species are the same. These results may confirm that the anisotropic growth control by the sulfate ions is performed through the specific adsorption of free sulfate ions. Actually, adsorption isotherms of the sulfate ion to the α-Fe_2O_3 particles with different crystal habit reveal that (1) the sulfate ions were strongly and selectively adsorbed on the plane parallel to the c-axis and (2) the sulfate ions were hardly adsorbed on {001} planes. The adsorption ability increased in the following order: {001} plane << {012} plane < plane parallel to the c-axis. Figure 4.18 summarizes FT-IR spectra of the fully adsorbed SO_4^{2-} ions on α-Fe_2O_3 and α-FeOOH particles of various shapes. The profiles enabled us to estimate the adsorption pattern of the sulfate ions, mono- or bidentate adsorption, on the surfaces. In this case, the sulfate ions might be adsorbed on ellipsoidal particles with the plane parallel to the c-axis (Fig. 4.18 (a)) and pseudocube surrounded by the {012} plane (b) through the bidentate adsorbtion, and monodentically adsorbed on thin hexagonal platelet particles mainly with {001} plane (c). Since the distance between O-O of SO_4^{2-} (2.45 Å) is closer to Fe-Fe on the plane parallel to the c-axis (2.29 Å) than that of the c plane (2.91 Å), SO_4^{2-} must be adsorbed bidentately on the side of the ellipsoid or {012} and monodentately on {001}. It is well-consistent with the results of FT-IR measurements. On the other hand, distance between Fe-Fe of the side plane of α-FeOOH (3.15 Å) is much larger than that between O-O of SO_4^{2-}, only the monodentate adsorption of sulfate occurred on these particles, in

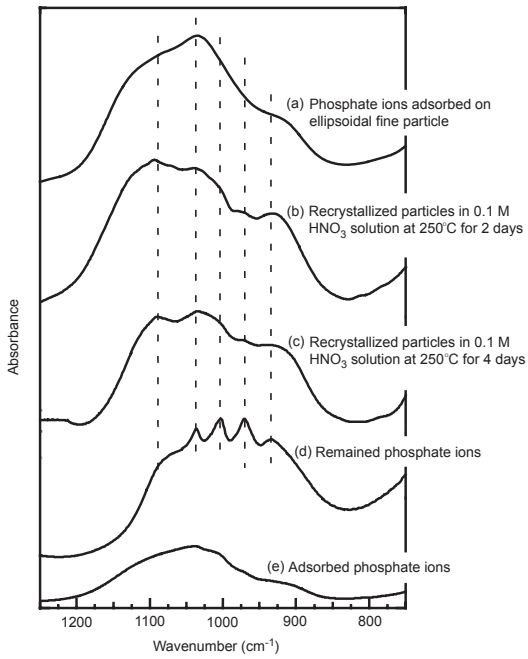

Fig. 4.19. FT-IR spectra of phosphate adsorbed α-Fe_2O_3 particles: (a) phosphate-adsorbed ellipsoidal fine particles; (b) particles obtained by recrystallization of sample a in 0.1 mol dm^{-3} HNO_3 aqueous solution at 250°C for two days; (c) particles formed by four days aging of sample a; (d) incorporated phosphate ions in peanut-type particles; (e) phosphate adsorbed pseudocubic particles

contrast to ellipsoidal particles. Such behavior is actually observed by FT-IR measurement (Fig. 4.18 (d)). Also, the adsorption mode of sulfate is changed from monodentate to bidentate with decreasing pH. The high positive potential of the hematite surface by adsorption of protons as well as the promoted desorption of OH^- ions from the Fe(III) sites may still enhance the strong adsorption of sulfate, leading to the bidentate adsorption. Figure 4.19 exhibits the results of similar adsorption experiments performed by using phosphate ions. PO_4^{3-} ion is also a typical shape controller to yield similar ellipsoidal and peanuts-type α-Fe_2O_3 particles, obtained in the presence of SO_4^{2-} ions. However, the adsorbed PO_4^{3-} ions on the α-Fe_2O_3 surfaces were hardly desorbed by the treatment with ammonia. To examine the different adsorption behavior of the PO_4^{3-} ions from the sulfate ions, PO_4^{3-} adsorbed polycrystalline ellipsoidal particles (Fig. 4.19 (a)) were recrystallized by treatment with 0.10 mol dm^{-3} HNO_3 at 250°C for two days. The peak positions of the FT-IR profile of the resulting particles (Fig. 4.19 (b)) are similar to the PO_4^{3-}-adsorbed peanut-type particles (Fig. 4.19 (d)). Thus, there is a possibility that the PO_4^{3-} ions are not only adsorbed on the surfaces of α-Fe_2O_3

particles like SO_4^{2-} ions but also incorporated in the crystal structure. Actually, single-crystalline monodispersed ellipsoidal α-Fe_2O_3 particles prepared in the presence of PO_4^{3-} ions contains large amounts of the PO_4^{3-} ions in the interior of the particles [66], and any chemical processing is impossible to remove the PO_4^{3-} ions from the particles [67].

As described above, FT-IR measurements have large potentials for the evaluation of the adsorption species on solid surfaces as well as incorporated ions in crystal structures. Further studies concerning analysis of formation mechanisms by using FT-IR equipment will attract attention in the fields of design and development of nano-materials, and so on.

References

1. E. A. V. Ebdworth, D. W. H. Rankin and S. Cradock: *Structural Methods in Inorganic Chemistry*, 3, (1991), Blackwell.
2. H. Kamata: Bunseki Kagaku III, 1, (1968), Korona-shya.
3. H. Kamata: Bunseki Kagaku III, 109, (1968), Korona-shya.
4. J. A. Gadsden: Infrared Spectra of Minerals and Related Compounds, 4, Butterworths (1975).
5. W. G. Spitzer, D. A. Kleinman: Phys. Rev., **121**, 1324 (1961).
6. F. Gervais B. Piriou: Phys. Rev. B, **11**, 3944 (1975).
7. M. Ocaña, V. Fornes, J. V. Garciaramos and C. J. Serna: Phys. Chem. Miner., **14**, 527 (1987).
8. D. Duonghong E. Borgarello and M. Gratzel: J. Am. Chem. Soc., **103**, 4685 (1981).
9. R. S. Sapieszko R. C. Patel and E. Matijević: J. Phys. Chem., **81**, 1061 (1977).
10. M. A. Desesa, L. B. Rogers: Anal. Chim. Acta, **6**, 534 (1952).
11. R. N. Heistand, A. Clearfield: J. Am. Chem. Soc., **85**, 2566 (1963).
12. A. Henglein, E. Janata and A. Fojtik: J. Phys. Chem., **96**, 4734 (1992).
13. A. Henglein, R. Tauschtreml: J. Colloid Interface Sci., **80**, 84 (1981).
14. S. Mosseri, A. Henglein and E. Janata: J. Phys. Chem., **93**, 6791 (1989).
15. B. G. Ershov, E. Janata, M. Michaelis and A. Henglein: J. Phys. Chem., **95**, 8996 (1991).
16. K. Kaneda: Shokubai Kouza IV: ed. by Catalysis Society of Japan, 175, Kodanshya, (1986).
17. Y. Suzuki, G. Kato, A. Muramatsu and T. Sugimoto: the Proceeding of the 51th of the Division of Colloid and Surface Chemistry, The Chemical Society of Japan, (1998).
18. M. A. Blesa, E. Matijević: Adv. Colloid Interface Sci., **29**, 173 (1989).
19. C. M. Jr. Flynn: Chem. Rev., **84**, 31 (1984).
20. B. O. A. Hedstrom: Arkiv for Kemi., **6**, 1 (1953).
21. T. H. III. Siddall, W. C. Vosburgh: J. Am. Chem. Soc., **73**, 4270 (1951).
22. R. M. Milburn, W. C. Vosburgh: J. Am. Chem. Soc., **77**, 1352 (1955).
23. L. N. Mulay, P. W. Selwood: J. Am. Chem. Soc., **77**, 2693 (1955).
24. P. H. Hsu, S. E. Ragone: J. Soil. Sci., **23**, 17 (1972).
25. A. B. Lamb, A. G. Jacques: J. Am. Chem. Soc., **60**, 1215 (1938).
26. T. G. Spiro, S. E. Allerton, J. Renner, A. Terzis, R. Bils and P. Saltman: J. Am. Chem. Soc., **88**, 2721 (1966).

27. R. S. Sapieszko, R. C. Patel and E. Matijević: J. Phys. Chem., **81**, 1061 (1977).
28. For examples; J. A. Gadsden: *Infrared Spectra of Minerals and Related Compounds*, Butterworths (1975); R. A. Nyquist; R. O. Kagel: *Infrared Spectra of Inorganic Compounds*, Academic Press, (1971); N. Nakamoto: *Infrared and Raman Spectra of Inorganic and Coordination Compounds*, 4th ed., Wiley international, (1986).
29. J. L. Rendon, J. Cornejo, P. de Arambarri and C. J. Serna: J. Colloid Interface Sci., **92**, 508 (1983).
30. S. Onari, T. Arai and K. Kudo: Phys. Rev., B, **16**, 1717 (1977).
31. G. N. Kustova, E. B. Burgina, V. A. Sadykov and S. G. Poryvaev: Phys. Chem. Minerals, **18**, 379 (1992).
32. J. J. Fripiat, H. Bosmans and P. G. Bouxhet: J. Phys. Chem., **71**, 1097 (1967).
33. D. J. Yates: J. Phys. Chem., **65**, 746 (1961).
34. M. L. Hair: *Infrared Spectroscopy in Surface Chemistry*, 1, Marcel Dekker, (1967).
35. J. B. Peri: *Catalysis Science and Technology*, edited by J. R. Anderson 5, M. Boudart, 171, SpringerVerlag, (1984).
36. J. W. Ward: J. Catal., **9**, 225 (1967).
37. J. W. Ward: J. Catal., **9**, 396 (1967).
38. A. V. Kiselev, V. I. Lygin: *Infrared Spectra of Surface Compounds*, 1st ed., 1, John Wiley & Sons, (1975).
39. H. Tominaga: *Science and applications of Zeolites* 75, Kodan-shya Scientific, (1987).
40. D. W. Breck, E. M. Flanigen: Molecular Sieves 47, (1968) Soc. Chem. Ind.
41. B. D. McNicol, K. R. Loos and G. T. Pott: J. Phys. Chem., **76**, 3388 (1972).
42. G. T. Kerr: J. Phys. Chem., **70**, 1047 (1966).
43. J. Ciric: J. Colloid Interface Sci., **28**, 315 (1968).
44. S. Ueda, H. Murata, M. Koizumi and N. Nishimura: Am. Mineral., **65**, 1012 (1980).
45. S. Ueda, K. Kageyama and M. Koizumi: Proc. 6th Intl. Zeolite Conf., edited by Olson, D.; Bisio, A.: 905, Butterworths, (1984).
46. F. Roozeboom, H. E. Robson and S. S. Chan: *Zeolites Science and Technology*, 1st ed., edited by Ribeiro, F. 85, Martinus Wijhobb, (1984).
47. W. B. Scott, E. Matijević: J. Colloid Interface Sci., **66**, 447 (1978).
48. J. H. A. Van der Woude, P. L. de Bruyn: Colloids Surf., **8**, 55 (1983).
49. A. Garg, E. Matijević: J. Colloid Interface Sci., **126**, 243 (1988).
50. A. Garg, E. Matijević: Langmuir, **4**, 38 (1988).
51. S. Kratohvil, E. Matijević: Adv. Ceram. Mater., **2**, 798 (1987).
52. T. Sugimoto, K. Sakata: J. Colloid Interface Sci., **152**, 587 (1992).
53. T. Sugimoto, K. Sakata and A. Muramatsu: J. Colloid Interface Sci., **159**, 372 (1993).
54. L. Genzel, T. P. Martin: Surf. Sci., **34**, 33 (1973).
55. S. Hayashi, N. Nakamori and H. Kanamori: J. Phys. Soc. Jpn., **46**, 176 (1979).
56. C. J. Serna, M. Ocaña and J. E. Iglesias: J. Phys. C, **20**, 473 (1987).
57. M. Ocaña, V. Fornes, J. V. G. Ramos and C.J. Serna: J. Solid. State Chem., **75**, 364 (1988).
58. M. Andes-Verges, A. Mifsud and C. J. Serna: J. Chem. Soc. Faraday Trans., **86**, 959 (1990).
59. Y. Wang, A. Muramatsu and T. Sugimoto: Colloids Surf. A: Physicochem. Eng. Aspects, **134**, 281 (1998).

60. C. G. Granqvist, O. Hunderi: Phys. Rev. B, **16**, 3513 (1977).
61. T. Sugimoto: Materia, **35**, 1012 (1996).
62. T. Sugimoto, M. M. Khan and A. Muramatsu: Colloids Surf. A: Physicochem. Eng. Aspects, **70**, 167 (1993).
63. T. Sugimoto, M. M. Khan, A. Muramatsu and H. Itoh: Colloids Surf. A: Physicochem. Eng. Aspects, **79**, 233 (1993).
64. T. Sugimoto, A. Muramatsu, K. Sakata and D. Shindo: J. Colloid Interface Sci., **158**, 420 (1993).
65. T. Sugimoto, Y. J. Wang: Colloid Interface Sci., **207**, 137 (1998).
66. M. Ozaki, S. Kratohvil and E. Matijević: J. Colloid Interface Sci., **102**, 146 (1984).
67. T. Sugimoto, A. Muramatsu: J. Colloid Interface Sci., **184**, 626 (1996).

5 Structural Characterization for a Complex System by Obtaining Middle-Range Ordering

Yoshio Waseda, Shigeru Suzuki, Masatoshi Saito

5.1 Introduction

The evolution of our understanding of most physical and chemical properties of new functional materials is known to depend heavily upon their structural information at a microscopic level. All atomic distribution in the crystals characterized by long-range ordering can be described when we introduce a few parameters of position and distance. Such simple definition is impossible in both the liquid and glassy states, but their atomic distributions in the near-neighbor region are known to be characterized using the concept of the short-range ordering [1]. However, we frequently find a system of interest which is not classified into these two categories. For example, the structure with non-periodicity is confirmed in the second-generation amorphous alloys called "bulk amorphous alloys" [2], but rather complex features are also recognized in the atomic distribution. This is partly attributed to their compositions, which always contain several types of atoms, at least three components. Then, information about their middle-range ordering should be included for materials characterization of bulk amorphous alloys.

On the other hand, the structural feature of corrosion products, which are mainly ferric oxyhydroxides with some alloying elements, is found to be very complicated [3], and some parts of these corrosion products have been assigned to the amorphous state [4]. This again suggests the requirement of middle-range ordering for characterization on the structure of corrosion products. However, an established method is not given yet for describing middle-range ordering. An idea for obtaining the partial structures in a binary non-crystalline system has been proposed by fitting the experimental interference functions with model calculation using the reverse Monte Carlo (RMC) simulation technique [5, 6]. Some successful results on molten salts [7, 8] and metallic liquid alloys [9] prompt us to extend this idea to a complex system.

The purpose of this chapter is to describe one useful way to obtain middle-range ordering in a few nanometers for a complex system including the results of corrosion products formed on the steel surface [10, 11].

5.2 Theoretical Background and Methods

Quantitative description of the atomic arrangements in non-crystalline systems featured by short-range ordering usually employs the radial distribution function (hereafter referred to as RDF). The RDF gives the probability of finding another atom from an origin atom as a function of radial distance [1]. This RDF can simply be extended to a crystalline system given by long-range ordering, so that it is worth mentioning that the RDF concept does give an almost unique way to present middle-range ordering without any change in its principle.

The environment of each atom is known to differ from those of other atoms in both crystalline and non-crystalline systems including more than two components. This frequently makes the interpretation of their RDF data less easy [12–14]. For this purpose, the near neighbor atomic correlation of the individual chemical constituents or the local chemical environment around a specific element is essentially needed for materials characterization of multicomponent systems. The anomalous X-ray scattering (hereafter referred to as AXS) method which involves applying the so-called anomalous dispersion effect near the absorption edge of the constituent elements has recently received much attention, because its usefulness and validity were sufficiently recognized by its providing information about the local chemical environment of a specific element without any assumption for many more elements in the periodic table [15]. The availability of the intense white X-rays produced from synchrotron radiation also dramatically improved both acquisition and quality of the AXS data by enabling the use of an energy in which the anomalous dispersion effect is the greatest. It would be the present authors' intention to employ the use of the experimental interference functions obtained from both conventional and anomalous X-ray scattering in order to get information of middle-range ordering. The method for analyzing the measured AXS intensity data has been described in detail [7, 15] and only some essential points are given below using the case of a binary non-crystalline system.

The reduced interference function, $i(Q,E)$ for a binary non-crystalline system can be described as follows [7]:

$$\begin{aligned} i(Q,E) &\equiv I(Q,E) - \sum_i c_i f_i^2(Q,E) \\ &= \sum_{i=1}^{2}\sum_{j=1}^{2} c_i c_j f_i(Q,E) f_j(Q,E)\{a_{ij}(Q) - 1\} \end{aligned} \tag{5.1}$$

where c_i is the atomic fraction, $I(Q,E)$ is the coherent X-ray scattering intensity which corresponds to the structurally sensitive part of the total scattering intensity. $f_i(Q,E)$ is the atomic scattering factor of i-component, Q and E are the wave vector and the incident X-ray energy, respectively. On the other hand, $a_{ij}(Q)$ is the partial structure factors of $i-j$ pair originally defined by Faber and Ziman [16] and it is connected with the partial pair

distribution function $g_{ij}(r)$ in the following Fourier transform:

$$a_{ij}(Q) = 1 + \frac{4\pi\rho_0}{Q}\int_0^\infty r[g_{ij}(r) - 1]\sin(Qr)dr \tag{5.2}$$

where ρ_0 is the average number density in the system.

As easily seen in Eq. (5.1), the coefficients of $\{a_{ij}(Q) - 1\}$ depend on the atomic scattering factors and concentrations, so that the partial structure factors, $a_{ij}(Q)$, can be estimated from three independent scattering experiments for which the coefficients are altered. The use of anomalous dispersion effect is one way to vary the atomic scattering factors and it makes possible sufficient scattering change in the close vicinity of the absorption edge relevant to K- or L-shell electrons of a constituent element.

When the incident X-ray energy is close to the absorption edge of the constituent elements, the atomic scattering factor should be expressed in the following form [17]:

$$f(Q, E) = f^0(Q) + f'(E) + \mathrm{i}f''(E) \tag{5.3}$$

where $f^0(Q)$ corresponds to the scattering factor of the constituent element at the energy sufficiently away from the absorption edge. The values of $f'(E)$ and $f''(E)$ are the real and imaginary components of the so-called anomalous dispersion terms, respectively.

At the lower energy side of the absorption edge, the $f'(E)$ value shows a drastic change and the absolute values of $f''(E)$ and their energy-variation are quite small. For these reasons, a distinct energy variation of $f'(E)$ at the lower energy side of the absorption edge is very convenient to the AXS measurement. Since the absorption edge of any element is separated by at least several hundred eV, sufficient atomic sensitivity could be detected even in a system containing the neighboring elements of the periodic table [15]. This suggests one of the advantages for the AXS method.

When the incident X-ray energies of E_1 and E_2 are tuned into the lower energy side of the absorption edge E_{abs} of A-element in an A-B binary system, the energy variation detected in intensity, $\Delta i_{\mathrm{A}}(Q, E_1, E_2)$, should be attributed mainly to a change in the real part of anomalous dispersion terms of the component A. Then, the following simple relation can readily be given:

$$\begin{aligned}
&\Delta\, i_{\mathrm{A}}\,(Q, E_1, E_2) \\
&\quad\equiv \frac{\left\{I(Q, E_1) - \left\langle f^2(Q, E_1)\right\rangle\right\} - \left\{I(Q, E_2) - \left\langle f^2(Q, E_2)\right\rangle\right\}}{c_{\mathrm{A}}\{f'_{\mathrm{A}}(E_1) - f'_{\mathrm{A}}(E_2)\}W(Q, E_1, E_2)} \\
&\quad= \frac{c_{\mathrm{A}}\Re\{f_{\mathrm{A}}(Q, E_1) + f_{\mathrm{A}}(Q, E_2)\}}{W(Q, E_1, E_2)}(a_{\mathrm{AA}}(Q) - 1) \\
&\quad+ \frac{c_{\mathrm{B}}\Re\{f_{\mathrm{B}}(Q, E_1) + f_{\mathrm{B}}(Q, E_2)\}}{W(Q, E_1, E_2)}(a_{\mathrm{AB}}(Q) - 1)
\end{aligned} \tag{5.4}$$

$$W(Q,E_1,E_2)=\sum_{k=\mathrm{A,B}} c_k\Re\{f_k(Q,E_1)+f_k(Q,E_2)\} \tag{5.5}$$

where $E1<E2<E_{\mathrm{abs}}$ and A denotes the real part of the values in the brackets. It may be worth mentioning that the quantity of $\Delta i_{\mathrm{A}}(Q,E_1,E_2)$ contains two partial structure factors, $a_{\mathrm{AA}}(Q)$ and $a_{\mathrm{AB}}(Q)$. Similarly, $\Delta i_{\mathrm{B}}(Q,E_3,E_4)$ includes $a_{\mathrm{BB}}(Q)$ and $a_{\mathrm{AB}}(Q)$. In other words, $\Delta i_{\mathrm{A}}(Q,E_1,E_2)$ in Eq. (5.4) enables us to provide the environmental interference function contributed from the structure related only to the A-element and the terms in the front of $\{a_{k\mathrm{A}}(Q)^{-1}\}$correspond to the effective weighting factors. Then, the environmental interference function can be extended to the generalized form and it is connected with the pair distribution function in the following form [15]:

$$\begin{aligned}&\Delta\, i_{\mathrm{A}}\ (Q,E_1,E_2)\\&=\sum_k \frac{c_k\Re\{f_k(Q,E_1)+f_k(Q,E_2)\}}{W(Q,E_1,E_2)}\left(\frac{1}{Q}\right)\int_0^\infty 4\pi r\rho_0\{g_{\mathrm{A}k}(r)-1\}\\&\times\ \sin(Qr)dr\end{aligned} \tag{5.6}$$

The effective weighting factors for the radial distribution function are usually approximated to an average value in the range of Q space. Therefore, the environmental radial distribution function around A, $4\pi r^2\rho_{\mathrm{A}}(r)$, could be described as follows:

$$4\pi r^2\rho_{\mathrm{A}}(r)=4\pi r^2\rho_0+\frac{2r}{\pi}\int_0^\infty Q\Delta i_{\mathrm{A}}(Q)\sin(Qr)dQ \tag{5.7}$$

The use of the environmental structure function around a specific element is found to be quite effective for discussing the structure/property relationships without carrying out the complete separation of all partial functions. This is particularly true in multi-component non-crystalline systems containing more than three elements [15]. It is also worthy of note that the basic concept of the partial structure is perfectly unchanged in the environmental structure function analysis. As shown in Fig. 5.1 using a ternary system as an example, there are six possible atomic pairs, A-A, A-B, A-C, B-B, B-C and C-C in the A-B-C ternary system. Then the ordinary RDF is reflected in these six partial RDFs. However, the environmental RDF around A obtained by the AXS measurement near the absorption edge of A contains three partials of A-A, A-B and A-C. Thus, a relatively easy interpretation of the experimental results can be allowed. An idea for obtaining middle-range ordering is presented in the following. A realistic model structure in a system of interest is estimated by fitting two or three independent experimental data with model calculation using the reverse Monte Carlo (hereafter referred to as RMC) simulation technique.

For example, the atomic distribution in the region of a few nanometers can be estimated by fitting both the ordinary interference function and the

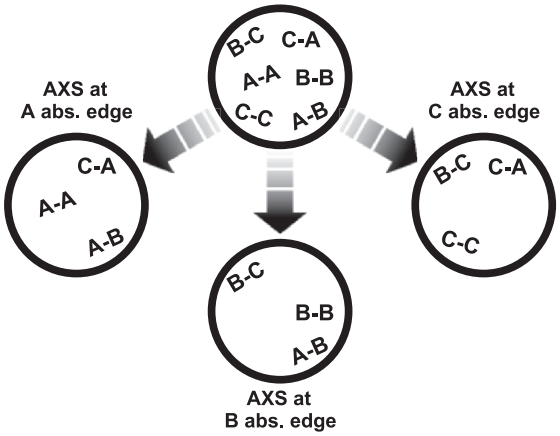

Fig. 5.1. Advantage of AXS method for reducing the number of atomic pairs in an A-B-C ternary system

environmental interference function obtained from the AXS data. Such a fitting process is made with the help of the RMC simulation technique [7–11]. Here, the RMC simulation technique is carried out in a way essentially identical to that originally proposed by McGreevy and Pusztai [5] with an initial configuration of particles in a super cell. The partial pair distribution functions, $g_{ij}(r)$, are computed under the condition where the usual periodic boundary conditions are set. By applying the Fourier transformation to $g_{ij}(r)$, the interference functions via structure factors are compared with the experimental AXS data by estimating the following statistic:

$$\chi^2 = \sum_{m=1}^{n} \frac{\left\{ i(Q_m) - i^c(Q_m) \right\}^2}{\sigma^2(Q_m)} + \sum_{\alpha} \sum_{m=1}^{n'} \frac{\left\{ \Delta i_\alpha(Q_m) - \Delta i_\alpha^c(Q_m) \right\}^2}{\sigma_\alpha^2(Q_m)} \tag{5.8}$$

where $i^c(Q_m)$ and $\Delta i_\alpha^c(Q_m)$ are the calculated interference function and its difference for α component, measured at Q_m, respectively. On the other hand, $\sigma(Q_m)$ and $\sigma_\alpha(Q_m)$ are the estimates of the experimental uncertainty. A new configuration is generated through the random movement of one particle in a computer. It may be stressed that the cut-off distance is set for each $g_{ij}(r)$ closer than the direct contact value of two particles, in order to prevent particles from approaching un-physically close to one another. When the new configuration violates these cut-off restrictions, it is rejected and the previous configuration data is restored. Otherwise the variation in $g_{ij}(r)$ is computed, and from this new $i^c(Q)$, $\Delta i^c(Q)$ and χ^2 are estimated. For convenience, the flow chart of the RMC technique is illustrated in Fig. 5.2. When the new value of χ^2 is smaller than the old one, the new configuration is accepted; otherwise it is accepted only with a probability less than unity. Such an

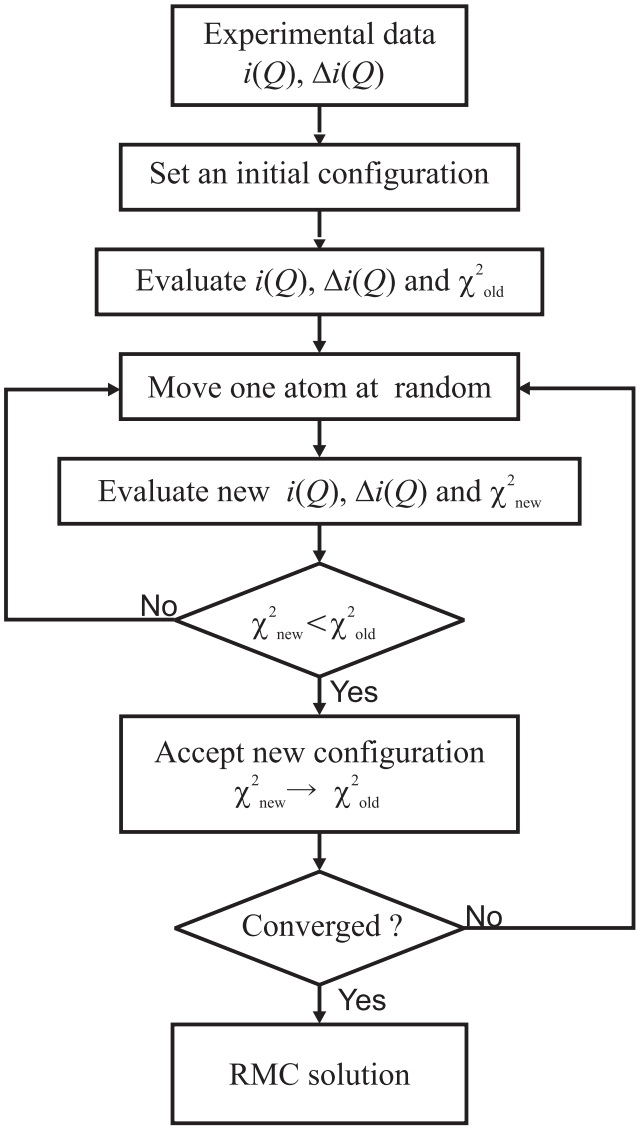

Fig. 5.2. Flow chart of the RMC simulation technique for analyzing the AXS data

iteration process is continued until the value of χ^2 indicates a reasonable convergence. It has been the intention of the present authors to suggest the following important point. The resultant atomic distribution is considered at least in a sense of the necessary condition at best for explaining two or three independent experimental data, although it might be not the sufficient condition [15].

5.3 Selected Examples of Middle-range Ordering Obtained by the AXS Method Coupled with the RMC Simulation Technique

5.3.1 GeO_2 Glass

GeO_2 glass is a prototype constituting the basis for a large family of non-crystalline materials together with SiO_2 glass. The partial structural functions of GeO_2 glass were determined firstly by Bondot [18] in 1974 using a combination of the AXS and neutron diffraction. His results have been referred to as a unique example for determining the partial structural functions of oxide glass, although they appear not to be complete regarding quantitative discussion, mainly due to difficulties of the AXS experiment in that stage. On the other hand, the availability of the intense white X-rays from a synchrotron radiation source has greatly improved both acquisition and quality of the AXS data by enabling the use of energy in which the AXS component is the greatest. Then, Matsubara et al. [19] carried out the AXS measurement for GeO_2 glass with synchrotron radiation and estimated the three partials directly by solving the simultaneous linear equation [20]. Their careful experiments provided more quantitative structural information relating to the nearest-neighboring correlations than Bondot's results. Nevertheless, the RMC simulation technique is strongly recommended for improving quality of the partial structural functions estimated from the AXS data [7, 9]. This prompts us to re-analyze the previous data of AXS and neutron diffraction [20] by applying the RMC simulation technique for obtaining a detailed model of GeO_2 glass structure through the precise determination of its three partial structural functions.

Figure 5.3 shows the experimental interference functions of GeO_2 glass obtained by the ordinary X-ray, $Qi(Q)$, and neutron diffraction, $Qi_{\mathrm{ND}}(Q)$, together with the environmental interference function, $Q\Delta i_{\mathrm{Ge}}(Q)$, by anomalous X-ray scattering at the Ge K absorption edge [19, 20]. Corresponding interference functions calculated by RMC simulation are also drawn with dotted lines in this figure. The RMC simulation starts from an initial arrangement with 3840 atoms (1280 Ge atoms and 2560 O atoms) in a cubic box of size $L^3 = 3.957^3\mathrm{nm}^3$, giving the average number density of 62.0 atoms/nm^3. It can be shown that these RMC simulation results reproduced three independent interference functions within experimental error. This agreement clearly indicates that the present approach basically works well.

The resultant partial structure factors $a_{ij}(Q)$ of GeO_2 glass determined by applying the RMC simulation technique are illustrated with solid lines in Fig. 5.4. Dotted lines correspond to the previous results estimated by directly solving the simultaneous linear equations [20]. These two results are, in the present authors' view, found to agree well qualitatively with each other by finding the following common meaningful features. The positions of strongest

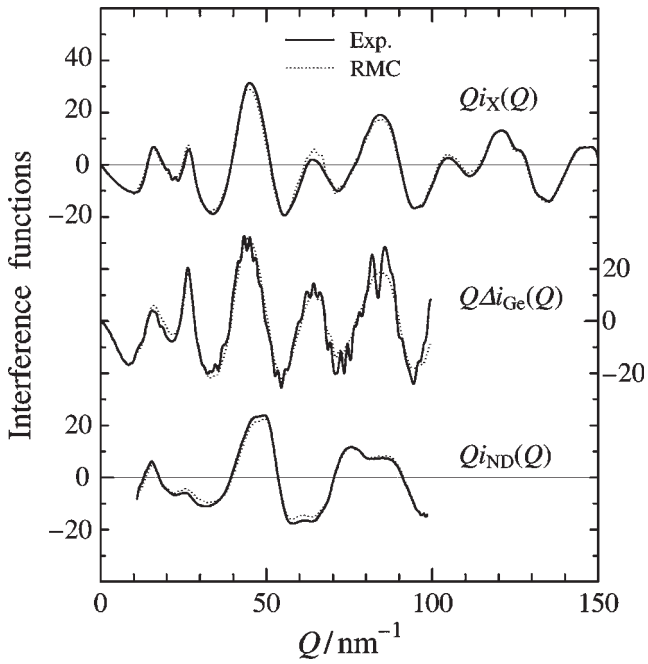

Fig. 5.3. Interference functions of GeO_2 glass from conventional X-ray diffraction, $QiX(Q)$, anomalous X-ray scattering measurements, $Q\Delta i_{Ge}(Q)$, and neutron diffraction, $Qi_{ND}(Q)$. *Solid lines* correspond to the experimental data and *dotted lines* denote the calculated functions by RMC simulation, respectively

peaks in $a_{GeGe}(Q)$ and $a_{OO}(Q)$ are situated in close vicinity of the first valley of $a_{GeO}(Q)$. In addition, distinct peaks in $a_{GeGe}(Q)$ and $a_{GeO}(Q)$ can be seen around $Q = 15\text{nm}^{-1}$, suggesting the intermediate range ordering in the correlation associated dominantly with Ge, as is generally the case in oxide glasses. However, there are some differences in detail between the present RMC results and the previous ones. There seems to be slightly ill conditioned in the previous results estimated by directly solving the simultaneous linear equations, giving some physically unreasonable behavior in the resultant radial distribution functions. This is mainly due to experimental uncertainty such as the relatively small difference between the anomalous dispersion terms at two energies and the unpredictable large fluctuation in numerical solution, when the pivot of matrix is close to zero [21]. Such small experimental errors cannot always be avoided to the best knowledge of the present authors. The RMC simulation technique used in this work might be one way for reducing such inconvenience. Considering many factors relevant to the experimental errors, the results of Fig. 5.4 are rather good because all RMC structure factors coincide with average values of the experimental error so as to produce a smooth continuous function. However, it should be kept

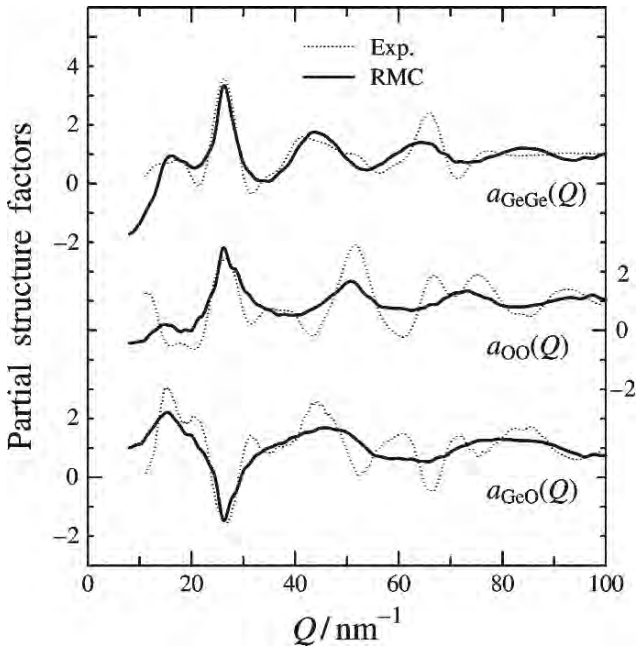

Fig. 5.4. Partial structure factors of GeO_2 glass estimated by RMC simulation. *Dotted lines* correspond to the previous results [20] estimated by directly solving the simultaneous linear equations

in mind that this RMC simulation technique is not a unique mathematical procedure. This means that the partial structure factors presently estimated are considered to be in a sense the necessary condition for best explaining the three independent experimental data, although they might not be the required condition.

The RDFs obtained by RMC simulation are illustrated with solid lines in Fig. 5.5. The results [20] estimated by directly solving the simultaneous linear equations are also illustrated with dotted lines in this figure. Every first peak profile in the previous results are found to be rather broader than those of the RMC results. This broadening should be attributed to the finite Q range in the Fourier transformation. In order to compare the results in a more reasonable base, the partial RDFs of RMC simulation are transformed in the same Q range 100 nm^{-1} as used in the previous work on direct solution of simultaneous linear equations and such results are represented by broken lines in Fig. 5.5. The agreement among them becomes fairly good, particularly for the first peak profiles. The interatomic distances r_{ij} and coordination numbers N_{ij} for i-j pairs defined by the integration up to the first minimum in the partial RDFs are estimated. The results are summarized in Table 5.1, together with the values obtained by directly solving the simultaneous linear equations [20] and those of the α-quartz type GeO_2 crystal as a reference.

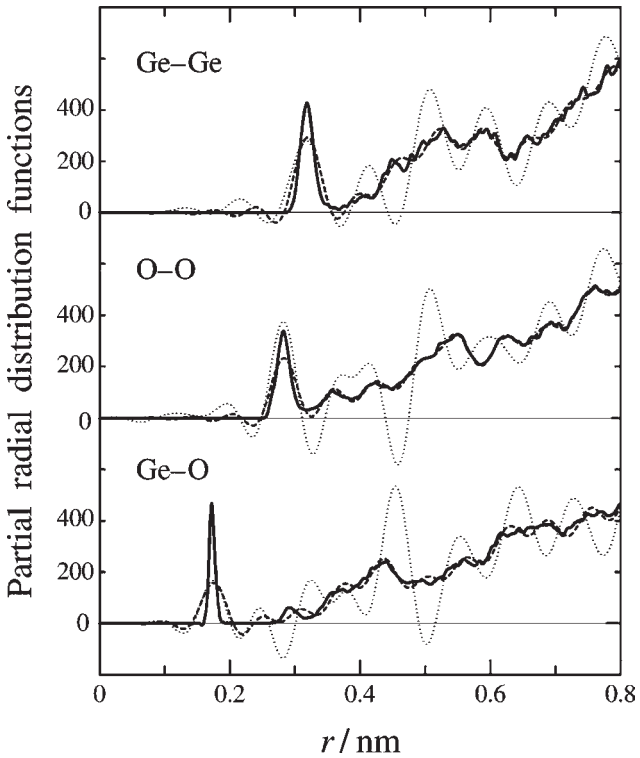

Fig. 5.5. Partial radial distribution functions of GeO_2 glass estimated by RMC simulation. *Dotted lines* correspond to the previous results [20] estimated by directly solving the simultaneous linear equation. *Broken lines* indicate the partial RDFs calculated from RMC partial structure factors by the Fourier transform in the Q range up to 10 nm^{-1}

Good agreement is recognized for all distances and coordination numbers of three pairs in this table.

It has been found that each Ge is surrounded by four oxygens with a distance of 0.172 nm. Thus, it can be confirmed that the GeO_4 tetrahedron is a fundamental local structure unit in GeO_2 glass. The O-O distance is nearly equal to the edge length of the tetrahedron. Since N_{GeGe} is about 4 and N_{OO} is about 6, each oxygen located at the corner of the tetrahedron is quite likely to be bonded with two Ge atoms, so that a network structure formed by the tetrahedral units joined at their corners is quite feasible in GeO_2 glass. From the realistic model structure for explaining the three independent experimental data, the orientational three-particle correlations in GeO_2 glass were also estimated by calculating the bond angle distribution $B_{\alpha\beta\gamma}$ defined as the number of angles between the two vectors joining a central atom (β) with any two neighbors (α and γ) of its coordination shell. The resultant

Table 5.1. Comparison of structure parameters in the present work with those of the previous result and the α-quartz type crystal structure

	Ge-O		O-O		Ge-Ge	
	r/nm	N_{GeO}	r/nm	N_{OO}	r/nm	N_{GeGe}
Present work (RMC)	0.172	3.7	0.282	6.5	0.319	4.0
Previous work [20]	0.175	4.0	0.282	6.8	0.318	4.5
α-Quartz type of GeO_2	0.1737 0.1741	2 2	0.2783 0.2805 0.2860 0.2902	2 1 1 2	0.3153	4

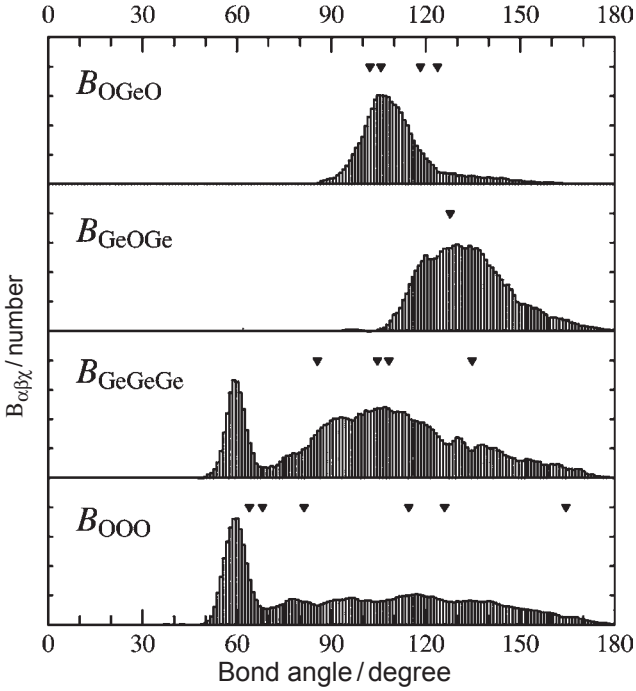

Fig. 5.6. Bond angle distributions for GeO_2 glass. *Solid triangles* denote the angle positions found in a-quartz type GeO_2 crystal

bond angle distributions are given in Fig. 5.6, where solid triangles denote the angle positions found in α-quartz type GeO_2 crystal.

The results of B_{OGeO} give a single peak averaged to about 105°, which is not far from the ideal intra-tetrahedral angle of 109.3°. On the other hand,

B_{OOO} shows a sharp peak located at 60°, which coincides with the value of an equilateral triangle. It can be concluded again from these two results that GeO_4 tetrahedra are the fundamental units of local ordering structure in GeO_2 glass. The results of B_{GeOGe} show a broad distribution with an average angle of 130° that is in agreement with the value of 130° in α-quartz type GeO_2 where the tetrahedral units of GeO_4 are connected at their corners. The bond angle distribution for B_{GeGeGe} indicates two peaks occurring at approximately 60° and 105°. The broader profile with an average angle of 105° may be attributed to the structure of α-quartz type GeO_2, although the distinct peak located at 60° is not detected in the crystalline case. It may be noted here that a similar sharp peak located at 60° is also found in B_{SiSiSi} for SiO_2 glass [22], suggesting the existence of three-membered rings in the glass structure. The first-principles molecular dynamics [23] for SiO_2 glass, which conclusively assigns its Raman defects lines to n-membered rings, suggests the clear proof for the occurrence of such small rings embedded in the network structure. These characteristic structural features can be confirmed in the projection of a representative RMC generated configuration of GeO_2 glass, as shown in Fig. 5.7. For convenience, ideal GeO_4 units are selected and drawn as tetrahedral in this figure. Most of GeO_4 tetrahedra are found to be joined together at their corners, forming a three-dimensional network structure. Furthermore, it would be worth mentioning that three-membered rings as expected from the bond angle distribution can be detected in the RMC results as illustrated at the bottom of Fig. 5.7 in the enlarged form.

5.3.2 Amorphous ZrO_2 Prepared by Hydrolytic Condensation

A number of interesting materials have been produced by sol-gel method [24] and zirconium oxide is included in this category. Thermal decomposition of amorphous ZrO_2 prepared from zirconium alkoxides [25] or from zirconium

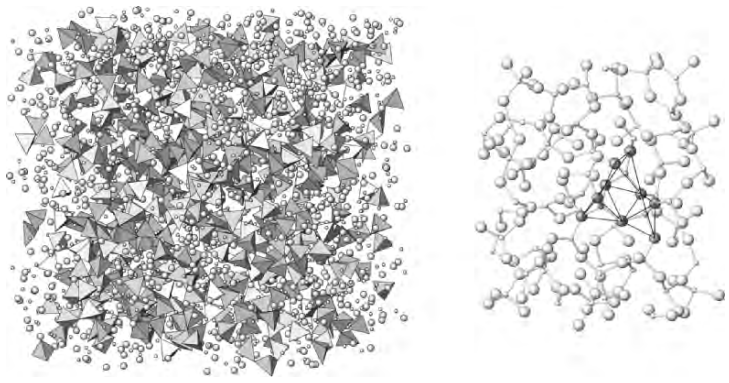

Fig. 5.7. A projection of atomic positions from a representative RMC configuration. *Larger atoms* are O, *smaller atoms* are Ge. GeO_4 units are selected and drawn by tetrahedra. An enlarged drawing is also given at the bottom of this figure

salts [26,27] is known to produce a metastable phase of tetragonal ZrO_2 (hereafter referred to as t-ZrO_2). On the other hand, it is noted that monoclinic ZrO_2 (hereafter referred to as m-ZrO_2) is actually stable at temperatures lower than 1273 K. Nevertheless, the formation of t-ZrO_2 at low temperature is still one of the controversial subjects. For example, Cypres et al. [28] propose that the stabilization of t-ZrO_2 is attributed to various anionic impurities such as OH^-. This is inconsistent with the comment of Mazdiyasni et al. [25] or Garvie [26] suggesting that it should be related to the particle size effect. Livage et al. [29] and Tani et al. [30] reported that the stabilization of t-ZrO_2 may be explained by the similarity of local ordering structure between amorphous and crystalline tetragonal ZrO_2. In these contexts, the structure of amorphous ZrO_2 holds the key to provide an answer with respect to the particular crystallization behavior of zirconium oxide during low temperature heating. Thus, the AXS method has been applied to obtain the atomic scale structure of hydrolytic condensed zirconium oxide at longer distance as well as the structure in the nearest neighbors including the structural similarity between amorphous ZrO_2 and crystalline ZrO_2 [31]. The results are summarized as follows.

Two scattering intensity profiles were measured at 17.973 and 17.698 keV, which correspond to 25 and 300 eV below the Zr K absorption edge (17.998 keV) and the resultant environmental interference function $Q\Delta i_{\mathrm{Zr}}(Q)$ for Zr of hydrolytic condensed zirconium oxide is shown in Fig. 5.8. The ordinary interference function $Qi(Q)$ estimated from the diffraction data of single energy of 17.698 keV is also given in this figure for comparison. These interference function profiles consist of the first peak at about 22 nm^{-1} followed by a number of peaks. This clearly indicates a considerable fraction of local ordering unit structures in this amorphous structure, although their distribution appears to be no long-range ordering. It would be of interest that these features contrast to the case of metallic glasses, where the rapid damping of interference function is clearly observed [32]. As easily seen in Fig. 5.8, the essential profile of the environmental $Q\Delta i_{\mathrm{Zr}}(Q)$ is very similar to that of ordinary $Qi(Q)$ of amorphous ZrO_2, although the environmental $Q\Delta i_{\mathrm{Zr}}(Q)$ includes the two partial functions of Zr-O and Zr-Zr pairs only. This is mainly due to the reason that the contribution of O-O pairs to the ordinary $Qi(Q)$ is not so significant. Nevertheless, it is stressed that the environmental $Q\Delta i_{\mathrm{Zr}}(Q)$ is rather distinct in detail in comparison with the ordinary $Qi(Q)$ case. The effective use of such different nature obtained by the AXS measurements is expected to improve the resolution and reliability of the structural parameters for Zr-O and Zr-Zr pairs even in the higher order correlation when using the RMC technique. The resultant partial structure factors $a_{ij}(Q)$ of amorphous ZrO_2 determined by applying the RMC simulation technique are illustrated in Fig. 5.9.

The RMC simulation starts from an initial arrangement with 1944 atoms (648 Zr atoms and 1296 O atoms) in a super cell of size $L^3 = 3.095^3 nm^3$,

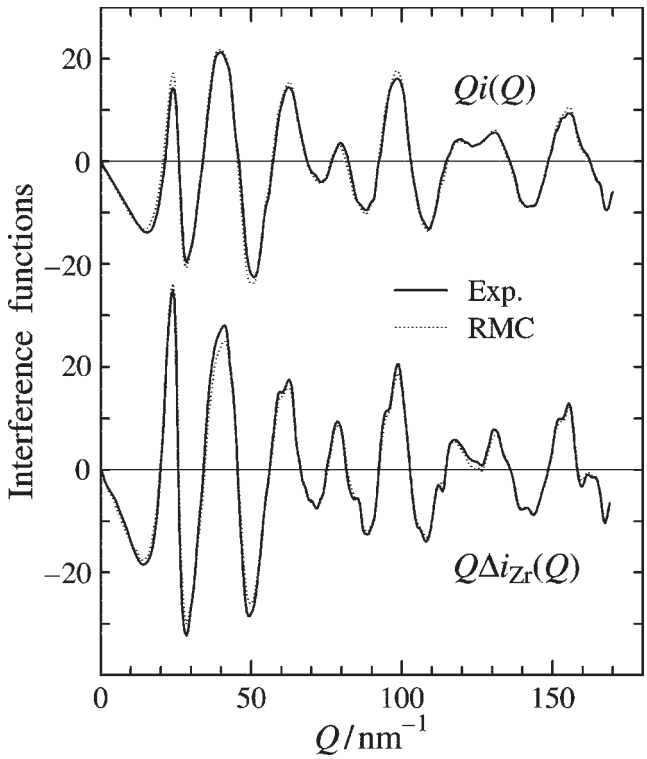

Fig. 5.8. Ordinary interference function $Qi(Q)$ and the environmental interference function $Q\Delta i_{\mathrm{Zr}}(Q)$ of amorphous ZrO_2. *Solid lines* correspond to the experimental data. *Dotted lines* denote values computed by the RMC simulation technique

giving the average number density of 65.5 atoms/nm^3. The positions of strongest peaks in $a_{\mathrm{ZrZr}}(Q)$ are situated in the close vicinity of the first valley of $a_{\mathrm{ZrO}}(Q)$. The partial pair distribution functions obtained by RMC simulation are illustrated in Fig. 5.10. The interatomic distances r_{ij} and coordination numbers N_{ij} for i-j pairs are estimated and the results are summarized in Table 5.2, together with those of the crystalline zirconium oxides [33, 34].

As shown in Table 5.2, the Zr atom is surrounded with 5.0 oxygens at 0.214 nm in the amorphous ZrO_2. The Zr-Zr pair around 0.34 nm and a pronounced subsidiary hump at around 0.4 nm are well coincident with the atomic pairs characterized by the m-ZrO_2 structure. A projection of the atomic positions from a representative configuration obtained in the RMC simulation process is shown in Fig. 5.11. Here, bonds between Zr and O atoms are drawn as sticks. Figure 5.12 shows the resultant bond angle distributions $B_{\alpha\beta\gamma}$ of amorphous ZrO_2, where solid triangles and squares denote the angle positions found in m-ZrO_2 and t-ZrO_2, respectively. B_{OZrO} gives a peak averaged to about 75°. B_{ZrOZr} shows a peak with an average angle of

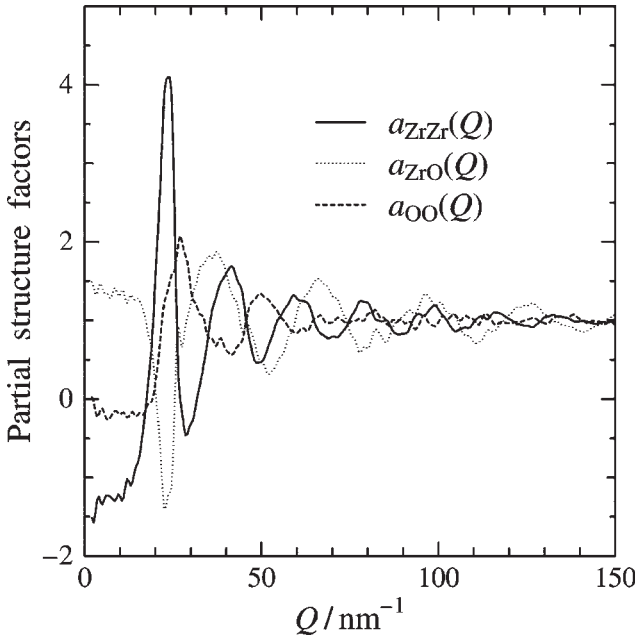

Fig. 5.9. Three partial structure factors of amorphous ZrO_2

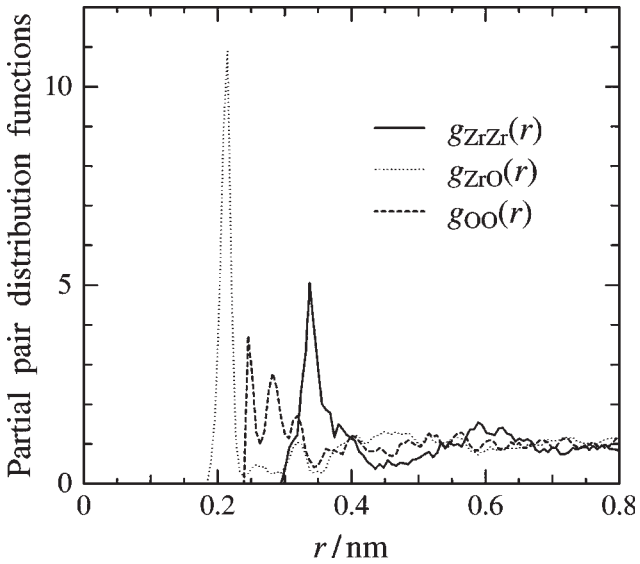

Fig. 5.10. Three partial pair distribution functions of amorphous ZrO_2

Table 5.2. Comparison of structure parameters of amorphous ZrO_2 with those of m-ZrO_2 and t-ZrO_2 crystal structures

	Zr-O		O-O		Zr-Zr	
	r/nm	N_{ZrO}	r/nm	N_{OO}	r/nm	N_{ZrZr}
Amorphous ZrO_2	0.215	5.0	0.282	7.7	0.337	8.0
m-ZrO_2	0.216	7.0	0.285	9.5	0.347 0.415	7.0 3.0
t-ZrO_2	0.226	8.0	0.265	6.0	0.366	12.0

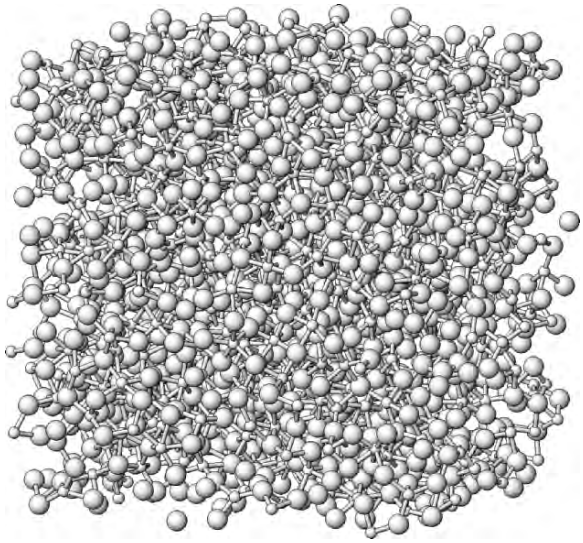

Fig. 5.11. A projection of the atomic positions from a representative RMC-generated configuration. *Larger atoms* are O, *smaller atoms* are Zr. Zr-O bonds denoted by the distance up to the first minimum of $g_{Zr-O}(r)$

105°. On the other hand, the bond angle distribution B_{ZrZrZr} indicates two pronounced peaks occurring at approximately 55° and 105°. B_{OOO} shows two main peaks at 60° and 95°, which are in agreement with values in m-ZrO_2. Considering all the results obtained in this work, the local ordering structure of amorphous ZrO_2 is found to be closer to that of m-ZrO_2 than in the t-ZrO_2 case. This conclusion could be drawn only from the realistic atomic scale model structure including the middle-range ordering estimated by fitting three independent experimental data using the RMC simulation technique. Nevertheless, it should be kept in mind that the crystallization

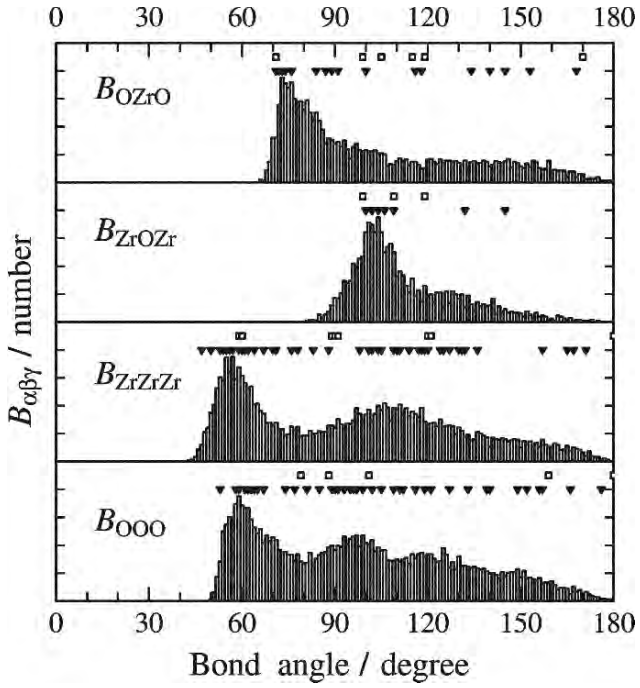

Fig. 5.12. Bond angle distributions of amorphous ZrO_2. *Solid triangles and squares* denote the angle positions found in crystalline m-ZrO_2 and t-ZrO_2, respectively

behavior of amorphous ZrO_2 produced by sol-gel method strongly depends on the conditions of sample preparation [27]. Therefore, it is difficult to determine which mechanism is actually significant in the formation of t-ZrO_2 from amorphous ZrO_2.

5.3.3 Corrosion Products formed on the Steel Surface

The corrosion process of steel is known to be severely affected by the variety of corrosion products (frequently referred to as rust) formed on the steel surface. For example, the corrosion rate of steel substrate in the atmosphere is found to be considerably reduced when the rust layer containing some small amounts of alloying elements covers the steel surface as a protective film. This urgently requires quantitative characterization of the atomic scale structure of corrosion products. However, the structure of corrosion products, which are ferric oxyhydroxides with some alloying elements, is not so simple and they are rather classified as complex systems. The corrosion products are formed by reaction of metallic elements, mainly iron, with oxygen and water originating from the atmosphere and then their structure appears to be greatly affected by conditions. The corrosion products are found to consist of various components such as α-FeOOH, β-FeOOH, γ-FeOOH and Fe_3O_4

[3, 35]. For these reasons, the crystallographic structure described by long-range ordering is not sufficiently confirmed and some components of rust of steel are frequently assigned to the amorphous state characterized by short-range ordering [4].

Advanced and powerful methods, such as electron probe microanalysis, infrared spectroscopy, Raman spectroscopy, Mössbauer spectroscopy and EXAFS analysis have been widely applied, in order to characterize the structure, chemical composition and morphology of corrosion products formed on the steel surface under various conditions [35–41]. The results provided some interesting and important information on their composition and structure. For example, the EXAFS results [40, 41] suggest the local ordering unit structure of corrosion products is represented mainly by the FeO_6 octahedral unit structure and the linkage of such FeO_6 octahedra is, more or less, distorted by chromium addition. In addition, hydrogen atoms are quite likely to be intercalated in these structure units. However, some reservations should be given regarding information about linkage of the FeO_6 octahedral unit structure, because the EXAFS data result only from the near neighbor atomic arrangements. This strongly suggests the great importance of middle-range ordering for characterizing the corrosion products. The use of the AXS method coupled with the RMC simulation technique has brought about a significant breakthrough in this particular subject.

Some details of sample preparation and measurements are given as follows. Five samples of iron, iron-2.0 mass% chromium, iron-3.0 mass% nickel and iron-1.6 mass% copper alloys were prepared from pure iron, chromium, nickel and copper by vacuum induction melting. These samples are hereafter referred to as Fe, Fe-2%Cr, Fe-3%Ni and Fe-1.6%Cu, respectively. The commercial weathering steel, of which the chemical composition is 0.10%C, 0.050%Si, 0.50%Mn, 0.096%P, 0.016%S, 0.15%Ni and 0.56%Cr in mass%, was also employed and is referred to as WS. These samples were shaped to 10 mm square sheets of 1 mm in thickness and they were leached in artificial seawater with 2.5 mass% NaCl, 1.1 mass% $MgCl_2$, 0.4 mass% Na_2SO_4 and 0.07 mass% KCl at room temperature for about 15 days, so as to form colloidal corrosion products, from which powder rust samples were obtained by filtering.

Conventional diffraction experiments were carried out in order to identify constituents of the corrosion products and precise diffraction measurements were also made using Mo $K\alpha$ radiation, which was generated at a power of 18 kW (Rigaku RINT-2000) with a graphite monochromator located on the diffracted beam line. AXS measurements were made for estimating the environmental interference function for Fe in the corrosion products. The incident X-ray energies were tuned at 7.087 and 6.812 keV. These energies correspond to 25 and 300 eV below the Fe K absorption edge (7.112 keV), respectively.

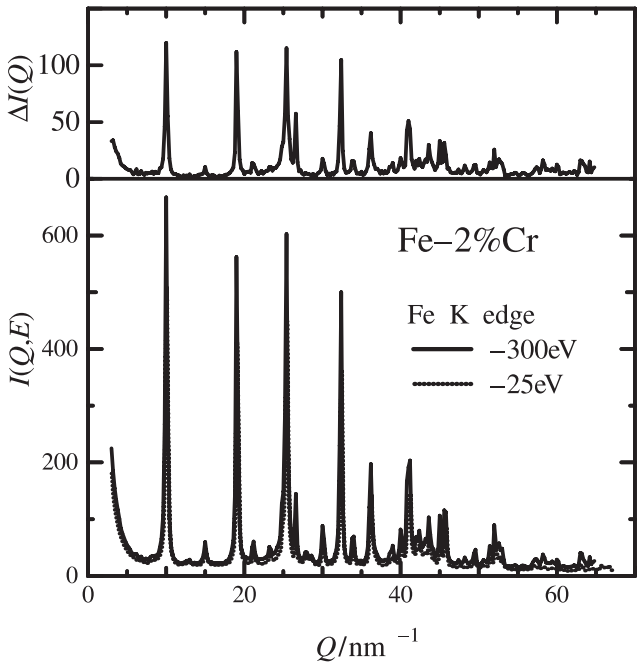

Fig. 5.13. Differential intensity profile (*top*) of rust formed on Fe-2%Cr obtained from the intensity profiles (*bottom*) measured at two energies of 7.086 and 6.811 keV near the Fe absorption edge [10]

The network structure consisting of FeO_6 octahedra corresponding to middle-range ordering was estimated using the RMC simulation technique. Simulation was started with an initial configuration of 4320 particles (1440 iron atoms and 2880 oxygen atoms) positioned in a similar way to an ideal structure of γ-FeOOH (lepidocrocite), in a super cell of a volume of $3.76 \times 3.88 \times 3.68$ nm^3. It has also been the focusing point of this work to reveal the network structure and its distortion from the ideal case found in a typical component of corrosion products, γ-FeOOH. This includes how the alloying elements affect the rust structure formed on the surface of iron-based alloys and commercial steel.

Figure 5.13 shows the differential intensity profile (top) of a rust sample obtained from two intensity profiles (bottom) by the AXS measurements using the results of formed on Fe-2%Cr as an example [10]. Such differential intensity profiles obtained in different samples in a similar manner were employed for analyzing the environmental interference functions for Fe.

On the other hand, the interference functions of five samples were obtained from diffraction measurements using Mo $K\alpha$ radiation and the results are given in Fig. 5.14 [10]. It may be worth mentioning here that the present rust samples consist mainly of γ-FeOOH for all five cases, although we

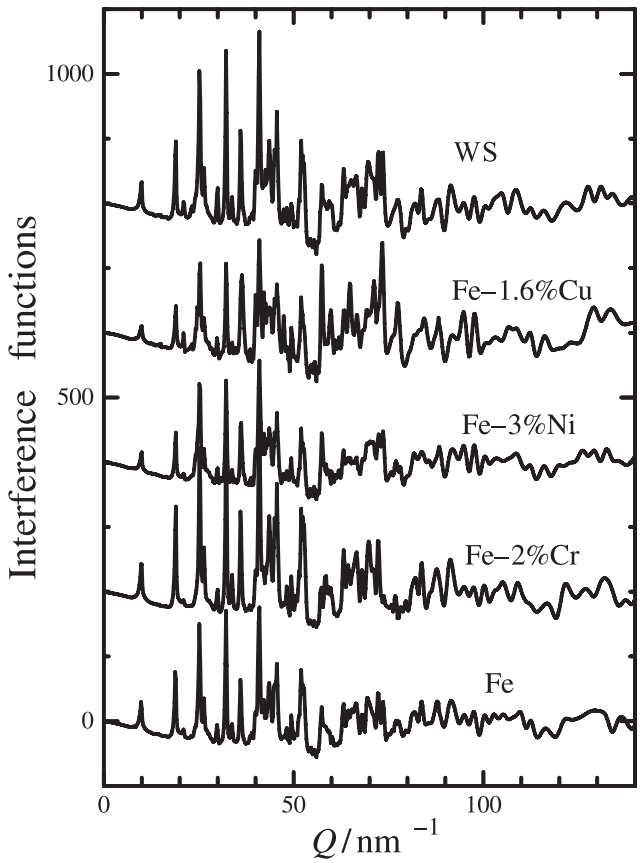

Fig. 5.14. Interference functions of rust formed on Fe, Fe-2%Cr, Fe-3%Ni, Fe-1.6%Cu and WS

detected a few signals of other components such as α-FeOOH (goethite) and Fe_3O_4 (magnetite). Figure 5.15 shows the RDFs for the γ-FeOOH component formed on the surface of Fe, Fe-2%Cr, Fe-3%Ni, Fe-1.6%Cu and WS, which were obtained from the interference functions of Fig. 5.14 by Fourier-Transformation. These results clearly suggest some differences in the atomic scale structure of five rust samples by detecting small changes in position, peak height and shape. However, any definite comment about the linkage of the FeO_6 octahedral unit structure cannot be drawn from these data alone.

The realistic atomic scale structure of the γ-FeOOH component in the range of a few nanometers can be estimated by fitting both the ordinary interference function $Qi(Q)$ and environmental interference functions $Q\Delta i_{\mathrm{Fe}}(Q)$ with the help of the RMC simulation technique. Figure 5.16 shows a comparison of the ordinary interference function $Qi(Q)$ and environmental interference functions $Q\Delta i_{\mathrm{Fe}}(Q)$ for Fe using the case of Fe-2%Cr [10]. Open circles denote the experimental data and solid lines are the results computed by the

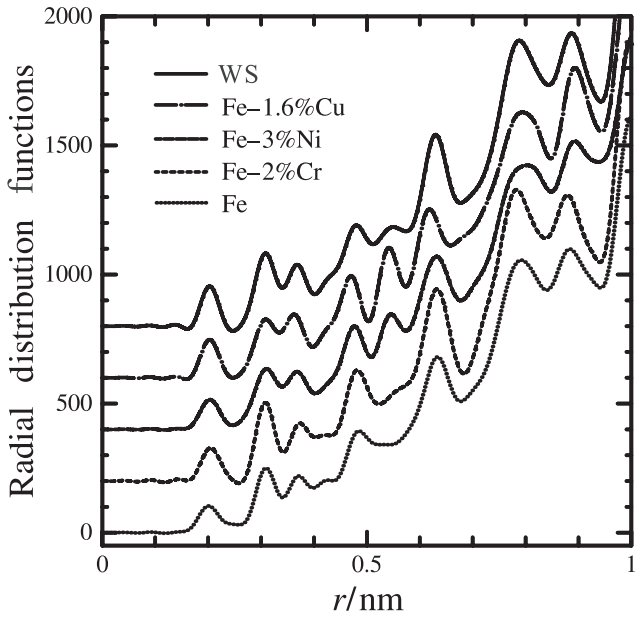

Fig. 5.15. Interference functions of rust formed on Fe, Fe-2%Cr, Fe-3%Ni, Fe-1.6%Cu and WS

RMC simulation. The resultant middle-range ordering of the γ-FeOOH component in rust formed on the surface of Fe-2%Cr is illustrated in Fig. 5.17, together with the ideal γ-FeOOH structure as a reference. The deviation of network structure from the ideal γ-FeOOH is clearly observed and it has been quantified in the γ-FeOOH component in rust formed on the surface of Fe-2%Cr. Such RMC simulation was made in another four cases: Fe, Fe-3%Ni, Fe-1.6%Cu and WS. Then the realistic model structure of the γ-FeOOH component in five rust samples formed on the different alloy surface was visualized and the results are summarized in Fig. 5.18. It is very interesting to note that the middle-range ordering in the range of a few nanometers for the γ-FeOOH component in rust significantly depends on the composition of substrate materials.

A new method for visually displaying the deviation of the FeO_6 network structure from the ideal γ-FeOOH case has also been proposed by introducing two parameters [10]: a bond angle between different orientations of two iron atoms in the network of the FeO_6 octahedral unit structure, θ, and a distance between the two Fe-Fe pairs, r, as shown in Fig. 5.19. In the ideal γ-FeOOH case, the bond angle θ can be found at about 0°, 60°, 90° and 120°. The present authors maintain the view that the bond angle distribution defined by $B(\theta, r)$ between Fe-Fe pairs as a function of angle θ and distance r is a useful method to represent the deviation of the network structure from the ideal case. The results are summarized in Fig. 5.20 [10]. From this systematic

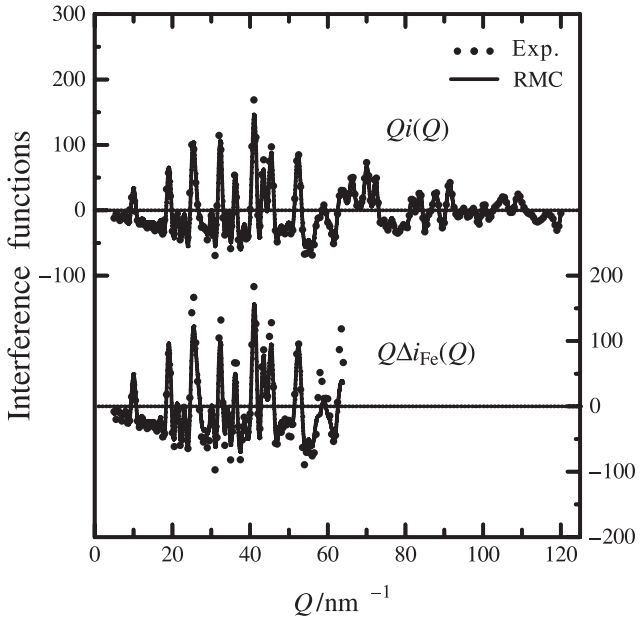

Fig. 5.16. The ordinary interference function $Qi(Q)$ and environmental interference functions $Q\Delta i(Q)$ for Fe of rust formed on Fe-2%Cr. *Open circles* and *solid lines* denote the experimental data and calculated values using the RMC simulation technique

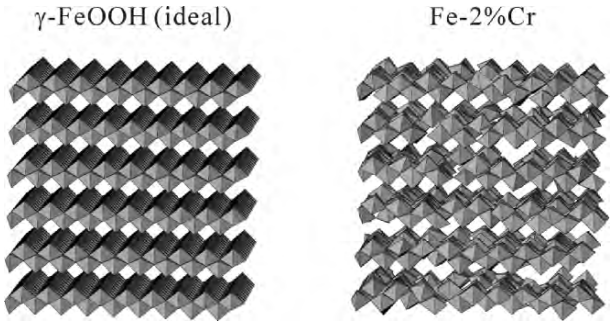

Fig. 5.17. A projection of the atomic positions in the middle-range ordering from a representative RMC-generated configuration for rust (**b**) formed on the Fe-2%Cr surface. The ideal structure found in γ-FeOOH is also given in (**a**) as a reference. Here, the FeO_6 octahedral unit structure is employed for presentation

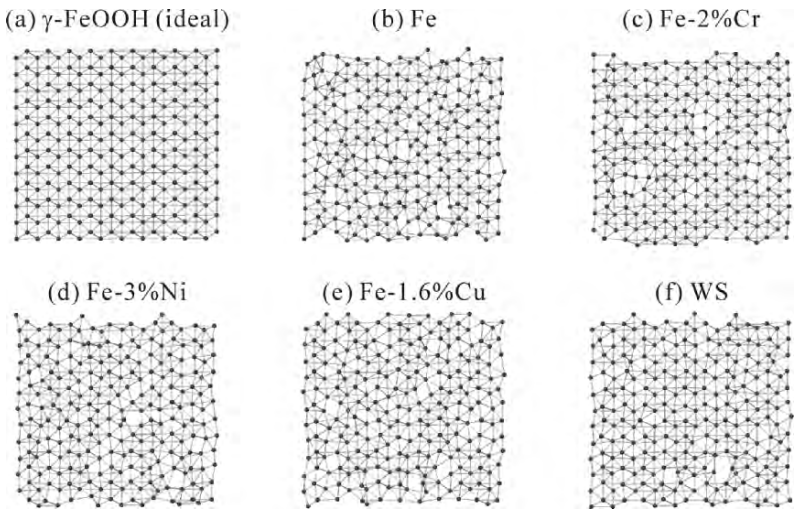

Fig. 5.18. A projection of the atomic positions in the middle-range ordering from a representative RMC-generated configuration for five rust samples. Here, bonds between nearest neighbor Fe atoms are drawn by sticks: (**a**) ideal γ-FeOOH, (**b**) Fe, (**c**) Fe-2%Cr, (**d**) Fe-3%Ni, (**e**) Fe-1.6%Cu and (**f**) WS

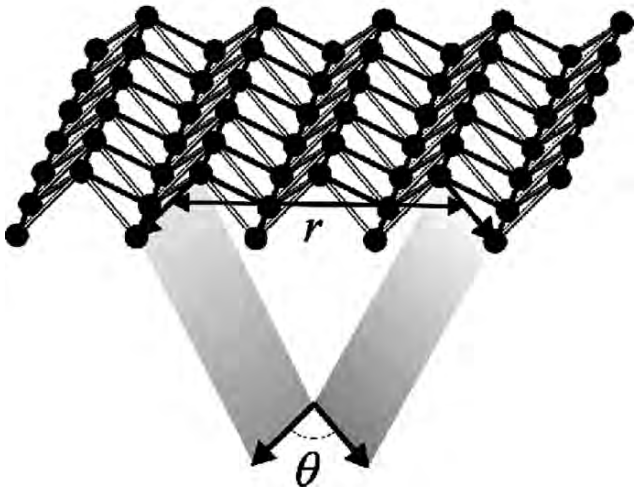

Fig. 5.19. Schematic diagram for analyzing the network structure of rust by estimating bond angle distribution $B(\theta, r)$ between Fe-Fe pairs

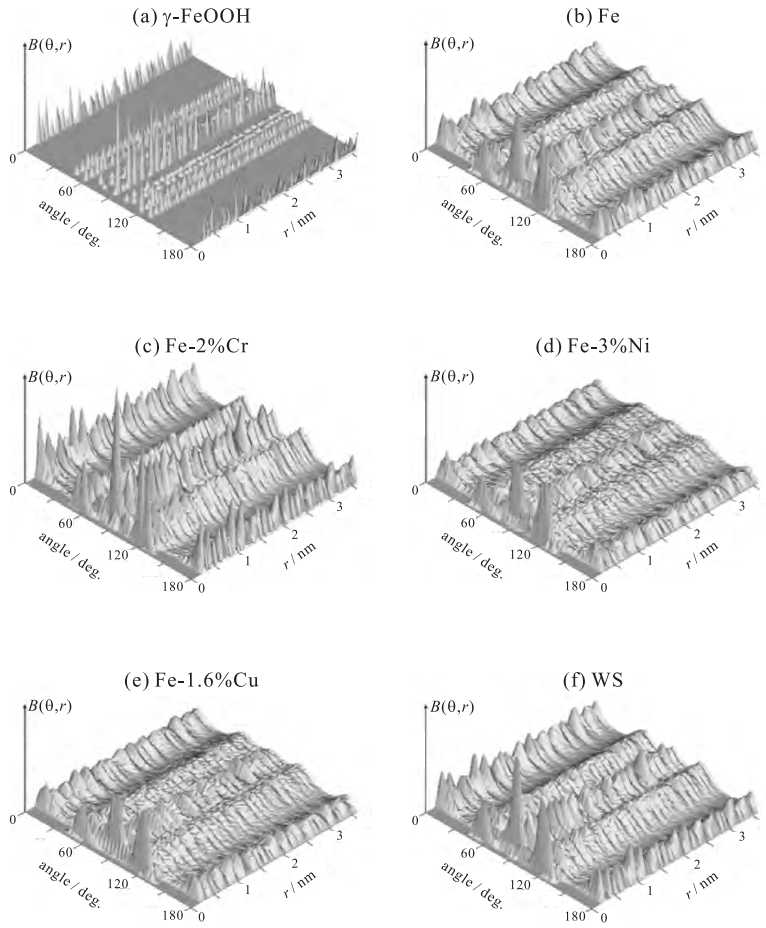

Fig. 5.20. Bird views of bond angle distribution B(q,r) between Fe-Fe pairs for five rust samples: (**a**) ideal γ-FeOOH, (**b**) Fe, (**c**) Fe-2%Cr, (**d**) Fe-3%Ni, (**e**) Fe-1.6%Cu and (**f**) WS

information on the middle-range ordering of the γ-FeOOH component in rust formed on the surface of iron-based alloys and commercial steel, the distortion of the FeO_6 octahedral units and their network structure from the ideal γ-FeOOH case is briefly summarized in Fig. 5.21.

These results suggest that the γ-FeOOH component in rust is quite likely to be represented by the distortion of the FeO_6 octahedral units and their network structure. Such features significantly depend on the composition of substrate materials. This implies that an alloying element is, more or less, to occupy a certain site of the FeO_6 unit structure formed during corrosion and such occupation may affect not only the short-range ordering but also the middle-range ordering characterized by the FeO_6 octahedral

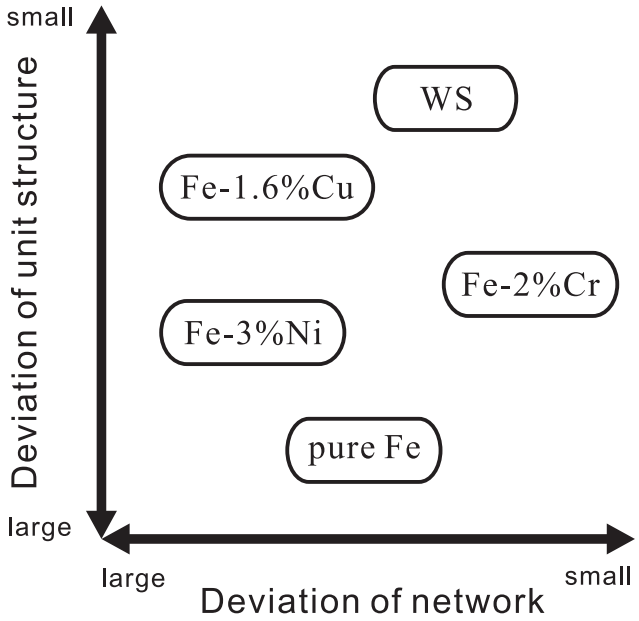

Fig. 5.21. Schematic representation of relationships between deviation from the ideal case with respect to the fundamental unit structure and the network structure for five rust samples

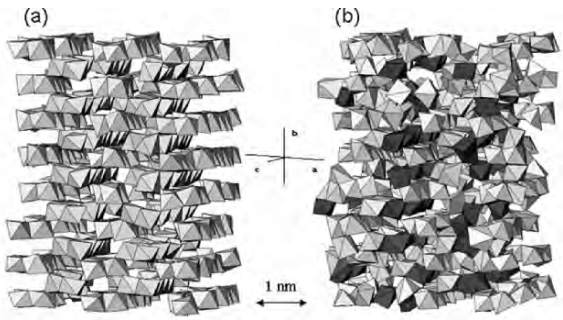

Fig. 5.22. A projection of the atomic positions in the middle-range ordering from a representative RMC-generated configuration for (**a**) α-FeOOH and (**b**) α-29Cr visualized by the FeO_6 octahedral unit structure. The CrO_6 octahedral units in α-29Cr are denoted as *dark octahedron* in (b) [11]

units. Figure 5.22 shows the results on the middle-range ordering recently obtained for two synthesized α-FeOOH samples containing chromium [11]. The linkage of the FeO_6 and CrO_6 octahedral unit structures is cited in α-FeOOH with 29% Cr. The distortion in linkage of these octahedral unit structures is considered to result from the substitution of iron for chromium in the α-FeOOH structure. Thus, it is not too much to say that the alloying

elements play an important role in the formation processes of the atomic scale structure of rust. As rust particles of ferric oxyhydroxides, such as γ-FeOOH and α-FeOOH, are precipitated in aqueous solutions [42], the atomic scale structure of rust appears to be influenced by the incorporation not only of foreign cations but also of foreign anions from the atmosphere. The incorporation of foreign anions is also considered to enhance the distortion of the structure of ferric oxyhydroxide particles, since anions are known to influence the particle species of ferric hydroxides, oxyhydroxides and oxides formed in aqueous solution [42,43]. While most foreign cations appear to be substituted at the FeO_6 structural units by their octahedral units during co-precipitation, occupation of foreign anions in the structure of ferric oxyhydroxide particles is not definitely specified [43]. In addition, the interaction between foreign cations and anions should be taken into account in the atomic scale structure of ferric oxyhydroxide particles containing foreign ions. Thus, foreign anions and cations originating from the atmosphere and alloying elements may modify the Fe-O bonding (the short-range ordering) and the linkage of FeO_6 structural units (the middle-range ordering) formed during precipitation.

Nevertheless, to the best knowledge of the present authors, systematic differences in the middle-range ordering structure of rust formed on iron and steel were quantified for the first time. The method described in this chapter is considered to be one way to reduce the difficulties on the subject of materials characterization of corrosion products, which is still a subject of some controversy. Although quantitative analyses has been performed of the atomic scale structure in the γ-FeOOH component of rust formed in salt water and the synthesized α-FeOOH particles, it would be very interesting to extend systematically the present method to practical rust components. By a series of such structural analyses together with corrosion experiments, the conditions for designing protective rust layers on low-alloyed steel may be optimized.

5.4 Summary

Middle-range ordering in the range of a few nanometers is of great importance for characterizing the structure of various substances, particularly for describing the structure of a complex system. An attempt has been made to propose a new method for obtaining information including middle-range ordering. In this method, the realistic atomic scale model structure is estimated by fitting both the ordinary interference function and the environmental interference function obtained from the anomalous X-ray scattering (AXS) data with the help of model calculation by applying the reverse Monte Carlo (RMC) simulation technique and then middle-range ordering in the range of a few nanometers can be visualized.

The usefulness of the present method has been confirmed by obtaining some interesting structural information, which is not sufficiently represented

yet, with respect to a complex system such as GeO_2 glass, amorphous ZrO_2 and corrosion products (ferric oxyhydroxides, such as FeOOH) formed on the steel surface. This method would be valuable for materials characterization not only of non-crystalline systems but also of crystalline systems in the variety of states.

On the other hand, it should be stressed that the present method for obtaining information including middle-range ordering is not a unique mathematical procedure. Nevertheless, the resultant model structure over the range of a few nanometers is considered, at least to some extent, to meet the necessary conditions for explaining two or three independent experimental data. For this reason, we believe that the method coupled with the RMC simulation technique could be a useful way to obtain a realistic model structure over the range of a few nanometers within the framework of information. It would also seem to be very promising to extend this method to the estimation of middle-range ordering of various systems, so that its validity may be tested on a wider base.

References

1. T.L. Hill: *Statistical Mechanics* (Mc-Graw Hill, New York 1956).
2. A. Inoue: *Bulk Amorphpous Alloys* (Trans. Tech. Uetkon-Zurich 1999).
3. T. Misawa, K. Asami, K. Hashimoto, S. Shimodaira: Corros. Sci. **14**, 279 (1974).
4. H. Okada, Y. Hosoi, K. Yukawa, H. Narita: Iron Steel Inst. Jpn. **55**, 355 (1969).
5. R.L. McGreevy, L. Pusztai: Mol. Simul. 1, 359 (1988).
6. R.L. McGreevy, L. Pusztai: Proc. Roy. Soc. London **A430**, 241 (1990).
7. M. Saito, C.Y. Park, K. Omote, K. Sugiyama, Y. Waseda: J. Phys. Soc. Jpn. **66**, 633 (1997).
8. M. Saito, S.C. Kang, Y. Waseda: J. Appl. Phys. Suppl. **38**, 596 (1999).
9. M. Saito, C.Y. Park, K. Sugiyama, Y. Waseda: J. Phys. Soc. Jpn. **66**, 3120 (1997).
10. S. Suzuki, M. Saito, M. Kimura, T. Suzuki, H. Kihira, Y. Waseda: ISIJ Inter. **43**, 336 (2003).
11. Y. Waseda, S. Suzuki, M. Saito: J. Alloy Compound (2005), in press.
12. J.E. Enderby, D.M. North, P.A. Egelstaff: Phil. Mag. **14**, 961 (1966).
13. C.N.J. Wagner: *Liquid Metals, Chemistry and Physics* (S.Z. Beer, Ed., Marce-Dekker, New York 1972) p. 258.
14. F.G. Edwards, J.E. Enderby, R.A. Howe, D.I. Page: J. Phys. **C. 8**, 3483 (1975).
15. Y. Waseda: *Anomalous X-ray Scattering for Materials Characterization* (Springer, Heidelberg 2002).
16. T.E. Faber, J.M. Ziman: Phil. Mag. **11**, 153 (1965).
17. R.W. James: *The Optical Principles of the Diffraction of X-rays* (G.Gell, London 1954).
18. P. Bondot: Acta Cryst. A**30**, 470 (1974); Phys. Status Solidi (a) **22**, 511 (1974).
19. E. Matsubara, K. Harada, Y. Waseda, M. Iwase: Z. Naturforsch. **43a**, 181 (1988).

20. Y. Waseda, K. Sugiyama, E. Matsubara, K. Harada: Mater. Tran. JIM **32**, 421 (1990).
21. R.G. Stantson: *Numerical Methods for Science and Engineering* (Prentice-Hall, New York 1961).
22. D.A. Keen, R.L. McGreevy: Nature **344**, 423 (1990).
23. A. Pasquarello, R. Car: Phys. Rev. Lett. **80**, 5145 (1998).
24. S. Sakka: J. Non-Cryst. Solids **42**, 403 (1980).
25. S. Mazdiyasni, C.T. Lynch, J. Smith: J. Amer. Soc. **48**, 372 (1965); J. Amer. Soc. **49**, 286 (1966).
26. R.C. Garvie: J. Phy. Chem. **69**, 1238 (1965).
27. Y. Murase, E. Kato, H. Matsumoto: Nippon Kagaku Kaishi (in Japanese) **12**, 2329 (1972).
28. R. Cypres, R. Wollast, J. Raucq: Ber. Dtsch. Keram .Ges. **40**, 527 (1963).
29. J. Livage, K. Doi, C. Mazieres: J. Amer. Cerm. Soc. **51**, 349 (1965).
30. E. Tani, M. Yoshimura, S. Somiya: J. Amer. Ceram. Soc. **66**, 11 (1983).
31. K. Sugiyama, Y. Waseda, S. Kudo: ISIJ Inter. **31**, 1362 (1991).
32. Y. Waseda: *The Structure of Non-Crystalline Materials* (McGraw-Hill, New York 1980).
33. J.D. McCullough, K.N. Trueblood: Acta Cryst. **12**, 507 (1959).
34. G. Teufer: Acta Cryst. **15**, 1187 (1962).
35. T. Misawa, M. Yamashita, K. Matsuda, H. Miyuki, J.H. Nagano: Iron Steel Inst. Jpn. **79**, 69 (1993).
36. M. Yamashita, H. Miyuki, Y. Matsuda, H. Nagano, T. Misawa: Corros. Sci. **36**, 283 (1994).
37. T. Okada, Y. Ishii, T. Mizoguchi, I. Tamura, Y. Kobayashi, Y. Takagi, S. Suzuki, H. Kihira, M. Itoh, A. Usami, K. Tanabe, K. Masuda: Jpn. J. Appl. Phys. **39**, 3382 (2000).
38. T. Kamimura, S. Nasu, T. Tazaki, K. Kuzushita, S. Morimoto: Materials Trans. **43**, 694 (2002).
39. T. Kamimura, S. Nasu, T. Segi, T. Tazaki, S. Morimoto, H. Miyuki: Corros. Sci. **45**, 1863 (2003).
40. M. Yamashita, T. Shimizu, H. Konishi, J. Mizuki, H. Uchida: Corros. Sci. **45**, 381 (2003).
41. S. Suzuki, Y. Takahashi, T. Kamimura, H. Miyuki, Y. Takagi, K. Shinoda, K. Tohji, Y. Waseda: Corros. Sci. **46**, 1751 (2004).
42. J.P. Jolivet, M. Henry, J. Livage, E. Bescher: *Metal Oxide Chemistry and Synthesis* (Wiley-VCH, Chichester 1994).
43. R.M. Cornell, U. Schwertmann: *The Iron Oxides* (Wiley-VHC, Weinheim 2003).

6 Corrosion Mechanism of Iron from an X-ray Structural Viewpoint

Eiichiro Matsubara, Shigeru Suzuki, Yoshio Waseda

6.1 Introduction

Corrosion products or rusts are formed and gradually grown on the surface of common steel and low-alloyed steel when they are exposed to humid air at room temperature. This phenomenon is referred to as atmospheric corrosion [1], and the corrosion products fundamentally consist of iron oxides, including iron oxyhydroxides, hydroxides, and so on [2]. The corrosion rate of substrate steel is dominated by the properties of a layer of the corrosion products, since it acts as a membrane of water. Thus, the structure and morphology of the corrosion products are very important; typically, a protective rust layer formed on the surface of weathering steel is known to suppress considerably the corrosion rate of weathering steel [3–9].

The mechanism of atmospheric corrosion of steel is generally interpreted on the basis of electrochemical reactions, in which the anodic dissolution reaction of metal is likely to be balanced by the cathodic reaction during corrosion. Actually, the corrosion processes of iron have been mainly studied using electrochemical methods and other techniques [10–14], by which the reduction and re-oxidation of corrosion products of ferric and ferrous ions are considered to occur in water. For instance, in order to confirm the reduction and re-oxidation of corrosion products of iron, in-situ ^{57}Fe Mössbauer spectroscopy was utilized to study the transformation of iron oxyhydroxides and hydroxides [12]. The results showed that ferric oxyhydroxides, i.e. α-FeOOH and γ-FeOOH, can be reduced to Fe_3O_4 or $Fe(OH)_2$ in water by controlling atmospheric conditions. ^{57}Fe Mössbauer spectroscopy has also been used for identifying components in corrosion products and analyzing their fine structures [4–7]. Other analytical methods, such as electron probe microanalysis, transmission electron microscopy, infrared spectroscopy, and Raman spectroscopy, are often used for analyzing corrosion products formed on the surface of steel. The results obtained by these methods provide information on the composition, morphology, and structure of corrosion products. However, structural information of corrosion products obtained by these methods is still limited, because corrosion products freshly formed on the iron surface contain ferrous ions and are easily changed due to further reaction with oxygen from the air. Therefore, corrosion products should be carefully prepared and characterized for studying the corrosion mechanism of iron, as in-situ ^{57}Fe

Mössbauer spectroscopy was successfully applied to detect oxide containing ferrous ions under well-controlled conditions [12].

The X-ray diffraction method is one of the most effective methods for identifying the structure of different components in corrosion products. In fact, in-situ X-ray diffraction measurements using synchrotron radiation and an in-house X-ray source enabled us to provide important information on components in corrosion products formed under various conditions [15, 16]. The results showed that the corrosion products containing ferrous ions as well as ferric ions are formed by reaction with aqueous solution on the iron surface. Furthermore, the ex-situ X-ray diffraction method using synchrotron radiation has also been utilized for analyzing a very small amount of corrosion products, which were freshly formed on the surface of iron at the initial stage of corrosion [16]. The results indicated that corrosion products containing ferrous ions are formed near the substrate iron, which are considered to be intermediate compounds transformed to corrosion products by air. This chapter describes typical experimental results of these in-situ and ex-situ X-diffraction analysis of corrosion products freshly formed under various conditions. The formation processes and mechanisms of corrosion products of iron and its alloys are discussed on the basis of the results.

6.2 Structure and Formation of Various Components of Corrosion Products

The fundamental structures of components of iron corrosion products should first be mentioned in order to understand characteristic features of various types of corrosion products. Figure 6.1 (a)–(c) show the ideal crystallographic structures of three ferric oxhydroxides, α-FeOOH, β-FeOOH and γ-FeOOH, which are described using FeO_6 octahedral units, respectively. Hydrogen is denoted as small circles in α-FeOOH and γ-FeOOH. Chlorine is given as medium circles in the β-FeOOH structure, in which the position of hydrogen has not been fully determined. In addition, the structure of a ferrous hydroxide $Fe(OH)_2$, which is sometimes called white rust, is composed of layers of FeO_6 octahedra intercalated with hydroxyl OH^-, as shown in Fig. 6.1 (d). The position of hydrogen in $Fe(OH)_2$ has not also been determined, as this hydroxide is easily oxidized by air. There are several kinds of green rust (GR) containing ferric and ferrous ions, which has a layered structure as $Fe(OH)_2$. In the structure of GR, the fractions of ferric and ferrous ions in layers of FeO_6 octahedra are variable and different anions and water molecules are intercalated between the layers [17–22]. Although there are other structures of iron oxides including hydroxides, their structures are fundamentally described in a similar manner [2, 23].

Figure 6.2 shows a schematic diagram of formation and transformation pathways of ferric and ferrous oxides in aqueous solution [2]. A number of experiments on synthesis of iron oxides in aqueous solution showed that ferrous

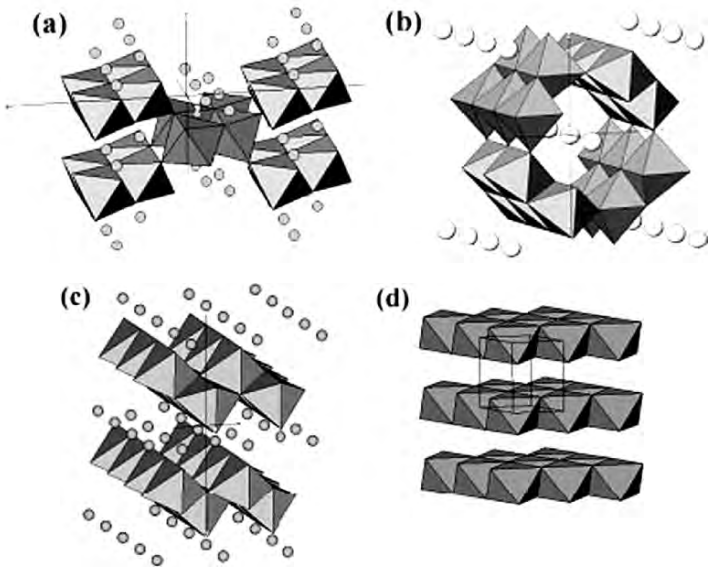

Fig. 6.1. Ideal crystallographic structures of (**a**) α-FeOOH, (**b**) β-FeOOH, (**c**) γ-FeOOH and (**d**) $Fe(OH)_2$. The structures are described using FeO_6 octahedral units. Small circles : hydrogen, medium circles : chlorine

and ferric ions in aqueous solution were changed to various structures of iron oxides. This diagram is important in discussing the formation of different corrosion products of iron, because metallic iron is dissolved as ferrous ions into aqueous solution and then these ions are precipitated as ferric oxyhydroxides in corrosion. It is to be noted in this diagram that a few intermediate oxides, which may be precursors of resultant corrosion products, are formed. For instance, ferrous hydroxide $Fe(OH)_2$ is likely to be converted to green rust (GR) by oxidation. As anions are intercalated among the atomic layered structures of $Fe(OH)_2$ and GR, the anions may play a crucial role in the formation of resultant corrosion products.

As related to the formation pathways of corrosion products, $Fe(OH)_2$ and GR containing ferrous ions are given in an electrochemical potential (E)-pH diagram [17–20], as shown in Fig. 6.3(a). However, these oxides containing ferrous ions have hardly been detected in corrosion conditions fully exposed to air, since they are easily oxidized under ambient conditions. Magnetite, Fe_3O_4, is sometimes shown instead of a GR region in the E-pH diagram depending on the conditions of a solution, since it also consists of ferrous and ferric ions [17–20]. Oxides containing ferrous and ferric ions are also observed in an iron oxide scale formed by high temperature oxidation, of which a cross-section is exemplified in Fig. 6.3(b). A layer of hematite, Fe_2O_3, of ferric ions is formed on the outer side of the oxide scale, and a layer of magnetite, Fe_3O_4, consisting of ferric and ferrous ions is formed below the hematite layer.

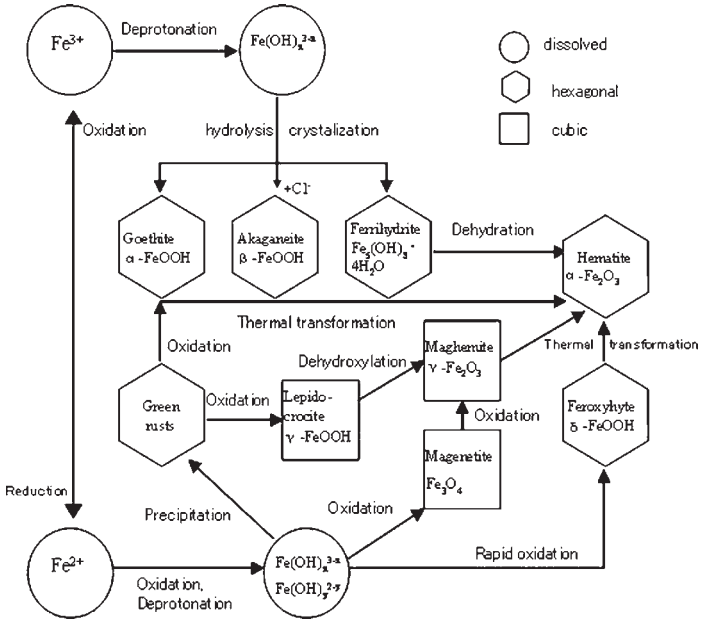

Fig. 6.2. Formation pathways of various iron oxides, which are fundamentally Fe-O-H system compounds, from ferrous and ferric ions dissolved in aqueous solution

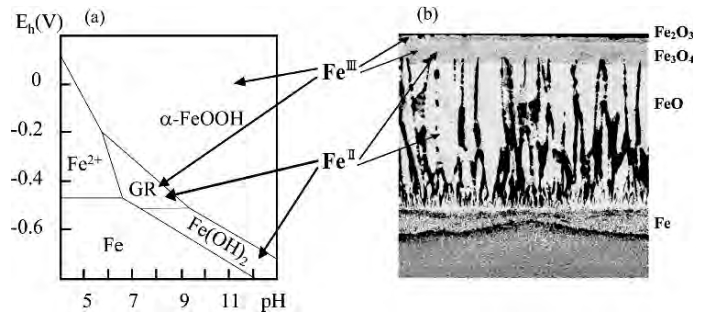

Fig. 6.3. (**a**) Electrochemical potential (E) - pH diagram for Fe in aqueous solution containing chloride ions and (**b**) a layered structure of thermally formed oxide scale on steel

At high temperatures, more than about 833 K, wustite, FeO, of ferrous ions is formed on the metallic iron [24]. The formation of such a layered structure of an oxide scale can be interpreted on the basis of a chemical potential gradient of oxygen in the layer. Thus, it is also expected that ferric oxides are predominantly formed on the outer side of a layer of corrosion products in water, while oxides containing ferrous ions are formed near the iron substrate. However, a flow of water may prevent us from observing a layered structure of different components in corrosion products.

From the viewpoint of the structural analysis, in-situ and ex-situ X-ray diffraction measurements have been utilized for characterizing various corrosion products formed on iron surfaces. The formation of different oxides containing ferric and ferrous ions and a layered structure of these oxide components in corrosion products freshly formed on the surface of iron are focused. In order to clarify factors influencing the formation of specific components in corrosion products, in-situ diffraction measurements using synchrotron radiation and an in-house X-ray source were conducted for identifying corrosion products formed by cyclic exposure to wet and dry atmospheres, which simulates the atmospheric corrosion. Ex-situ X-ray diffraction measurements using synchrotron radiation were carried out for identifying a small amount of samples extracted from different parts of corrosion products formed in aqueous solutions.

6.3 Methods for In-situ and Ex-situ X-ray Diffraction

6.3.1 Sample Preparation

Sample sheets of pure iron and two iron-based alloys, iron-5 mass% nickel and iron-2 mass% silicon, were prepared by vacuum melting and rolling. These two alloys were selected to study the effect of alloying elements on iron corrosion products, since nickel and silicon are important elements in commercial steel. The pure iron, iron-5 mass% nickel and iron-2 mass% silicon samples are hereafter referred to as Fe, FeNi and FeSi, respectively. The sheets of about 0.5 mm in thickness were cut to 20-mm square, and mechanically polished. In order to investigate the influence of an oxide scale on the formation of corrosion processes, some samples were oxidized at 773 K for 600 s in air. An oxide scale of about 3 μm in thickness covered sample surfaces by this treatment.

Corrosion products formed during one-cycle exposure to wet and dry atmospheres were in-situ analyzed in the follow way. Approximately 0.3 ml of aqueous solution containing 2 mass% sodium chloride (NaCl) or 2 mass% sodium sulfate (Na_2SO_4) was dropped onto the sample surfaces, as shown in Fig. 6.4(a). The samples were held for about 100 h under nearly 100% relative humidity at room temperature. Then, corrosion products were formed on the sample surfaces, as shown in Fig. 6.4(b). The samples were transferred to a cell covered with Kapton films, and X-ray diffraction measurements of the samples were carried out under a humid atmosphere [15]. Corrosion products, which were subsequently dried using silica gel in the cell as shown in Fig. 6.4(c), were also analyzed. Backgrounds in diffraction patterns were relatively reduced in the one-cycle exposure to wet and dry atmospheres, although the corrosion atmosphere was not necessarily fully controlled.

In-situ X-ray diffraction measurements of corrosion products formed during multi-cycle exposure to wet and dry atmospheres were also carried out, in order to obtain sequential X-ray diffraction patterns under a controlled

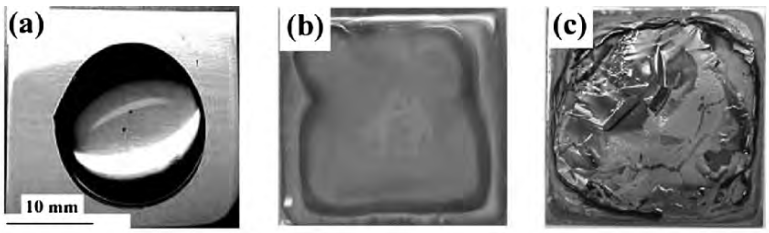

Fig. 6.4. Photographs of iron sheets (**a**) just after being dropped auto by aqueous NaCl solution, (**b**) corroded in an aqueous NaCl solution, and (**c**) dried after corrosion by the solution

atmosphere [16]. After aqueous solutions containing a salt were dropped onto sample surfaces with organic lacquer on its edges, the humidity of the atmosphere was cyclically controlled using water and silica gel in a cell. While water was supplied around a sample in the cell in a wet atmosphere, an amount of silica gel was fed into the cell in a dry atmosphere. The relative humidity was cyclically changed between approximately 40% and 100% for a period of two days. The corrosion atmosphere was controlled, although backgrounds in diffraction patterns were influenced by water on the sample in the multi-cycle exposure.

Small amounts of corrosion products formed freshly on the surface of iron samples were analyzed using ex-situ X-ray diffraction measurements by synchrotron radiation. The corrosion products were prepared by keeping the iron samples with a dip of aqueous solution for approximately 24 h under approximately 100% relative humidity at room temperature. Approximately 10^{-3} ml samples of corrosion products with water were extracted from the upper and lower wet corrosion layers using a syringe. They were filled with glass capillaries or sample holders covered with Kapton films for ex-situ X-ray diffraction measurements. This operation was carried out in an inert gas atmosphere to avoid oxidation of samples by air.

6.3.2 Diffraction Measurements

In-situ X-ray diffraction measurements of corrosion products in one-cycle exposure to wet and dry atmospheres were conducted using synchrotron radiation as well as an in-house X-ray apparatus with a Cr target (Cr $K\alpha$ 0.2290 nm). High brilliant synchrotron radiation at the BL14B1 station of SPring-8 in Japan Synchrotron Radiation Research Institute, Hyogo, Japan was used for diffraction measurements. The synchrotron radiation with wavelength of 0.20416 nm was selected, of which the wavelength was comparable to that of Cr $K\alpha$. A cell for in-situ measurements was attached to be horizontal on a goniometer, and it was then tilted in the $\theta - 2\theta$ scan mode. Diffraction patterns were obtained from about 1 mm×4 mm of corrosion area. Sample planes in the in-house apparatus were kept to be horizontal on a sample stage,

and a diffraction pattern from about 10 mm×20 mm area of the center of a sample was measured in the $\theta - 2\theta$ scan mode by moving the X-ray source and counter. As the wavelength in synchrotron radiation measurements was slightly different from that of Cr $K\alpha$ in the in-house X-ray apparatus, diffraction patterns shown in this chapter are plotted against the scattering wave vector of $Q = 4\pi \sin\theta/\lambda$, where λ is the wavelength. The positions of diffraction peaks were referred to d-values given by JCPDS database.

An in-house X-ray diffraction apparatus with a Mo target (Mo $K\alpha$ 0.0709 nm) was used for in-situ X-ray diffraction measurements of corrosion products formed under multi-cycle exposure to wet and dry atmospheres. As the penetration depth of Mo $K\alpha$ is larger than that of Cr $K\alpha$, diffraction patterns of corrosion products prepared by multi-cycle exposure include information of deeper positions of corrosion products compared to those obtained in one-cycle exposure. Sample sheets in the cell were maintained horizontal on a sample stage and diffraction patterns were measured in the $\theta - 2\theta$ scan mode in a similar manner to the one-cycle procedure.

Ex-situ X-ray diffraction measurements for a small amount of samples extracted from wet corrosion products were carried out using high-brilliant synchrotron radiation in BL14B1 of SPring-8. The synchrotron radiation with wavelength 0.0620 nm (20 keV) was selected by a monochrometer. A capillary or small cell for X-ray diffraction measurements was attached horizontally on a goniometer, and then its diffraction pattern was measured according to the $\theta - 2\theta$ scan mode using a synchrotron radiation beam of dimensions of approximately 0.5 mm × 1 mm.

6.4 X-ray Diffraction of Corrosion Products Formed Under Various Conditions

6.4.1 In-situ X-ray Diffraction of Corrosion Products Formed During One-cycle Exposure to Wet and Dry Atmospheres

Figure 6.5(a) shows an X-ray diffraction pattern from corrosion products formed on the Fe surface by aqueous NaCl solution. Most diffraction peaks are assigned to γ-FeOOH, which is frequently formed as corrosion products [25], although relative ratios of the peak heights seem to be deviated from those given by JCPDS database. The deviation is likely to arise from a change of the measured position in the sample containing water by tilting the sample cell in measurements using synchrotron radiation. Small but clear diffraction peaks assigned to α-FeOOH and $Fe(OH)_2$ are detected in this pattern, together with a peak from the iron substrate. As a pH value of the aqueous solution was about 7 the formation of $Fe(OH)_2$ appears to agree with the E-pH diagram shown in Fig. 6.3.

A diffraction pattern from corrosion products dried after corrosion by the NaCl solution is given in Fig. 6.5(b). Heights of diffraction peaks, assigned to α-FeOOH and Fe_3O_4, were increased relative to those for γ-FeOOH by

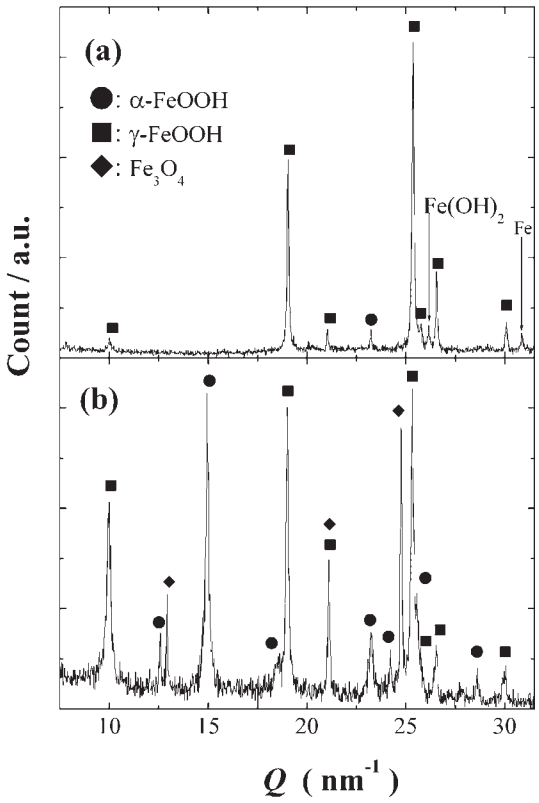

Fig. 6.5. X-ray diffraction patterns from (**a**) corrosion products formed on the Fe surface in NaCl aqueous solution, and (**b**) corrosion products subsequently dried

the drying process. It is noted that diffraction peaks assigned to $Fe(OH)_2$ containing ferrous ions almost disappeared, indicating that α-FeOOH was formed as a new component in corrosion products, presumably by oxidation of ferrous ions. Corrosion components are influenced by corrosion conditions, such as wetting and drying processes, in which the oxidation rate of metallic iron and ferrous ions can be changed [14]. In fact, the selective formation of either α-FeOOH or γ-FeOOH was found to depend on oxidation conditions of ferrous ions [26]. In order to characterize corrosion products formed under well-controlled cyclic conditions, the experimental results obtained by in-situ diffraction measurements of corrosion products formed during multi-cycle exposure are shown in the next section.

As the steel surface is often covered with an oxide scale formed thermally as well as a native oxide layer, the influence of oxide scale on the corrosion processes in aqueous solution is of importance. Thus, X-ray diffraction patterns were also measured for corrosion products formed on the Fe surface covered with oxide scale of about 3 mm thickness. Figure 6.6(a), (b) shows

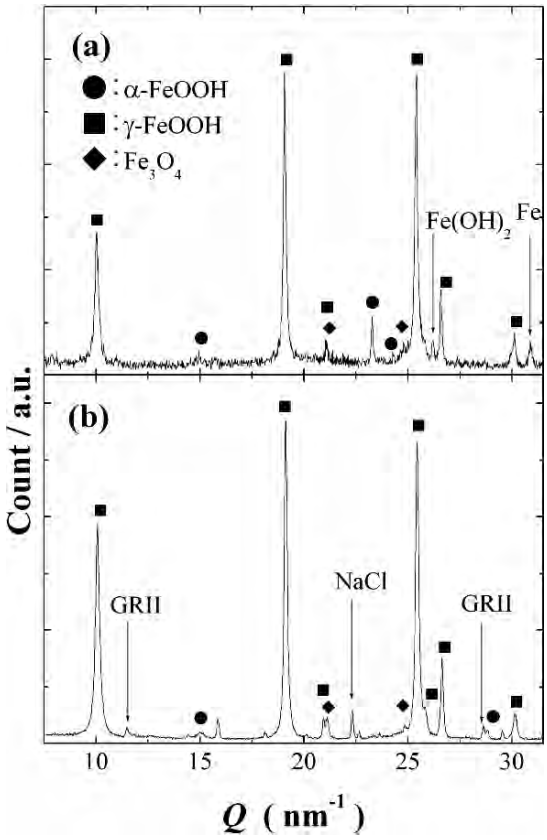

Fig. 6.6. X-ray diffraction patterns for (**a**) corrosion products formed on the Fe surface with oxide scale in NaCl aqueous solution, and (**b**) subsequently dried corrosion products

diffraction patterns from corrosion products formed by aqueous NaCl solution, and corrosion products subsequently dried, respectively. Diffraction peaks assigned to γ-FeOOH are primarily observed in the sample formed by aqueous NaCl solution, together with peaks assigned to $Fe(OH)_2$ and substrate Fe. On the other hand, diffraction patterns assigned to green rust II (GRII), α-FeOOH and NaCl are also detected in the diffraction pattern from the dried corrosion products. As the formation of GR and $Fe(OH)_2$ is expected from the E-pH diagram shown in Fig. 6.3, $Fe(OH)_2$ seems to be transformed to GR by oxidation during the drying process. Appearance of a peak of NaCl suggests the precipitation of sodium and chloride ions from the solution during the drying process. Although there is the oxide scale between the metallic iron and aqueous solution, corrosion products are formed by penetration of the aqueous solution through the oxide scale. It may safely

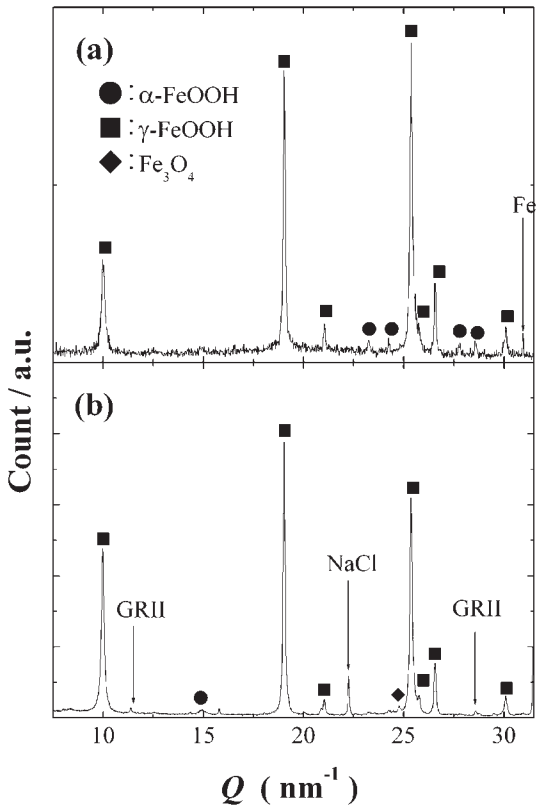

Fig. 6.7. X-ray diffraction patterns from (**a**) corrosion products formed on the FeNi surface in NaCl aqueous solution, and (**b**) corrosion products subsequently dried

be said that oxygen ions in the oxide scale contribute more or less to the formation of new components of corrosion products.

Alloying elements are also likely to affect components of corrosion products formed on steel surfaces, as the fraction of components in corrosion products formed in weathering steel is different from that for mild steel [4,6]. As nickel is one of the most important elements for reducing atmospheric corrosion [15], the effect of nickel on corrosion products was focused upon. X-ray diffraction patterns from corrosion products formed on the FeNi surface by the NaCl solution and corrosion products dried after corrosion by the solution are shown in Fig. 6.7(a), (b) respectively. Although the diffraction pattern from the corrosion products formed on the FeNi surface in wetting process seems to be similar to that for the Fe surface, as shown in Fig. 6.5(a), diffraction peaks of $Fe(OH)_2$ were not detected in the sample. On the other hand, small diffraction peaks, which are allocated to green rust II (GRII) and α-FeOOH, were detected in the dried corrosion products. The diffraction

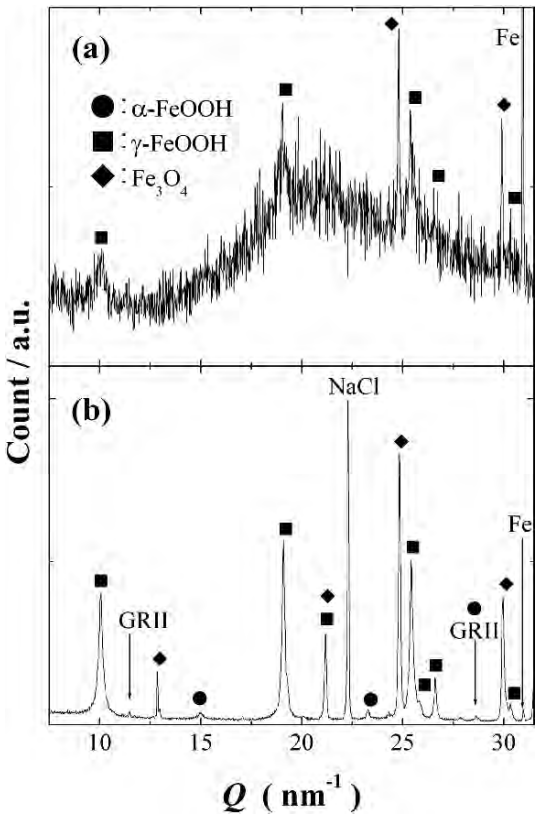

Fig. 6.8. X-ray diffraction patterns for (**a**) corrosion products formed on the FeNi surface with oxide scale in NaCl aqueous solution, and (**b**) subsequently dried corrosion products

peaks from α-FeOOH and Fe_3O_4 in this pattern are not so high as those from corrosion products formed on the Fe surfaces in the drying process. Therefore, nickel is also considered to influence the formation of different oxides containing ferrous and ferric ions.

In addition, the effect of oxide scale on corrosion products formed on the FeNi surface was also studied. Figure 6.8.(a), (b) shows X-ray diffraction patterns from corrosion products formed by aqueous NaCl solution on the FeNi surface covered with the oxide scale and corrosion products subsequently dried, respectively. The diffraction pattern from corrosion products formed by the solution shows a broad scattering profile with peaks allocated to γ-FeOOH, indicating that colloidal γ-FeOOH particles are suspended in the large amount of solution in this case. The diffraction pattern from the dried corrosion products shows that major components in corrosion products were γ-FeOOH and Fe_3O_4, and minor components were green rust II

and α-FeOOH. Diffraction peaks of Fe_3O_4 are likely to originate from not only the oxide scale but also Fe_3O_4 formed in the drying process. The relatively high peaks from Fe_3O_4 are a contrast to those from corrosion products formed on the Fe surface covered with oxide scale, as shown in Fig. 6.6(a). This result may be related to the effect of nickel on the stability of Fe_3O_4.

6.4.2 In-situ XRD Diffraction of Corrosion Products Formed During Multi-cycle Exposure to Wet and Dry Atmospheres

In order to analyze corrosion products formed under well-controlled atmospheres, X-ray diffraction patterns of the corrosion products were measured while monitoring the atmospheric humidity. A NaCl aqueous solution was dropped onto Fe, and it was subsequently cyclically exposed to wet and dry atmospheres. Figure 6.9(a) shows the sequential X-ray diffraction patterns from the sample surface, of which the numbers correspond to a time denoted in the relative humidity curve shown in Fig. 6.9(b). Large diffraction peaks assigned to γ-FeOOH are observed, together with peaks assigned to Fe_3O_4, α-FeOOH and GR(Cl). Diffraction peaks from the iron substrate are detected, indicating that the Mo $K\alpha$ X-ray penetrates the substrate through water and corrosion products. As the peak intensity of Fe appears to decrease with increasing corrosion time, it is suggested that the layer of corrosion products has grown. Diffraction patterns of NaCl show that NaCl is precipitated under a drying process and is dissolved under a wetting process. Although the fractions of α-FeOOH to γ-FeOOH in this experiments do not seem to be the same as those obtained in one-cycle exposure shown in Fig. 6.5, the difference may result from the fact that the formation of these ferric oxyhydroxides depends on the oxidation rate of ferrous ions [26].

As the chemical character of silicon is different from that of iron, the addition of silicon to iron is considered to change components of corrosion products. Actually, corrosion products formed on the FeSi surface were found to differ considerably from those on the Fe surface. Figure 6.10(a) shows the sequential X-ray diffraction patterns of the surface of FeSi, which was cyclically exposed to wet and dry atmospheres after dropping of a NaCl aqueous solution. The relative humidity during the cyclic exposure is given in Fig. 6.10(b). Clear peaks assigned to β-FeOOH are found, together with small peaks assigned to γ-FeOOH, GRII, and GR(Cl). The results indicate that the addition of silicon to iron suppresses the formation of γ-FeOOH and enhances the formation of β-FeOOH in corrosion products. In order to compare the variation in component fractions of corrosion products with time, the integrated intensities of a main peak from γ-FeOOH formed on the surface of Fe and Fe-Si were obtained as shown in Fig. 6.11(a). The integrated intensities of the β-FeOOH (200) peak, at 6.486 degree, as shown in the diffraction patterns in Figs. 6.9 and 6.10, from corrosion products formed on the surface of Fe and FeSi. Figure 6.11(b) shows the integrated intensities of the β-FeOOH (200) peak, at 7.709 degree, in the diffraction patterns from

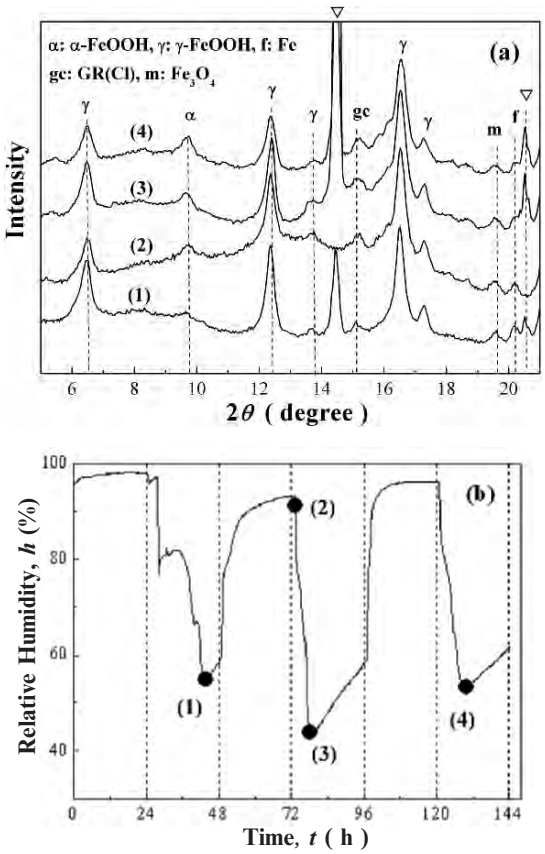

Fig. 6.9. (**a**) X-ray diffraction patterns from the Fe surface, on which a NaCl aqueous solution was dropped and subsequently cyclically exposed to wet and dry atmospheres, as shown in (**b**). The number denoted in the diffraction profiles corresponds to the condition in the cycle. Triangles denote the diffraction peaks of NaCl

corrosion products formed on the surface of FeSi, as a function of time. As periodic changes in intensity peaks of γ-FeOOH appear to correspond to the cycle of the relative humidity, X-rays are absorbed by water in measurements in a wet atmosphere. These results also indicate that the formation of γ-FeOOH in corrosion products is suppressed by the addition of silicon, and the amount of β-FeOOH is increased with increasing time in FeSi.

Figure 6.12 (a) shows the sequential X-ray diffraction patterns of the surface of Fe, on which a Na_2SO_4 aqueous solution was dropped. The sample was subsequently cyclically exposed to wet and dry atmospheres according to the humidity changes with time, as shown in Fig. 6.12(b). Major diffraction

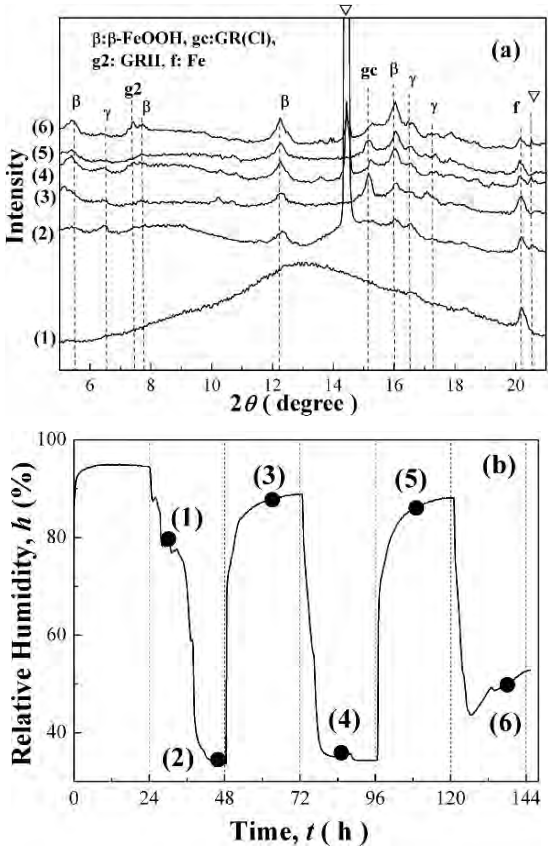

Fig. 6.10. (**a**) X-ray diffraction patterns from the FeSi surface, on which a NaCl aqueous solution was dropped and subsequently cyclically exposed to wet and dry atmospheres, as shown in (**b**). The number denoted in the diffraction profiles corresponds to the condition in the cycle. Triangles denote the diffraction peaks of NaCl

peaks of the corrosion products formed on Fe were assigned to γ-FeOOH, while the small peaks assigned to α-FeOOH and GRII are observed. In contrast to the case of corrosion products formed by a NaCl solution, peaks of GR(Cl) are not observed in the diffraction patters. However, the fundamental components of the corrosion products formed by the Na_2SO_4 solution appear to be similar to the case of corrosion products formed by a NaCl solution.

Sequential X-ray diffraction patterns of corrosion products formed on the surface of FeSi, which were cyclically exposed to wet and dry atmospheres after dropping of a Na_2SO_4 aqueous solution are shown in Fig. 6.13. Diffraction peaks of the corrosion products formed on the FeSi surface are assigned to GRII, α-FeOOH, and γ-FeOOH. Diffraction of β-FeOOH and GR(Cl) was not observed, as these oxides need chloride ions for formation. It is noted that

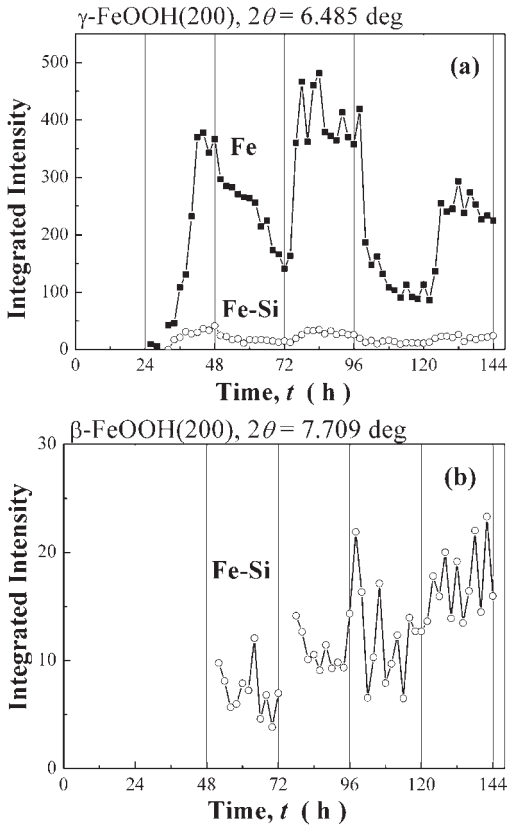

Fig. 6.11. Integrated intensities of (**a**) the γ-FeOOH (200) peak from corrosion products formed on the Fe and FeSi surfaces, and (**b**) the β-FeOOH (200) peak from corrosion products formed on the surface of FeSi as a function of corrosion time

the formation of γ-FeOOH is suppressed by the addition of silicon, compared to the case of Fe as shown in Fig. 6.12. This suggests that the addition of silicon to the Fe substrate influences components in corrosion products formed not only by a NaCl solution but also by a Na_2SO_4 solution. Therefore, it is not too much to say that silicon dissolved from FeSi, presumably silicate ions, interacts with other anions such as chloride ions and sulfate ions in water, which can change components in the resultant corrosion products.

6.4.3 Ex-situ XRD Diffraction of Corrosion Products Extracted from Different Layers

In order to study differences in corrosion products formed at different locations, ex-situ X-ray diffraction measurements were carried out. Figure 6.14(a)

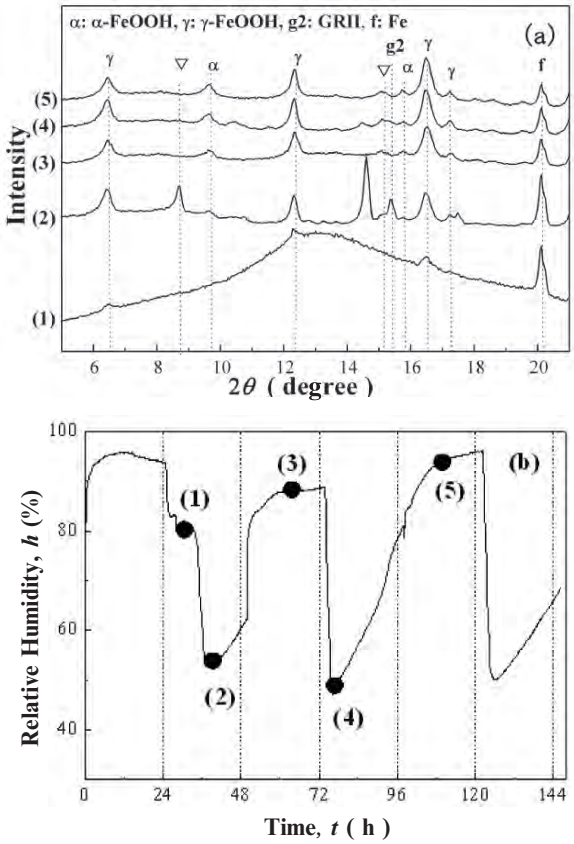

Fig. 6.12. (**a**) X-ray diffraction patterns from the surface of the Fe surface, on which a Na_2SO_4 aqueous solution was dropped and subsequently cyclically exposed to wet and dry atmospheres, as shown in (**b**). The number denoted in the diffraction profiles corresponds to the condition in the cycle. Triangles denote the diffraction peaks of Na_2SO_4

shows X-ray diffraction patterns of samples extracted from the outer side of wet corrosion products formed on the Fe and FeSi surfaces by dropping a NaCl solution. The diffraction peaks are assigned to γ-FeOOH, and a broad profile below the peaks, which arises from water and capillary glass, is observed. A sample extracted from an intermediate layer of wet corrosion products did not reveal clear diffraction peaks, which are not shown here, indicating that the intermediate layer was filled with water. On the other hand, X-ray diffraction patterns from samples extracted from the inner side of the wet corrosion products are shown in Fig. 6.14(b). The diffraction peaks assigned to γ-FeOOH are clearly observed in the corrosion products of Fe, along with small peaks allocated to Fe_3O_4, GR(Cl), and α-FeOOH are observed. On the

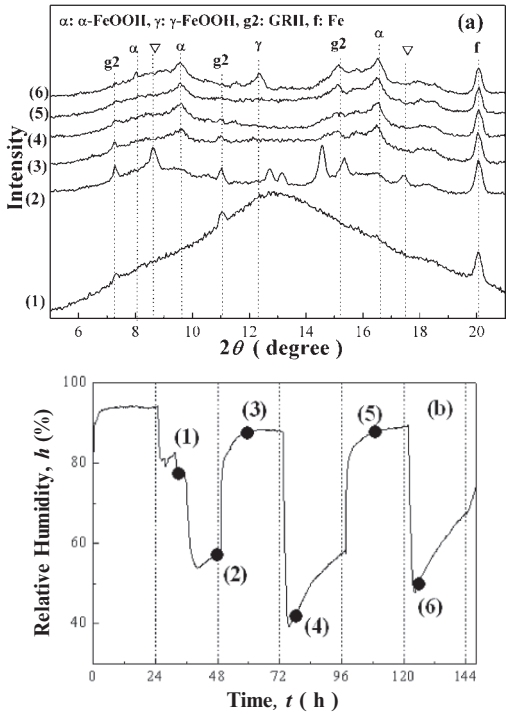

Fig. 6.13. (**a**) X-ray diffraction patterns from the FeSi surface, on which a Na_2SO_4 aqueous solution was dropped and subsequently cyclically exposed to wet and dry atmospheres, as shown in (**b**). The number denoted in the diffraction profiles corresponds to the condition in the cycle. Triangles denote the diffraction peaks of Na_2SO_4

other hand, the diffraction peaks of corrosion products formed on the surface of FeSi show that β-FeOOH was primarily formed, and small amounts of γ-FeOOH and GR(Cl) were also formed. The overall characteristic features of corrosion products formed in these conditions are in agreement with the results of multi-cycle exposure experiments as shown in Figs. 6.9 and 6.10. In addition, it is interesting to note that GR(Cl) and Fe_3O_4 consisting of ferric and ferrous ions are formed in the inner layer of corrosion products freshly formed on the iron surface. These results are explained on the basis of the E-pH diagram shown in Fig. 6.3. Corrosion products, which were dried after corrosion by the NaCl solution, were also analyzed. Figure 6.15 (a),(b) shows X-ray diffraction patterns of samples extracted from the outer and inner sides of the corrosion products formed the Fe and FeSi surfaces, respectively. It can safely be stated that a difference in corrosion species between the inner and outer layers is small, although the diffraction signals are noisy for a very small amount of sample. This suggests that the corrosion products formed

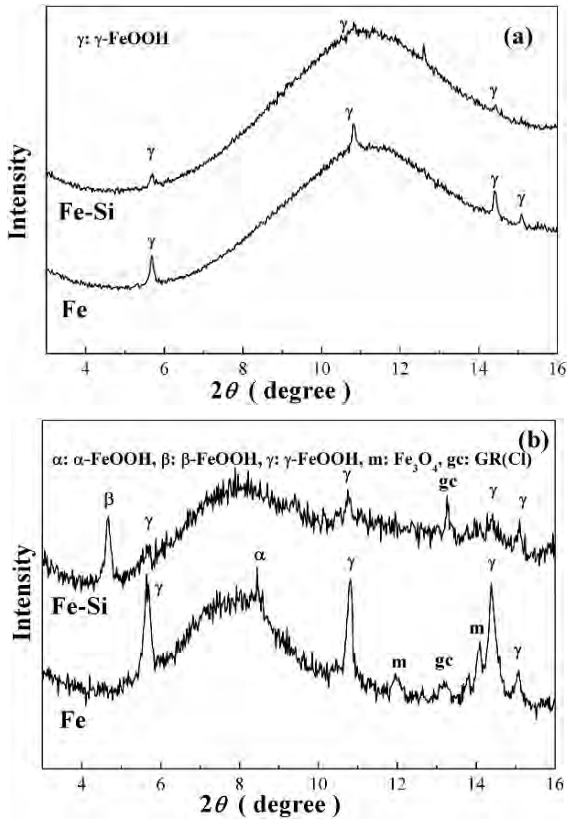

Fig. 6.14. X-ray diffraction patterns from samples extracted from (**a**) the outer side and (**b**) the inner side of the wet corrosion products freshly formed on the Fe and FeSi surface by dropping a NaCl aqueous solution

under wet condition may be mixed during the drying process or evaporation of water. Major diffraction peaks from the corrosion products of Fe are allocated to γ-FeOOH, although the peaks of NaCl precipitated are increased in the drying process. Diffraction peaks assigned to β-FeOOH and γ-FeOOH are observed in the corrosion products of FeSi together with small peaks assigned to GRII and GR(Cl).

A small amount of corrosion product formed by the Na_2SO_4 aqueous solution was also analyzed, in order to study the effect of anion species in an aqueous solution on corrosion products. Figure 6.16 (a),(b) shows X-ray diffraction patterns of samples extracted from the outer and inner sides of wet corrosion products freshly formed on the Fe and FeSi surfaces by a Na_2SO_4 aqueous solution, respectively. The diffraction peaks of the outer corrosion products formed in Fe are assigned to γ-FeOOH, while clear peaks were not observed for corrosion products formed in Fe-Si. In the inner layer of the

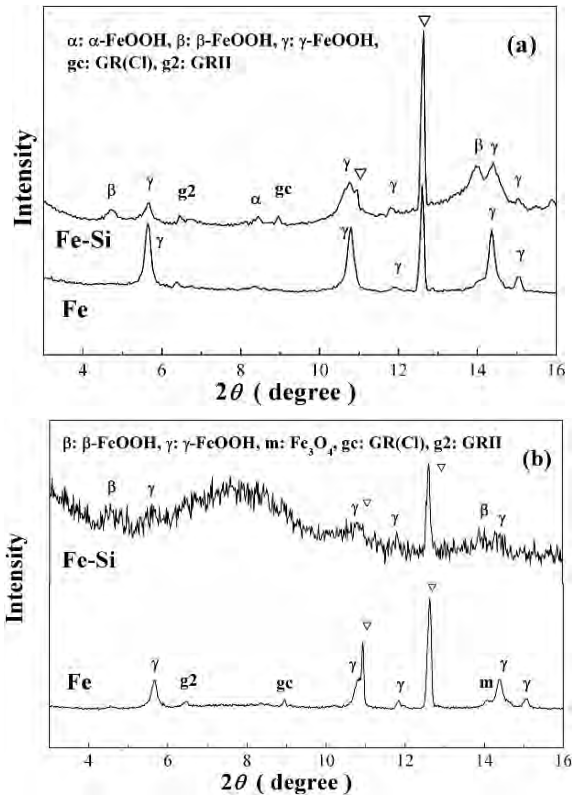

Fig. 6.15. X-ray diffraction patterns from samples extracted from (**a**) the outer side and (**b**) the inner side of the corrosion products formed on the Fe and FeSi surfaces, which were dried after being corroded by dropping a NaCl aqueous solution. Triangles denote the diffraction peaks of NaCl

corrosion products of Fe, a small peak is assigned to the green rust GRII in addition to the major peaks of γ-FeOOH. Clear peaks assigned to GRII appear in the corrosion products formed on the FeSi surfaces. The formation of GRII is characteristic of corrosion products formed by the Na_2SO_4 solution, while β-FeOOH, which originally contains chloride ions, is formed by the NaCl solution.

Figure 6.17 (a),(b) shows X-ray diffraction patterns of samples extracted from the outer and inner sides of the dry corrosion products formed on the surface of Fe and Fe-Si, respectively. They were dried after being corroded in the Na_2SO_4 solution. Many diffraction peaks assigned to salts containing sulfate ions, such as Na_2SO_4, $Fe_2(SO_4)_3 \cdot 9H_2O$, $Na_2Fe(SO_4)_2 \cdot 4H_2O$, are observed, indicating that the salts were precipitated during the drying process. In spite of such precipitation, the results show that the major component of the corrosion products is γ-FeOOH, and small amounts of GRII and α-FeOOH are formed. On the other hand, GRII is formed as corrosion

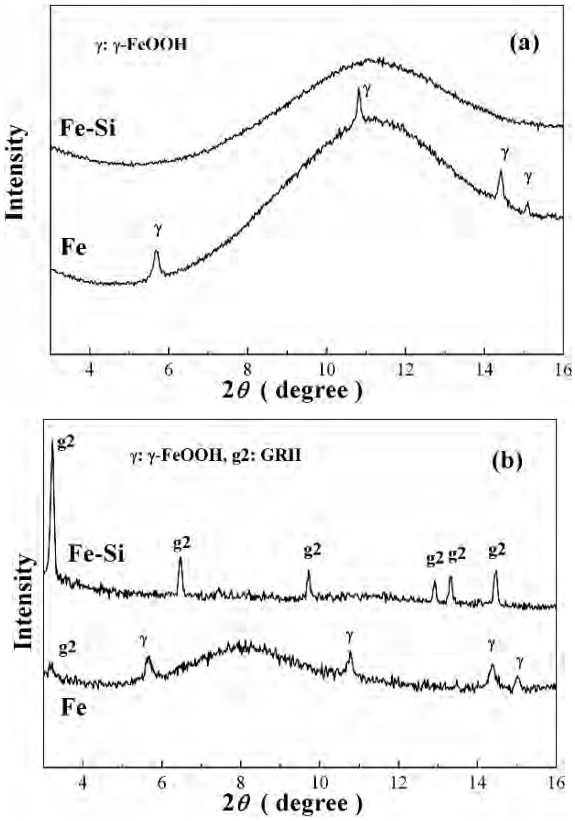

Fig. 6.16. X-ray diffraction patterns from samples extracted from (**a**) the outer side and (**b**) the inner side of the wet corrosion products freshly formed on the Fe and FeSi surfaces by dropping a Na_2SO_4 aqueous solution

product on the FeSi surface, while the formation of γ-FeOOH is suppressed. These results again indicate that the addition of silicon to iron suppresses the formation of γ-FeOOH. In fact, it has been reported that the synthesis of γ-FeOOH in an aqueous solution is influenced by the addition of silicate ions [27,28]. Such an effect of the silicate ions may act as a modifier of components in corrosion products. These results are fundamentally consistent with those obtained in in-situ measurements, as shown in Figs. 6.12 and 6.13.

6.5 Formation Conditions of Different Components of Corrosion Products

Components of corrosion products, which were freshly formed on the metallic surfaces, should be summarized on the basis of the above experimental

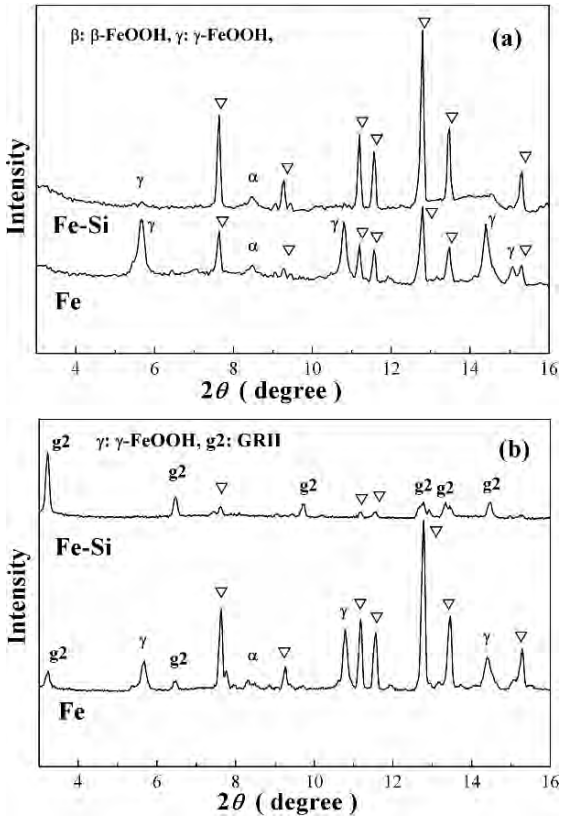

Fig. 6.17. X-ray diffraction patterns from samples extracted from (**a**) the outer side and (**b**) the inner side of the corrosion products formed on the Fe and FeSi surfaces, which were dried after being corroded by dropping a Na_2SO_4 aqueous solution. Triangles denote the diffraction peaks of salts, such as Na_2SO_4, $Fe_2(SO_4)_3 \cdot 9H_2O$, $Na_2Fe(SO_4)_2 \cdot 4H_2O$, etc

results, taking into account the inhomogeneous formation of corrosion products. Figure 6.18 shows schematics representing the cross-sections of layers of corrosion products formed on the surfaces of Fe and FeSi by dropping a NaCl solution onto these sample surfaces; thereafter, the corrosion products dried. The precipitation of the salt, NaCl, is not included in these schematics. These results should stress that components consisting of ferric and ferrous ions, such as GR(Cl), are formed in the inner layer of corrosion products. The addition of silicon suppresses the formation of γ-FeOOH, and enhances the formation of β-FeOOH. It was also suggested that corrosion products formed under wet conditions may be mixed in the drying process.

In a similar manner, the schematics representing the cross-sections of species of corrosion products formed on the Fe and FeSi surfaces by dropping

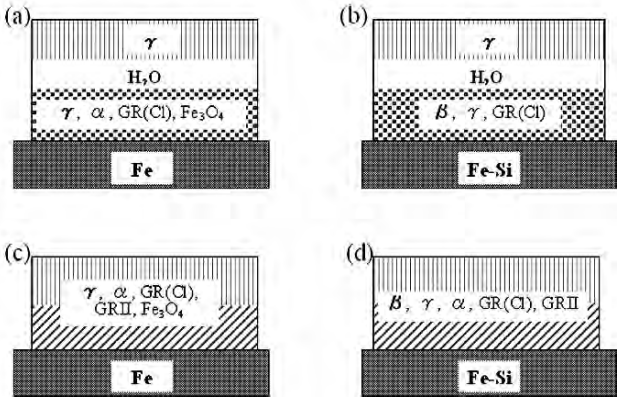

Fig. 6.18. Schematics representing the cross-section of species of corrosion products formed on the surfaces of (**a**) Fe and (**b**) FeSi by dropping a NaCl solution, and (**c**) Fe and (**d**) FeSi dried thereafter

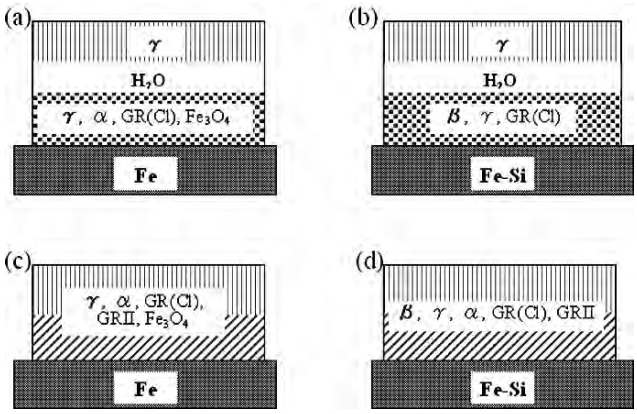

Fig. 6.19. Schematics representing the cross-sections of species of corrosion products formed of the surfaces of (**a**) Fe and (**b**) Fe-Si by dropping a Na_2SO_4 solution, and (**c**) Fe and (**d**) FeSi dried thereafter

Na_2SO_4 solution, and the corrosion products that dried thereafter are shown in Fig. 6.19. Sulfate salts, such as Na_2SO_4, precipitated during the drying process are omitted in these schematics. Instead of β-FeOOH and GR(Cl) formed in corrosion by chloride ions, GRII consisting of ferric and ferrous ions was found in the inner layer of these corrosion products. As the formation of γ-FeOOH is suppressed in the corrosion products of FeSi, silicate ions presumably play an important role in changing the constituent species of corrosion products.

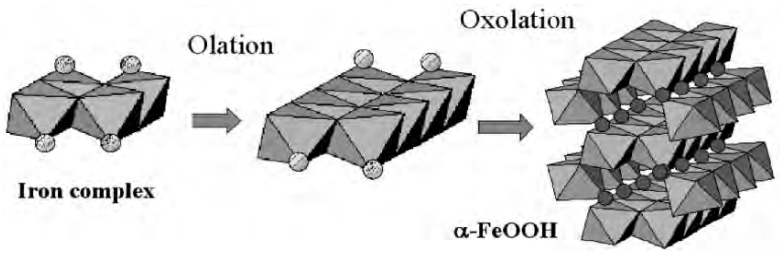

Fig. 6.20. Schematics representing the formation of ferric oxyhydroxide, α-FeOOH, through olation and oxolation of iron complexes in water

The above reactions of corrosion products take place fundamentally through the formation pathways of oxides from ferrous ions shown in Fig. 6.2. However, it is to be noted in atmospheric corrosion that there are gradients of the amounts of dissolved oxygen, hydrogen ions, anions and cations in aqueous solution on the metallic surface. The amount of oxygen in the outer side of the solution is likely to be higher than that in the inner side, whereas the amounts of cations of iron and metallic alloying elements in the substrate side are higher than those in the atmospheric side. The amount of aqueous solution on the surface of iron is cyclically changed in wetting and drying processes in atmospheric corrosion. Although the atmospheric conditions for the formation of corrosion products are experimentally monitored, different corrosion products can be formed in wetting and drying processes. This is because anions and cations greatly influence formation of iron oxides.

Figure 6.20 shows schematics representing atomic-scale formation processes of ferric oxyhydroxide, typically α-FeOOH, from iron complexes, FeO_6 tetramer. In these processes, solid iron oxides are formed through bridging of cations by hydroxo (OH), which is referred to as olation, and bridging cations by oxo (O), that is oxolation in aqueous solution [20]. In atmospheric corrosion, the precipitation of the oxides occurs while ferrous ions in solution are transformed to ferric ions, which are influenced by dissolved oxygen, hydrogen ions, cations, anions from an alloying element and so on. For instance, silicate ions originating from an iron silicon alloy may competitively behave against anions such as chloride ions and sulfate ions in water, and modify components in resultant corrosion products. Furthermore, the elementary corrosion reactions may differ among the outer side and inner side of water for the gradients of chemical species.

6.6 Summary

This chapter has examined various components in corrosion products formed on the surface of pure iron and a few iron-based alloys, which were analyzed using in-situ X-ray diffraction measurements with synchrotron radiation and

in-house X-ray sources. A specially designed cell was used for in-situ diffraction measurements of corrosion products freshly formed on the surface of the iron samples by cyclic exposure to wet and dry atmospheres. Ex-situ X-ray diffraction measurements by synchrotron radiation have also been carried out for a very small amount of sample extracted from wet corrosion products. These results stressed that corrosion products are formed of ferrous ions as well as ferric ions in atmospheric corrosion.

Rust layers formed in mild and weathering steel is known to consist primarily of fine α-FeOOH particles, which are almost all ferric ions [3–6], since these corrosion products are likely to be oxidized by air. However, the formation of ferrous ions must occur at the corrosion front, which is the vicinity of the substrate iron, by anodic reaction. The above experiments may simulate the formation of different oxides from such ferrous ions. Although corrosion conditions in this work are not necessarily identical to the case for the protective rust layer formed in the atmospheric cycle, the results show that components of corrosion products are influenced by atmospheric factors. Since several alloying elements are contained in weathering steel, they are incorporated in the rust layer as cations and anions. Thus, a rust layer with a very complicated structure may be formed in the weathering steel, and as a result, a protective membrane acts against water, oxygen and detrimental anions such as chloride ions.

Acknowledgements

The authors would like to express sincere thanks to Dr. H. Konishi and Dr. J. Mizuki, Dr. K. Kanie and Prof. A. Muramatsu for their help on synchrotron radiation experiments and their discussion.

References

1. C. Leygraf and T. Graedel: *Atmospheric Corrosion*, Wiley-Interscience, New York (2000).
2. R. M. Cornell and U. Schwertmann: *The Iron Oxides*, John-Wiley VCH, Weinheim (2003).
3. T. Misawa, M. Yamashita, K. Matsuda, H. Miyuki, J. H. Nagano: Iron Steel Inst. Jpn., **79**, 69 (1993).
4. T. Okada, Y. Ishii, T. Mizoguchi, I. Tamura, Y. Kobayashi, Y. Takagi, S. Suzuki, H. Kihira, M. Itoh, A. Usami, K. Tanabe, and K. Masuda: Jpn. J. Appl. Phys, **39**, 3382 (2000).
5. S. Nasu, T. Kamimura, and T. Tazaki: Hyp. Interact., **139/140**, 175 (2002).
6. T. Kamimura, S. Nasu, T. Tazaki, K. Kuzushita, S. Morimoto: Materials Trans. JIM **43**, 694 (2002).
7. T. Kamimura, S. Nasu, T. Segi, T. Tazaki, S. Morimoto, and H. Miyuki: Corros. Sci., **45**, 1863 (2003).
8. K. Asami and M. Kikuchi: Corros. Sci., **45**, 2671 (2003).

9. M. Yamashita, T. Shimizu, H. Konishi, J. Mizuki, and H. Uchida: Corros. Sci., **45**, 381 (2003).
10. U. R. Evans and C. A. J. Taylor: Corros. Sci., **12**, 227 (1972).
11. M. Stratmann, K. Bohnenkamp, and H. J. Engell: Corros. Sci., **23**, 969 (1983).
12. M. Stratmann and K. Hoffmann: Corros. Sci., **29**, 1329 (1989).
13. M. Stratmann and J. Müller: Corros. Sci., **36**, 327 (1994).
14. T. Kamimura and M. Stratmann: Corros. Sci., **43**, 429 (2001).
15. Y. Takahashi, E. Matsubara, S. Suzuki, Y. Okamoto, T. Komatsu, H. Konishi, J. Mizuki, and Y. Waseda: Mater. Trans., **46**, 637 (2005).
16. S. Suzuki, E. Matsubara, K. Kiyoshi, A. Muramatsu and Y. Waseda: Current Advances in Materials and Processes ISIJ, **18**, 1680 (2005).
17. J. -M. R. Genin, A. A. Olowe, Ph. Refait, and L. Simon: Corros., Sci., **38**, 1751 (1996).
18. Ph. Refait, M. Abdelmoula, and J. -M.R.Genin: Corros., Sci., **40**, 1547 (1998).
19. Ph. Refait, S. H. Drossi, J. Pytkiewicz, and J. -M. R. Genin: Corros., Sci., **39**, 1699 (1997).
20. Ph. Refait, A. Gehin, M. Abdelmoula, and J. -M. R. Genin: Corros., Sci., **45**, 659 (2003).
21. J. -P. Jolivet, C. Chaneac, and E. Tronc: Chem. Commun. 477 (2004).
22. J. -P. Jolivet, M. Henry, J. Livage, and E. Bescher: *Metal Oxide Chemistry and Synthesis*, Jon Wiley & Sons, Chichester (2000).
23. K. Shinoda, E. Matsubara, A. Muramatsu and Y. Waseda: Mater.Trans JIM, **35**, 394 (1997).
24. P. Kofstad: *High Temperature Corrosion*, Elsevier Applied Science, London (1988).
25. S. Suzuki, M. Saito, M. Kimura, T. Suzuki, H. Kihira, and Y. Waseda: ISIJ Inter., **43**, 366 (2003).
26. K.Kimijima, K.Kiyoshi, S. Suzuki and A. Muramatsu: Current Advances in Materials and Processes ISIJ, **18**, 1673 (2005).
27. U. Schwertmann and R. M. Taylor: Clays Clay Min., **20**, 151 (1972).
28. U. Schwertmann and R. M. Taylor: Clays Clay Min., **20**, 159 (1972).

7 Surface Analysis of Oxides and Corrosion Products Formed on Surfaces of Iron-based Alloys

Shigeru Suzuki

7.1 Introduction

When an iron-based alloy is exposed to an atmosphere containing oxygen at room temperature as well as high temperatures, an oxide layer and/or oxide particles are, to a greater or lesser extent, formed on the surfaces of the alloy. The characteristic features of the oxides formed on the surfaces of the iron-based alloy strongly depend on temperature, constituent elements in the alloy, chemical species in atmospheric gas, etc. [1, 2]. Since such surface oxides influence the surface properties of the iron-based alloy, it is critical to characterize systematically the surface layers of various iron-based alloys exposed to different atmospheres.

Figure 7.1 shows the Ellingham diagram for iron and several relevant elements by which the formation of oxides of elements may be predicted [3]. The different annealing conditions are denoted as zones (A) to (D) in Fig. 7.1; these zones are specified in terms of the temperature and partial pressure of oxygen in the atmosphere. For example, the oxidation conditions at room temperature and high temperature in air correspond to zones (A) and (B) in Fig. 7.1, respectively. If an iron-based alloy is annealed under a low partial pressure of oxygen, as shown in zone (C) of Fig. 7.1, reactive alloying elements, such as chromium, manganese, silicon, titanium, and aluminum, may be selectively oxidized while iron is not oxidized. Thus, a surface layer formed by annealing under a low partial pressure of oxygen differs from that formed under a high partial pressure of oxygen. Furthermore, if an iron-based alloy is annealed at high temperature under an ultra-high vacuum, which corresponds to an extremely low partial pressure of oxygen, as denoted in zone (D) of Fig. 7.1, the surface chemical composition is likely to be controlled by the surface energy rather than oxygen. Therefore, the in-depth distribution of alloying elements in the surface layers of iron-based alloys is classified into different cases, depending on the temperature and partial pressure of oxygen in the atmosphere. This chapter deals with the characteristic distribution of alloying elements in the surface layers of iron-based alloys, which were annealed under various conditions.

Corrosion products are formed on the surface of iron-based alloys by atmospheric corrosion and wet corrosion at room temperature. The corrosion

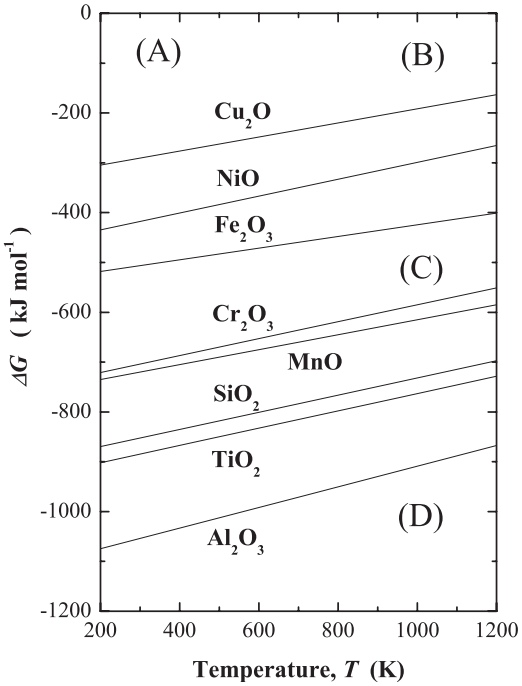

Fig. 7.1. Ellingham diagram for some oxides in the high temperature oxidation of metals and alloys

products are fundamentally composed of hydroxides, oxyhydroxides, and oxides of iron [4, 5], which will be referred to as iron oxides hereafter. Water as well as oxygen in air plays a crucial role in the formation of corrosion products, in which hydrogen originating from water is often incorporated as ferric oxyhydroxides [4]. The thickness of a layer of corrosion products or rust formed by atmospheric corrosion is considerably larger than that of an oxide layer formed at room temperature in air, whose thickness is estimated from the temperature dependence of the oxide thickness. Thus, the mechanism of atmospheric corrosion or wet corrosion is essentially different from that of thermal oxidation or high temperature oxidation.

The phase stability of corrosion products formed in wet or atmospheric corrosion is described using an electrochemical potential (E)-pH diagram in an aqueous solution. The diagram has been carefully investigated despite the difficulties encountered in the control of reaction conditions, such as residual oxygen from the atmosphere. Thus, electrochemical potential (E)-pH diagrams for iron-water containing various salt ions systems have been proposed, as a potential (E)-pH diagram for the iron-chloride containing water iron ions is exemplified in Fig. 7.2 [6, 7]. Since ferrous hydroxide $Fe(OH)_2$ and green rust (GR), which contain ferrous ions, are able to be in equilibrium with metallic iron, they are likely to be formed as intermediate corrosion products, which are precursors of the final corrosion products. However, they

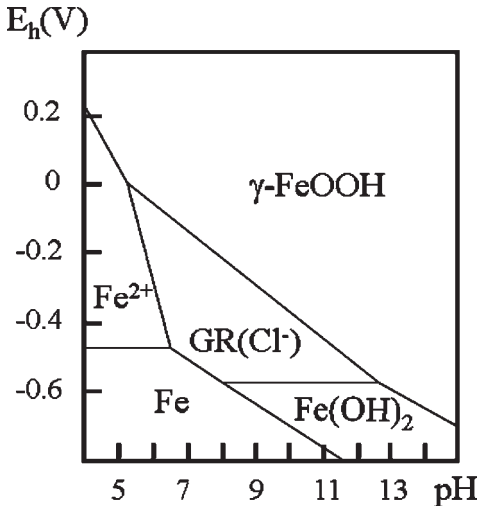

Fig. 7.2. Potential (E)-pH equilibrium diagram of iron in chloride-containing aqueous solution at 298 K

are quickly transformed to ferric oxyhydroxides, e.g. γ-FeOOH, since ferrous ions are easily oxidized in a normal aqueous solution. Thus, ferric oxyhydroxides are detected as a component of final corrosion products, indicating that the formation of corrosion products is strongly affected by atmospheric air. Corrosion products of iron-based alloys are also formed by adsorption of water vapor in ambient atmosphere, in which electrochemical reactions occur in a similar manner.

Oxides and corrosion products formed on the surfaces of iron-based alloys often act as a protective layer for the substrate of the alloys because they reduce the oxidation and corrosion rate of iron-based alloys. Typically, the formation of a layer of aluminum oxides or chromium oxides is known to provide resistance to oxidation for iron-based alloys, because the permeation of oxygen from the atmosphere to the iron substrate is suppressed by the formation of a dense layer of these oxides. Corrosion products formed in atmospheric corrosion can also reduce the corrosion rate of the substrate of iron-based alloys, as observed in a protective rust layer of weathering steel. Various surface analytical methods have been utilized for characterizing oxides and corrosion products formed on iron-based alloys, and the fundamental processes of oxidation and corrosion of alloys have been discussed on the basis of the thermodynamic properties of elements.

7.2 Surface Analytical Methods

Surface analytical methods, such as X-ray photoelectron spectroscopy (XPS), Auger electron spectroscopy (AES), and secondary ion mass spectroscopy (SIMS), are used for characterizing the chemical composition and state of

elements on the surfaces of various materials [8–12]. Electron probe microanalysis (EPMA) is occasionally included in the surface analytical methods although the information depth in EPMA is relatively large [13, 14]. Nevertheless, the information on microscopic and in-depth distributions of elements obtained by these surface analytical methods is generally very local in the surface layers of materials. Chemical information obtained by the surface analytical methods is complementary to the structural information of materials obtained by structural analytical methods such as the X-ray diffraction method described in Chapters 5 and 6.

Since the information depth in XPS is of the order of a few nanometers, it is often employed for analyzing the chemical composition and state of elements in a thin layer on the surfaces of iron-based alloys. The incident X-ray used in conventional XPS is mainly Al-Kα or Mg Kα, while synchrotron radiation has recently been trendily used in photoelectron spectroscopy. When an in-depth surface analysis of the alloys is carried out using XPS, the spectra obtained are generally measured while the sample surface is sputtered by ions - typically argon ions. The surface chemical composition of elements is evaluated on the basis of their photoelectron intensities measured in the XPS spectra coupled with their relative sensitive factors or spectra of reference materials. AES is also an electron spectroscopy method that enables us to obtain information on a very small area by using a focused electron beam. On the other hand, EPMA, which also involves the irradiation of a sample surface by an electron beam, is often utilized for determining the chemical composition in a microscopic region. Although the X-ray intensities depend on the measurement conditions and sample, the characteristic X-rays measured in EPMA originate from a region of nearly 1μm from a metallic sample. Among the surface analytical methods, EPMA provides the most reliable and quantitative information on chemical composition because the information depth in EPMA is relatively large and insensitive to very thin contaminants adsorbed on the sample surface by exposure to air. Therefore, the quantitative compositions of elements determined by EPMA are often compared with the model values proposed by thermodynamic theories. For instance, the segregation of a specific element in multi-component alloys, which occurs during the processing or utilization of the alloys at high temperatures, is analyzed using EPMA, and the distribution of the element obtained by EPMA is compared with that predicted by a thermodynamic model.

While XPS, AES, and EPMA are essentially non-destructive analytical methods, the ions sputtered from the sample surface are analyzed in SIMS. Primary positive ions, such as O_2^+, Cs^+, or Ga^+ ions, are usually irradiated to the sample surface, whereas positive or negative secondary ions are counted using a mass spectrometer. If the mass number of secondary ions emitted from an element of interest is close to that of the secondary ions from a different element, the different ions interfere in the detection of secondary ions

of interest. A mass spectrometer with high mass resolution is then applied to the analysis, or cluster ions combined with primary ions, e.g. CsM^+, are sometimes analyzed [15–17]. In addition, positive and negative secondary ions are alternatively measured in SIMS because the ionization characteristics or sensitivity of secondary ions depend strongly on the type of elements. The sputtering rate of a surface layer is estimated from the sputtered depth and sputtering time measured under a given condition, and the sputtered depth is measured using a surface profilometer.

Glow discharge optical emission spectrometry (GDOES) is also useful in the study of the depth profile of a surface layer, in which the relationship between the composition and sputtered depth is determined [18]. Depth profiles for surface layers measured by GDOES have been shown to be consistent with those obtained by SIMS. In GDOES, although the analyzed area is large, the measuring time is very short and it is not necessary to maintain an ultra-high vacuum in the analysis chamber. In addition, the signals measured in GDOES are almost independent of the sample matrix, whereas intensities of secondary ions in SIMS largely depend on the matrix species.

When the surface layers formed on an iron-based alloy are characterized using surface analytical methods, the characteristic features of elements in the surface layer should be considered along with the thermodynamic properties and reactions of elements as mentioned above. This chapter describes several characteristic features of elements in a thin oxide layer or fine oxides formed on the surface of iron-based alloys by corrosion or oxidation, which were characterized by the surface analytical methods. The experimental results on oxidation and corrosion of alloys are discussed on the basis of microscopic models of reactions and properties of elements.

7.3 Characterization of Thermally Oxidized Surface Layers

The oxidation of iron-based alloys is accompanied by complicated phenomena, such as changes in the elemental distribution and morphology in a surface layer, which depend on the annealing conditions. Oxidation of metallic alloys is sometimes classified into external oxidation or internal oxidation on the basis of the morphology of oxides. For example, a layer of oxides comprising all the constituent elements is formed on the metallic substrate during external oxidation, whereas only fine oxide particles of less noble elements are distributed in the surface layer of noble elements during internal oxidation. The occurrence of external or internal oxidation depends on the alloy composition and oxidation conditions, such as the partial pressure of oxygen in atmosphere. This section shows the experimental results of surface layers containing oxides formed on the surfaces of iron-based alloys under various

conditions, which are discussed along with the chemical characters of alloying elements.

7.3.1 Oxidation of a Compositionally Modified Surface Layer

Fe-Mn-Si austenitic alloys, which do not contain any precious elements, exhibit the shape memory effect and are promising from the viewpoint of industrial use [19]. However, Fe-Mn-Si alloys are easily corroded under humid atmospheric conditions or oxidized during annealing. The chemical compositions of these alloys have been modified by the addition of a small percentage of chromium [20]. Since the chemical composition of the surface layer may be modified by further treatment, the effect of chromium addition on oxidation and corrosion resistance has been further exploited for improving surface properties. For instance, a chromium-enriched layer formed by annealing under ultra-high vacuum reduces the native oxide layer formed at room temperature [21]. Thus, the influence of the modification of the surface compositions on the oxidation of an Fe-Mn-Si-Cr shape memory alloy has been studied using EPMA, SIMS, and XPS [22].

Surface layers of the alloys, which were as-lapped and subsequently annealed under vacuum, formed by oxidation in air were characterized in this study. A sheet of Fe-28mass%Mn-6mass%Si-5mass%Cr (Fe-27at%Mn-11at%Si-5at%Cr) alloy was lapped to a mirror surface, which is hereafter referred to as LA. Some of the samples were subsequently annealed at 1173 K for 3600 s under a vacuum of 10^{-2} Pa, and they are referred to as AN. These samples were oxidized in air at 673 K and 873 K in order to compare the oxidation resistance of samples LA and AN. These oxidation temperatures lie in the range in which the shape recovery of this shape memory alloy occurs.

Figure 7.3 is a diagrammatic representation of the chemical composition of samples LA and AN obtained by EPMA [22]. These samples were oxidized

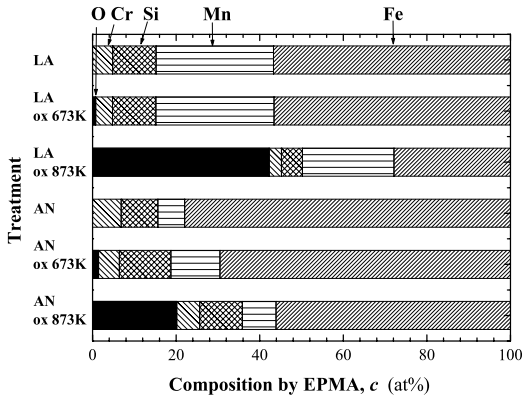

Fig. 7.3. Chemical compositions of samples LA and AN that were subsequently oxidized at 673 and 873 K in air (ox 673 K and ox 873K), determined by EPMA

in air at 673 K and 873 K, respectively. Information on the composition obtained by EPMA originates from a surface layer of approximately 1 μm thickness. Since the information obtained from a native oxide layer on sample LA is negligible, the chemical composition of the surface layer of the sample LA is almost the same as the bulk composition. On the other hand, the composition of sample AN annealed under vacuum obtained by EPMA differs from that of sample LA: there is a decrease in the amount of manganese, whereas there is an increase in the amounts of chromium, silicon, and iron. The increase in the amount of oxygen by oxidation at 673 K and 873 K depends on the chemical composition of the surface layers of the samples, as shown in Fig. 7.3. The amount of oxygen in sample AN is lower than that in sample LA, indicating that the surface of sample AN has a good oxidation resistance. Although the relative amounts of iron, manganese, silicon, and chromium are marginally changed by oxidation, this phenomenon can be attributed to the increase in the amount of chromium in the surface layer during annealing. This corresponds to the fact that the oxidation resistance of iron-based alloys is improved by the addition of chromium [1, 23, 24].

Figure 7.4 (a), (b) shows the SIMS depth profiles of samples LA and AN, respectively [22]. Depth profiles of up to approximately 0.4 μm were obtained in these measurements. As the surface of these samples was covered with a native oxide layer, the oxygen-relevant ion CsO^+ was detected in the depth profiles. It is noted that the intensity of manganese-relevant ions $CsMn^+$ is significantly decreased in sample AN by annealing, although quantitative

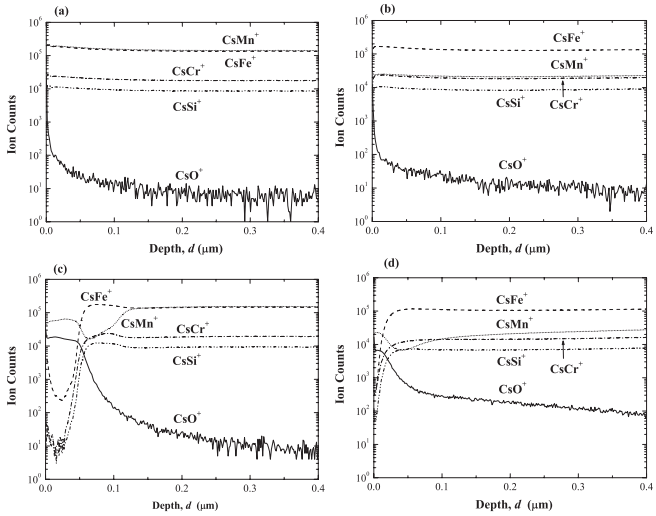

Fig. 7.4. SIMS depth profiles of the samples that were as-lapped (sample LA) (**a**) and those that were as-lapped and subsequently annealed under vacuum (sample AN) (**b**). SIMS depth profiles of samples LA (**c**) and AN (**d**) oxidized at 873 K in air

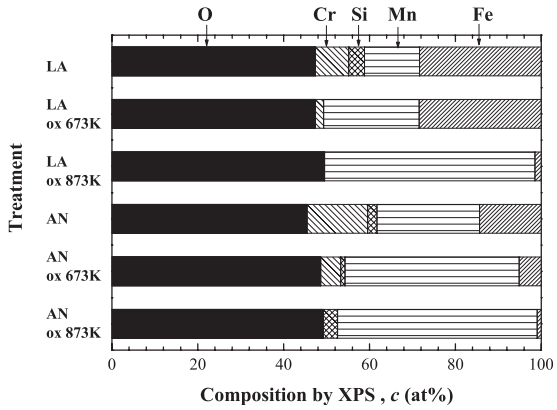

Fig. 7.5. Chemical compositions of samples LA and AN that are subsequently oxidized (in air) at 673 or 873 K, (ox 673 K or ox 873K), determined by XPS

amounts of elements should be carefully considered in SIMS. Nevertheless, this result is consistent with that obtained by EPMA, as shown in Fig. 7.3. On the other hand, the SIMS depth profiles for samples LA and AN oxidized in air at 873 K are shown in Fig. 7.4 (c), (d), respectively [22]. The results show that the oxide layer formed in the surface layer of sample AN is thinner than in sample LA. This result is also consistent with that obtained by EPMA, which includes information pertaining to the layered structure comprising the oxide layer and the surface layer, as shown in Fig. 7.3.

In order to obtain information on the very thin layer formed on the oxide layer, XPS measurements were carried out. Figure 7.6 summarizes the chemical composition of samples LA and AN obtained by XPS. Since the chemical composition of elements in the surface layer up to a few nanometers is available in a conventional XPS, the large amount of oxygen detected using XPS is attributed to the native oxide layer covering the sample surface. The chemical composition of metallic elements in sample LA was almost the same as the bulk composition despite the native oxide layer. On the other hand, the amount of manganese and silicon on the surface of sample AN was higher than that on the surface of sample LA. These phenomena are considered to result from the characteristics of silicon and manganese occurring on the iron surface during annealing [23, 24] although apparently they may be inconsistent with the results shown in Fig. 7.2.

Since such compositional changes in this alloy can induce a phase transformation, the constituent phase of the surface layer of sample AN was examined using the orientation image (OIM) obtained by the electron backscattering pattern (EBSP). The surface layer whose thickness is nearly 20 μm in sample AN was electrochemically polished in close proximity to the interface between the surface layer and the austenitic matrix. Figure 7.7 shows the top-view OIM images of face centered cubic (fcc) and body centered cubic (bcc) phases,

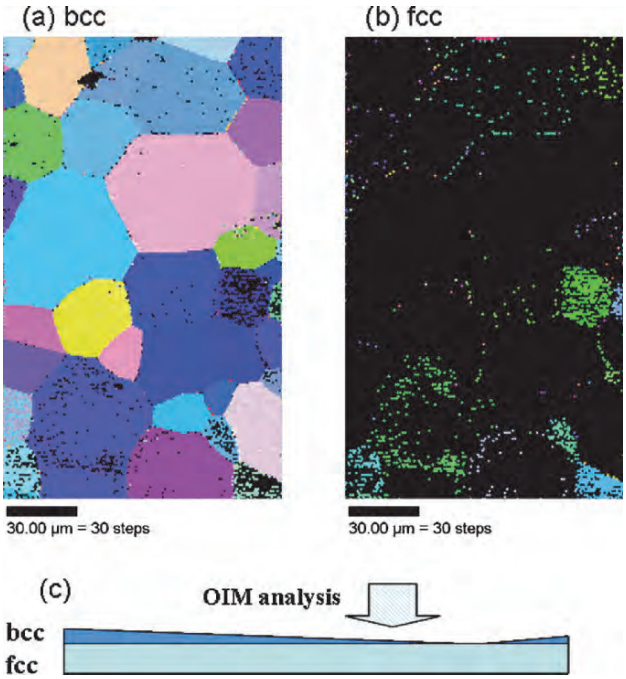

Fig. 7.6. OIM images of (**a**) bcc and (**b**) fcc phases in the surface layer of sample AN, which are shown as orientations in the top view, as shown in (**c**). The *black contrast* corresponds to an area to which the phase cannot be assigned

which is illustrated in Fig. 7.7 (c) [22]. The black contrast in these images corresponds to an area, in which the structure could not be determined as fcc or bcc. The results show that the main phase of the surface layer is bcc or ferrite, while that of the alloy substrate is fcc or austenite. This observation is consistent with the fact that manganese, one of the elements stabilizing austenite, depletes in the surface layer ca. 20 µm in thickness, and correspondingly the amount of chromium, one of the elements stabilizing ferrite, increases in the surface layer.

The rate-controlled process of surface layer formation should be considered on the basis of the diffusion process in order to understand the formation mechanism of the surface layer with manganese depletion. The surface layer was formed at 1173 K under vacuum, and the diffusion coefficients D of manganese in ferritic iron and austenitic iron at 1173 K are approximately 5.4×10^{-15} and $3.4 \times 10^{-17}\mathrm{m}^2/\mathrm{s}$, respectively. From these values, the diffusion distances $2\sqrt{Dt}$ after annealing for 3600 s are estimated to be approximately 0.7 and 10 µm for manganese in ferritic iron and austenitic iron, respectively. The latter diffusion distance is comparable to the thickness of the present surface layer although the diffusion coefficients of manganese at 1173 K were simply estimated from the temperature dependence of the

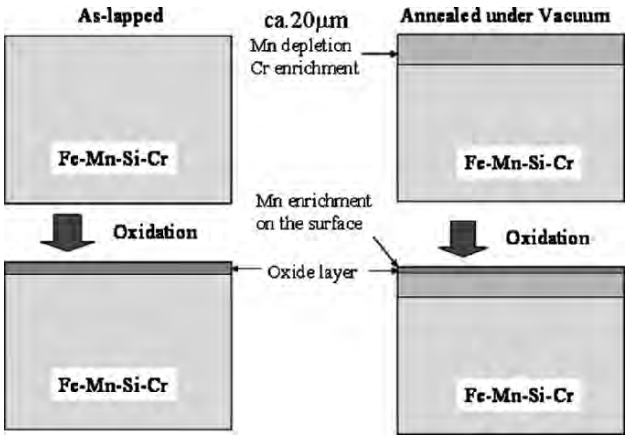

Fig. 7.7. Schematics of the cross-sectional layered structure of (**a**) sample LA, (**b**) sample AN, (**c**) oxidized sample LA, and (**d**) oxidized sample AN

diffusion coefficients of manganese. Therefore, the rate-controlled process of surface layer formation is probably dominated by the diffusion of manganese in ferritic iron.

The alloying elements were redistributed in the surface layer of the Fe-Mn-Si-Cr alloy during oxidation, as shown in Figs. 7.4 and 7.5. Figure 7.7 illustrates the schematics of the cross-sectional layered structure of samples LA and AN as well as the corresponding samples oxidized at 873 K. It is noteworthy that the chemical composition of the nearly 20 μm thick surface layer, which was modified during annealing under vacuum, improved the oxidation resistance of the alloy. Although the characteristic enrichment of manganese is observed on the surface of the alloy during oxidation, the role of manganese enrichment in oxidation appears insignificant. Thus, several characteristic features of elements related to oxidation processes were explained by a combination of different surface analyses.

7.3.2 Selective Oxidation of Less-noble Elements in Surface Layers

Under the above-mentioned oxidation conditions, the constituent metallic elements of the alloy can be reacted with oxygen. On the other hand, a less noble element in iron-based alloys may be selectively oxidized while iron is not oxidized under a low partial pressure of oxygen, as shown in zone (C) of Fig. 7.1. Oxygen then penetrates into an iron-based alloy to react selectively with a less-noble element, and the resultant oxides are distributed in the metallic iron of the surface layer. This phenomenon is referred to as internal oxidation, in which the morphologies of fine oxides formed in a surface layer are influenced by the chemical character, amount of less noble elements, oxidation conditions, etc. [26]. Such a surface layer containing oxides of less

noble elements can be formed in practical steel sheets and thereby influence their surface properties [27–29]. For instance, a surface layer formed on the surfaces of sheets of low-alloyed steel annealed under a low partial pressure of oxygen is known to influence significantly the hot dip galvanized coatings of high-strength steel sheets. The Fe-Si alloys are typical alloy systems, in which internal oxidation is observed. In reality, this alloy system is very important from the viewpoint of steel products since silicon is often added to high-strength steel, high performance silicon steel sheets, etc. An internal oxidation zone formed in the surface layer of silicon steel sheets is controlled in the manufacturing process, particularly in the decarburization process of the alloy, in which the partial pressure of oxygen is adjusted using hydrogen gas and water vapor.

Since the internal oxidation zones were so far analyzed in rough sheets of polycrystalline silicon steel, the details of internal oxidation were not necessarily clarified. However, fundamental processes in internal oxidation have been clarified owing to the characterization of internal oxidation zones formed in smooth single crystalline steel sheets [27, 29]. A flat 0.23 mm thick Fe-3mass%Si steel sheet was produced by the process for grain-oriented silicon steel, which was fully decarburized and secondary-recrystallized under dry hydrogen gas [30]. The chemical composition of the steel is 3.2mass%Si, 0.07mass%Mn, 0.03mass%Cr, and 0.1mass%Sn, and hereafter, it is referred to as Fe-3%Si. The average grain size of this shell sheet was nearly 10 mm in diameter, and single crystal samples were cut from the large grain sheet. The surface orientation of this sheet was nearly (011). The sample sheets were annealed in the temperature range between 948 and 1023 K for 1800 s in 10%H_2-Ar gas containing water vapor, in which the H_2O/H_2 ratio was controlled. As the partial pressure of oxygen is ca. 10^{-15} Pa at 948 K and ca. 10^{-13} Pa at 1023 K in the annealing atmosphere, iron is not oxidized while silicon is. Hereafter, the Fe-3%Si samples annealed at 948 and 1023 K are referred to as samples A and B, respectively.

Figure 7.8 (a), (b) shows the SIMS depth profiles of $CsFe^+$, CsO^+, and Si^- for samples A and B, respectively [27]. The ion counts are plotted on a linear scale as a function of sputtering time, and the level of CsO^+ and Si^- ion counts are adjusted to compare the oxygen and silicon profiles with the iron profile. The $CsFe^+$, CsO^+, and Si^- ions fairly represent the amount of iron, oxygen, and silicon in surface layers, as iron is depleted in the internal oxidation zone in which silicon oxides are formed. The iron-rich layer is observed on the outer side of the internal oxidation zone. It can safely be said from these results that the thickness of the internal oxidation zone increases with an increase in the annealing temperature. The thickness of the internal oxygen zones formed under the present conditions lies in the range of about 0.8–2.5 μm when a sputtering time interval at the half maximum of the CsO^+ ion count is assumed to be the effective thickness of the internal oxidation zone. Although the growth kinetics of internal oxidation is not discussed based only

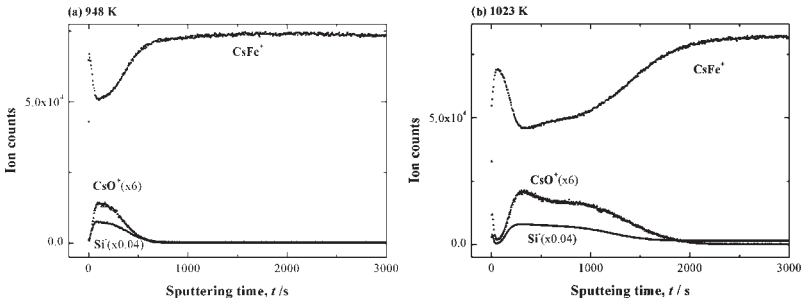

Fig. 7.8. SIMS depth profiles of $CsFe^+$, CsO^+, and Si^- for Fe-3%Si alloys annealed at (**a**) 948 and (**b**) 1023 K

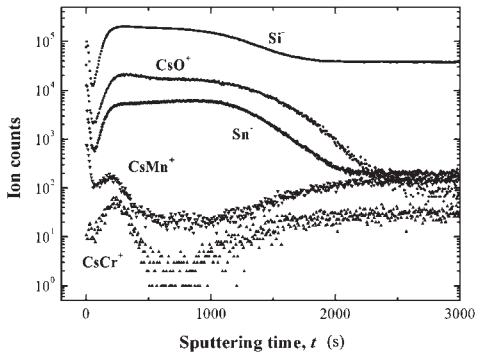

Fig. 7.9. SIMS depth profiles of Si^-, CsO^+, Sn^-, $CsMn^+$, and $CsCr^+$ for an Fe-3%Si alloy annealed at 1023 K. The ion counts are plotted on a logarithmic scale

on these results, these annealing conditions are considered to represent the formation processes of the internal oxidation zone.

Since SIMS is a very sensitive method for the detection of a small amount of elements, the depth distribution of residual elements in the internal oxidation zone is characterized. Figure 7.9 shows the SIMS depth profiles of Si^-, CsO^+, Sn^-, $CsMn^+$, and $CsCr^+$ for sample B [27]. The depth distribution of tin almost corresponds to those of silicon and oxygen, and this phenomenon does not imply that tin is present in silicon oxides. This is because tin is not oxidized under these annealing conditions, and metallic tin is rather segregated at the interface between the iron matrix and silica particles [29]. On the other hand, chromium and manganese, which are oxidized under the annealing conditions, were enriched up to the outer internal oxidation zone. These elements are considered to move to the outside where the oxygen potential is higher than that inside. Although it is noted in the depth profiles that the ion counts of chromium and manganese relevant ions are lower in the internal oxidation zone than the substrate, this may result from the matrix effect, which occurs due to a difference in the formation of secondary ions.

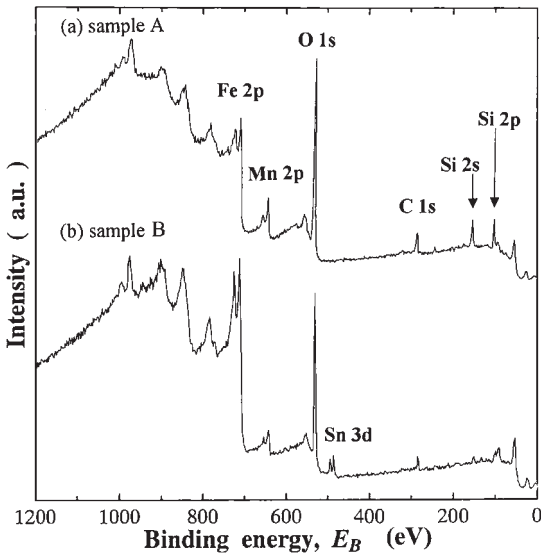

Fig. 7.10. XPS wide-scan spectra from the surface of Fe-3%Si alloy annealed at (**a**) 948 and (**b**) 1023 K

The XPS wide spectra from the surface of samples A and B are shown in Fig. 7.10 (a), (b), respectively [27]. The surface composition was changed by the annealing temperature, although a small amount of contaminated carbon remained on both sample surfaces. Oxygen detected in XPS primarily originates from two types of oxides: some oxide formed during annealing and a native oxide formed by exposure to air after annealing. Oxides of a silicon-manganese and/or silicon-iron system are likely to be formed on the sample surface since silicon and manganese are oxidized during annealing in these conditions [31]. Silicon-rich oxides seem to be formed in sample A annealed at a lower temperature, while the surface composition of manganese in sample A is comparable to that of silicon in sample B annealed at a high temperature. Tin is enriched on the surface of sample B, in which the surface composition of iron increases. This enrichment appears to be related to an iron-rich layer formed beneath the surface. In addition, the O 1s XPS narrow spectra were also studied for characterizing the chemical state of elements by comparison with a database [32]. The dominant peak at approximately 533.0 eV in the O 1s XPS spectra observed in sample A was attributed to the silicon-rich oxide formed during annealing at 948 K, while the dominant peak at 530.5 eV in the O 1s XPS spectra for sample B was considered to arise mainly from a native iron oxide. These results were consistent with those obtained in the XPS spectra of metallic counter elements.

Since fine oxides of less noble elements are formed in a metallic matrix, the diffusion paths of elements in an internal oxidation zone are complicated.

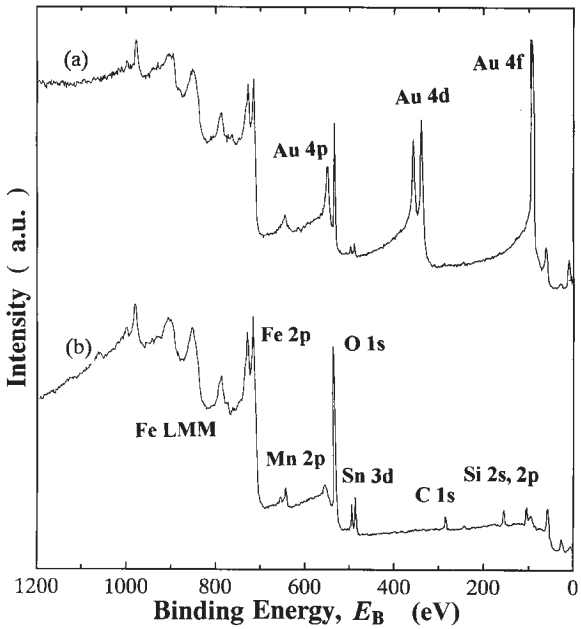

Fig. 7.11. XPS wide-scan spectra from the surface of (**a**) an Fe-3%Si alloy deposited by gold and (**b**) the Fe-3%Si alloy subsequently annealed at 1023 K for 1800 s

In order to study the diffusion path of elements, XPS and SIMS were used for characterizing the elemental distribution in the internal oxidation zones of Fe-3%Si sheets, on which a very thin layer of an inert element, gold, was deposited [33]. Figure 7.11(a) shows a wide XPS spectrum from the sample surface, which was slightly sputtered by argon ions in order to remove contaminated carbon from the surface. The XPS spectrum shows that a very thin gold film is deposited on a Fe-3%Si substrate on which a thin native oxide layer is formed by exposure to air during sample transfer. After the deposition of gold, the samples were annealed in the temperature range between 948 K and 1023 K for 1800 s in 10%H_2-Ar gas containing water, by which internal oxidation occurs. Figure 7.11(b) shows an XPS spectrum of the surface of Fe-3%Si, which was annealed at 1023 K for 1800 s after gold deposition. The result shows that the amount of gold on the sample surface considerably decreases, and the surface composition of the sample is rather comparable to that of a sample without gold annealed under a similar condition, as shown in Fig. 7.9(b). This indicates that while internal oxidation occurs, the deposited gold is diffused into a surface layer of the sample.

In order to compare a SIMS depth profile of gold in the Fe-3%Si sample with that of pure iron, the pure iron samples deposited with gold were

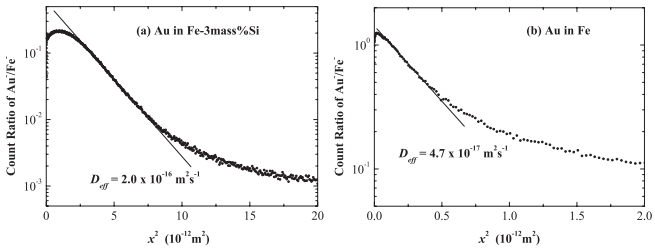

Fig. 7.12. Count ratio of Au^-/Fe^- as a function of the square of the distance of the depth for pure Fe and Fe-3%Si alloy annealed at 973 K

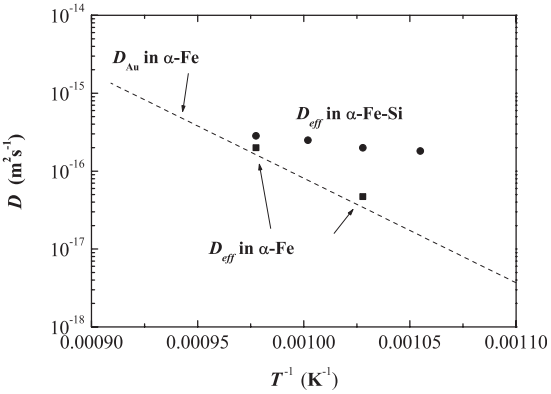

Fig. 7.13. Arrhenius plot of the effective diffusion coefficients of gold in Fe-3%Si alloy and Fe

annealed under an identical condition. The effective diffusion coefficients of gold in surface layers are utilized to evaluate the degree of gold penetration into these samples. At first, a small quantity of gold M is deposited as a thin film on the sample surface. After the sample is annealed for a time t, the diffusion coefficient of gold in the samples is calculated from a slope in a plot of log C vs x^2 [34]. In this study, the concentration of gold was regarded as the ratio of gold to iron ion counts, as the concentration of gold in the surface layer is very small. Figure 7.12 (a), (b) shows the count ratio vs x^2 by using the results of Fe-3%Si and Fe annealed at 973 K for 1800 s, respectively [33]. Although the plot for Fe-3%Si does not simply reveal a linear relation, it may arise from the complicated microstructure formed during internal oxidation. Nevertheless, a linear part is observed in the plot, and it is used for evaluating the penetration of gold. The effective diffusion coefficients of gold estimated in this manner are denoted in Fig. 7.13, which clearly indicates that the penetration depth of gold in the Fe-3%Si alloy is larger than that in Fe. The effective diffusion coefficients of gold obtained at different temperatures are summarized in the Arrhenius plot shown in Fig. 7.13 in order to compare the penetration of gold in Fe-3%Si alloy and Fe. The temperature dependence of

the diffusion coefficients of gold in iron measured in a previous study [35], $D = 21.6\ \exp(-256[\mathrm{kJ/mol}]/\mathrm{k}T)\ [\mathrm{m}^2/\mathrm{s}]$, is also given in Fig. 7.13. The effective diffusion coefficients of gold in iron obtained by SIMS depth profiling are comparable to the results obtained in the previous study. On the other hand, the effective diffusion coefficients for Fe-3%Si alloy are higher than those for Fe, and an apparent activation enthalpy for diffusion of gold in Fe-3%Si alloy is estimated to be ca. 50 kJ/mol. However, the penetration process of gold is not considered to be as simple in internal oxidation because gold penetration is correlated with the selective oxidation of silicon in the surface layer, in which the morphology and distribution of silicon oxides change with the oxidation temperature and time. For instance, the oxidation rate may be suppressed by a layer of silicon oxides that is formed inside and parallel to a sample sheet. Therefore, the apparent activation enthalpy of gold penetration may be correlated with the formation of silicon oxides in a surface layer rather than bulk diffusion of gold in the Fe-3%Si alloy. Indeed, it has been shown that a complicated microstructure is formed in the surface layers of Fe-3%Si annealed under a low partial pressure of oxygen in the previous work [29].

Figure 7.14 illustrates schematic diagrams of cross-sections of the surface layers formed by annealing Fe-3%Si and pure Fe under a low partial pressure of oxygen. Under this condition, fine silicon oxides are formed and interconnected in the surface layer so as to form a network, while iron oxides are not formed in the surface layer. The volume of the surface layer is increased by the penetration of oxygen or the formation of silicon oxides. This volume expansion induces the metallic iron to squeeze out from the surface layer, which causes the formation of an outer iron-rich layer on the surface layer, as shown in Fig. 7.8. In these processes, gold penetrates into the surface layer of Fe-3%Si while the fine silicon oxides are formed. A possible penetration path of gold in Fe-3%Si is likely to be the interface between the matrix and network of silicon oxides since oxygen in the annealing atmosphere is considered to penetrate along the interface.

7.4 Iron Oxides Formed Under Atmospheric Corrosion

Corrosion products of iron-based alloys and steels are formed on the iron surface under a humid atmosphere at around room temperature, and they consist primarily of ferric oxyhydroxides [4]. The structure of the oxyhydroxides is described using various linkages of FeO_6 octahedral units along with hydrogen [37–39]. In addition to such structural information, elemental information is also required to understand the formation processes of the corrosion products. For example, ferrous and hydroxyl ions may be formed in a non-acid aqueous solution by the following reactions [5]:

$$\mathrm{Fe} \rightarrow \mathrm{Fe}^{2+} + 2\mathrm{e}^- \qquad \text{(anodic reaction)} \qquad (7.1)$$

$$\mathrm{H_2O} + 1/2\mathrm{O_2} + 2\mathrm{e}^- \rightarrow 2\mathrm{OH}^- \qquad \text{(cathodic reaction)} \qquad (7.2)$$

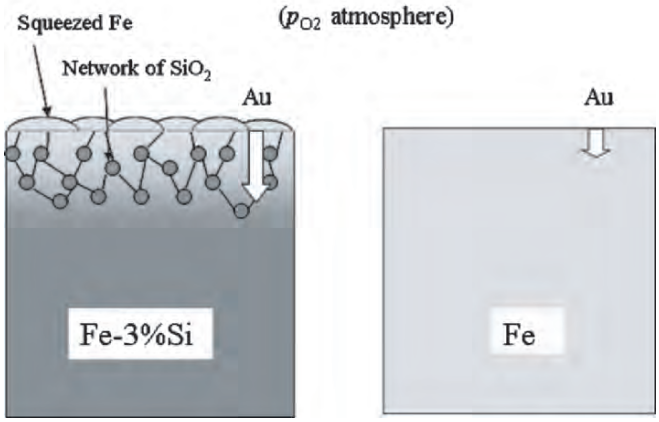

Fig. 7.14. Schematic diagram of the cross section of the surface layer formed in Fe-3%Si alloys by selective oxidation. A network of silicon oxides is formed in the surface layer, and iron is squeezed out from the surface layer

Ferric oxyhydroxides FeOOH are formed or precipitated from these ferrous and hydroxyl ions and dissolved oxygen molecules in an aqueous solution through further reactions. However, since information on the constituent elements–oxygen and hydrogen–in corrosion products or ferric oxyhydroxides appeared to be unclear, surface analytical methods have been used for analyzing thin or fine corrosion products of iron.

7.4.1 Fine Corrosion Products Formed on a Native Oxide Layer

High-purity iron sometimes demonstrates prominent properties as compared to iron that is not as pure since high-purity iron specially prepared by the ion exchange and zone refining technique was found to show an extremely low reaction rate in acid aqueous solutions [40]. Therefore, high-purity iron is one of the promising materials for stable thin films deposited on silicon wafer [41]. High-purity iron is also useful in the study of the formation of a native oxide layer and heterogeneous fine corrosion products on the iron surface by exposure to atmosphere. Angle resolved X-ray photoelectron spectroscopy (AR-XPS) was used for the non-destructive characterization of native oxide layers formed on the surface of high-purity iron and iron-based alloys at room temperature, and the thickness of the oxide layers was systematically evaluated [21, 42]. Furthermore, it is known that fine corrosion products, consisting of oxyhydroxides, are locally formed on the iron surface by exposure to air with normal moisture for a prolonged time. Since conventional XPS and AR-XPS analyses are limited to such a local area, the micro-XPS method has been comprehensively utilized for characterizing fine corrosion products and heterogeneous native oxide layers [43].

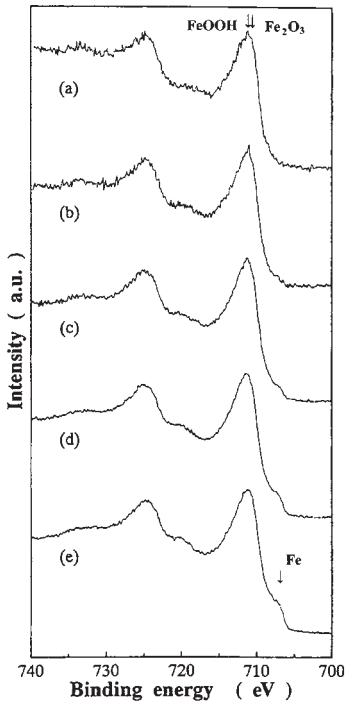

Fig. 7.15. Fe 2p AR-XPS spectra obtained in the take-off angle of (**a**) 15°, (**b**) 30°, (**c**) 45°, (**d**) 60°, and (**e**) 75° for high-purity iron exposed to air

A sheet of high-purity iron was exposed to air with normal moisture at room temperature for 15 years. Fine dark corrosion products along with a native oxide layer were observed on the sample surface. AR-XPS measurements were carried out for analyzing the metallic bright surface of the high-purity iron [43]. The take-off angle, corresponding to the angle between the direction of an electron analyzer and the plane of a sample, was changed from 15° to 75° in the measurements. Figure 7.15 (a)–(e) shows the Fe 2p AR-XPS spectra obtained in the take-off angle from 15° to 75° in steps of 15° for a bright part of the high-purity iron exposed to air. The Fe 2p spectra can be allocated to the signals from Fe (Fe^{3+} oxide (Fe $2p_{3/2}$: 710.9 eV)) and metallic iron (Fe^0 (Fe $2p_{3/2}$: 707.0 eV)). A peak due to metallic iron of Fe^0 is clearly observed for increasing take-off angles from (a) to (e). These results indicate that the metallic iron substrate is covered by an oxide layer, whose thickness of ca. 3 nm is comparable to the inelastic mean free path of X-ray photoelectrons. The relative intensities of the oxide peaks to the metallic peaks in Fe 2p spectra given in Fig. 7.15 are comparable to those for oxide layers formed on the iron surface by air exposure for a short duration of time [42]. Therefore, the chemical state of a high-purity iron surface appears to be almost unchanged with exposure time.

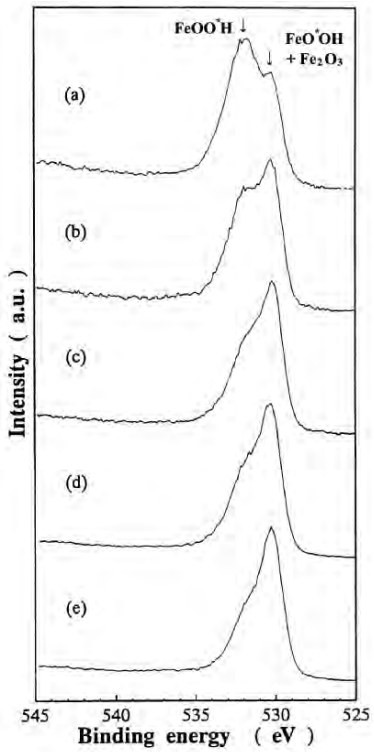

Fig. 7.16. O 1s AR-XPS spectra obtained in the take-off angle of (**a**) 15°, (**b**) 30°, (**c**) 45°, (**d**) 60°, and (**e**) 75° for high-purity iron exposed to air

On the other hand, O 1s AR-XPS spectra for high-purity iron exposed to air are shown in Fig. 7.16. Two peaks are observed in these spectra although the energy resolution in the AR-XPS is not sufficient. These peaks may be assigned to oxygen in an O-H component of ferric oxyhydroxides and oxygen in an Fe-O component of ferric oxides and oxyhydroxides [42]. This indicates that a very thin layer of oxyhydroxides covers a native oxide layer formed on the iron surface.

In order to estimate the layered structure consisting of oxides and oxyhydroxides formed on the surface on the basis of the above-mentioned spectral information, XPS intensities of constituent elements on the sample surface were measured as a function of the take-off angle. Figure 7.17 shows the values of the composition of iron, oxygen, and carbon estimated from the AR-XPS intensities measured for the bright part of high-purity iron exposed to air plotted as marks as a function of the take-off angle. The O 1s XPS spectra were divided into an O-H component and an Fe-O component. The decrease in the composition of carbon with the increasing take-off angle suggests that a very thin contaminated layer of hydrocarbon covers the sample. The take-off

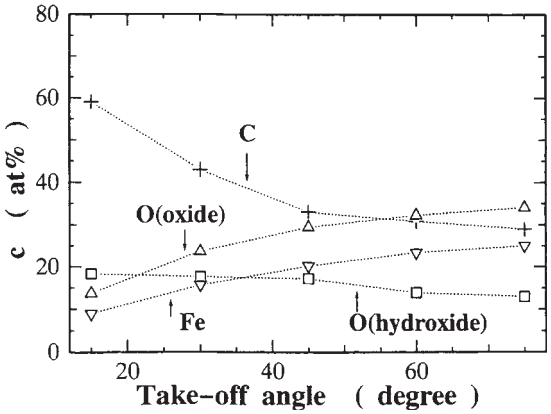

Fig. 7.17. The composition of iron, oxygen, and carbon vs the take-off angle in a high-purity iron sample, which is exposed to air for 15 years. The oxygen composition is divided into two components

angle dependence of the oxygen composition in an O-H component indicates that a layer of oxyhydroxide is formed between the contaminated layer and a native oxide layer. On the other hand, the increase in both the iron composition obtained from Fe 2p and the oxygen composition obtained from a Fe-O component of O 1s with increasing take-off angle may be attributed to the covering of both the oxyhydroxide layer and contaminated layer on the substrate and the native oxide layer. Thus, a thin layer of oxyhydroxides is formed on the native oxide layer with exposure to air over long duration, while the thickness of the native oxide layer is almost unchanged.

Furthermore, X-ray photoelectron imaging by micro-XPS was carried out for studying the two-dimensional distribution of elements in an area in the vicinity of fine corrosion products formed on the surface of high-purity iron. X-ray photoelectrons emitted from an area of 1 mm square were imaged in micro-XPS, in which an X-ray beam of about 20 μm in diameter was scanned. Figure 7.18 (a)–(c) shows an optical micrograph, an O 1s XPS image, and an Fe 2p XPS image from an area around the corrosion products, respectively. The photoelectron intensities of oxygen and iron on the sample surface correspond to a microstructure of fine corrosion products. However, some oxygen enriched part, which may result from the formation of oxyhydroxides, is observed in the bright parts in front of the corrosion products, as denoted in Fig. 7.18(a). This suggests that fine corrosion products heterogeneously grow on a thin layer of oxyhydroxides.

On the basis of the above results, the formation process of layers of oxide and oxyhydroxide, and fine corrosion products on the surface of high-purity iron are summarized, as shown in Fig. 7.19. A native oxide layer is easily formed on the surface of high-purity iron by air exposure [42], and a layer of oxyhydroxide is further formed on the iron surface as shown in Fig. 7.17.

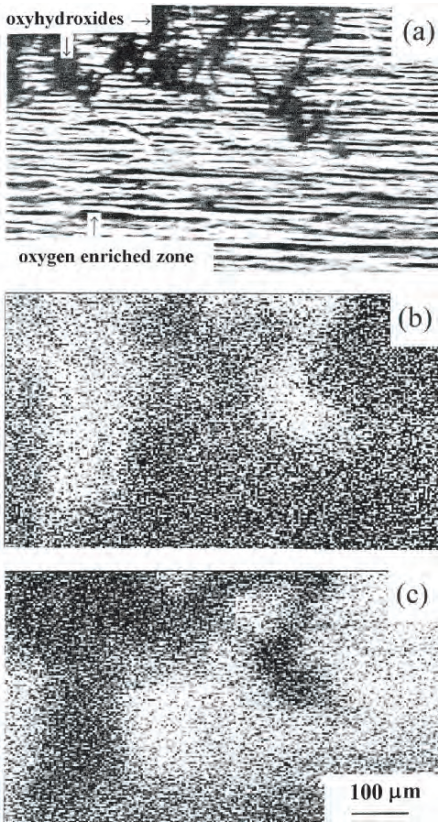

Fig. 7.18. (**a**) Optical micrograph, (**b**) O 1s XPS image, and (**c**) Fe 2p XPS image taken by micro-XPS

Subsequently, fine corrosion products of oxyhydroxide are heterogeneously formed on a layer of oxyhydroxide by air exposure for a prolonged duration, while the thickness of a native oxide layer is almost unchanged. Thus, a combination of AR-XPS and micro-XPS was very effective in the microstructural characterization concerning the chemical information of elements in a surface layer. In particular, these methods are reasonable for analyzing a small amount of oxyhydroxides since they may be easily damaged or decomposed in analytical methods using incident ions and electrons.

7.4.2 Sources of Corrosion Products Formed on Iron Surfaces

Hydrogen in the corrosion products of iron is generated from an aqueous solution, while oxygen originates from aqueous solution and oxygen molecules in air, as described in Eqs. (1) and (2). If hydrogen or oxygen in aqueous solution is labeled with their isotopes, the mass spectra from corrosion products

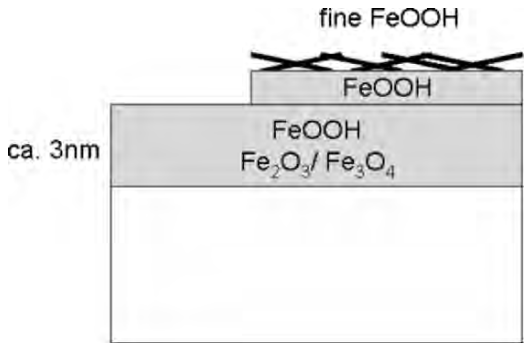

Fig. 7.19. Schematic illustration of the layered structure consisting of oxide and oxyhydroxide formed on the surface of high-purity iron

provide information on the sources of constituent elements of corrosion products. In order to study the formation processes of corrosion products of iron, the mass spectra of ions sputtered from corrosion products were systematically measured using SIMS [44, 45]. The corrosion products were prepared by the reaction of the iron substrate with aqueous solution–H_2O, D_2O, or $H_2^{18}O$–containing a small amount of sodium chloride, which enhances the corrosion of iron.

Sheets of an iron sample of 1 mm thickness were a starting sample, hereafter referred to as sample S. A drip of H_2O, D_2O (99.9%), or $H_2^{18}O$ (95%) solution containing 2 mass% sodium chloride for corrosion enhancement was dropped on the surface of sample S. After the surface of sample S was corroded by the solution at room temperature for about 8.6×10^4 s, the corrosion products formed were dried under an ambient atmosphere. As the corrosion products are non-conductive, most of the corrosion products were mechanically removed from the sample surface. Then, the mass spectra from the corrosion products in close proximity to the corrosion front of the iron substrate were analyzed using SIMS. The corrosion products formed by reaction with H_2O, D_2O, and $H_2^{18}O$ are hereafter referred to as samples H, D, and O, respectively.

In order to distinguish the significant effects of the isotopes on the mass spectra, narrow mass spectra of positive ions from samples H, D, and O are shown in Fig. 7.20 (a)–(c), respectively [44, 45]. The relative counts of different ions of interest should be compared among the different spectra because the amounts of corrosion products and sodium chloride precipitated during drying are not constant in these samples. Ions with mass numbers of 1 and 2 appear to be influenced not only by hydrogen and deuterium in corrosion products but also by residual hydrogen in the ultra-high vacuum analyzer and adsorbed hydrocarbon. Nevertheless, some differences are found in oxygen relevant ion peaks in the spectra. The relative count of ions with mass numbers from 18 to 16 in sample O is clearly higher than those in

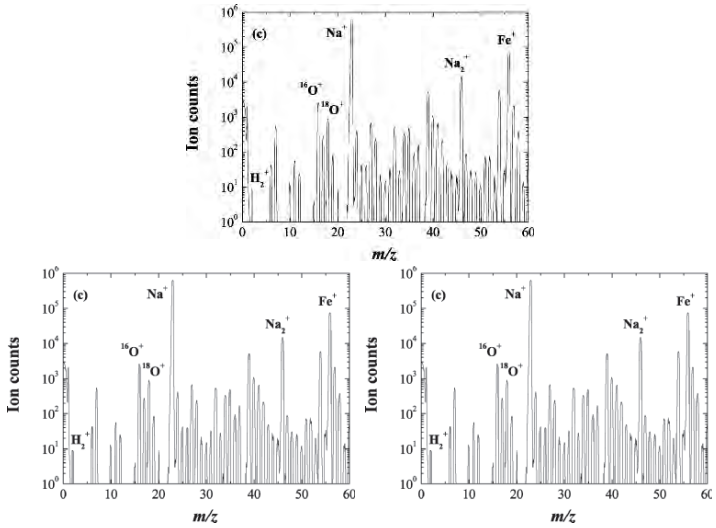

Fig. 7.20. Narrow mass spectra of positive ions from samples H, D, and O

samples H and D. This implies that ^{18}O from an aqueous solution was incorporated in the corrosion products, which were formed by the reaction of the iron surface with $H_2^{18}O$ solution. It is also interesting to note that an ^{16}O positive ion peak is observed with an ^{18}O peak in mass spectra from sample O.

Isotope ions measured by SIMS are also found in the mass spectra of negative ions from samples H, D, and O, as shown in Fig. 7.21 (a)–(c), respectively [44, 45]. The peak of mass number 2 is high in sample D, which is the peak assigned to deuterium ions, although ions of hydrogen molecules are observed as the background in samples H and O. Furthermore, the peaks of mass numbers 18 and 36 in sample O are higher than those for sample H and D, which are assigned to $^{18}O^-$ and $^{36}O_2{}^-$, respectively. The peaks of mass number 19, which is assigned to $^{18}OH^-$, in sample O is also higher than those for samples H and D. Phosphorus relevant ions, such as ^{31}P and ^{31}PO, which arise from residual elements in samples, are observed in the mass spectra of negative ions.

Figure 7.22 (a), (b) shows mass spectra of negative ions from samples H and O, respectively [44, 45]. The effect of the oxygen isotope on the formation of corrosion products is clearly observed in iron-relevant cluster ions in these spectra. Iron cluster ions with single oxygen, such as FeO^- and Fe_2O^-, are particularly effective in distinguishing the two isotopes–^{16}O and ^{18}O–in corrosion products, while iron cluster ions with two or more oxygen atoms give complicated mass spectra for the mixing of the different oxygen isotopes such as FeO_2^- and FeO_3^-.

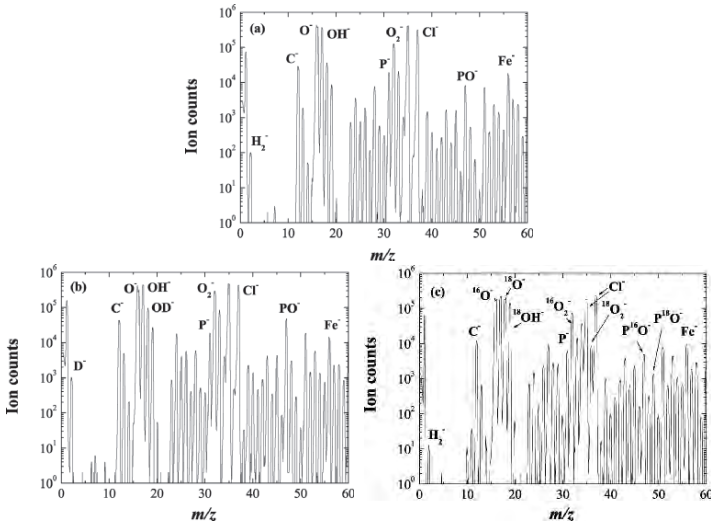

Fig. 7.21. Narrow mass spectra of negative ions from samples H, D, and O

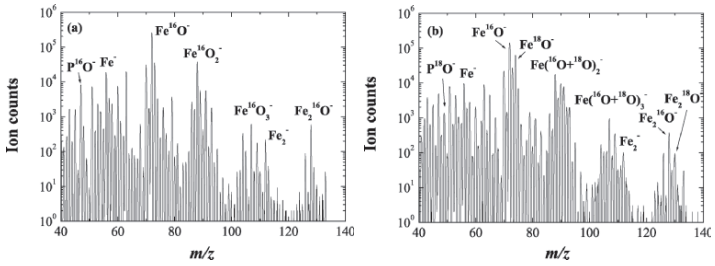

Fig. 7.22. The effect of oxygen isotope found in iron relevant cluster ions in mass spectra of negative ions from samples H and O

The formation processes of corrosion products of iron should be discussed on the basis of the above results. Figure 7.23 illustrates the schematics representing the formation of corrosion products from iron ions (as FeO_6 octahedral unit), oxygen, and hydroxyl dissolved in an aqueous solution as well as the subsequent formation of corrosion products form these supersaturated ions by water evaporation. The structures of corrosion products of iron are shown using the linkage of FeO_6 octahedral units. Ferrous ions are dissolved from the metallic iron substrate and most of them were transformed into ferric ions, whereas oxygen molecules are supplied from air and transformed into hydroxyls in water, as given in Eqs. (7.1) and (7.2). The ferric and ferrous ions are reacted with anions such as hydroxyls to form polycations, which are the resultant corrosion products. In the above experiments, most of the oxygen in air is $^{16}O_2$, and sample O comprises corrosion products formed in $H_2^{18}O$. Then, the hydroxyl in Eq. (7.2) is composed of ^{16}O in air and ^{18}O in

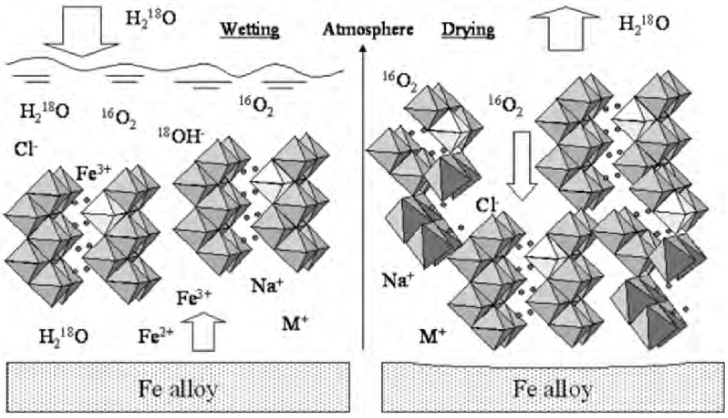

Fig. 7.23. Schematics representing (**a**) the formation of corrosion products from iron ions, oxygen, and hydroxyl in aqueous solution and (**b**) the formation of corrosion products from supersaturated iron ions by water evaporation

$H_2^{18}O$. Thus, the resultant sample O is considered to contain ^{16}O and ^{18}O, as shown in Figs. 7.20, 7.21, and 7.22.

When water–$H_2^{18}O$–containing the corrosion products is evaporated from the aqueous solution, the ferric and ferrous ions in the solution are precipitated. Then oxygen in air easily penetrates in between particles of corrosion products formed beforehand to form additional corrosion products, as shown in Fig. 7.23(b). Thus, the formation process of corrosion products is strongly affected by $^{16}O_2$, and it is for this reason that the ^{16}O relevant ions were largely detected in sample O. Therefore, a careful analysis of the mass spectra of isotope-labeled corrosion products by SIMS is effective in the characterization of the microscopic formation process of corrosion products.

7.5 Summary

Materials are, more or less, interacted with atmospheric gases and liquids, and thereby the materials are sometimes degraded. Typically, iron-based alloys are oxidized and corroded in air and water. Surface analysis methods are used for characterizing chemical products formed through solid/liquid and solid/gas reactions on the alloy surfaces.

The characteristic features of the distribution of several elements in iron-based alloys annealed under varying partial pressure of oxygen were discussed based on the results obtained by the surface analytical methods in this chapter. Some alloying elements, typically chromium, enriched at the surface layer were shown to suppress the oxidation of iron-based alloys. Oxides of a less noble element, such as silicon oxides, are formed in the surface layer of iron-based alloys during annealing under a low partial pressure of oxygen. The

formation of such oxides induces a change in the microstructure of the surface layer. A number of relevant phenomena in iron-based alloys were discussed along with the thermodynamic characteristics of their elements.

In the analysis of corrosion products of iron, it is generally difficult to analyze directly hydrogen in electron spectroscopy. Nevertheless, oxygen bound with hydrogen reveals a characteristic XPS spectrum, which is due to a chemical change in the oxides. Hydrogen is also detected by the mass analysis of the corrosion products, although residual gas may interfere with mass spectra to some extent. In addition, the chemical reactions of corrosion products formed via gas and liquid are studied by analyzing the mass spectra of corrosion products, which are labeled with stable isotopes.

Thus, surface analytical methods are effectively utilized in the understanding of the microscopic mechanism of oxidation and corrosion, whereas morphological and structural results of oxides formed by oxidation and corrosion are complementary to the elemental information. This is because the structures of polymorph compounds, like FeOOH, are distinguished using a structural method. By a combination of the surface analytical method with morphological and structural methods, all the characteristic features of microscopic processes of oxidation and corrosion as well as the roles of foreign elements in the processes become clear.

The author wishes to express sincere gratitude to Professor Y. Waseda for his support in characterization of advanced materials and processing.

References

1. P. Kofstad: *High Temperature Corrosion*, (Elsevier Applied Science, London, 1988).
2. A. S. Khanna: *Introduction to High Temperature Oxidation and Corrosion*, (ASM International, Materials Park, 2002).
3. I. Barin: *Thermochemical Data of Pure Substances*, (VCH, Weinheim, 1989).
4. C. Leygraf, T. Graedel: *Atmospheric Corrosion*, (Wiley Interscience, New York, 2000).
5. R. M. Cornell, U. Schwertmann: *The Iron Oxides*, (Wiley-VHC, Weinheim, 2003).
6. Ph. Refait, M. Abdelmoula, J.-M. R. Génin: Corros. Sci. **40**, 1547 (1998).
7. Ph. Refait, A. Géhin, M. Abdelmoula, J.-M. R. Génin: Corros. Sci. **45**, 659 (2003).
8. D. J. O'Connor, B. A. Sexton, R. St. C. Smart, Ed.: *Surface Analysis Methods in Materials Science*, (Springer Series in Surface Sciences), (Springer-Verlag, Heidelberg, 2002).
9. D. Briggs, M. P. Seah, Ed.: *Practical Surface Analysis, vol.1 - Auger and X-ray Photoelectron Spectroscopy*, second edition, (John Wiley & Sons, New York, 1990).
10. D. Briggs, M. P. Seah, Ed.: *Practical Surface Analysis, vol.2 - Ion and Neutral Spectroscopy*, second edition, (John Wiley & Sons, New York, 1992).

11. J.M. Walls Ed.: *Methods of surface analysis*, (Cambridge University Press, Cambridge, 1989).
12. A. Benninghoven, F. G. Rüdenauer, H. W. Werner: *Secondary Ion Mass Spectrometry*, (John Wiley & Sons, New York, 1987).
13. V. D. Scott, G. Love, S. J. B. Reed: *Quantitative electron-probe microanalysis*, 2nd ed., (Ellis Horwood, New York, 1995).
14. D. Newbury, P. Kchlin, D. C. Joy, C. E. Lyman, E. Lifshin, L. Sawyer, J. R. Michael, J. Goldstein: *Scanning Electron Microscopy and X-Ray Microanalysis*, (Plenum Pub Corp, New York, 2003).
15. C. W. Magee, W. L. Harrington, M. Botnick: Int. J. Mass Spectrom. Ion Processes **103**, 45 (1990).
16. T. Gao, Y. Marie, F. Saldi, H. -N. Migeon: Int. J. Mass Spectrom. Ion Processes **143**, 11(1995).
17. W. Dummler, S. Weber, C. Tete, S. Scherrer: Int. J. Mass Spectrom. Ion Processes **164**, 155 (1997).
18. R. Payling, D. G. Jones, A. Bengtson Ed.: *Glow Discharge Optical Emission Spectrometry*, (John Wiley & Sons, New York, 1997).
19. A. Sato, T. Mori: Mater. Sci. Eng. A **146**, 197 (1991).
20. H. Ohtsuka, H. Yamada, T. Maruyama, H. Tanahashi, S. Matsuda, M. Murakami: ISIJ Inter. **30**, 674 (1990).
21. S. Suzuki, T. Kosaka, H. Inoue, M. Isshiki, Y. Waseda: Appl. Surf. Sci. **103**, 495 (1996).
22. H. Fukai, S. Suzuki, N. Masahashi, S. Hanada, T. Maruyama, H. Kubo, Y. Waseda: Mater. Trans. **46**, 1745 (2005).
23. S. Suzuki, K. Suzuki: Surf. Interface Anal. **17**, 551 (1991).
24. S. Suzuki, M. Wake, M. Abe, Y. Waseda: ISIJ Inter. **36**, 700 (1996).
25. S. Suzuki, T. Kosaka, M. Saito, Y. Waseda, E.Matsubara, M.Oku: Scripta Mater. **36**, 841 (1997).
26. D. L. Douglass: Oxid. Metals **44**, 81 (1995).
27. S. Suzuki, K. Yanagihara, S. Yamazaki, K. Tanaka, Y. Waseda: Surf. Interface Anal. **35**, 276 (2003).
28. S. Suzuki, H. Hasegawa, S. Mizoguchi, Y. Waseda: ISIJ Inter. **43**, 71 (2003).
29. K. Yanagihara, S. Suzuki, S. Yamazaki: Oxid.Metals **57**, 281 (2002).
30. S. Suzuki, Y. Ushigami, H. Homma, S. Takebayashi and T. Kubota: Mater. Trans. **42**, 4201 (2001).
31. S. K. Saxena, N. Chatterjee, Y. Fei, G. Shen: *Thermodynamic data on oxides and silicates*, (Springer-Verlag, Heidelberg, 1993).
32. J. F. Moudler, W. F. Sticle, P. E.Sobol and K. Bomben: *X-ray photoelectron spectroscopy*, (Physical Electronics, Minnesota, 1993).
33. S. Suzuki, K. Yanagihara, S. Yamazaki, Y. Waseda: Mater. Trans. **44**, 1655 (2003).
34. P. G. Shewmon: *Diffusion in Solids*, (McGraw-Hill, New York, 1963).
35. R. J. Borg and D. Y. D. Lai: Acta Metall. **11**, 861(1963).
36. M. A. Blesa, P. J. Morando, A. E. Regazzoni: *Chemical Dissolution of Metal Oxides*, (CRC, Boca Raton, 1993).
37. J. -P. Jolivet, M. Henry, J. Livage, E. Bescher: *Metal Oxide Chemistry and Synthesis*, (John Wiley & Sons, Chichester, 2000).
38. S. Suzuki, T. Suzuki, M. Kimura, Y. Takagi, K. Shinoda, K. Tohji, Y. Waseda: Appl. Surf.Sci., **169-170**, 109 (2001).

39. S. Suzuki, Y. Takahashi, T. Kamimura, H. Miyuki, K. Shinoda, K. Tohji and Y. Waseda: Corros. Sci. **46**, 1751 (2004).
40. K. Sugimoto, S. Matsuda, M. Isshiki, T. Ejima, K. Igaki: J. Japan Inst. Metals **46**, 155 (1982).
41. K. Miyake, K. Ohashi, H. Takahashi, T. Minemura: Surf. Coat. Technol. **65**, 208 (1994).
42. S. Suzuki, Y. Ishikawa, M. Isshiki, Y. Waseda: Mater.Trans.JIM **38**, 1004 (1997).
43. S. Suzuki, K. Yanagihara, Hirokawa: Surf. Interface Anal. **30**, 372 (2000).
44. S. Suzuki, Y. Takahashi, Y. Waseda: Mater. Trans. **44**, 1400 (2003).
45. S. Suzuki, K. S. Kwon, Y. Waseda: J. Surf. Anal. **12**, 223 (2005).

8 Characterization of Rust Layers on a Plain-Carbon Steel and Weathering Steels Exposed to Industrial and Coastal Atmosphere for Years

Katsuhiko Asami

8.1 Introduction

It is well known that corrosion products of iron come in a variety of forms. For example, α-, β-, γ-, δ-FeOOH, Fe_3O_4 and amorphous rust are formed in atmospheric corrosion. They also transform to each other [1]. Low alloy steels form similar rust. In particular, those called weathering steels, which contain small amount of Cu, Ni, P and Cr, have much higher protectiveness against atmospheric corrosion than plain-carbon steel after long-term exposure to atmosphere. The effect of addition of these elements on corrosion resistance is especially clear at sites where concentration of air-born chloride is not very high. However, the mechanism of differences in their protectiveness is not well understood.

Recently, the importance of low-alloy weathering steels has been increasing. Weathering steels are used widely in Japan in large land structures such as iron bridges because of their high protectiveness against weathering and, therefore, their low maintenance cost. When applied to bridges without painting under mild environments, the results are quite satisfying. It is believed that the origin of their protective nature comes from rusts formed during exposure. However, even under a mild atmosphere, their mechanism regarding rust has not been clarified yet. There are also various arguments about the species of rusts and formation conditions of the protective rust layer on weathering steels, and this is not solved fully yet. Okada et al. [2] studied the rust layer formed by air exposure for several years, and surmised that the dense and compact amorphous oxide layer in an inner layer where Cu and P were enriched, and they attributed the Cu and P enriched layer to protectiveness of the weathering steel. Misawa et al. [3] and Yamashita et al. [4] have analyzed the steels exposed to air for 26 years in an industrial area, and reported that γ-FeOOH had been formed at an early stage and changed to amorphous rust, which furthermore changed to α-FeOOH. They also stated that iron species were partly replaced with alloyed Cr and formed more protective rust.

Morales et al. [5] studied the relation between corrosion rate and corrosion products from low carbon steel, and reported that, after long-term corrosion, an increase of the relative magnetite content was observed as the corrosion rate increases. Siddique et al. [6] characterized the rust of mild steel

in a simulated acid rain environment using transmission Mössbauer spectroscopy, and reported that the main corrosion products were identified as α-FeOOH, γ-FeOOH and an amorphous-like substance together with a small amount of γ-Fe_2O_3 (6–8%). Kumar et al. [7], also using Mössbauer spectroscopy, studied a mild steel exposed to SO_2 and SO_2+HCl artificial environments and found α-FeOOH, γ-FeOOH and non-stoichiometric $Fe_{3-x}O_4$. They found that the non-stoichiometric $Fe_{3-x}O_4$ varied with environment and also in internal to external corrosion products and concluded that the non-stoichiometry $Fe_{3-x}O_4$ was an important factor in corrosion protective ability. Okada et al. [8] studied rust formed on weathering steel and mild steel by using Mössbauer spectroscopy at various temperatures from room temperature to 12 K, and explained that the corrosion protective property of weathering steel came from continuous volume distribution of α-FeOOH particles being favorable for accommodating a closely packed structure. Yamamoto et al. [9] found by using transmission electron microscopy (TEM) that the amorphous and the crystalline portions were intermingled in the inner layer of the rust layer of weathering steels exposed to air at a rural area for 35 years. Shiotani et al. [10] analyzed the rust layer formed on the 27-year-old weathering steel bridge exposed at a coastal industrial zone, and reported that γ-FeOOH and β-FeOOH existed in an outer layer and amorphous rust in an inner layer, and that α-FeOOH spread over a wide range of the inner rust layer, that Cr, Ni and Cu were enriched in the inner layer, and that Cu concentrated both at the crack of the inner rust layer and in pits of the steel. Furthermore, Kihira [11], referring to the work by Sakashita and Sato [12], tried to explain the difference in the protectiveness of the rust layer by cation selectivity. Keiser *et al.* [13] studying steels exposed for several years in an industrial area, reported that they found δ-FeOOH in the rust layer and reported that there coexisted about 10% of γ-FeOOH and a small amount of α-FeOOH. Yamashita et al. [14] investigated the properties and functions of protective rust layers formed on weathering steels exposed to air for 17 years in various parts of Japan, and reported that the protective rust layer on weathering steels contained alloying elements such as Cr and Cu, was mainly composed of α-FeOOH type structure, and that the concentration of β-FeOOH and also the rust particle size increased with the increase in the level of air-borne salt. They also suggested that protective properties of the rust layers were related to the suppression of ion transport due to its densely packed structure as indicated by nitrogen adsorption isotherm analysis. Recently, Kamimura et al. [15] characterized rusts which were formed on a weathering steel exposed for 32 years and a mild steel for 15 years in an industrial environment by using Mössbauer spectroscopy and X-ray diffraction (XRD). They suggested that the rust formed on both steels consisted of crystalline α-FeOOH, γ-FeOOH and an amorphous-like phase, and the amount of the amorphous-like phase exceeded 50% of the total amount. The Mössbauer spectra observed at 10 K indicated that the

rust contained α-FeOOH, γ-FeOOH and $Fe_{3-x}O_4$ (γ-Fe_2O_3) for mild steel, and only α-FeOOH and γ-FeOOH for weathering steel. The amorphous-like substance in the rust layer formed on mild steel possessed structures which consisted mainly of α-FeOOH with super-paramagnetism owing to its small particle size and $Fe_{3-x}O_4$ (γ-Fe_2O_3). They observed that $Fe_{3-x}O_4$ (γ-Fe_2O_3) was distributed both in the inner rust layer and in the outer rust layer, and therefore they concluded that the amorphous-like phase in the rust layer formed on weathering steel was mainly α-FeOOH. The present authors [16] studied in detail the distribution of rusts and elements in the rust layer in weathering steels and a plain-carbon steel by X-ray diffraction (XRD) and electron probe microanalysis (EPMA), and reported that the rust layer consisted of three layers; the inner layer, outer layer and outermost layer which was about 3 μm and enriched with atmospheric deposits. It was also reported that the concentration of β-FeOOH was especially high on the skyward surface of all the specimens irrespective of steel composition, and that alloying elements Cu and Cr were enriched in the inner layer of rust as well as Si, while P and Ni did not show any characteristic distribution [16].

Thus, it can be said that details of composition and structure of the rust layer is not easily obtained. Consequently, it is important to characterize the rust layer on the weathering steels in more detail as well as the rust layer on a plain-carbon steel in relation to exposure conditions. In this work, the rust layers formed on plain and weathering steels exposed at a coastal-industrial region for 17 and 18 years were characterized in detail by X-ray diffraction (XRD), electron probe microanalysis (EPMA), scanning electron microscopy (SEM), transmission electron microscopy (TEM), and electron diffraction method (ED), and the results were compared with each other to find the effects of additional elements on the rusts formed. Most of this review is based on the published data [14, 16–20].

8.2 Experimental Procedures

8.2.1 Compositions of Steel Specimens

Four types of weathering steels (Steels B, C, D and E in Table 8.1) and a plain-carbon steel (Steel A in Table 8.1) were exposed to air for 17 years from 1981 to 1998. Exposure sites were Yokkaichi on Route 23 (a coastal industrial region, Site No. = 19) and Mikuni Pass on Route 17 (a rural region, Site No. = 08), in Japan. Two types of steels, a weathering steel and a plain-carbon steel (Steel C and Steel A, respectively, in Table 8.1) were exposed for 18 years from 1981 to 1999 at Ishikari and Arida (coastal regions, Site No. = 01 and 20, respectively) in Japan. Rusts formed on weathering steels and a plain-carbon steel were studied after exposure to atmosphere for respective durations. Details of steels used for the experiments and their chemical analysis data are listed in Table 8.1.

Table 8.1. Chemical compositions of steels

Notation of steel	Steel type	Chemical composition(wt%) C	Si	Mn	P	S	Cu	Cr	Ni	Nb,Ti,V	Remarks
Steel A	SM50	0.17	0.32	1.39	0.016	0.012	–	–	–	–	Plain-carbon steel
Steel B	SMA50AW	0.12	0.39	0.90	0.008	0.006	0.36	0.61	0.22	0.014Nb	
Steel C	SMA50AW	0.11	0.20	0.68	0.014	0.010	0.30	0.51	0.13	–	
Steel D	P-Cu-Cr-Ni	0.06	0.36	1.26	0.091	0.006	0.34	0.35	0.30	0.015Ti 0.05V	Low carbon high P steel with Cr, Ni, Ti, & V
Steel E	P-Cu	0.06	0.53	1.42	0.085	0.004	0.32	–	–	0.02Nb 0.02Ti	Low carbon high P steel with Nb & Ti

8.2.2 Exposure Conditions

Average deposition rates of air-born chloride ions and sulfate ions are listed in Table 8.2 the environmental data being obtained in 1990. During a long exposure time, there would have been some change in the environmental conditions. The deposition rate of Cl^- is expressed as weight of NaCl assuming all Cl^- is in the form of NaCl. Similarly, the deposition of sulfur is expressed as weight of SO_3.

Steel coupons were placed horizontally on weathering test racks under bridges at respective sites and exposed to the atmosphere. Notation of specimens was expressed by a combination of steel name, exposure site number, facing direction (all "horizontal" in this report), and specimen face (skyward or earthward). For example, A19H-b corresponds to a specimen of "Steel A" exposed at Site "19" (Yokkaichi), with its face parallel to the ground (horizontal), "H", and the earthward-side face "b". The measurements for the skyward face "a" were distinguished from those for the earthward face "b" because skyward faces cannot be equal to the earthward faces from the environmental point of view.

8.2.3 Specimen Preparation for Characterization

X-ray diffraction (XRD) and electron probe microanalysis (EPMA) of the surface regions of rusts were carried out without removal of rust from the steel substrates. The surfaces were just cleaned with water.

A Cross-Section of a specimen for scanning electron microscopy (SEM) and EPMA measurements was prepared by embedding the specimen in resin followed by cutting. The Cross-Section was finished by polishing with silicon carbide paper followed by diamond paste polishing, rinsing in distilled water and methanol. Thickness of rust layer was estimated from the Cross-Section images of the rust layer observed by SEM.

Specimens for transmission electron microscopy (TEM) and electron diffraction (ED) were prepared from the thinly polished Cross-Section of rust layer by using the ion milling method. In Fig. 8.1, the process of TEM specimen preparation is shown. The specimen preparation procedure was as follows

Cross-section of resin-embedded specimen was sliced as thinly as possible, and both sides of the Cross-Section of rust layer were polished down to 50 μm thick with SiC paper, followed by rinsing in distilled water and in methanol successively. The 50 μm thick specimen was mechanically polished by a dimpler, followed by ion milling from both sides. During milling, the specimen was cooled by liquid nitrogen.

8.2.4 Characterization Methods

Without removing the rusts from the steels after the surfaces were cleaned with water, rusts on the skyward and earthward surfaces of specimens were

Table 8.2. Environments of the exposure sites in Japan

Site no.	Bridge	Exposure location	Deposition rate of Cl^-, g $NaCl/m^2 \cdot s$	Concentration of Sulfurous acid gas, g $SO_3/m^2 \cdot s$	Distance from coastline, km
01	Ishikari river estuary bridge	Ishikari river estuary, Hokkaido Coastal region	45.8×10^{-8}	–	1.5
08	Oominezawa-bridge	Mikuni Pass,Gumma Pref. Rural mountainous region	1.16×10^{-8}	1.2×10^{-9}	155.0
19	Yokkaichi-overhead bridge	Yokkaichi, Mie Pref. Industrial and coastal region	9.49×10^{-8}	1.26×10^{-8}	1.6
20	Arida-Ohashi bridge	The Kii Channel, Wakayama Pref. Coastal region	18.1×10^{-8}	–	1.8

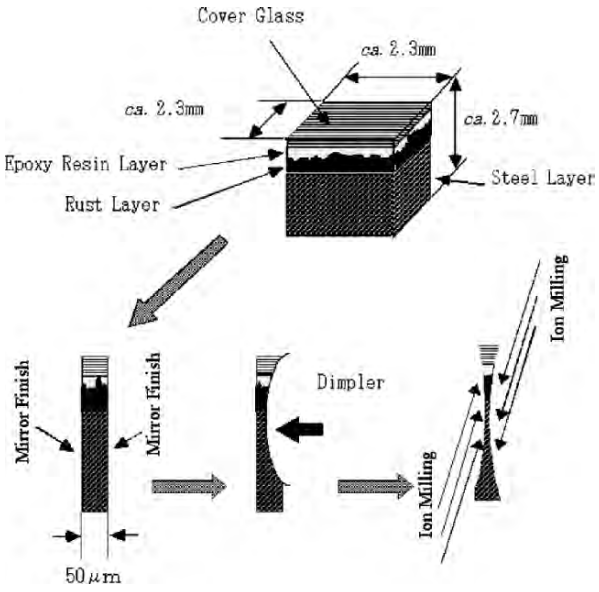

Fig. 8.1. Preparation procedure of TEM specimen [19]

examined by EPMA (JEOL JXA-8621MX) and XRD (Rigaku Rotaflex RU-200B with a rotary Cu target and monochromator of pyrolytic graphite; $\lambda = 0.15148$ nm for Cu Kα). However, the loose components such as very loose rust on surfaces were spalled off easily from the surface of the steels during handling and specimen preparation, and therefore their data were not included. XRD measurement was carried out by fixed glancing angle incidence XRD method (α-2θ method). The X-ray incidence angle α was fixed at 10°.

Composition of the rust layer from the surface to about 1 μm deep was obtained by EPMA measurements from the surface. For compositions at deeper regions in the rust layer, the Cross-Section was also analyzed by EPMA. For EPMA measurements, a wave length dispersive X-ray spectrometer was used. The electron acceleration voltage was 20 kV and the incident electron beam current was 50 nA. Pentaerythritol (PET) crystal was used for measurements of P, S, Cl, K, Ca, Ti, Cr and Mn, thallium acid phthalate (TAP) crystal for Na, Mg, Al and Si, and lithium fluoride (LIF) crystal for Fe, Ni, Cu and Zn. Quantitative analysis was carried out by a standardless method with ZAF (atomic number, absorption, fluorescence) matrix correction using intensities of Kα lines of all the detected elements in the rust layer except oxygen. Moreover, the data were normalized by taking the sum of the detected elements except oxygen as 100%. Quantitative and ZAF correction softwares used in this experiment were XM-86PACWE and XM-86PACZAF, respectively, which were installed to the EPMA apparatus. A mean value of a set of

data at different five positions on the same surface of a specimen was taken as an EPMA analysis result.

The elemental distribution in the Cross-Section of rust was also quantitatively measured by EPMA. The EPMA measurements in the Cross-Section of rust were done at the position where the thickness of rust layer was largest or the most corroded region within the Cross-Section of 3 cm in length. Two-dimensional distribution of the major elements for a region of 200 μm or 250 μm square was first measured by mapping method, and the data was converted to depth profiles by summing up all the counts parallel to the steel surface. The background counts of the mapping data were subtracted for quantitative estimation. Components of rust in the rusted layer were determined by electron diffraction (ED) for the plain-carbon steel specimens (A19H-a and A19H-b) and weathering steel specimens. Morphology of the rust components was examined by transmission electron microscopy (TEM).

For TEM observation, JEOL 200EX was used at an acceleration voltage of 200 kV, with a 0.6 μm selected area aperture. The proportion and distribution of goethite (α-FeOOH), akaganéite (β-FeOOH), lepidocrocite (γ-FeOOH), magnetite (Fe_3O_4), and amorphous rust were identified by ED patterns. Since maghemite (γ-Fe_2O_3), which could be formed by dehydration of γ-FeOOH, cannot be distinguished from magnetite by ED, it was simply expressed as magnetite if it existed.

The abundance of each rust was semi-quantitatively estimated by comparison with ED intensities of respective pure rusts by the naked eye, and classified into five levels, that is, the most intense, intense, medium, faint and zero intensities of ED patterns were allotted to abundances 10, 6, 3, 1 and 0. These values were converted to percentage by taking the sum of abundances of all rust components as 100%. Observation was carried out at 40–480 points on a thin portion around a hole for each specimen where the electron beam can pass through. By controlling the size of a hole, it was possible to observe the whole depth range of the rust layer from the surface to the interface between the rust layer and the steel. For very thick rust, observation and ion-etching were repeated several times to observe the whole thickness range as shown in Fig. 8.2, where TEM/ED observation were carried out along the edges of pit holes of the TEM/ED specimen shown in numbers in circles. In thin specimens, we did not need to repeat the ion etching. For specimens exposed to environments that were not too severe, two parts of the rust layer were clearly distinguished, that is, a thick part and a thin part of the rust layer as shown in Fig. 8.3. We therefore observed each part separately to obtain information at each point.

Other than the five components listed above, a rust corresponding to $(FeOOH)_3{\cdot}(Fe_2O_3)_4$ was also observed occasionally, but it was found to be an artifact caused by heating of rust during specimen preparation for TEM by the ion milling method when cooling was insufficient. Therefore, when

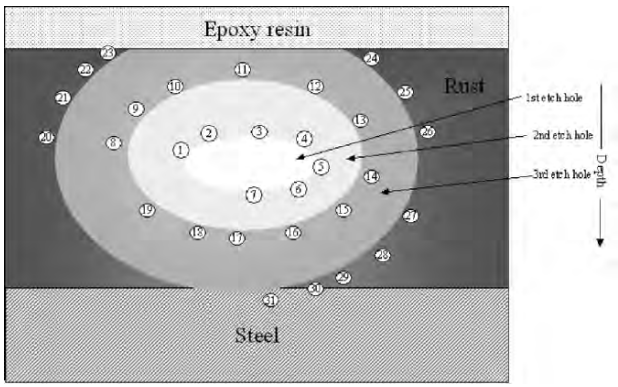

Fig. 8.2. Schematic illustration of a TEM specimen and observation points

$(FeOOH)_3 \cdot (Fe_2O_3)_4$ was found, we discarded the specimen and prepared a TEM/ED specimen again from another part.

8.3 Results

8.3.1 SEM Observation of Cross-Sections of Rust Layers

As shown in Fig. 8.3, it can be seen that corrosion proceeds deeply in part but it does not develop at another place, and accordingly the thickness of rust layer varies in different places. The rust layer thickness shown in Fig. 8.3 does not correspond to real corrosion depth because the loose rust layer on the surfaces had been removed when the Cross-Section was prepared. But for specimens exposed at Sites 08 and 19, exfoliation was trivial. On the other hand, on the rust formed at Sites 01 and 20, a number of parts were exfoliated. In Fig. 8.3 there are many cracks. However, most of the cracks between the steel and rust are artifacts. The average corrosion rate of a plain-carbon steel (Steel A) at the industrial coastal region (Site 19) was $4.2 \times 10^{-13} \mathrm{m} \cdot \mathrm{s}^{-1}$, and that of a weathering steel (Steel B) was $3.0 \times 10^{-13} \mathrm{m} \cdot \mathrm{s}^{-1}$, and those values at Site 08 were reported as $1.3 \times 10^{-13} \mathrm{m} \cdot \mathrm{s}^{-1}$ and $0.93 \times 10^{-13} \mathrm{m} \cdot \mathrm{s}^{-1}$, respectively [21]. The ratio of corrosion rates of Steel A to Steel B can be calculated as about 1.4 at both the industrial coastal region and the rural mountainous region. The maximum thickness of the rust layer of Steel A at the rural mountainous region is 165 μm, and 115 μm for Steel B; that is, the thickness ratio is 1.44, which is almost equal to the ratio of the corrosion rates. At the industrial coastal region, the thickness of the rust layer on Steel A is 142 μm, and that on Steel B is 150 μm. This results in the ratio of rust layer thickness being 0.95, indicating that the rust layer on Steel A (a plain-carbon steel) easily spalled off from the surface, and the measured thickness of the rust layer on Steel A appeared thin whereas that on Steel B did not exfoliated because of high adhesiveness.

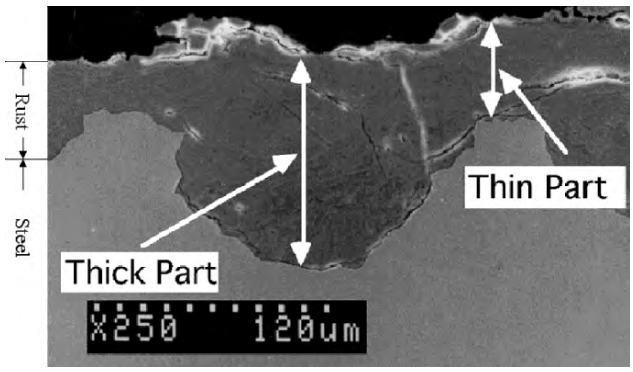

Fig. 8.3. An example of cross section of rusted steel showing thick and thin parts of rust layer [18, 19]

At Sites 01 and 20, Steels A and C were exposed for 18 years. The average corrosion rates of Steels A and C at Site 01 were 7.95×10^{-13} and $7.29 \times 10^{-13}\mathrm{m} \cdot \mathrm{s}^{-1}$, and at Site 20, 4.02×10^{-13} and $3.21 \times 10^{-13}\mathrm{m} \cdot \mathrm{s}^{-1}$, respectively. The deposition rate of chloride at Site 19 (coastal and industrial region) was about half of that at Site 20 (coastal region), and yet the average corrosion rate was almost the same. It might be the additional effect of high sulfurous concentration at Site 19 in comparison to other exposure sites. At Site 01, the deposition rate of chloride was very high. It resulted in very high average corrosion rates. The corrosion rate for Steel C (a weathering steel) was almost the same as that of Steel A. It means that under a very high deposition rate of chloride, even a weathering steel cannot form a protective surface rust layer, and a large part of the rust layer was easily spalled off from the surface. The deposition rates of chloride ions at Sites 01 and 20 should be over the tolerable level even for weathering steels.

8.3.2 XRD Analysis of Rust Surface

X-ray diffraction (XRD) patterns were obtained from rust layers of exposed specimens without removing the substrate. The incident angle of the X-ray was fixed at 10°, and the depth of the rust layer where diffraction signal comes from is limited to ca. 1.2 μm under the assumption of a completely flat surface [22]. Since the analyzing depth of XRD is not more than 2 μm, the XRD measurements give information only at the surface region of the rust. There was no clear difference between XRD patterns of rust layers formed on a plain-carbon steel and those on weathering steels. However, there was a clear difference in XRD patterns between the skyward and earthward surfaces. The averaged XRD patterns of the skyward surfaces and those of earthward surfaces of all specimens exposed for 17 years at Site 19, and the differential diffraction pattern between the skyward and earthward surfaces, are shown in Fig. 8.4, where XRD patterns of the standard substances,

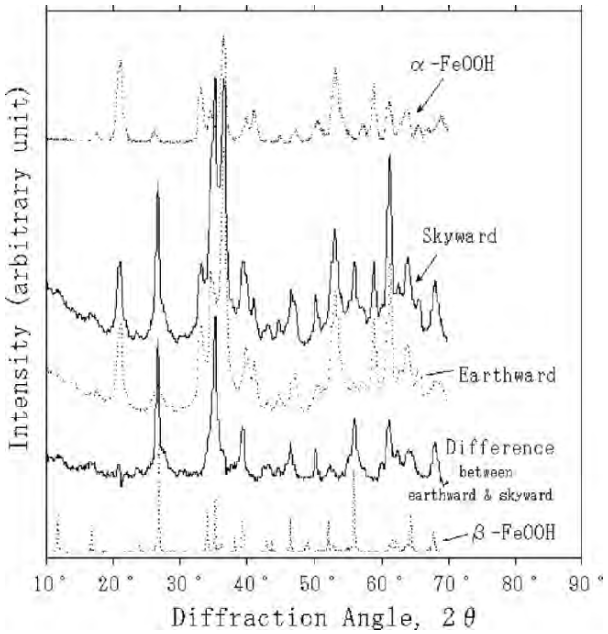

Fig. 8.4. X-ray diffraction patterns from the rust surfaces on skyward, earthward, and difference between earthward and skyward. X-ray diffraction patterns of standard α-FeOOH and β-FeOOH are also inserted for comparison [16]

goethite (α-FeOOH) and akaganéite (β-FeOOH) are also plotted. The main difference in XRD pattern between the skyward and earthward surfaces exists between $2\theta = 30°$ and $40°$ where the pattern obtained from earthward surfaces has two strong peaks while the rust layer on skyward surfaces has only one strong peak. As can be seen clearly in Fig. 8.4, the main constituent is α-FeOOH in both the skyward and earthward surfaces. In addition, β-FeOOH and lepidocrocite (γ-FeOOH) also exist although the pattern of the standard γ-FeOOH XRD pattern is not shown in Fig. 8.4. There is an apparent difference between the XRD patterns of skyward and earthward surfaces. By comparing with the standard XRD patterns, it can be seen that the differential pattern between the skyward and earthward surfaces corresponds almost to β-FeOOH, that is, all specimens contain more β-FeOOH on the skyward surfaces. It can be said that the concentration of β-FeOOH was especially high on all the specimens irrespective of steel compositions. Similar results were obtained for specimens exposed at Site 08, Mikuni Pass.

Magnetite was not detected on both surfaces. As mentioned above, the incident angle of the X-ray was fixed at 10°, and the depth of the rust layer where diffraction signal can be obtained is limited to ca. 1.2 μm. The sampling depth by XRD will be much less than the total rust layer thickness although there is remarkable unevenness in the sample surface. The results shown in

Fig. 8.4 are, therefore, the results of the rust layer in the range of 2–3 μm from the top surface at maximum even if we consider the unevenness in the sample surface. It means, therefore, these results does not deny the existence of magnetite (Fe_3O_4) underneath. The rust layer in the deeper region should contain different species from those in the surface region observed by XRD.

8.3.3 EPMA Analysis of Rust Surface

The average concentrations of main elements except Fe and O detected by EPMA on the surface regions of the rust layer are shown in Fig. 8.5 (a), (b) for specimens exposed at Site 08 (Mikuni Pass) and at Site 19 (Yokkaichi), respectively. The concentration values shown in Fig. 8.5 are those normalized to 100 at% for all the elements detected except oxygen, and they are also averaged for all steels.

At Mikuni Pass (Site 08), Cl and Ca are remarkably concentrated on skyward surface in comparison to the earthward surface. The environmental data at all exposure site were those obtained in 1990. The environmental data at Site 08 in Table 8.2 suggest no such large concentration of Cl and Ca values. The biggest change in environmental conditions at Site 08 during exposure will be the usage of calcium chloride for melting snow on the roads during winter. It is well known that calcium chloride is often used for the purpose. Actually, there is a large amount of snowfall in the region of Site 08 during winter. Some fraction of the calcium chloride may have come down on the exposure racks as droplets rather than aerosol. If chloride ions had come as aerosol, it should have deposited on both side equally. The concentration of Na is very low in comparison with Cl while that of Ca is comparable to Cl at Site 08 indicating the origin of Cl is certainly calcium chloride rather than NaCl. Probably, data shown in Table 8.2 did not take the chloride sprayed on road during winter into the Cl^- deposit measurement. On the other hand, in the data at Yokkaichi (Site 19) shown in Fig. 8.5 (b), the concentration of Na is almost equal to that of Cl indicating its origin is NaCl from the ocean.

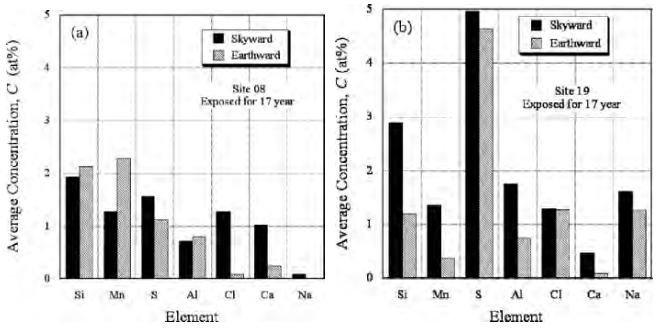

Fig. 8.5. EPMA results of the rusts on the skyward and earthward surfaces of steels exposed at (**a**) Mikuni Pass (Site 08) and (**b**) Yokkaichi (Site 19) for 17 years [16]

Actually, the distance from the ocean to Site 19 is only 1.6 km as shown in Table 8.2. Moreover, NaCl should be assumed to be very fine particles or aerosol because both Na and Cl appear almost equally on both the earthward and skyward surfaces.

Concentrations of S on specimens exposed at Site 19 are about four- to five fold of that at Site 08. This is reasonable because the SO_3 concentration in air at Site 19 is very high as shown in Table 8.2. However, the concentration of S measured on specimens at Site 08 is also high in comparison with the SO_3 concentration in air as shown in Table 8.2. The concentration of S at Site 08 cannot be realized from the SO_3 concentration in air. Its origin is, therefore, unable to be attributed to SO_3 gas in air. It can be derived from MnS in steels since concentrations of Mn and S are approximately equal on specimens exposed at Site 08.

Nickel and chromium were found only on steels which contain them as alloying elements. On specimens exposed at Site 08, Cu was detected only on a few specimens. On the other hand, Cu was detected on all the Cu-containing specimens exposed at Site 19. This is because the analyzing depth of EPMA is usually ca. 1 μm. Measurements from the top surface give information of only the surface region of rust. Distribution of elements may well depend on structure and conditions when rust is formed. To obtain more information, we need measurements from inside the rust, or from a Cross-Section of the rust.

8.3.4 EPMA Analysis of Cross-Section of Rust Layers

In order to examine the depth distribution of elements in rust layers, EPMA measurements through the Cross-Sections of specimens were carried out. Mapping of elements in the Cross-Section of rust layer was measured first. The results of mapping showed that the distribution of elements in rust layers did not show the complete layered structure. However, the rust showed a kind of layered-like structure. Therefore, mapping of elements was converted to quantitative depth profiles to show clearly the depth distribution of elements. For conversion from mapping data into depth profiles, background counts were removed, and then counts of respective elements were added to the direction parallel to the surface. By removal of background counts, the accuracy of the quantitative measurements was markedly improved. An example is shown in Fig. 8.6, where the mapping image of Ni Kα on the Cross-Section of rust formed on specimen B19H-a is illustrated. The line profile shown in Fig. 8.6 does not exactly represent the concentration profile, but only shows detected intensity profile. In order to convert it into a real depth profile of concentration, not only normalization of the intensity but also more corrections were given to the intensity such as ZAF corrections.

The converted and corrected depth profiles are shown in Figs. 8.7–8.10, where data are obtained from the skyward and earthward sides of rust layers

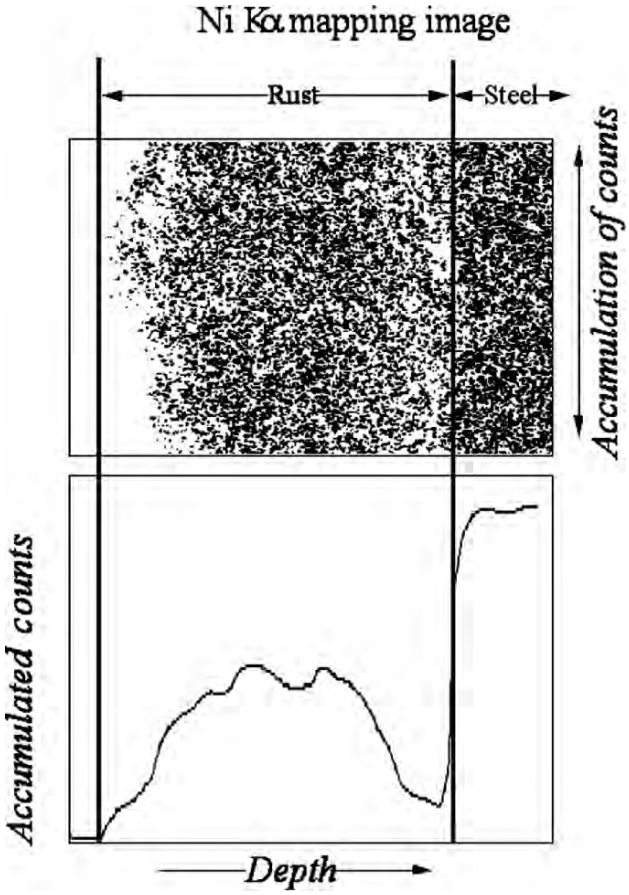

Fig. 8.6. An example of mapping measurement of an element and its conversion to a line profile

formed on the plain-carbon steel (steel A) and the weathering steel (steel D) exposed at Site 19 for 17 years. Roughly speaking, it can be seen that a rust layer consists of inner and outer layers. On the skyward rust layer of Steel A (a plain-carbon steel), Cl, Mn and S distribute mainly in the outer layer, and Si in the inner layer. On the earthward rust layer on Steel A, the situation is similar. However, distribution of Cl is rather uniform and its concentration is low.

On the weathering steel specimen D19H, Cl and Na are situated in the outer layer. Na is specifically in the outermost position. Similar to Steel A, Mn is distributed mainly in the outer layer, and Si in the inner layer. In Steel D, Cr, Cu, P and Ni are present. Those elements also appear in the rust. Among them, Cr and Cu are clearly distributed in the inner layer, while Ni and P are rather uniformly distributed over the whole layer although their

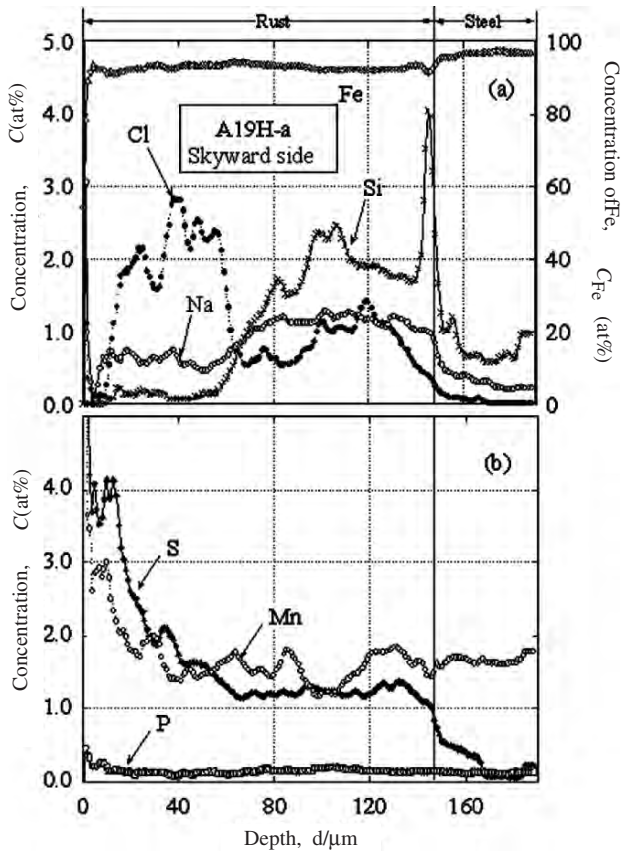

Fig. 8.7. Depth distribution of elements in the rust formed on A19H-a specimen [16]

distribution is slightly biased towards the inner direction, that is, in the inner layer. Sulphur also does not show a clear deviation of distribution.

It was found that the results were essentially the same when exposed at the Mikuni Pass, a rural mountainous region. Moreover, almost the same results were obtained for the other steels shown in Table 8.1. Looking at the depth profiles we can see that every element shows a sharp increase in concentrations at the surface except for the Fe profile.

The structure of rust layer on a weathering steel is estimated from all the above observation and the analysis of the rust layer surface, and is schematically illustrated in Fig. 8.11, where the distribution of the detected elements except Fe, O, Ni and P is shown. It is well known that Ni and P are important elements which impart a protective function to the weathering steel. However, they are omitted in the figure because their distribution is rather flat and does not show clear enrichment in a special layer. Thus, rust consists fundamentally of three layers, the outermost layer with a thickness of ca. 3 μm or less, an outer layer, and an inner layer.

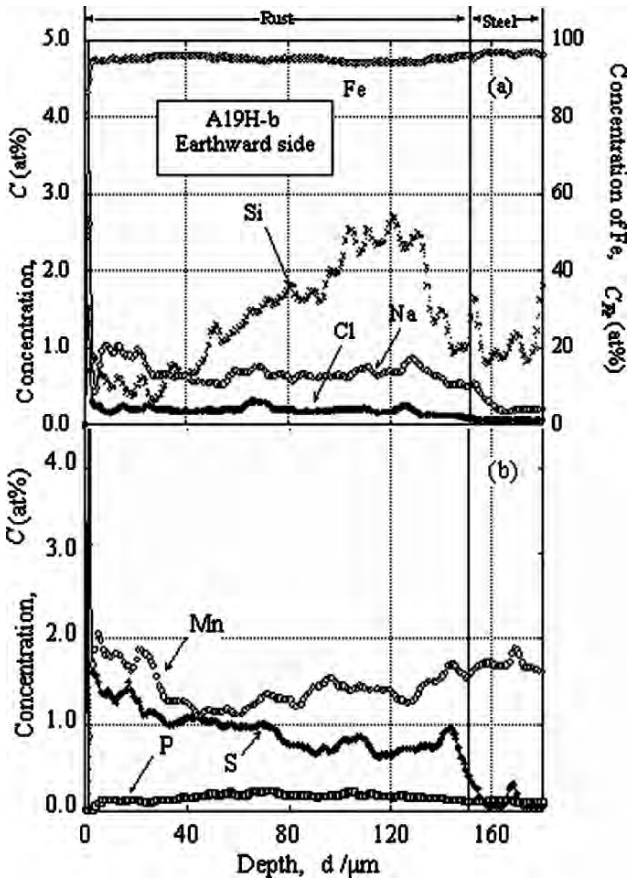

Fig. 8.8. Depth distribution of elements in the rust formed on A19H-b specimen [16]

The thicknesses of an outer layer and an inner layer depend on steels, sides (skyward-side or earthward-side) and the environment of the exposure sites. Thickness of inner layer did not seem sensitive to the side of surface, that is, there was no large difference between inner layer thicknesses of the skyward and earthward surfaces. The thickness of outer layer was, however, dependent on side; the thickness was smaller on the earthward-side surface than on the skyward-side surface.

Concentration of Mn is generally high in the outer layer. In steels, manganese existed as MnS particles. When the concentration of SO_2 is low in the exposure environment, most of the S in the rust layer can be explained by S that comes from MnS in steels. However, distributions of Mn and S in the rust layer were not in accordance because MnS reacts with air easily and forms stable substances in the rust layer. When the concentration of SO_2 is

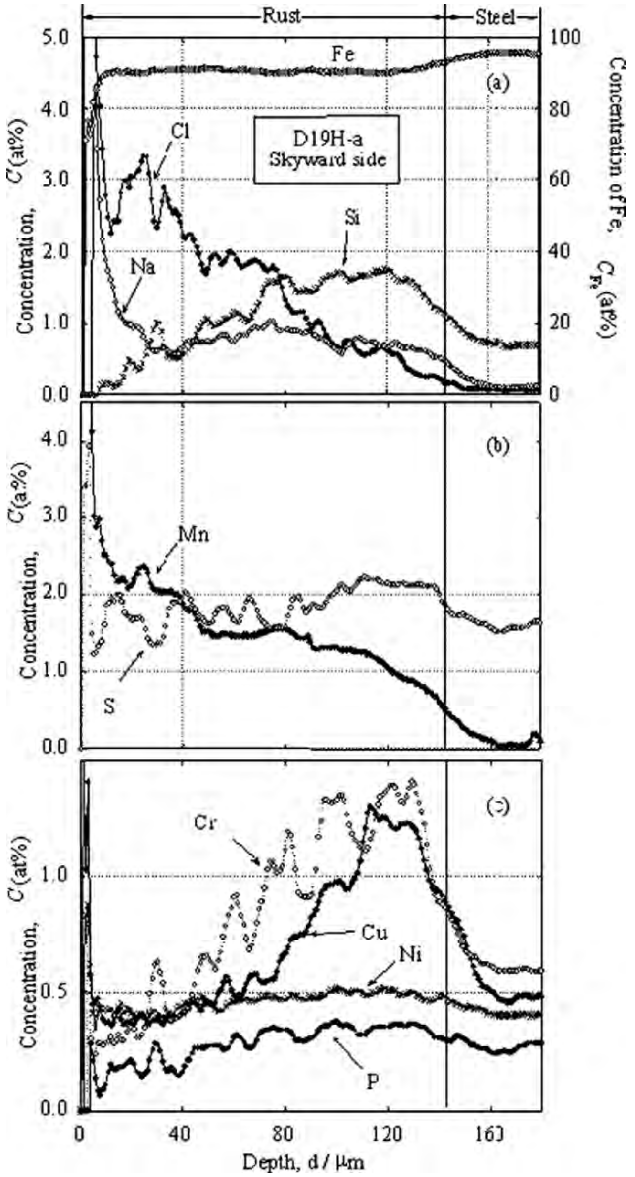

Fig. 8.9. Depth distribution of elements in the rust formed on D19H-a specimen [16]

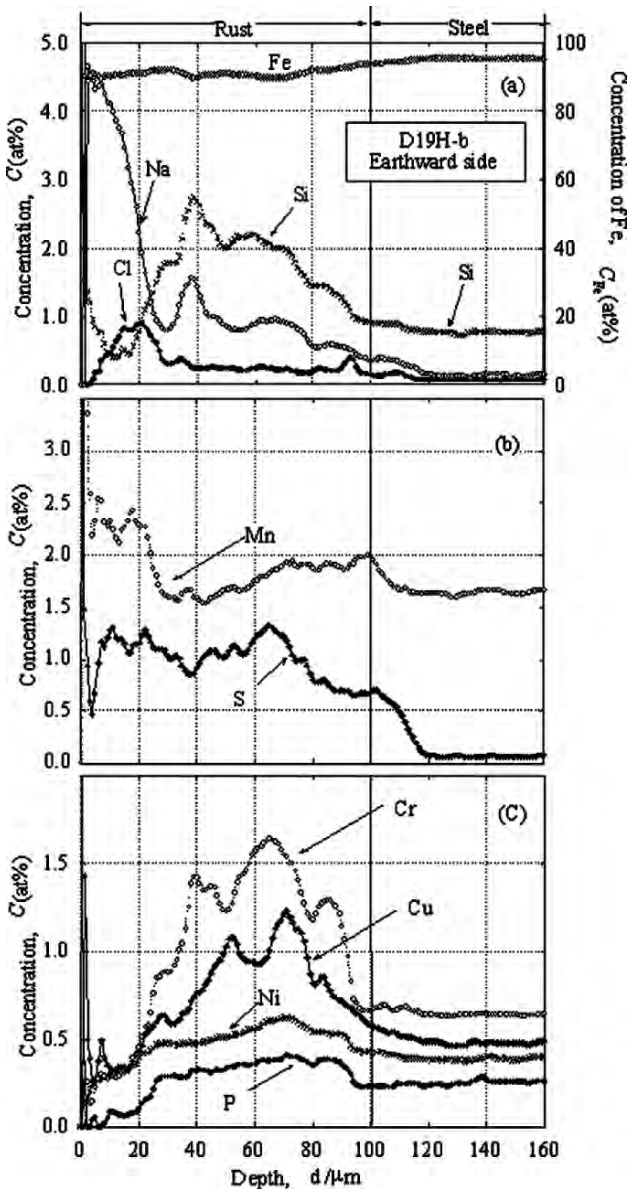

Fig. 8.10. Depth distribution of elements in the rust formed on D19H-a specimen [16]

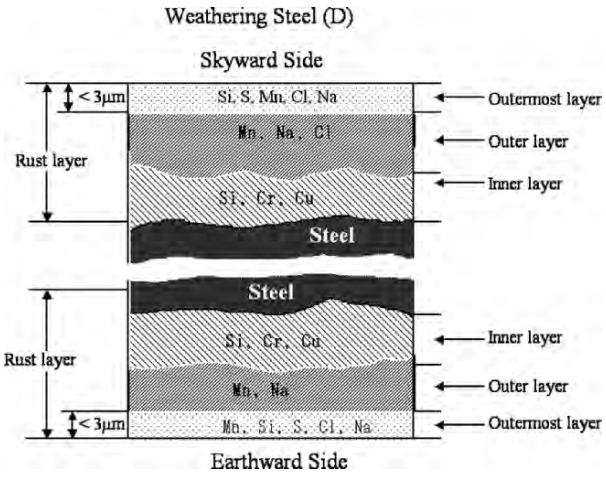

Fig. 8.11. Schematics of cross section of rust on a weathering steel

high in the environment, sulfur in the rust layer originated not only from MnS in the alloy, but also comes from the environment.

8.3.5 TEM/ED Analysis of Cross-Section of Rust Layers

An example of low magnification TEM image of a specimen with an array of observed positions is shown in Fig. 8.12. Numbers attached in the image correspond to the observation points by TEM and ED. At each observation point, ED patterns were obtained and analyzed. In Fig. 8.12, the rust layer thickness is ca. 145 μm. An example of distribution and abundance measurements from ED intensity is shown in Table 8.3 where intensities are semi-quantitatively judged from comparison with ED intensities of respective pure rusts by the naked eye. The intensities were simply classified into five levels, that is, 0, 1, 3, 6 and 10. The example shown in Table 8.3 is the data obtained from a rust layer (61 μm thick) on C19H-a specimen, where α, β, γ, M and A represent α-FeOOH, β-FeOOH, γ-FeOOH, magnetite and amorphous rust, respectively. Intensities were normalized to percentage by taking the sum of intensities of α, β, γ, M and A to be 100%.

In Fig. 8.13 (a)–(e), TEM images of α-FeOOH, β-FeOOH, γ-FeOOH, magnetite and amorphous rust are shown. Selected area electron diffraction (ED) patterns corresponding to the respective TEM images are also shown in Fig. 8.13. The TEM images are all obtained from the plain-carbon steel.

α-FeOOH consists of fine crystallites. It can be observed that their grain sizes are several nm and more, and it is a very fine fibrous structure. They are intricately entangled. On the other hand, β-FeOOH is belt-like shaped, several nm in width and several μm in length. The β-FeOOH image shown in Fig. 8.13 (b) is only a small part of long fibres of rust. These fibres extend

Table 8.3. Distribution and abundance of α-FeOOH, β-FeOOH, γ-FeOOH, magnetite and amorphous rust judged from electron diffraction intensities for a thin rust part on C19H-a specimen

Position(μm)				M	A	Position(μm)				M	A	Position(μm)				M	A
0	6	0	0	6	0	18.6	6	0	0	3	0	41.3	6	0	0	0	6
1.2	6	0	0	6	0	19.3	6	0	0	1	0	42	0	0	0	3	6
3.4	10	0	0	0	0	20.3	10	0	0	0	0	42.4	1	0	0	0	6
3.7	6	0	0	3	0	23.0	6	0	0	1	0	44.7	0	0	0	3	6
3.9	10	0	0	0	0	25.1	6	0	0	1	0	47.4	6	0	0	0	6
5.2	10	0	0	0	0	26.4	6	0	0	3	0	48.8	6	0	0	0	3
5.8	6	0	0	3	0	28.4	6	0	0	0	0	51.5	6	0	0	0	6
7.3	6	0	0	1	0	29.8	10	0	0	0	0	54.2	3	0	1	0	6
7.8	6	0	0	1	0	33.8	6	0	0	1	0	56.9	6	0	1	0	6
8.5	6	0	0	1	0	33.9	3	0	6	1	0	58.3	6	0	3	0	3
12.2	10	0	0	0	0	36.6	10	0	0	0	0	59	6	0	0	1	3
14.9	6	0	0	1	0	37.3	6	0	0	3	0	59.6	6	0	0	1	3
16.6	6	0	0	1	0	38.0	6	1	0	0	0	61	0	0	6	1	3
17	10	0	0	0	0	40.7	6	0	0	3	3	Metal	-	-	-	-	-

α: α-FeOOH, β: β-FeOOH, γ: γ-FeOOH, M: magnetite, and A: amorphous rust

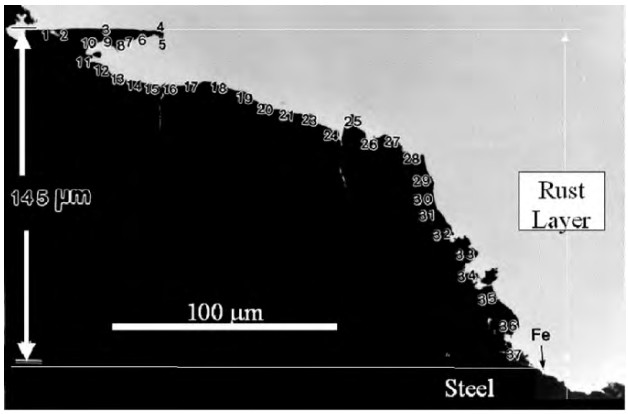

Fig. 8.12. A low magnification TEM image of part of a perforated specimen by ion-etching. The numbers attached correspond to the observed points by TEM and ED [18]

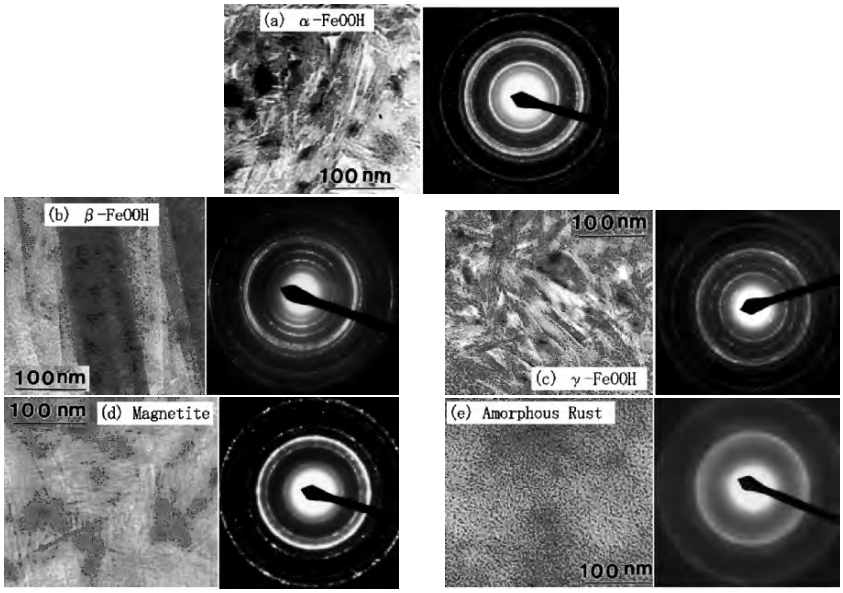

Fig. 8.13. Transmission electron microscopic images of (**a**) α-FeOOH, (**b**) β-FeOOH, (**c**) γ-FeOOH, (**d**) magnetite and (**e**) amorphous rust and their respective selected electron diffraction patterns [16, 19]

as long as several μm in the rust on a plain-carbon steel. Since belt-like crystallites are gathered well ordered, it turns out that ED shows strength distribution peculiar to fiber structure. α-FeOOH and γ-FeOOH look similar to each other as far as their images are concerned. They look to consist of

flaky rusts. Magnetite also looks very compact and featureless. Amorphous rust gives a halo-like ED pattern. It looks very compact and homogeneous. Its structure is different from any structure of other rusts.

Among rust constituents, α-FeOOH was found most frequently, and was estimated as the main constituent in all specimens. The distribution of β-FeOOH was not regularly distributed, but it was rather abundant at the outer region. On a plain-carbon steel specimen (A19H-a), amorphous rust and magnetite were abundant at the bottom of the rust layer. The clear boundary between the inner layer and outer layer observed by EPMA was not clearly observed by TEM/ED. One of the reasons will be the difference in sampling spots. EPMA can obtain data from all the scanned region but TEM/ED data are only at the spots. However the depth distribution of elements would be reflected to the depth distribution of constituents of rust layer.

8.3.6 In-depth Distribution of Rust Components

For the rust layers on the plain-carbon steel (specimens A19H-a and A19H-b) and weathering steels (specimens C19H-a and C19H-b, and E19H-a and E19H-b), depth distribution and abundance of α-FeOOH, β-FeOOH, γ-FeOOH, magnetite and amorphous rust were estimated from ED patterns semi-quantitatively. Some of the results are shown in Figs. 8.14–8.16, where a thick part and a thin part in a rust layer are distinguished and separately displayed.

In Fig. 8.14, depth distribution of rust components in a thick part of rust layer on the skyward surface of the plain-carbon steel exposed at Yokkaichi, an industrial coastal region (A19H), are given. One of characteristic features of the depth distribution of rust components in the rust shown in Fig. 8.14 is distribution of β-FeOOH and amorphous rust. The former distributes mainly in the surface region, whereas the latter distributes at the bottom of the rust layer. Goethite (α-FeOOH) has rather a uniform distribution. Lepidocrocite (γ-FeOOH) and magnetite (Fe_3O_4) are also distributed without any special tendency, but their abundances are much less than that of α-FeOOH.

Depth distribution of rust components in a thick part of rust developed on the skyward of a weathering steel specimen C19H-a is presented in Fig. 8.15. The distribution feature of β-FeOOH and amorphous rust is essentially the same as that found on the plain-carbon steel, that is, β-FeOOH distributes mainly near the surface, and amorphous rust near the bottom of the rust layer. Distribution patterns of α-FeOOH, γ-FeOOH and magnetite are also similar to those corresponding rust components.

Depth distributions of α-FeOOH, β-FeOOH, γ-FeOOH, magnetite and amorphous rust in a thin part of rust layer developed on the weathering steel specimen C19H-a are shown in Fig. 8.16. The main component is apparently α-FeOOH. Amorphous rust distributes at the bottom of the rust layer. Magnetite ranges widely. Concentration of γ-FeOOH in this specimen is small. Lepidocrocite locates mainly at the bottom of the rust layer. Almost no or

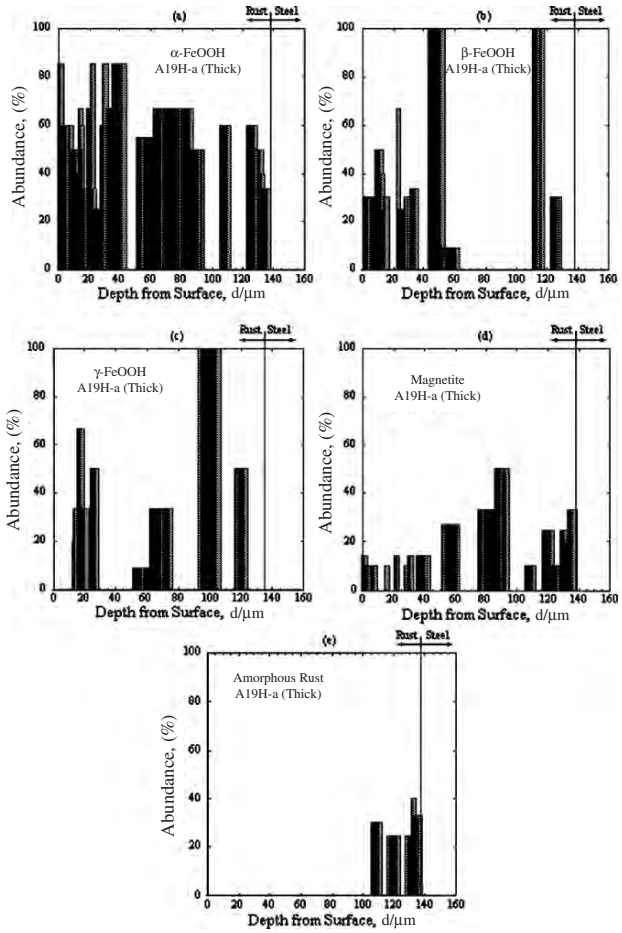

Fig. 8.14. Distribution of (**a**) α-FeOOH, (**b**) β-FeOOH, (**c**) γ-FeOOH, (**d**) magnetite and (**e**) amorphous rust at a thick part of A19H-a specimen, the skyward surface of a plain-carbon steel exposed at Yokkaichi coastal industrial region for 17 years [19]

only a very small amount of β-FeOOH was found in the thin parts on both skyward side and earthward side of the weathering steel specimen C19H. On the plain-carbon steel, content of β-FeOOH in the thin part was much smaller than that in the thick part.

At Ishikari river estuary where the deposition rate of chloride ion was the highest among exposure locations in this experiment, weathering steels were attacked and they did show almost no difference to the plain-carbon steel. The rusts formed on steel specimens (A01H and C01H) were also examined by TEM/ED. However, a considerable part of the rust layers near surface region had been exfoliated. Therefore, the ED data obtained for these specimens may

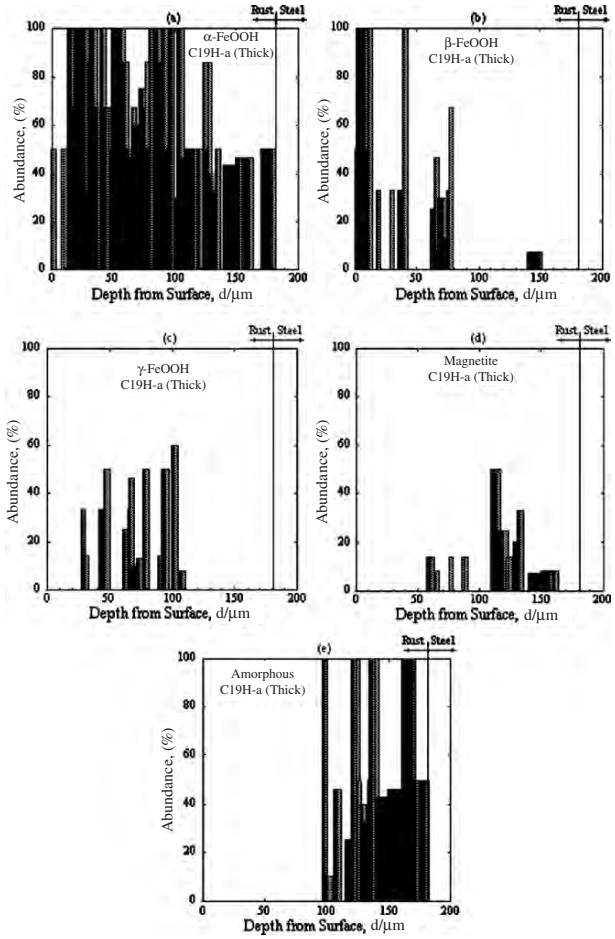

Fig. 8.15. Distribution of (**a**) α-FeOOH, (**b**) β-FeOOH, (**c**) γ-FeOOH, (**d**) magnetite and (**e**) amorphous rust at a thick part of C19H-a specimen, the skyward surface of a weathering steel exposed at Yokkaichi coastal industrial region for 17 years [19]

lack data for the very surface regions. Even after exfoliation, the very thick rust still remained. For C01H-b, the rust remained more than ca. 460 μm, while that of A01H-b was ca. 720 μm. This suggests a large part of the rusts on both steels was easily spalled off.

In Figs. 8.17 and 8.18, depth distribution of rust components for A01H-b and C01H-b are illustrated. It is clear that α-FeOOH is the main constituent even though the environment is very severe. It is also apparent that amorphous rust exists at the bottom of the rust layer. This fact was observed on all specimens. Moreover, the amorphous rust only existed at the bottom. This phenomenon is common to all samples examined in this experiment. On the

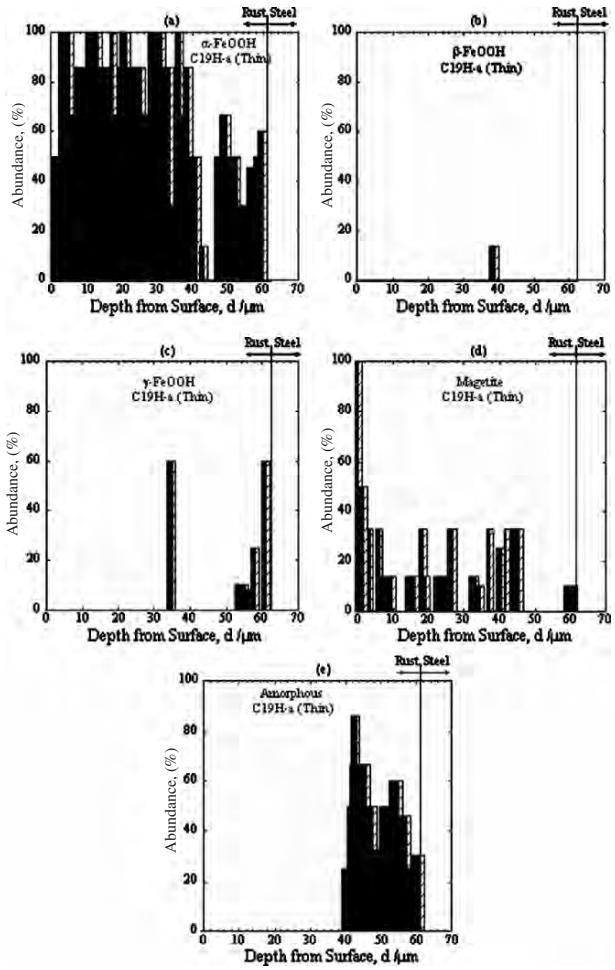

Fig. 8.16. Distribution of (**a**) α-FeOOH, (**b**) β-FeOOH, (**c**) γ-FeOOH, (**d**) magnetite and (**e**) amorphous rust at a thin part of C19H-a specimen, the skyward surface of a weathering steel exposed at Yokkaichi coastal industrial region for 17 years [19]

other hand, β-FeOOH and magnetite exist in alternate layers and form the sandwich structure. γ-FeOOH distributes irregularly from the bottom region to the top region.

8.3.7 Abundance of Rust Components

As well as X-ray diffraction results for the rust layer from the surface, α-FeOOH was a main component of the rust layer on a plain-carbon steel and on weathering steels. Magnetite appeared more on the earthward side than

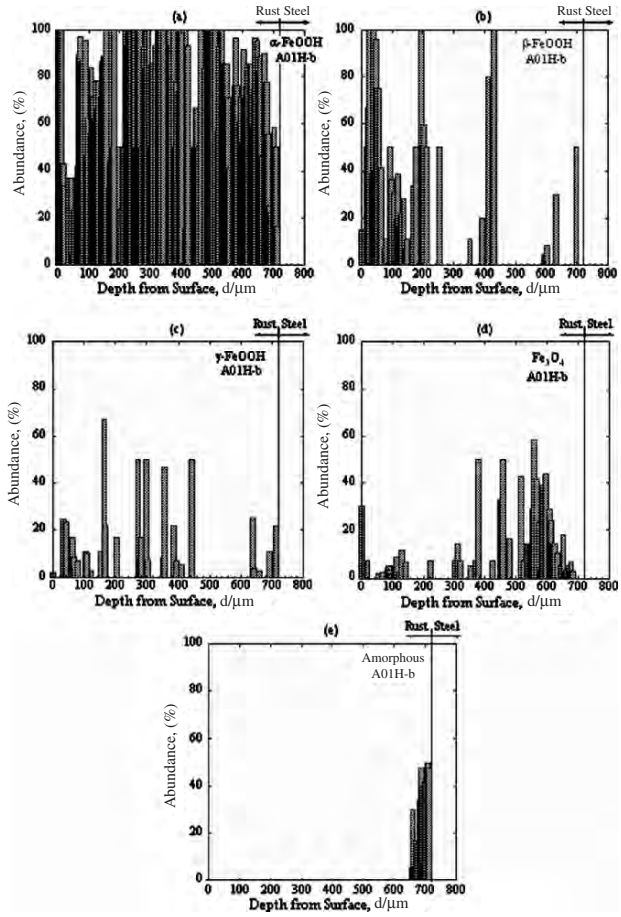

Fig. 8.17. Distribution of (**a**) α-FeOOH, (**b**) β-FeOOH, (**c**) γ-FeOOH, (**d**) magnetite and (**e**) amorphous rust in A01H-b specimen, the earthward surface of a plain-carbon steel exposed at Ishikari river estuary for 18 years

the skyward side, and more on Steel A than Steel E, while γ-FeOOH was more abundant on the skyward side than the earthward side. Moreover, γ-FeOOH appeared much more on the plain-carbon steel than the weathering steel. There was no special tendency in the abundance of β-FeOOH in contrast to XRD taken from the rust layer surface. The depth range observed by XRD from the surface was only in the range of at most 2–3 μm from the surface. As shown in Fig. 8.4, XRD observation of the rust layer surface clearly showed high abundance of β-FeOOH on the skyward surface for every specimen. This result may be caused by the fact that the elements convoluted in the outermost region were different in quantity and species from other parts (both inner layer and outer layer) of the rust layer. On the other hand, TEM/ED

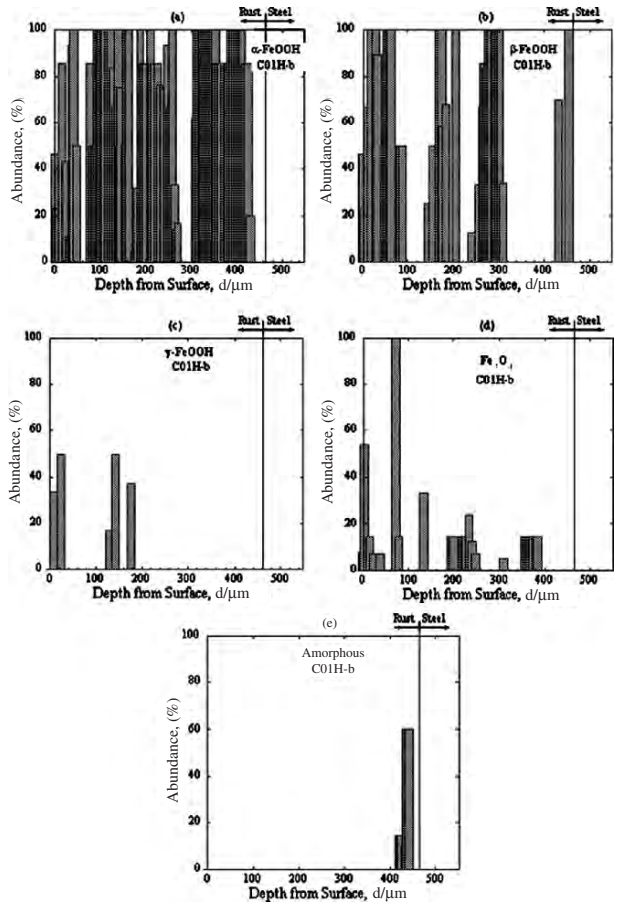

Fig. 8.18. Distribution of (**a**) α-FeOOH, (**b**) β-FeOOH, (**c**) γ-FeOOH, (**d**) magnetite and (**e**) amorphous rust in C01H-b specimen, the earthward surface of a weathering steel exposed at Ishikari river estuary for 18 years

measurements of the Cross-Section can cover the whole specimen rather than the surface region.

The total abundances of rust components were semi-quantitatively estimated from the sum of the abundance of rust components all over the rust layer. The results are displayed in Fig. 8.19, where compositions of skyward and earthward sides and thick and thin parts of the rust on a weathering steel specimen C19H-a and C19H-b are compared. From Fig. 8.19, it is clear that α-FeOOH is the main component in all the rust layers. Its concentration is 60–70% irrespective of thick part or thin part or skyward side or earthward side. It is also very clear that β-FeOOH exists only in the thick part of the

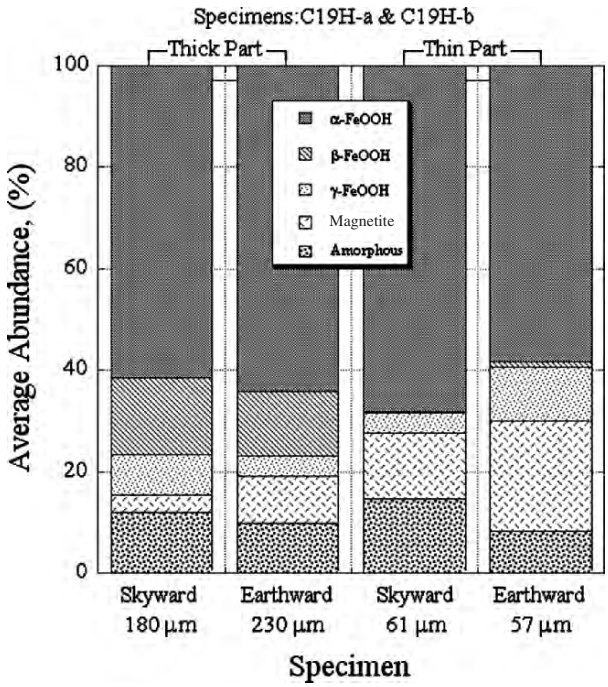

Fig. 8.19. Average abundance of rust constituents at thick and thin parts of rust layer on C19H-a and C19H-b specimens [18, 19]

rust layer. Magnetite has a tendency to exist more on the thin part than the thick part. This fact does not depend on the side of specimen, i.e. skyward or earthward.

In Fig. 8.20, the average abundance of magnetite is plotted vs that of β-FeOOH. It is clearly indicated that there exists negative correlation between total abundance of β-FeOOH and magnetite. Regardless of the steel type, an equation [Magnetite] = K_0 –$0.8\times$[β-FeOOH] holds between abundance of magnetite and β-FeOOH, where [M] represents the abundance of rust component M and K_0 is a constant which depends on specimens. The constant K_0 is much larger for the plain-carbon steel than that of the weathering steel. It will need more work to clarify whether this can be generally applicable to rust formed on all low alloyed steels exposed to environment.

Average abundance of β-FeOOH is plotted vs thickness of rust layer in Fig. 8.21. We can see that the equation [β-FeOOH] = $K_1\times(t-50)$, where K_1 is a constant which depends on specimen and its unit is μm^{-1}, is applicable to all datum sets obtained from a thick part and a thin part of the same specimen. This equation suggests that β-FeOOH does not exist in the rust thinner than 50 μm regardless of steels although there are only three sets of data applicable in this experiment. It can be seen that the constant K_1

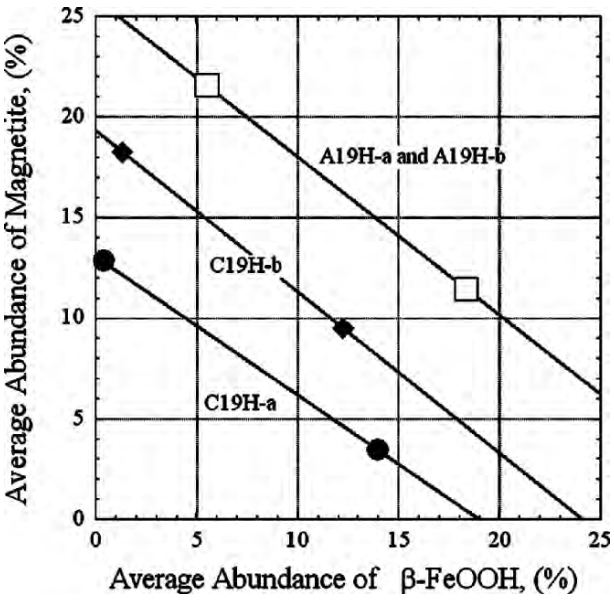

Fig. 8.20. Correlation between average abundance of magnetite and β-FeOOH [19]

is obviously larger for the plain-carbon steel than that for the weathering steel.

There is a view that the quantity ratio of α/γ, where α = [α-FeOOH] and γ = [γ-FeOOH] is a good index for judgement of the protective nature of a rust layer [23,24]. Similarly, the α/γ^* ratio was the more elaborated one [24], where α = [α-FeOOH] + [amorphous rust], and γ^* is the sum of [γ-FeOOH], [β-FeOOH], and [magnetite], or $\alpha/\gamma^* = (\alpha+\mathrm{A})/(\gamma+\beta+\mathrm{M})$ where α, A, γ, β and M correspond to [α-FeOOH], [amorphous rust], [γ-FeOOH], [β-FeOOH] and [magnetite], respectively. In Fig. 8.22, the α/γ^* ratio for all specimens exposed at Site 19 in this experiments are displayed. At a thick part of rust layers, the α/γ^* ratio on a plain-carbon steel is about 1/2–1/3 of those for weathering steels. This tendency is also observed at thin parts of rust layers although it is not notable. In Fig. 8.23, the α/γ^* ratio of specimen exposed at Sites 01 and 20 is plotted. Here, the tendency is different from those in Fig. 8.22, i.e. the α/γ^* ratio is much larger for specimens A01 than C01 or A20.

Average abundance of amorphous rust for all data are plotted vs rust layer thickness in Fig. 8.24. For data from specimens exposed at Sites 01 and 20, real thickness might have been larger. Arrows are attached, therefore, on these data to indicate that they might have been plotted at larger thickness values. It is interesting that the average abundance of amorphous rust decreases exponentially with the rust layer thickness. Both a plain-carbon steel and weathering steels have the same tendency. Within the accuracy of the present

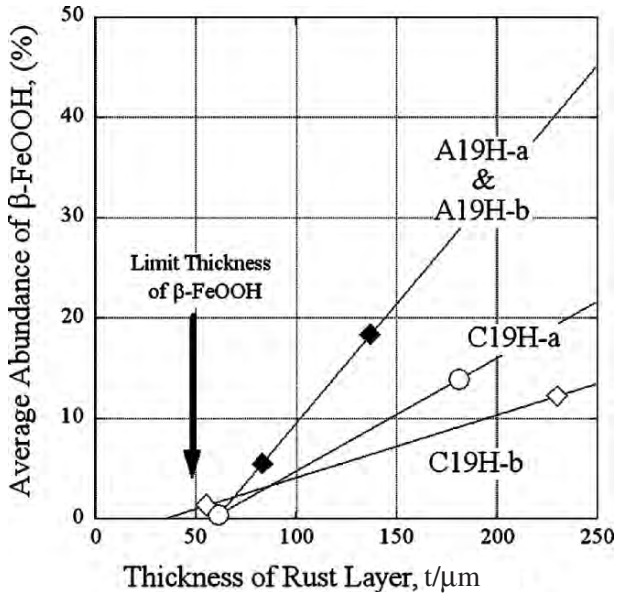

Fig. 8.21. Correlation between average abundance of β-FeOOH and thickness of rust layer [19]

experiment, they seem to fall on the same line. Similarly, average abundance of α-FeOOH is also plotted in Fig. 8.25. In the case of the weathering steels, α-FeOOH abundance is almost constant regardless of the thickness. On the other hand, that of the plain-carbon steel has a large scatter. However, an average, its tendency is almost the same with that of weathering steels.

8.4 Discussion

It was reported that the corrosion loss of weathering steels at Yokkaichi (Site 19) was in general about twice that of Mikuni Pass (Site 08) [21]. However, there is no such difference in the rust layer thickness obtained from Cross-Sectional observation of both specimens. Rust layers formed on weathering steels were compact and adhesive, and therefore they did not easily exfoliate. This characteristic will contribute to promote protectiveness of the rust layers. Okada et al. [2] reported that a large quantity of amorphous rust was formed because of condensation of Cu and P in the inner layer within the rust layer. They stated that the amorphous layer containing Cu and P could impart protectiveness to the weathering steels. In this report, however, the enrichment of P was not observed in the inner layer. The relation of P and amorphous rust was not clear, either. Misawa et al. [3, 4] studied Cr-containing steels and claimed that α-FeOOH formed on Cr-containing steels had much higher protectiveness than conventional α-FeOOH. They

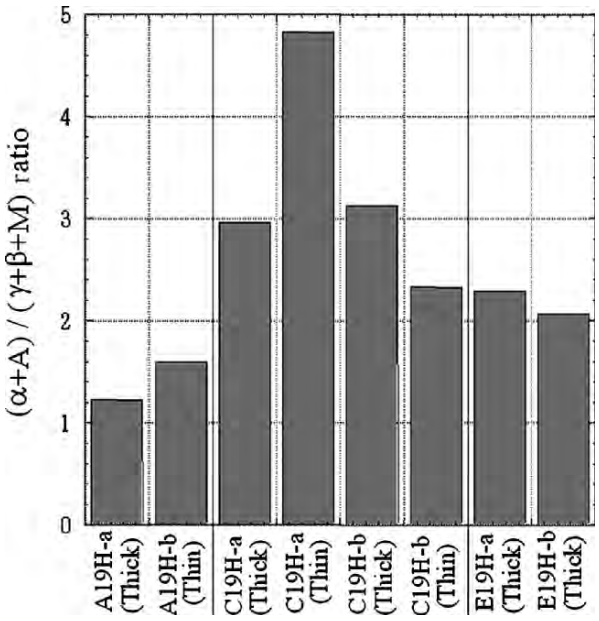

Fig. 8.22. (α+A)/(γ+β+M) ratio for specimens exposed at Site 19, Yokkaichi, an industrial and coastal region for 17 years [19]

explained that Cr was partly substituted for Fe and it imparted corrosion protectiveness to α-FeOOH. In this work, not only Cr but also Cu and Si are enriched in the inner rust layer as shown in Figs. 8.7–8.10. Sakashita and Sato [12] mentioned that the ion selectivity of rust has an important role for the protectiveness of rust; i.e., oxyhydroxides in general have anion selectivity, but they change to cation selective when some anions such as phosphate and molybdate ions are adsorbed. If the rust formed on a weathering steel is cation selective, the penetration of anions such as Cl^- will be hindered, and then the rust layer will become protective against corrosion. If elements enriched in the inner layer can impart cation selectivity to the rust layer, the rust layer formed on the steels will also become protective. Yamashita et al. [13] reported that when Cr(III) was substituted for Fe(III), cation selectivity certainly increased. However, Kimura, using X-ray absorption fine structure analysis, denied existence of α-FeOOH substituted by Cr [25].

8.4.1 Effect of Amorphous Rust Layer

By the XRD method, considerable amount of amorphous rust was found [30]. In general, most of the amorphous rust found by XRD is believed to be aggregation of very fine α-FeOOH. In the case of the XRD method, rust assigned as amorphous rust might be amorphous plus aggregated very fine α-FeOOH particles. However in this chapter we denote rust which has a halo diffraction

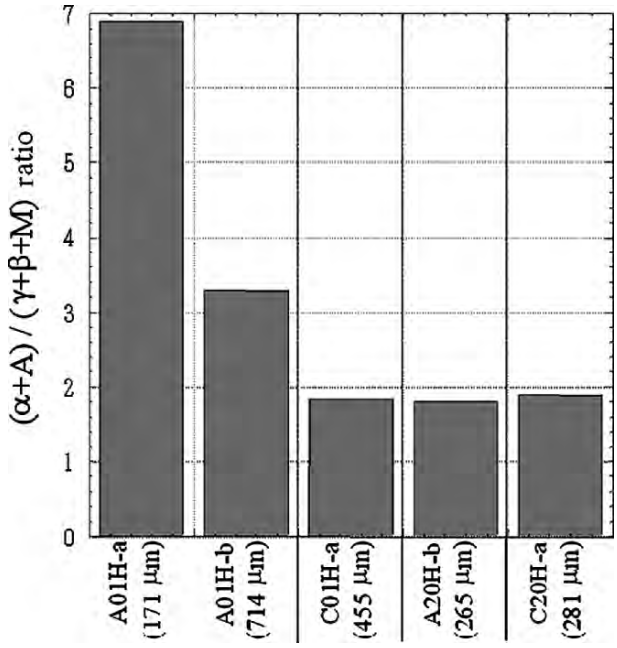

Fig. 8.23. (α+A)/(γ+β+M) ratio for specimens exposed at Sites 01 and 20, coastal regions with heavy chloride depositions

pattern as amorphous because we cannot identify it as any other rust. According to results reported by Kamimura et al. [15] by Mössbauer spectroscopy at 10 K, the rust contained only α-FeOOH, γ-FeOOH and $Fe_{3-x}O_4$ (γ-Fe_2O_3) for mild steel, and only α-FeOOH and γ-FeOOH for weathering steel, and the amorphous-like phase in the rust layer formed on weathering steel was mainly α-FeOOH. However, the amorphous ED pattern is clearly different from that of α-FeOOH as shown in Fig. 8.13. The ED pattern of the amorphous rust is rather close to that of magnetite (Fe_3O_4). As magnetite has spinel-structure and γ-Fe_2O_3 ($Fe_{3-x}O_4$) has the same structure, and as conventional ED cannot distinguish between them, it might be γ-Fe_2O_3 ($Fe_{3-x}O_4$) although Kamimura et al. reported that γ-Fe_2O_3 ($Fe_{3-x}O_4$) did not exist in the rust on weathering steel. By comparing in Fig. 8.14(e) and Fig. 8.15(e), it can be said that the amorphous rust in the rust layer on plain-carbon steel is much less than that on weathering steel. The conclusion by Okada et al. [2], therefore, seems rather reasonable from the present TEM/ED observation, i.e. the dense and compact amorphous oxide layer located in an inner layer where Cu and P were enriched was attributable to protectiveness of the weathering steel. Kumar et al. [7] also reported that the non-stoichiometric $Fe_{3-x}O_4$ was an important factor in its corrosion protective ability. By using Mössbauer spectroscopy, Siddique et al. [6] found α-FeOOH, γ-FeOOH and an amorphous-like substance together with a small amount of γ-Fe_2O_3

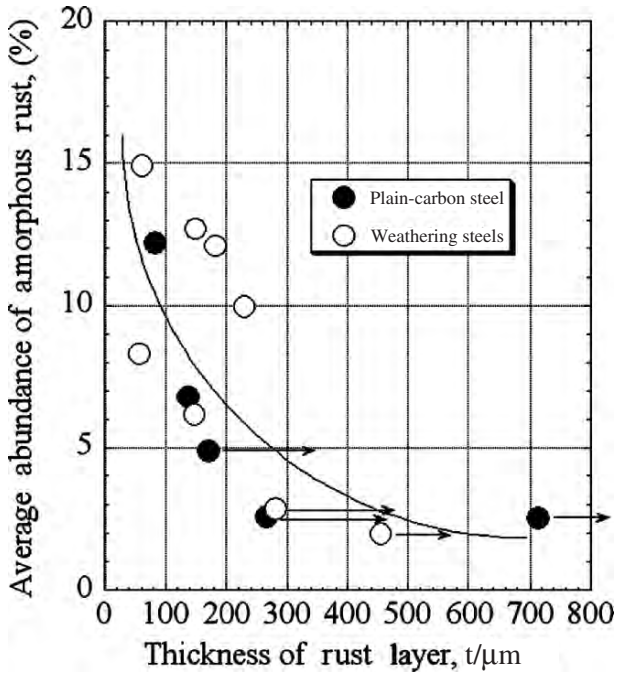

Fig. 8.24. Average abundance of β-FeOOH plotted versus thickness of rust layer

(6–8%) in the rust layer on a mild steel. Consequently, corrosion resistance of weathering steel will be imparted by amorphous rust and/or nanocrystalline $Fe_{3-x}O_4$ which becomes compact by additional elements such as Cr, Ni, Cu and P. Actually, weathering steels contain some of these elements as shown in Table 8.1. Among these elements, Cr and Cu exist mainly in the inner rust layer (Figs. 8.9 and 8.10), but depth distribution of Ni and P is rather uniform [16]. Nickel and phosphorus addition may have another effect. Ishikawa et al. [26] elucidated the effect of Cr(III), Ni(II) and Cu(II) ions on the particle size of γ-FeOOH and magnetite formed by air-oxidation of $FeSO_4$ solutions. They also found that all the ions they have studied impeded the crystallization and particle growth of Fe_3O_4. Accordingly, it will be possible to form a protective rust layer with compact and fine particles. As mentioned above, the inner layer of the rust layer on weathering steels consists of amorphous rust and/or nanocrystalline $Fe_{3-x}O_4$ where these elements are enriched.

The average abundance of amorphous rust decreases with increase in rust layer thickness as shown in Fig. 8.24, where there is almost no difference among steels. It seems that the production of amorphous rust and thickness is almost constant. Half of the data in this experiment fit well. However, some of data does not match with this expectation. In this experiment, all amorphous rust is found only at the bottom of the rust layer (Figs. 8.14–

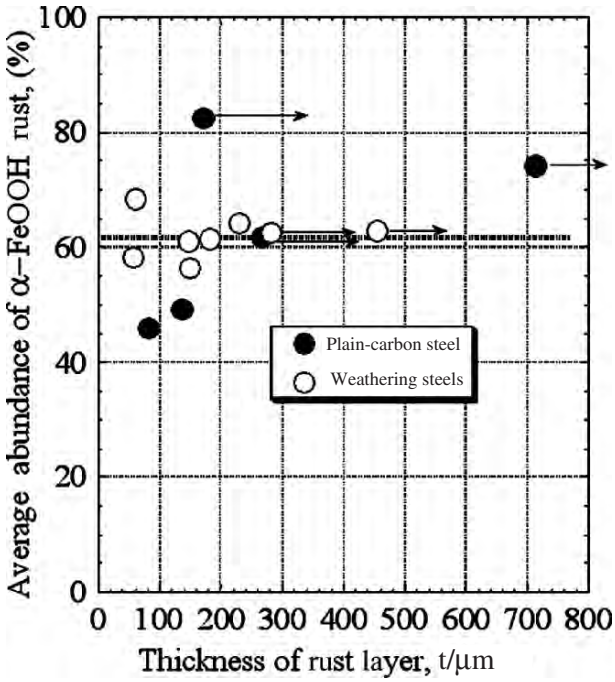

Fig. 8.25. Average abundance of amorphous plotted versus thickness of rust layer

8.18). It is also found that the thickness of the amorphous rust layer does not increase with the increase of the total rust layer.

8.4.2 Effects of Akaganéite

Akaganéite (β-FeOOH) distributes in general at the surface region of the rust layer. The formation of β-FeOOH needs halogen ions such as Cl^- and F^- which stabilize the tunnel structure of β-FeOOH crystals [27–29]. Akaganéite distributes mainly in the outer layer of the rust layer, especially on the top surface of the skyward side. It also appears in the inner layer as shown in Figs. 8.14, 8.17 and 8.18. The depth distribution of β-FeOOH occurs sometimes alternately with magnetite. Water deposits containing chloride ions penetrates into cracks of the rust layer. The depth distribution of β-FeOOH at inner positions may happen by formation of β-FeOOH at cracks through reaction of chloride-containing water with unstable rust such as non-stoichiometric magnetite. Since β-FeOOH has relatively large volume per iron, when β-FeOOH is formed once, it will open cracks more and make the penetration of chloride-containing water easier. It is known that β-FeOOH has a tunnel-like structure, which is stabilized by halide ions such as chloride ions. As shown in Fig. 8.13 (b), β-FeOOH has a belt-like morphology in the rust on a

plain-carbon steel. Therefore, β-FeOOH may easily convey Cl^- ions through the tunnel space. When the environment does not contain chloride ions, even the dissolved non-stoichiometric magnetite and similar rust will be able to form the same rust again at dry cycle, and the crack will be filled up with the deposited rust components.

8.4.3 Correlation between Akaganéite and Magnetite

In general, the rusted surface of steel has many hollows. The interface between the rust layer and steel substrate is wavy and undulating, and the rust layer has thin and thick parts. Thus, the thickness of the rust layer is quite uneven. There will be no argument about the fact that the origin of unevenness comes from non-uniform distribution of physical and chemical factors such as deposits from the environment and directions of crystallites of the steel. Generally, it is taken that the thin parts of the rust layer will correspond to parts where the corrosion protective rust layer covers the steel, whereas in the thick parts, less protective rust layer exists. As shown in Fig. 8.19, the main difference between thin and thick parts is in concentrations of β-FeOOH and magnetite; β-FeOOH exists more and magnetite less at the thick part of the rust layer. Average concentration of magnetite in the rust layer is negatively correlated with concentration of β-FeOOH as shown in Fig. 8.20. Judging from the relation demonstrated in Fig. 8.20, formation of magnetite (or $Fe_{3-x}O_4$) and β-FeOOH is competitive, or magnetite changes to β-FeOOH, i.e., β-FeOOH is preferentially formed and magnetite is dissolved when chloride ions exist.

As shown in Fig. 8.21, there is a minimum thickness for β-FeOOH containing rust layer. It means that development of the rust layer is about 50 μm at maximum when there is no significant deposits of corrosive species such as chloride ions, irrespective of whether a plain-carbon steel or weathering steel. Addition of elements which effectively increase protectiveness of rust layer may depress formation of β-FeOOH by depressing crystal growth [26].

Yamashita et al. showed nearly linear relationship between corrosion loss and mass% of β-FeOOH [30]. Stratmann et al. studied the corrosion behavior of pure iron, and reduction of rust and its re-oxidation in detail, and reported relation between rusts and early stage of iron corrosion [31, 32], and that α-FeOOH was electrochemically stable inhibiting corrosion whereas γ-FeOOH and magnetite were easily reduced and active for corrosion during dry-wet cycles. Nishimura et al., studying steels covered with rust layer, which contained β-FeOOH electrochemically, showed that β-FeOOH was also easily reducible and promotes corrosion under environments with chloride [33]. The present results showed that β-FeOOH exists mainly at the thick part of the rust layer. This means that corrosion proceeds more quickly at the position where β-FeOOH exists. As is well known, β-FeOOH is formed when chloride ions exist [27–29]. Chloride ions are combined with rust but easily separate and promote iron corrosion. Once β-FeOOH is formed, consequently, it may

work as a reservoir of Cl^- and the rust layer itself will become porous and introduce chloride ions easily from outside. On the other hand, a thin rust part, where the main constituent is α-FeOOH and concentration of β-FeOOH is very low, has a protective nature because of stabilized α-FeOOH and it will be difficult for chloride ions to enter into the rust layer.

8.4.4 Effect of Lepidocrocite and Goethite

Concentration and distribution of γ-FeOOH in this work had no apparent relationship with type of steels, side of exposure or rust thickness. According to Yamashita et al. [23], γ-FeOOH should exist on the top of a α-FeOOH rust layer. However, its distribution is not necessarily in the upper part of the rust layer as shown in Figs. 8.14–8.17. Concentration of α-FeOOH was higher and that of γ-FeOOH was lower on weathering steels than on a plain-carbon steel. This fact suggests that elements added to weathering steels may accelerate transformation of γ-FeOOH to α-FeOOH. It is necessary to quantify rust components from ED intensity at each point more extensively. It is also necessary to improve specimen preparation for TEM observation and in-situ analysis of elements to elucidate the role of added elements more clearly [34].

8.4.5 α/γ^* Ratio

The corrosion rate of a steel in an environment depends on the composition of the rust layer which contains α-FeOOH, β-FeOOH, γ-FeOOH, magnetite and amorphous rust. There is a view where the quantity ratio of α-FeOOH to β-FeOOH+γ-FeOOH+magnetite (α/γ^* ratio) detected by X ray diffraction can be used as an index for protection nature of a rust layer [23,24,35]. Based on this view, the α/γ^* ratio was plotted using ED data in this experiment. Without counting amorphous rust, which was identified by ED (ED-amorphous), as α-FeOOH, the α/γ^* ratios were 1.51 and 1.15 for E19H-a (skyward) and E19H-b (earthward), respectively, and 0.97 and 0.74 for A19H-a (skyward) and A19H-b (earthward), respectively. On a weathering steel, the ratio $\alpha/\gamma^* > 1$, while that on a plain-carbon steel is less than 1, and the α/γ^* value was larger on the skyward side than that on earthward side. It can be said that the α/γ^* ratio determined by ED seems to be a good index for the protective nature of the rust layer within the specimens exposed at Sites 08 and 19.

When ED-amorphous rust was counted as a part of α-FeOOH, every α/γ^* was more than 1.2, and it was largest on the earthward side of plain-carbon steel. Yamashita et al. analyzed quantitatively rust constituents on weathering steels exposed for 17 years by XRD method [30], and they reported that the quantity of amorphous rust amounted to 61–87 mass% and the others were only a small amount of γ-FeOOH and magnetite. By the present study, quantities are semi-quantitatively determined from the electron diffraction intensities. However, the quantity of amorphous rust is 16% at maximum as shown in Fig. 8.19. This large discrepancy must come from the difference in

resolution of XRD and ED. Although a part of XRD-amorphous rust could be identified as crystalline rust in this work, there still exists amorphous rust even in ED analysis. As mentioned above, however, the quantitative results cannot be obtained for ED-amorphous rust because the intensity from ED-amorphous rust is not very clear and accurate. The α/γ^* ratio by ED may be applicable to the evaluation of the rust layer without counting ED-amorphous rust, but it is not effective to use ED data to evaluate corrosion of steels by α/γ^* ratio.

For steels exposed to very severe environment at Sites 01 and 20 in this experiment, α/γ^* ratio shown in Fig. 8.23 is not in agreement with the mild environment data. It is reported that when the total rust thickness is more than 300 μm, the rust under such conditions will be anomalous, and α/γ^* ratio cannot be applied anymore [21].

8.5 Summary

Four types of weathering steels and a plain-carbon steel were exposed to air for 17 years at an industrial coastal region, and at a rural region, in Japan. Two types of steels, a weathering steel and a plain-carbon steel were exposed for 18 years at coastal regions, in Japan.

All specimens were placed under bridges with their faces horizontally set and were investigated by EPMA, XRD, SEM, TEM and ED. The following conclusions were drawn:

(1) Rust consists essentially of three layers; the inner, outer and outermost layers irrespective of whether a plain-carbon steel or a weathering steel. The rust layer consists of α-FeOOH, β-FeOOH, γ-FeOOH, magnetite and amorphous rust.
(2) The outermost layer is about 3 μm thick and enriched with atmospheric deposits. In the outer layer, Cl and S are enriched. Alloying elements, Cu, Cr and Si are concentrated in the inner layer while P and Ni are mostly distributed uniformly over the whole rust layer.
(3) Regardless of steel, the major component on the outermost rust layer is α-FeOOH and minors are β-FeOOH and γ-FeOOH. β-FeOOH is especially abundant on the skyward surfaces.
(4) In the outer and inner layers, the main constituent is α-FeOOH on all specimens. α-FeOOH appears almost homogeneously through the rust layer. Its concentration is higher on weathering steels than on a plain-carbon steel when the environment is not very severe.
(5) Rust layer usually lacks uniformity; it has thick parts and thin parts. β-FeOOH exists at thick parts of the rust layer, but is scarce at the thin parts of the rust layer. β-FeOOH also exists in considerable quantity on severely corroded specimens.
(6) Average abundance of α-FeOOH is higher and that of β-FeOOH is much lower in the rust of weathering steels than that on a plain-carbon steel.

(7) Amorphous rust is located at the bottom of the rust layer irrespective of steel type and exposure environment.
(8) Concentration of magnetite is negatively correlated with concentration of β-FeOOH when steels are exposed in mild environments. From the negative correlation of magnetite and β-FeOOH, a model of degradation mechanism of rust layer was suggested.
(9) There are almost no differences between specimens exposed at the industrial coastal region and the rural mountainous region because of effect of calcium chloride sprayed for melting snow on road during winter at the rural mountainous region.
(10) The α/γ^* ratio, the quantity ratio of α-FeOOH to β-FeOOH + γ-FeOOH + magnetite, obtained by ED, is larger than 1 on a weathering steel, and less than 1 on a plain-carbon steel. However, when we take $\alpha = \alpha$-FeOOH + amorphous rust, all values become greater than unity. Moreover, the α/γ^* ratio is very large on a plain-carbon steel for specimens exposed at very severe environment. It is not convenient to use the ED determined data to evaluate α/γ^* value of the rust layer.

Acknowledgements

The authors are very grateful to the Independent Administrative Institution Public Works Research Institute (IAI-PWRI), Japan Association of Steel Bridge Construction and The Japan Iron and Steel Federation for specimens and environmental data, and to Dr. T. Nakayama, Kobe Steel for several standard X-ray diffraction patterns. Thanks are also due to Mr. M. Kikuchi for TEM and ED measurements and analysis, and to Mr. Y. Murakami for EPMA measurements, and to Mr. S. Itoh and Mr. T. Sato for preparation of TEM specimens.

References

1. T. Misawa, K. Hashimoto and S. Shimodaira: Corros. Sci., **14**, 131 (1974).
2. H. Okada, Y. Hosoi, K. Yukawa and H. Naito: Tetsu-to-Hagane, **55**, 355 (1969).
3. T. Misawa, M. Yamashita, Y. Matsuda, H. Miyuki and H. Nagano: Tetsu-to-Hagane, **79**, 69 (1993).
4. M. Yamashita, H. Miyuki, H. Nagano and T. Misawa: Zairyo-to-Kankyo, **43**, 26 (1994).
5. A. L. Morale, D. Cartagena, J. L. Rendon and A. Valencia: Phys. Status Solidi B, **220**, 351 (2000).
6. M. Siddique, M. Anwar-ul-Islam, N. M. Butt, N. Hussain, S. Rehman and M. Arshed: J. Radioanal. Nucl. Chem., **241**, 239 (1999).
7. A. V. R. Kumar, R. K. Nigam and S. S. Monga: Bull. Electrochem., **15**, 115 (1999).
8. T. Okada,Y. Ishii, T. Mizoguchi, I. Tamura, Y. Kobayashi, Y. Takagi, Suzuki, H. Kihira, M. Itou, A. Usami, K. Tanabe and K. Masuda: Jpn. J. Appl. Phys., **39**, 3382 (2000).

9. M. Yamamoto, H. Katayama, T. Kodama: Current Advances in Materials and Processes, **12**, 422 (1999).
10. K. Shiotani, W. Tanimoto, C. Maeda, F. Kawabata and K. Amano: Zairyo-to-Kankyo, **9**, 67 (2000).
11. H. Kihira: *Electrochemical Phenomena at Interface*, edited by (H. Ohshima and K. Furukawa, Marcel Dekker Inc, New York, (1998), p. 429.
12. M. Sakashita and N. Sato: Boshoku Gijutsu (Corros. Eng.), **28**, 450 (1979).
13. J. T. Keiser, C. W. Brown and R. H. Heidersbach: Corros. Sci., **23**, 251 (1983).
14. M. Yamashita, K. Asami, T. Ishikawa, T. Ohtsuka, H. Tamura and T. Misawa: Zairyo-to-Kankyo (Corros. Eng.), **50**, 521 (2001).
15. T. Kaminura, S. Nasu, T. Tazaki, K. Kuzushita and S. Morimoto: Mater. Trans., **43**, 694 (2002).
16. K. Asami and M. Kikuchi: Mater. Trans., **43**, 2818 (2002).
17. K. Asami and M. Kikuchi: J. Japan Inst. Metals, **66**, 649 (2002).
18. K. Asami, M. Kikuchi, T. Sato and S. Itoh: Proce. 15th Intl. Corrosion Congress, (Granada, Spain, 2002), Paper No. 27 (2002) p.1.
19. K. Asami and M. Kikuchi: Corros. Sci., **45**, 2671 (2003).
20. K. Asami: Kinzoku, **73**, 105 (2003).
21. Private communication: *Public Works Research Institute Ministry of Construction, Japan Association of Steel Bridge Construction and the Kozai Club*, (2005).
22. K. Asami: Trans. JIM., **21**, 302-308 (1980).
23. M. Yamashita, H. Miyuki, Y. Matsuda, H. Nagano and T. Misawa: Corros. Sci., **36**, 283 (1994).
24. H. Kihira, T. Misawa, T. Kusunoki, T. Tanabe and T. Saito: Zairyo-to-Kankyo, **48**, 727 (1999).
25. M. Kimura: Kinzoku, **73**, 79 (2003).
26. T. Ishikawa, M. Kumagai, A. Yasukawa, K. Kandori, T. Nakayama and F. Yuse: Corros. Sci., **44**, 1073 (2002).
27. H. B. Weiser: J. Am. Chem. Soc., **57**, 238 (1934).
28. A. L. Makay: Miner. Mag., **32**, 545 (1960).
29. V. P. Keller: Corrosion, **20**, 102 (1969).
30. M. Yamashita, A. Maeda, H. Uchida, T. Kamimura and H. Miyuki: J. Japan Inst. Metals, **65**, 967 (2001).
31. M. Stratmann, K. Bohnenkamp and H. -J. Engell: Corros. Sci., **23**, 969 (1983).
32. M. Stratmann and K. Hoffmann: Corros. Sci., **29**, 1329 (1989).
33. T. Nishimura, I. Tanaka and Y. Shimizu: Tetsu-to-Hagane, **81**, 1079 (1995).
34. M. Yamamoto, H. Katayama and T. Kodama: Tetsu-to-Hagane, **86**, 578 (2000).
35. T. Kamimura, M. Yamashita, H. Uchida and H. Miyuki: J. Japan Inst. Metals, **65**, 922 (2001).

9 Synchrotron Radiation Study on Structure of Atmospheric Corrosion Products Formed on Steel Surfaces

Hiroyuki Konishi, Masato Yamashita, Jun'ichiro Mizuki, Hitoshi Uchida

9.1 Introduction

A rust layer formed on a low-alloy steel surface is generally considered to be responsible for protecting the steel against corrosives in the atmosphere. Therefore, the rust layer plays an important role in corrosion control. Certain alloying elements promote the formation of a so-called "protective rust layer" on the surface of the steel. For example, it is well known that weathering steel, which contains small amounts of anticorrosive alloying elements such as Cr, P, Cu and Ni, possesses a high corrosion resistance of approximately twice that of carbon steel. Consequently, weathering steel is recognized to be a structural material that does not require painting.

We have only a nominal understanding of the mechanism of the protective ability of the rust layer. The properties of a material can generally be explained on the basis of its atomic structure. Therefore, it is meaningful to study the structural properties of the protective rust layer of weathering steel. It is particularly necessary to analyze the local structural and chemical properties of anticorrosive alloying elements and corrosive ions in the rust layer. In addition, it is also desirable to observe the corrosion process directly. Information obtained in this manner can be the guiding principle of the research and development of high-performance weathering steel.

As is well known, X-rays and gamma rays are easily available for analyses of the chemical state and structure of a material on a nanometer scale. Recently synchrotron radiation has been particularly useful for this purpose in a wide variety of scientific fields. Synchrotron radiation is electromagnetic radiation emitted from a fast electron moving at approximately the velocity of light following a curved trajectory under a magnetic field in an accelerator. It has a number of unique properties as follows:

(1) High brilliance and high brightness: synchrotron radiation is extremely intense. The photon flux of synchrotron radiation X-rays on a sample is usually hundreds or thousands of times higher than that of conventional X-ray tubes.
(2) Wide energy spectrum: the spectrum of synchrotron radiation includes a wide energy band, ranging from infrared to gamma rays. Photons of any energy are available.

(3) Polarization: synchrotron radiation is generally highly linearly polarized in the horizontal direction. The polarization of photons can be controlled using a specially designed light source called an insertion device. For example, photons with circular polarization are used for the measurement of the magnetic circular dichroism of matter.
(4) High collimation: the angular divergence of a synchrotron radiation beam is very small, typically less than several microradians.
(5) Pulse light: synchrotron radiation is emitted in very short pulses, because electrons form groups called "bunches" as they move in the accelerator. A typical pulse width is on the scale of sub-picoseconds to less than one nanosecond. The interpulse length can be varied, depending on the operating mode of the accelerator, from nanosecond to picosecond.

Such properties enable us to perform investigations which are otherwise difficult using conventional X-ray sources. The number of accelerator facilities exclusively for synchrotron radiation science is increasing globally. Recently, facilities with electron energies over 6 GeV, which are called the "third generation synchrotron radiation facilities", have been constructed in the USA (APS, 6 GeV), France (ESRF, 7 GeV) and Japan (SPring-8, 8 GeV). A large number of researchers utilize these facilities and produce excellent results in many scientific and industrial fields.

We have recently performed structural studies of the rust layer on steel using synchrotron radiation. In this chapter, these studies will be introduced as examples of the application of synchrotron radiation to the studies of atmospheric corrosion on steel.

9.2 Composition of Protective Rust Layer Formed on Weathering Steel

According to the recent understanding of the rust layer on weathering steel, its main constituents vary, depending on the atmospheric exposure periods, from γ-FeOOH (less than a few years) to an X-ray amorphous substance (several years) and finally to a goethite (α-FeOOH)-type phase (decades) [1]. The goethite-type phase is considered to form due to the concentration of Cr and the substitution of Cr for Fe in the goethite structure. It is thought that the X-ray amorphous substance consists of ultrafine particles of FeOOH and other products, because it does not show a well-defined Bragg peak on the X-ray diffraction spectrum.

Goethite is isostructural with diaspore (α-AlOOH). The structural unit of the goethite crystal is an $Fe(OH)_3O_3$ octahedron in which Fe^{3+} is surrounded by three O^{2-} and three OH^-. Double chains of $Fe(OH)_3O_3$ octahedra formed by edge-sharing run parallel to one of the principal axes. These chains are linked to adjacent double chains by corner-sharing to give a 2×1 tunnel

structure with orthorhombic symmetry. Therefore, this structure consists of double chains of $Fe(OH)_3O_3$ octahedra alternating with double chains of vacant sites [2].

The typical Cr content in the protective rust layer is approximately 4 mass%. The protective rust layer is believed to possess the structure of α-$(Fe_{1-x},Cr_x)OOH$, which is called Cr-goethite. The corrosion rate of weathering steel decreases as the X-ray amorphous substance forms and matures into the goethite phase. The protective rust layer of weathering steel after long-term exposure indeed consists of a large amount of Cr-goethite [3].

Structural studies by various spectroscopic methods, such as X-ray diffraction [3–5], Raman [6,7], infrared [8,9], and Mössbauer [10–12] spectroscopies, have revealed that the protective rust layer has a double-layer structure. The inner layer consists mainly of ultrafine particles of Cr-goethite and has a densely packed texture with few cracks or pinholes. The protective ability is derived from the characteristic texture of the rust layer, because such a texture works efficiently as a physical barrier against corrosive ions and/or water [13].

The composition ratio of the protective rust layer of weathering steel correlates with the protective ability. The chemical reactivity and electric conductivity of goethite are lower than those of other corrosion products. For this reason, the α/γ^* ratio, where α is the mass of goethite and γ^* is the sum of the masses of akaganéite (β-FeOOH), lepidocrocite (γ-FeOOH) and magnetite (Fe_3O_4), can be used to estimate the protective ability of the rust layer [14]. As the α/γ^* ratio becomes larger, the corrosion rate decreases. Such a rust layer appears dense and continuous. In a saline environment, the mass ratio of goethite to akaganéite, α/β, also corresponds well to the protective ability.

Additionally, Cr-goethite with Cr content greater than about 3 mass% possesses cation selectivity that prevents the penetration of aggressive corrosive anions such as chloride ions [15]. This property of Cr-goethite is thought to provide electrochemical protection to the rust layer.

9.3 Structural Study on the Protective Rust Layer using X-ray Absorption Spectroscopy

While considerable progress has undoubtedly been made on understanding the protective rust layer [7], and the protective properties due to Cr-goethite have been clarified in the last decade, the role of Cr in the goethite structure has remained unclear regarding the formation of the densely packed goethite layer with cation selectivity. In order to discuss the effect of Cr on the structural properties and the formation of the protective rust, it is necessary to elucidate the local structure around Cr in the protective rust layer. We have performed an X-ray absorption fine structure (XAFS) study of Cr-goethite

as the main constituent of the protective rust layer. XAFS is the most effective technique for identifying the local structural properties around a specific element [16, 17].

9.3.1 X-ray Absorption Fine Structure Analysis

The X-ray absorption coefficient $\mu(E)$ of a material is a function of the X-ray photon energy, E. When the X-ray photon energy is tuned to the binding energy of some core level of an atom in a material, an abrupt increase in the absorption coefficient occurs. This is well known as the absorption edge. For a molecule or a condensed material, the X-ray absorption coefficient shows a characteristic oscillation at energies beyond the absorption edge as a function of photon energy. The fine structure on the absorption coefficient curve is known as the X-ray absorption fine structure (XAFS). Such fine structure may extend up to 1 keV above the absorption edge.

The XAFS is generally divided into different categories based on the excited electron behavior. An X-ray absorption near-edge structure (XANES) appears from the edge up to about 50 eV. If the photon energy is insufficient, an excited inner shell electron cannot propagate from the absorbing atom and is trapped in the empty discontinuous level or orbital of the absorbing atom. Therefore, the XANES spectrum is very sensitive to the chemical bonding and electronic structure of the absorbing atom.

In contrast, extended X-ray absorption fine structure (EXAFS) refers to the region of 50–1000 eV. When the core electron is given sufficiently high energy from X-ray photons, it propagates toward neighboring or more distant atoms and is scattered by them. Consequently, the photoelectron can return to the absorbing atom. An EXAFS oscillation arises from the interference between the final state and initial state of the photoelectron. Briefly, the EXAFS spectrum depends on the arrangement and the species of the neighboring atoms that scatter the photoelectrons.

XAFS spectroscopy is useful for the analysis of the chemical state of a specific atom and the local structure around it [18]. In particular, it enables us to obtain structural information even on a material with low crystallinity that exhibits no distinct diffraction peak.

However, this method requires an intense X-ray source with energy selectivity. Synchrotron radiation fulfils these conditions. The permeation of synchrotron radiation has proven XAFS spectroscopy to be highly advantageous.

EXAFS analysis is generally performed according to a procedure formulated [19] on the basis of Fourier transformation. The EXAFS function $\chi(k)$, where k is the wave number of photoelectrons, can be derived from the observed absorption spectra $\mu(E)$ after background removal, normalization and E-k conversion. Namely, the normalized EXAFS function is defined by

$$\chi(k) = (\mu(k) - \mu_0(k))/\mu_0(k) \tag{9.1}$$

The background $\mu_0(k)$ consists of the gradual oscillation that an isolated absorbing atom must show on the absorption spectrum. It is usually obtained from experimental data by a mathematical smoothing method. The value of k is expressed in terms of the mass of a photoelectron, m, the photon energy of an X-ray, E, the edge energy of the absorbing atom, E_0, and Planck's constant, $\hbar(= h/2\pi)$, as

$$k = [2m(E - E_0)/\hbar^2]^{1/2} \tag{9.2}$$

The Fourier transform of $\chi(k)$ provides the one-dimensional radial structure function (RSF) which contains such information as the number and kind of neighboring atoms and their distances away from the absorbing atom. The peak position in the RSF is ordinarily shifted by 0.02–0.05 nm in the negative direction from the actual distance between the absorbing and neighboring atoms because the phase shift correction is not taken into account.

A single-shell contribution to the EXAFS oscillation can be isolated by Fourier filtering of the EXAFS data. Namely, the single-shell EXAFS oscillation can be obtained by inverse Fourier transformation of the RSF multiplied by a window function. Curve fitting by the least-squares method is aimed at obtaining the best fit of the filtered EXAFS oscillation to a plane wave and the single scattering EXAFS formula using

$$\chi(k) = \frac{N}{kR^2} f(k) \exp(-2\sigma^2 k^2) \exp(-2R/\lambda) \sin(2kR + \phi) \tag{9.3}$$

where N is the coordination number, R is the atomic distance, and σ is the Debye-Waller factor. These are parameters for determining the local structure around the absorbing atom. The term λ is the mean free path of a photoelectron. The photoelectron backscattering factor $f(k)$ and phase shift ϕ are obtained theoretically. As a measure of the fit, the residual (R-factor) is defined by

$$R = \frac{\sum(k^n \chi_{\mathrm{obs}} - k^n \chi_{\mathrm{calc}})^2}{\sum(k^n \chi_{\mathrm{obs}})^2} \tag{9.4}$$

where n is a weighting factor used in Fourier transformation, and the subscripts 'obs' and 'calc' denote observed and calculated values, respectively. Unfortunately, we still have no analytical procedure for XANES spectra. XANES studies are usually performed for the characterization or identification of an unknown material by comparing its XANES spectrum to that of reference materials. However, several methods in which the molecular orbital method or multiple-scattering theory is applied have recently been developed.

9.3.2 Sample Preparation

We prepared three rust samples for XAFS measurements. A powder sample of atmospheric rust was gathered from a weathering steel specimen after a

long-term exposure test [7]. The test specimen was provided by The Public Works Research Institute, Japan Association of Steel Bridge Construction and The Japan Iron and Steel Federation. The corrosion product of an Fe-Cr alloy film corroded in the laboratory [16] and artificial goethite [13, 15] were employed for comparison.

(1) Atmospheric Rust on Weathering Steel

The weathering steel specimen with dimensions of 100 mm (w) × 150 mm (l) × 8 mm (t) was supported horizontally and was exposed to the atmosphere underneath the girder of a bridge at Yokkaichi, Japan, for 17 years. The chemical composition of the steel is listed in Table 9.1. This exposure site can be categorized as an industrial zone, with an airborne salt content and atmospheric SO_2 content of 0.041 and 0.109 mdd (mg/100 cm^2/day), respectively. The total corrosion loss per single side of the steel was 0.106 mm, which is a typical value for weathering steel in an industrial zone. The corrosion rate after 17 years of exposure was 0.006 mm/year. This is comparable to the passivity-maintaining current density for stainless steel and is sufficiently low for weathering steel. Thus, the rust layer can be categorized as a protective one. The thickness of the rust layer formed on the skyward and earthward surfaces was 0.18 and 0.14 mm, respectively.

A rust sample was removed from the skyward surface using a razor until the steel surface became visible, and the sample was ground into powder. The powdered rust sample was desiccated for one week prior to the experiments.

(2) Corrosion Product of Fe-Cr Alloy Film

The rust layer of weathering steel actually used outdoors contains many species of atmospheric pollutants and alloying elements. In order to enhance the effect of Cr, it is meaningful to employ the rust layer formed in a simplified system as a reference material. For this reason, Fe-Cr film was corroded in a laboratory and the rust sample was obtained from it.

Fe-5 mass% Cr alloy film with a thickness of 100 nm was vapor deposited onto a Si(100) single-crystal substrate. The concentration of Cr in the alloy film was selected to be approximately ten times higher than that in weathering steel to study the effect of Cr on the structure of a rapidly formed rust layer. The surface of the alloy film was covered with 100 μm thick (0.1 kmol/m^3 Na_2SO_4 + 0.005 kmol/m^3 H_2SO_4) electrolyte film, and the

Table 9.1. Chemical composition of weathering steel (in mass%)

C	Si	Mn	P	S	Cu	Cr	Ni	Nb
0.12	0.39	0.9	0.008	0.006	0.36	0.61	0.22	0.014

sample was placed inside an airtight receptacle for approximately 200 h at room temperature. The Fe-Cr alloy film was rapidly and completely corroded under these conditions and, finally, the rust layer was formed. The thickness of the electrolyte film was adjusted to simulate atmospheric corrosion under very thin layers of electrolytes where a large Tafel slope can be observed due to essentially complete coverage by an intermediate corrosion product, which amounts to partial passivation of the metal surface [20]. The relative humidity of the air in the receptacle was fixed by initially placing a large amount of the same electrolyte in the receptacle, which allowed the water vapor pressure of the electrolyte film to equilibrate under controlled humidity so that the chemical composition and thickness of the electrolyte film were kept constant.

(3) Artificial Goethite

Pure goethite and Cr-goethite with 1.5, 3 and 10 mass% Cr powder samples were prepared as additional reference materials by the following synthesis method: $2.50 \times 10^{-4}\,m^3$ solution of $0.6\,kmol/m^3$ $FeSO_4(NH_4)_2SO_4 \cdot 6H_2O$, Mohr's salt (outgassed with N_2 beforehand) was titrated to pH 13.2–13.5 with 4 mass% NaOH solution with stirring. The solution was hydrolyzed for 30 h at room temperature and $Cr_2(SO_4)_3$ was added so that the mole ratio Cr(III)/Fe(II) became the desired value. The suspension was diluted to $1.0 \times 10^{-3}\,m^3$ with ion-exchanged water. After stirring, the suspension was air oxidized for 20 h and was aged for 14 days. The precipitate was washed and dried repeatedly and collected in a Büchner funnel. The product was washed with ion-exchanged water until alkaline reaction with phenolphthalein was no longer observed and, finally, the product was dried.

9.3.3 Measurements and Results

The EXAFS measurements using synchrotron radiation X-rays were carried out at BL27B of the Photon Factory (PF) in Tsukuba, Japan. The synchrotron radiation with a white spectrum from a bending magnet was monochromatized with a Si(111) double-crystal monochromator. To eliminate the higher harmonics, the monochromator was detuned so that the intensity of the monochromatized beam was 40–50% of the maximum at each absorption edge. Energy calibration was based on the well-known absorption edge of 5.989 keV for metallic Cr and that of 7.113 keV for metallic Fe.

Figure 9.1 shows the Cr K-edge EXAFS spectra of the artificial Cr-goethite powders. Figure 9.2 shows those of the rust layers of Fe-5 mass% Cr alloy film, 3 mass% Cr-goethite and 10 mass% Cr-goethite. That of the rust layer formed on the weathering steel is shown in Fig. 9.3. All absorption spectra show similar features as a function of photon energy.

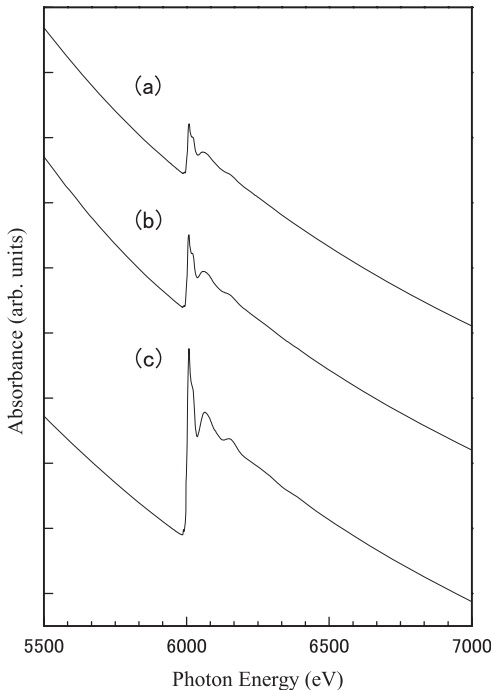

Fig. 9.1. Cr K-edge EXAFS spectra of artificial Cr-goethite taken in the transmission mode. The Cr content is (**a**) 1.5, (**b**) 3.0 and (**c**) 10 mass%

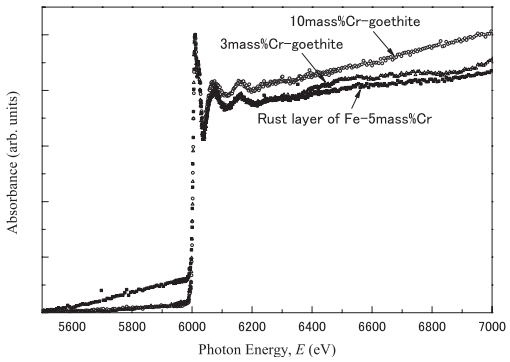

Fig. 9.2. Cr K-edge EXAFS spectra of Fe-5 mass% Cr alloy film, artificial 3 mass% Cr-goethite, and artificial 10 mass% Cr-goethite, taken in the fluorescence mode

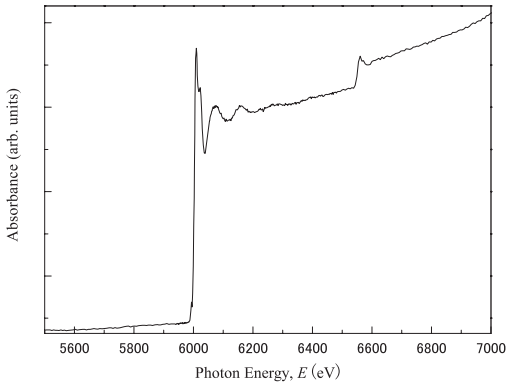

Fig. 9.3. Cr K-edge EXAFS spectrum of rust layer on weathering steel exposed horizontally to the atmosphere for 17 years underneath the girder of a bridge at Yokkaichi, taken in the fluorescence mode

Because the weathering steel contains 0.90 mass% Mn that is inevitably transferred to the rust layer, a small bump at the Mn K-edge is also seen at 6.539 keV in Fig. 9.3. Thus, the spectra obtained at energies lower than the Mn K-edge were further analyzed.

The observed photon energy of the Cr K-edge was 5.995 keV, i.e., 6 eV more positive than that of metallic Cr, which is consistent with the trivalent Cr^{3+} absorption edge reported previously [21]. In addition, the well-known pre-edge peak at 5.985 keV for hexavalent Cr^{6+} was not observed in any XAFS spectrum. This indicates that no Cr^{6+} is contained in the goethite structure. These results reveal that the oxidation state of most Cr ions in the rust layers is +3.

Figure 9.4 shows the normalized EXAFS spectra as a function of k after background removal, normalization and $E-k$ conversion, $k^3\chi(k)$, of artificial 3 mass% Cr-goethite, the corrosion product of the Fe-Cr alloy film and the rust layer on the weathering steel around the Cr K-edge. These spectra are very similar, which indicates that the local structures around Cr in artificial Cr-goethite and rust layers are almost the same. Therefore, it can be said that most Cr in the rust layers is contained in Cr-goethite.

The normalized Fe K-edge EXAFS function of pure goethite and the normalized Cr K-edge EXAFS function of 3 mass% Cr-goethite are shown in Fig. 9.5. It must be noted that the peaks indicated by arrows in the Fe K-edge spectra are not observed in the Cr K-edge spectra. Similar differences are observed between the normalized Cr K-edge EXAFS spectrum of the rust layer on the weathering steel and the normalized Fe K-edge EXAFS spectrum of pure goethite in Fig. 9.6. These results indicate that the local structure around Cr in Cr-goethite is different from that around Fe in the goethite structure. Most Cr in Cr-goethite is not positioned at the Fe lattice point as a substitutional element in the goethite structure.

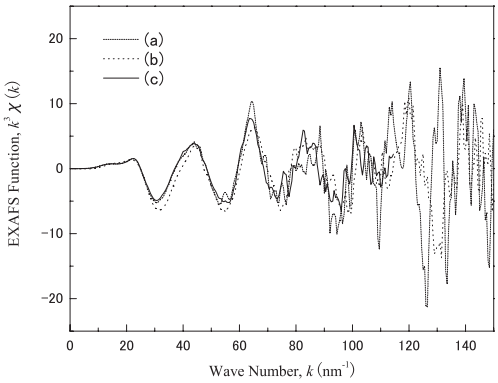

Fig. 9.4. Normalized Cr K-edge EXAFS spectra as a function of wave number, $k^3\chi(k)$, of (**a**) artificial 3 mass% Cr-goethite, (**b**) rust layer of Fe-Cr alloy film, and (**c**) rust layer of weathering steel

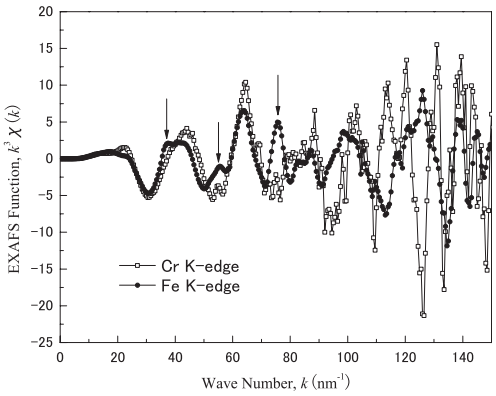

Fig. 9.5. Normalized EXAFS spectra of artificial 3 mass% Cr-goethite at Cr and Fe K-edges measured using PF synchrotron radiation X-rays. *Arrows* indicate characteristic peaks of the Fe K-edge spectrum

Figures 9.7 and 9.8 show the Fourier transforms, i.e., the radial structure functions (RSFs), of the Cr K-edge EXAFS spectra of the corrosion product of the Fe-Cr alloy film and the rust layer on the weathering steel, respectively, with those of artificial goethite powders at Fe or Cr K-edges. The RSFs are not phase corrected; hence, the peak positions are shifted to approximately 0.06 nm in the negative direction from the actual distances. The strongest peak in the RSF around Cr appears at approximately 0.16 nm; the corresponding corrected distance is estimated to be 0.16–0.20 nm. Because the oxidation state of Cr is considered to be +3 and the ionic radii of Cr^{3+}, Fe^{3+}, Fe^{2+} and O^{2-} are 0.07, 0.075, 0.069 and 0.13 nm, respectively, as is generally known, this most intense peak must originate from a nearest-neighbor

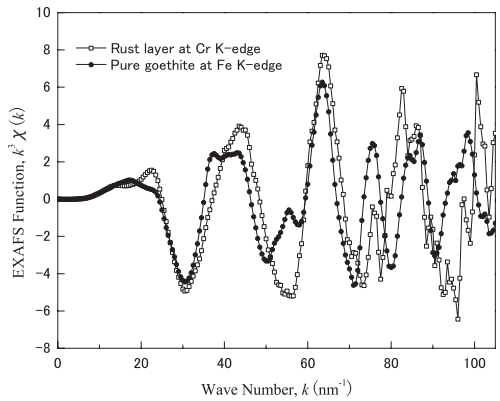

Fig. 9.6. Normalized EXAFS spectrum of rust layer on weathering steel exposed horizontally to the atmosphere for 17 years underneath a girder of a bridge at Yokkaichi, at Cr K-edge, and that of pure goethite at Fe K-edge measured using PF synchrotron radiation X-rays

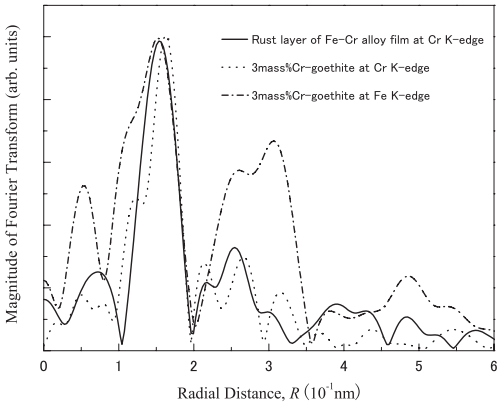

Fig. 9.7. Fourier transforms of the EXAFS spectra of rust layer of Fe-5 mass% Cr alloy film at Cr K-edge and those of artificial 3 mass% Cr-goethite powder at Fe and Cr K-edges

O^{2-} with an ionic radius of 0.13 nm. Therefore, these results reveal that most Cr^{3+} ions are coordinated with O^{2-} ions in the rust.

The above Cr–O distance is not markedly different from the nearest Fe-O bonding length, 0.196 nm, in the goethite structure which gives the strongest peak in the RSF around Fe^{3+} in artificial pure goethite and in 3 mass% Cr-goethite. However, it should be noted that the peaks corresponding to the next nearest-neighbor Cr–Fe and/or the Cr–Cr distance do not appear clearly in the RSFs, as shown in Figs. 9.7 and 9.8, compared with the RSF around Fe^{3+} in artificial Cr-goethite. In other words, a lower correlation was obtained above 0.20 nm in the RSF around Cr^{3+}.

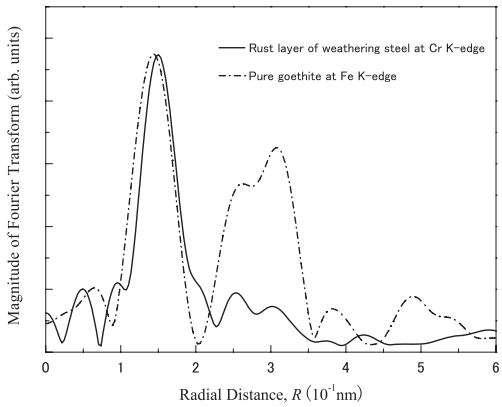

Fig. 9.8. Fourier transforms of EXAFS spectra of rust layer on weathering steel exposed horizontally to the atmosphere for 17 years underneath a girder of a bridge at Yokkaichi, at Cr K-edge, and that of pure goethite at Fe K-edge

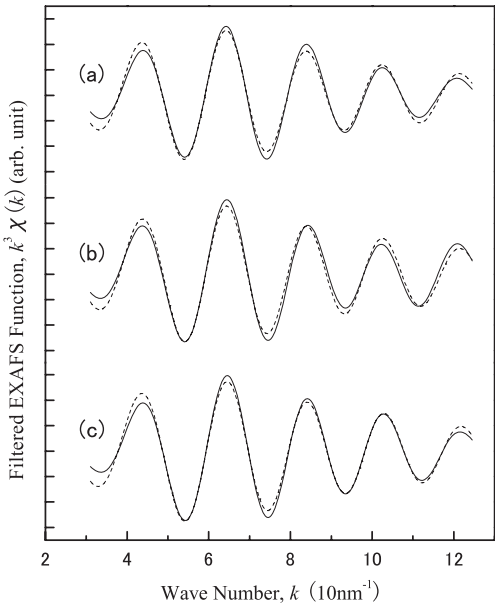

Fig. 9.9. Inverse Fourier transforms of the first peak of Fourier transformed data. *Dashed curves* are the best fit results with the single distance model: (**a**) 1.5 mass% Cr-goethite; (**b**) 3 mass% Cr-goethite; (**c**) 10 mass% Cr-goethite

As all the RSFs exhibit similar features, the number of O^{2-} ions coordinating with Cr^{3+} in only artificial Cr-goethite was calculated [22]. Figure 9.9 shows Fourier-filtered EXAFS oscillations obtained by inverse Fourier transformation of the first peaks of the RSFs of the Cr-goethite powders multiplied

by the Hanning function. Curve fitting for the first shell data was performed in order to obtain local structural parameters. No specific structural model of the CrO_x^{3-2x} complex ion was used in the analysis. However, it was assumed that Cr^{3+} was coordinated with O^{2-} at a constant distance.

In the curve fitting, the photoelectron backscattering factor $f(k)$ and phase shift ϕ are obtained from McKale's table [23] automatically in the software. However, in general it is difficult to obtain a precise value of λ, the mean free path of a photoelectron, theoretically. Although λ is strictly a function of k, its k-dependence is usually neglected and λ is regarded as a constant in the calculation. Because of the weak dependence of λ on the absorbing atom species, the λ obtained from the EXAFS data around the Fe K-edge of pure goethite, the structure of which is well known, was adopted for the EXAFS analysis of the Cr-goethite powders. As Fe is positioned at the center of the $Fe(OH)_3O_3$ octahedron in the goethite structure, the coordination number of Fe in pure goethite was fixed at 6 in the curve-fitting calculation for the pure goethite EXAFS data around the Fe K-edge. The term λ was regarded as a fitting parameter in this calculation. The analytical results for pure goethite are listed with errors in Table 9.2. The value of λ obtained was used in the analysis of the EXAFS data around the Cr K-edge for artificial Cr-goethite. Curve fitting was performed for each sample using the minimum, central and maximum values of λ in the range of its error.

The best-fit structural parameters are listed in Table 9.3. The R-factors for the successive fittings using different λ values are almost identical. Accordingly,

Table 9.2. EXAFS analytical results for artificial pure goethite (Cr = 0%). The coordination number N was fixed at 6 in the calculation

N	r_{Fe-O} (10^{-1}nm)	σ_{Fe-O} (10^{-1}nm)	λ (10^{-1}nm)	R-factor
6	1.992±0.018	0.107±0.019	3.206±0.415	5.43

Table 9.3. EXAFS analytical results for artificial Cr-goethite. The photoelectron mean free path λ was fixed at minimum, central and maximum values in the error range obtained for artificial pure goethite

	λ (10^{-1}nm)	N	r_{Cr-O} (10^{-1}nm)	σ_{Cr-O} (10^{-1}nm)	R-factor
1.5 mass%	2.8	8.457±0.450	1.999±0.004	0.056±0.008	2.216
Cr-goethite	3.2	7.023±0.373	1.999±0.004	0.056±0.008	2.214
	3.6	6.090±0.323	1.999±0.004	0.056±0.008	2.216
3 mass%	2.8	8.361±0.414	1.999±0.004	0.049±0.008	2.423
Cr-goethite	3.2	6.933±0.344	1.999±0.004	0.049±0.008	2.424
	3.6	6.013±0.298	1.999±0.004	0.049±0.008	2.426
10 mass%	2.8	8.470±0.411	1.990±0.004	0.049±0.008	2.000
Cr-goethite	3.2	7.045±0.341	1.990±0.004	0.049±0.008	2.001
	3.6	6.112±0.296	1.990±0.004	0.049±0.008	2.003

it was found that the coordination number is approximately (7 ± 1). Its inaccuracy could be due to the error in λ in this study.

9.3.4 Structural Properties of the Protective Rust Layer

The oxidation state of Cr in the goethite structure is estimated to be +3, Cr^{3+}, from the absorption edge. By considering a spatial site in the network of $Fe(OH)_3O_3$ octahedra, there are considered to be two possible sites for Cr^{3+} in the goethite structure: one is the substitutable Fe^{3+} site and the other is in the double chains of vacant sites.

The Cr K-edge EXAFS spectra for the artificial Cr-goethite powders and the rust layers were almost identical. Those spectra are different from the Fe K-edge spectrum of pure goethite and Cr-goethite. The peaks above 0.20 nm in the RSF around the Cr K-edge of Cr-goethite and rust layers were not clearly observed in comparison with those of the RSF around the Fe K-edge. The RSFs around the Fe K-edge show two strong peaks at around 0.26 and 0.32 nm corresponding to the nearest-neighbor Fe-Fe distance, which is approximately 0.30–0.35 nm, in the goethite structure. Therefore, there is a lower correlation above 0.20 nm around Cr^{3+} in the rust layers. These results indicate that most Cr^{3+} ions do not substitute into the Fe^{3+} sites at the centers of the $Fe(OH)_3O_3$ octahedra because the Fe^{3+} site should be strongly correlated to the neighboring Fe^{3+} sites. Therefore, it is suggested that Cr^{3+} ions are located in the double chains of vacant sites in Cr-goethite in the rust layer, where no coordination geometry is defined by surrounding ions, except for the nearest-neighbor O^{2-}; namely, there is no fixed distance between Cr^{3+} and neighboring Fe^{3+} or Cr^{3+}.

Kimura et al. [24] mentioned similar interstitial sites for Cr^{3+} in the rust layer of weathering steel. They considered that $Cr(O, OH)_6$ octahedra may be formed, but that the units were strongly deformed or that Cr atoms occupy a different type of site than those of Fe atoms. In both cases, however, they did not point out the presence of O^{2-} coordinated with Cr^{3+} at the interstitial sites.

The most characteristic protective effect of the rust layer on weathering steel can be attributed to the cation selectivity of Cr-goethite. Generally, the cation selectivity of materials can be interpreted in terms of the presence of fixed negative charges. Because the oxidation state of Cr in goethite is +3, the substitution of Cr^{3+} for Fe^{3+} or for interstitial Cr^{3+} itself does not result in a fixed negative charge. Thus, Cr^{3+} in the double chains of vacant sites is expected to explain the presence of the negative charge.

While the picture is still not fully understood, the probable site of Cr^{3+} is explained in the following way. From the above results, it was shown that Cr^{3+} in the rust layer is coordinated with (7 ± 1) O^{2-}. Accordingly, Cr^{3+} forms a negatively charged complex ion ${CrO_x}^{3-2x}$. The complex ion provides negative charge to goethite, leading to cation selectivity. Because of the insufficient spacing, this complex anion cannot substitute into the Fe^{3+} lattice

site in the $Fe(OH)_3O_3$ octahedron. As a logical consequence, the CrO_x^{3-2x} complex anion should be positioned in the double chains of vacant sites. Because the CrO_x^{3-2x} complex anion has a much larger volume than Fe^{3+}, it may distort and possibly break the double chains of vacant sites, which destroys any definite coordination geometry between Cr^{3+} and neighboring Fe^{3+} and/or Cr^{3+}. Consequently, this collapse of the double chains of vacant sites causes the formation of the ultrafine crystals of Cr-goethite, and the CrO_x^{3-2x} complex anion should be located at the surface and/or grain boundary of the Cr-goethite crystals.

9.4 In situ Observation of Corrosion Process in Wet/Dry Cycles

Atmospheric corrosion proceeds under a very thin electrolyte film containing many kinds of ions, which are dissolving elements from steel and corrosive ions from the atmosphere. A small amount of a corrosion product can appreciably change the composition, and the amount of corrosion product can very quickly exceed the solubility limit. Then an irresoluble corrosion product covers the steel surface. This process is the initial stage of rust layer formation. Many chemical reactions proceed in this process. In order to understand the effect of alloying elements on the protective rust layer, it is necessary to know how those alloying elements affect the formation process of the rust layer.

As discussed in the previous section, Cr plays the most important role among anticorrosive alloying elements on the protective property of the rust layer formed on weathering steel. However, it is known that the effect of Cr on the formation of the protective rust layer decreases markedly in a saline environment. In contrast, the increase of the mass percent of Ni as an alloying element is very effective in reducing the corrosion rate in the saline environment. Therefore, it is meaningful to compare the corrosion processes of Fe-Cr and Fe-Ni alloys under chloride solution film.

In the present study, we carried out in situ observation of the rust layer formation process on Fe-Cr and Fe-Ni alloys under well-defined conditions with special attention focused on the effect of alloying Cr and Ni [25]. For comparison, we employed 3.5% NaCl solution and 3.5% Na_2SO_4 solution as electrolyte films. A corrosion chamber was designed to promote the wet/dry cycle of the thin electrolyte film on the surface of the specimen. Energy dispersive X-ray diffraction with synchrotron radiation white X-rays allowed easy real-time observation of the rust layer formation process.

9.4.1 Experimental Method

(1) Design of Corrosion Chamber

A photograph of a specially designed corrosion chamber is shown in Fig. 9.10. This chamber is made of transparent acrylic resin. The chamber was fixed to a

Fig. 9.10. Photograph of specially designed corrosion chamber

swivel stage which rotates it from a level position. Two water receptacles were made inside the chamber. Relative humidity inside the chamber is controlled by water injected into and drained from the receptacles, and by changing the flow rate of dry air (N_2 base + 21% O_2) supplied into the chamber from an air cylinder. The relative humidity and temperature of the inside were recorded with an electronic hygrothermograph installed at the lid of the chamber. In order to reduce the absorption of X-rays, X-ray windows were made of Kapton (polyimide film). The corrosion chamber was surrounded by Pb shield plates to reduce the background level in the X-ray diffraction measurement.

(2) Experimental Procedure

Specimens employed for this study were Fe-5 mass%Cr and Fe-9 mass%Ni alloys. They were prepared by vacuum melting of 99.9%-pure materials. Their dimensions were 10 mm × 10 mm × 3 mm. Their surfaces were polished by a series of emery paper up to #600.

Before the in situ observation, the surface of a specimen, placed in the corrosion chamber, was covered with thick electrolyte film of solution poured with a syringe. The surface of the specimen was tilted by 1° off the horizontal by adjusting the swivel table, then X-rays impinged on the surface with a 1° incidence angle. The inner relative humidity reached 95% after putting on the lid. Subsequently, the thickness of the electrolyte film on the specimen must be kept constant. After the wet stage of 2 h, dry air was supplied into the chamber, so that relative humidity was reduced to below 30%. In this dry stage, the electrolyte film evaporated within 1 h. At the beginning of the next wet stage, distilled water was again poured onto the dry surface of the steel. X-ray diffraction measurement was continuously and repeatedly performed during the cyclic wet and dry stages.

The X-ray diffraction experiments were carried out at BL14B1 of SPring-8. Since this beamline is installed at the bending magnet section, white X-rays with rectangular cross section of 50 μm (vertical) × 500 μm (horizontal)

can be used. X-ray diffraction measurements were carried out by an energy dispersive method with a Si solid-state detector. The incident angle and 2θ were fixed at 1.0° and 3.5°, respectively. The diffraction measurement with 5 min integrated time was repeated.

9.4.2 Results

(1) Initial Form of Corrosion Product

The corrosion products detected in the earlier wet/dry cycles were $Fe(OH)_2$ and $Fe(OH)_3$ independent of alloying elements and ion species in the electrolyte film. $Fe(OH)_3$ is formed by oxidation of $Fe(OH)_2$. X-ray diffraction spectra of the rust on the Fe-Cr alloy under the Na_2SO_4 solution in the first several wet/dry cycles is shown in Fig. 9.11 as an example. Observed

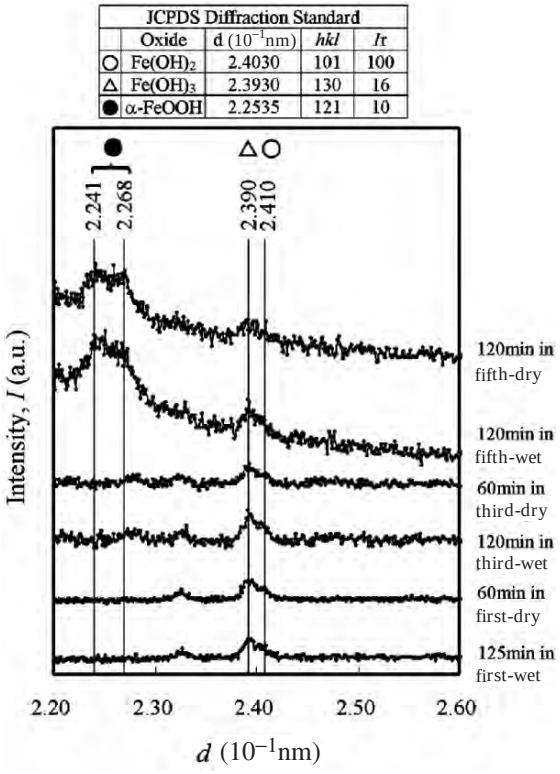

Fig. 9.11. X-ray diffraction spectra of corrosion products formed on Fe-5 mass% Cr alloy under 3.5% Na_2SO_4 solution film between first and fifth wet/dry cycles. Each spectrum was obtained at the corresponding time in the wet or dry stage indicated at the right-hand side of the spectrum. Observed diffraction peaks are compared with JCPDS diffraction standards indicating candidate oxide, *d*-value, crystal plane *hkl* and relative intensity *Ir*

diffraction peak positions are compared with standard diffraction data in JCPDS [26]. Obtained d-values indicated in the figure were found to deviate slightly from the bibliographic data. It probably shows that the corrosion products in the initial stage of the corrosion process have lower crystallinity. Those initial corrosion products were subsequently transformed mainly to polymorphs of FeOOH, depending on the alloying elements and ion species in the electrolyte film.

(2) Corrosion Process of Fe-Cr Alloy

Figure 9.12 shows the X-ray diffraction spectra of the rust on the Fe-Cr alloy under the Na_2SO_4 solution after the seventh wet/dry cycle. Very weak diffraction peaks were detected in all cycles. The most distinct peak arises due to the formation of α-FeOOH.

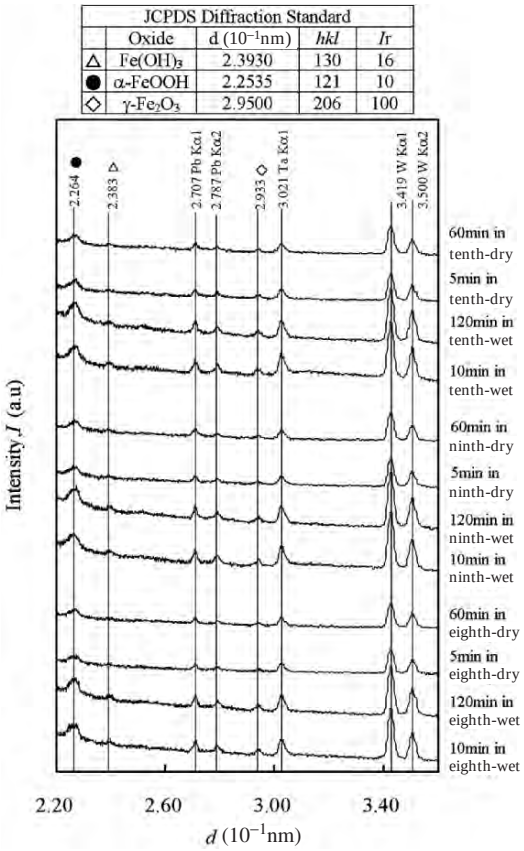

Fig. 9.12. X-ray diffraction spectra of corrosion products formed on Fe-5 mass% Cr alloy under 3.5% Na_2SO_4 solution film between eighth and tenth wet/dry cycles

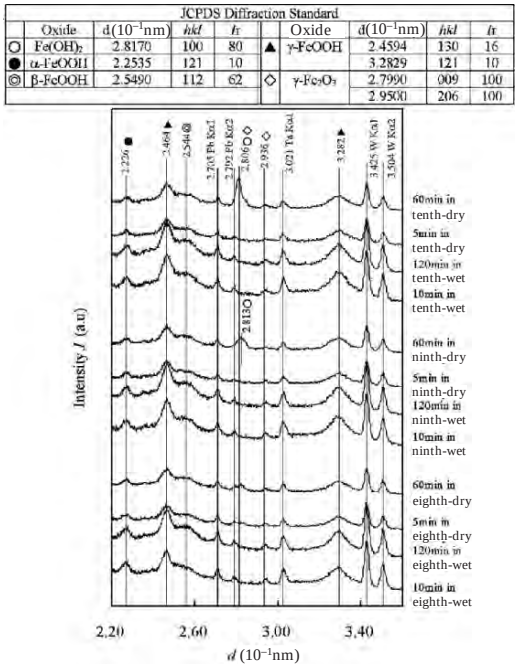

Fig. 9.13. X-ray diffraction spectra of corrosion products formed on Fe-5 mass% Cr alloy under 3.5% NaCl solution film between eighth and tenth wet/dry cycles

The X-ray diffraction spectra of the rust on the Fe-Cr alloy under the NaCl solution after the seventh wet/dry cycle are shown in Fig. 9.13. A relatively distinct peak due to γ-FeOOH was observed as well as weak peaks originating from α-FeOOH and β-FeOOH. The α-FeOOH peak height was comparable to that observed in the case of the Na_2SO_4 solution. This indicates that the Na_2SO_4 solution suppresses the growth of γ-FeOOH crystal compared with the NaCl solution. The observation of β-FeOOH is consistent with the fact that β-FeOOH is often found in the rust layer on steel exposed to a saline environment [7].

(3) Corrosion Process of Fe-Ni Alloy

The X-ray diffraction spectra of the rust on the Fe-Ni alloy under the Na_2SO_4 solution and the NaCl solution after the seventh wet/dry cycle are shown in Figs. 9.14 and 9.15, respectively.

For the corrosion process under the Na_2SO_4 solution, the most distinct diffraction peaks in Fig. 9.14 indicate the formation of α-FeOOH. In addition, a certain amount of γ-FeOOH was probably formed. From the present results, it can be concluded that the preferential formation of α-FeOOH under the Na_2SO_4 solution occurs on both Fe-Cr and Fe-Ni alloys.

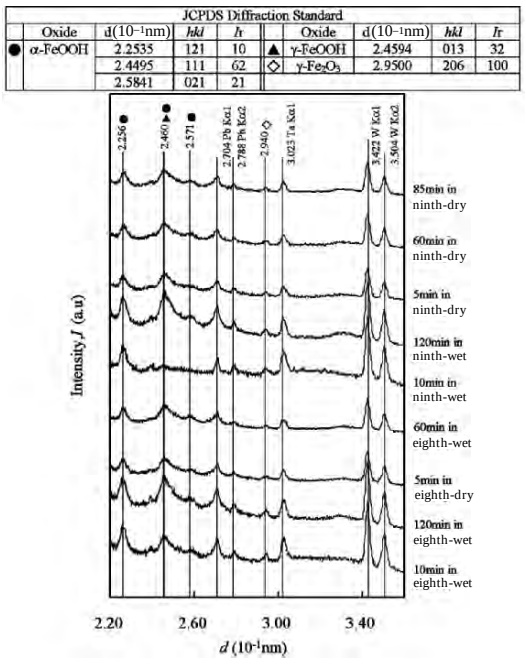

Fig. 9.14. X-ray diffraction spectra of corrosion products formed on Fe-9 mass% Ni alloy under 3.5% Na_2SO_4 solution film between eighth and ninth wet/dry cycles

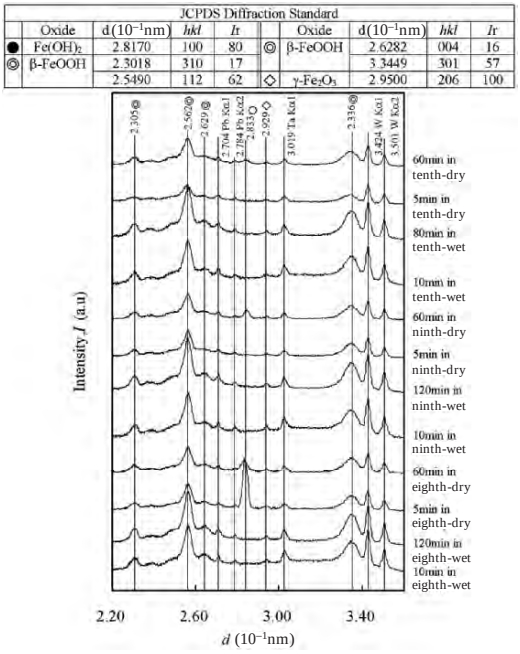

Fig. 9.15. X-ray diffraction spectra of corrosion products formed on Fe-9 mass% Ni alloy under 3.5% NaCl solution film between eighth and tenth wet/dry cycles

It was clearly found that the formation of β-FeOOH was predominant in the corrosion process of the Fe-Ni alloy under the NaCl solution, as shown in Fig. 9.15. Usually, the mass fraction of β-FeOOH is less than that of α-FeOOH after long-term exposure of a conventional weathering steel to high-salinity environments [7], as mentioned previously. Moreover, the diffraction peak of β-FeOOH observed on the corrosion process of the Fe-Cr alloy was very weak, as shown in Fig. 9.13. Thus, it can be said that the predominant formation of β-FeOOH is promoted by a larger amount of Ni used as an alloying element.

9.4.3 Discussion

$Fe(OH)_2$ and $Fe(OH)_3$ were formed at early wet/dry cycles. These initial corrosion products were transformed mainly to polymorphs of FeOOH. This transformation probably results from the dissolution of Fe^{2+} ion from the Fe-based alloys and subsequent oxidation and dehydration. As we could see a separation or shift of the diffraction peaks due to FeOOH products from their bibliographic d-value, these corrosion products are not well crystallized in the early several wet/dry cycles, as shown in Fig. 9.11.

The distinct diffraction peaks due to α-FeOOH were observed both for the Fe-Cr alloy and for the Fe-Ni alloy under the Na_2SO_4 solution. Therefore, it can be said that SO_4^{2-} ion promotes the formation of α-FeOOH. Cornell and Schwertmann [2] also pointed out the similar effect of SO_4^{2-} ion. On the other hand, Tamaura et al. [27] showed that air oxidation of $Fe(OH)_2$ suspension under a low concentration of SO_4^{2-} ions results in the formation of Fe_3O_4, and that α-FeOOH is preferentially formed at the SO_4^{2-} ion concentration of 0.1 M. In the present experiment, the concentration of SO_4^{2-} ions was higher than 0.1 M; thus the preferential formation of α-FeOOH on the Fe-based alloys is consistent with the above arguments. The diffraction peaks due to α-FeOOH on the Fe-Cr alloy were very weak compared with those on the Fe-Ni alloy in the case of the Na_2SO_4 solution. This is consistent with the effect of Cr on the formation of ultrafine crystal of α-FeOOH, as mentioned previously.

It should be noted that β-FeOOH is observed only under the NaCl solution both for the Fe-Cr alloy and for the Fe-Ni alloy. It is generally known that the rust layer formed on steel in a high-salinity environment contains a certain amount of β-FeOOH [7]. The structure of β-FeOOH consists of parallel double chains of edge-shared $FeO_3(OH)_3$ octahedra that form tunnels bounded by double rows of corner-shared chains [2]. The tunnels in β-FeOOH can be stabilized by Cl^- ions. This might be the reason why β-FeOOH was formed under the NaCl solution film. It should also be noted that the formation of β-FeOOH is much more predominant for the Fe-Ni alloy than for the Fe-Cr alloy under the NaCl solution. This preferential formation of β-FeOOH must inevitably be due to the effect of the large amount of Ni^{2+} ions dissolved from the Fe-Ni alloy under the NaCl solution film.

The relationship between the high corrosion resistance due to Ni alloying and the preferential formation of β-FeOOH for the Fe-Ni alloy under

the NaCl solution is unclear. We assume that β-FeOOH containing a certain amount of Ni possesses some effective properties for protecting corrosives, for example, the ability to trap Cl^- ions in the crystal and/or cation selectivity. The crystal symmetry of akaganéite (β-FeOOH), usually observed in the rust layer on a conventional weathering steel exposed to the atmosphere, is tetragonal. However, it has been pointed out by Post and Buchwald [28] that akaganéite found in an iron-nickel meteorite is monoclinic and contains Ni and Cl, $Fe_{7.6}Ni_{0.4}O_{6.35}(OH)_{9.65}Cl_{1.25}$. In addition, Yamashita et al. [29] pointed out that the rust layer formed on weathering steel containing 0.5%Cr-0.3%Cu-0.06%P-0.5%Ni under a NiSO4 solution includes monoclinic akaganéite. Those arguments imply that the preferential formation of akaganéite in the corrosion process of the Fe-Ni alloy probably results from the coexistence of Ni^{2+} and Cl^- ions in the electrolyte film covering the alloy surface. Although the properties of the monoclinic akaganéite are not known, it is expected that the coexistence of Ni^{2+} and Cl^- ions on the atmosphere corroded surface of a Fe-based alloy results in the formation of a considerable amount of monoclinic akaganéite.

9.5 Summary

We applied synchrotron radiation to XAFS and diffraction experiments for the structural study of the rust layer on steel and Fe-based alloys, focusing on the protective ability of the rust layer formed by atmospheric corrosion. XAFS analysis is very effective for elucidating the local structural and chemical properties of a specific element in a substance. However, we cannot identify the local structure from a spectrum observed by this technique a priori. It merely allows the evaluation of the reasonability of the structure model being considered. Therefore, it is also necessary to examine the structure model from several aspects using various other experimental techniques. For example, anomalous dispersion X-ray diffraction using the tunability of synchrotron radiation is applicable for judging whether a specific atom is positioned at a certain site of the crystal structure of a material. We would like to apply this technique to determine the crystal site of Ni in the rust layer produced in a saline environment, which is expected to be in the β-FeOOH phase, in the near future.

It is difficult to detect the initial state of a corrosion product using the observation technique based on the diffraction method, because the initial corrosion product possesses low crystallinity. In addition, it is necessary to observe a complex ion as a precursor of a corrosion product in order to learn the details of the corrosion process. Thus, an in situ observation technique based on XAFS measurement is required. Energy dispersive XAFS (DXAFS) is developed in many synchrotron radiation facilities. This technique enables the measurement of time-dependent XAFS spectra with a time resolution less than about 50 ms using a white synchrotron radiation X-ray.

References

1. M. Yamashita, H. Miyuki, H. Nagano and T. Misawa: Corrosion Engineering, **43**, 26 (1994).
2. R. M. Cornell and U. Schwertmann: "*The Iron Oxides, 2nd ed.*", WILEY-VCH, Weinheim (2003).
3. M. Yamashita, H. Miyuki, Y. Matsuda, H. Nagano and T. Misawa: Corros. Sci., **36**, 283 (1994).
4. T. Misawa, K. Asami, K. Hashimoto and S. Shimodaira: Corros. Sci., **14**, 279 (1974).
5. M. Yamashita and H. Uchida: Hyper. Interact., **139/140**, 153 (2002).
6. H. Kihira, S. Ito and T. Murata: Corros. Sci., **31**, 383 (1990).
7. M. Yamashita, K. Asami, T. Ishikawa, T. Ohtsuka, H. Tamura and T. Misawa: Corrosion Engineering, **50**, 733 (2001).
8. T. Misawa, T. Kyuno, W. Suetaka and S. Shimodaira: Corros. Sci., **11**, 35 (1971).
9. J. Keiser, C. Brown and R. H. Heidersbach: J. Electrochem. Soc., **129**, 2686 (1982).
10. D. C. Cook, R. Balasubramanian, S. J. Oh and M. Yamashita: Hyper. Interact., **122**, 59 (1999).
11. M. Yamashita, T. Misawa, H. E. Townsend and D. C. Cook: J. Japan Inst. Metals, **64**, 77 (2000).
12. T. Kamimura, S. Nasu, T. Tazaki, K. Kuzushita and S. Morimoto: Mater. Trans., **43**, 694 (2002).
13. M. Yamashita, H. Miyuki, H. Nagano and T. Misawa: Proc. 13th Int. Corros. Congress, Melbourne, (1996) pp. 258.
14. T. Kamimura, M. Yamashita, H. Uchida and H. Miyuki: J. Japan Inst. Metals, **65**, 922 (2001).
15. H. Miyuki, M. Yamashita, M. Fujiwara and T. Misawa: Zairyo-to-Kankyo, **47**, 186 (1998).
16. M. Yamashita, T. Shimizu, H. Konishi, J. Mizuki and H. Uchida: Corros. Sci., **45**, 381 (2003).
17. M. Yamashita, H. Konishi, J. Mizuki and H. Uchida: Mater. Trans., **45**, 1920 (2004).
18. D. C. Koningsberger and R. Prins (eds.): "X-ray Absorption: Principles, Applications, Techniques of EXAFS", John Wiley & Sons, New York (1988).
19. B. K. Teo: "EXAFS: Basic Principles and Data Analysis", Springer-Verlag, Berlin (1986).
20. M. Yamashita, H. Nagano and R. A. Oriani: Corros. Sci., **40**, 1447 (1998).
21. S. W. M. Chung, G. E. Thompson, G. C. Wood, J. Robinson and K. Shimizu, Proceedings of the Symposium on X-ray Methods in Corrosion and Interfacial Electrochemistry, The Electrochemical Society. (A. Davenport and J. G. Gordon, eds.), **92-1** Pennington, NJ, pp. 325 (1992).
22. H. Konishi, M. Yamashita, H. Uchida and J. Mizuki: Mater. Trans., **46**, 337 (2005).
23. A. D. McKale, B. W. Veal, A. P. Pailikas, C. K. Chan and G. S. Knapp: J. Am. Chem. Soc., **110**, 3764 (1988).
24. M. Kimura, T. Suzuki, G. Shigesato, H. Kihira and S. Suzuki: ISIJ International, **42**, 1534 (2002).

25. M. Yamashita, H. Konishi, T. Kozakura, J. Mizuki and H. Uchida: Mater. Trans., **46**, 1004 (2005).
26. JCPDS, International Center for Diffraction Data, Newton Square (1995).
27. Y. Tamaura, P. V. Buduan and T. Katsura: J. C. S. Dalton, 1807 (1981).
28. J. E. Post and V. F. Buchwald: American Mineralogist, **76**, 272 (1991).
29. M. Yamashita, T. Yonezawa and H. Uchida: J. Jpn. Inst. Metals, **63**, 1332 (1999).

10 Analysis of Iron Rusts by X-ray Diffraction and X-ray Absorption Fine Structure Measurements

Takenori Nakayama, Tatsuo Ishikawa

10.1 Introduction

Recently, much attention has been devoted to steels with better atmospheric corrosion resistance especially in chloride environments of the various industries. For example, new weathering steels have been researched and developed, according to the increase of requirements of reduced initial construction and maintenance costs for steel bridges [1,2]. So far, uncoated conventional weathering steels for bridges have not been adopted in the chloride environments such as marine and coastal areas. This is because the steels encountered the formation of flaky rust with poor adherence, resulting in deterioration of corrosion resistance to the same level as that of mild steel. The amounts of de-icing salts have also been much increased due to the establishment of domestic laws banning tires with spikes being used on expressways since 1991. Thus, there have been great demand for new weathering steels that are resistant to chloride environments. It is thought that the improved resistance to atmospheric corrosion of steel could be due to the formation a protective rust layer preventing the intrusion of chloride species. β-FeOOH, one of the polymorphs of ferric oxy-hydroxides, is known as a component of corrosion products of steel in the presence of Cl^- ions [3]. The authors have recently found that corrosion resistance in chloride environments was well correlated to the formation of β-FeOOH rust and increased with the decrease of the fraction [4–6]. Shiotani et al. [7] and Yamashita et al. [8] have also confirmed good correlation between fraction of β-FeOOH rust and corrosion thickness loss of weathering steels involving on-site exposure tests at 41 bridges for periods of 17–18 years by Public Works Research Institute, Kozai Club, and Japan Association of Steel Bridge Construction [2]. The authors have found that Ti was effective as an alloying element to improve corrosion resistance of steel in chloride environments by decreasing the formation of β-FeOOH [4–6].

From the above, numerous studies on atmospheric corrosion of weathering steels have been carried out from the veiwpoint of composition, structure or various properties of the iron rusts, by using X-ray diffraction (XRD), electron diffraction (ED), transmission electron microscopy (TEM), infra-red spectroscopy (IR), laser Raman spectroscopy (LRS), Mössbauer spectroscopy, X-ray absorption fine structure (XAFS), electrochemical impedance spectroscopy (EIS), and so on. On the other hand, the authors have also been

conducting fundamental experiments involving artificial rust synthesis to elucidate the influence and role of various alloying elements on the formation of β-FeOOH rust [9]. As well as β-FeOOH, α-FeOOH, γ-FeOOH, Fe_3O_4 and poorly crystallized iron oxide (XRD amorphous rust) are also known as a major component of corrosion products of steel formed by atmospheric corrosion [1]. So far, Cr, Cu, and Ni have been widely used as alloying elements to improve resistance to atmospheric corrosion of steels [1]. Atmospheric corrosion resistance of steel is thought to be improved through the control of not only β-FeOOH but also α-FeOOH, γ-FeOOH, Fe_3O_4 and poorly crystallized iron oxide (XRD amorphous rust) by the addition of alloying elements such as Ti, Cr, Cu, and Ni.

This chapter reviews characterization techniques of iron rusts by X-ray diffraction (XRD) such as quantitative measurement of rust composition and estimation of rust crystallite size. Analysis of iron rusts by X-ray diffraction (XRD) and X-ray adsorption fine structure (XAFS) using ultra-bright synchrotron radiation (SR) are also explained. In addition, this chapter also introduces the study of artificial rust synthesis to elucidate improvement mechanism of resistance to atmospheric corrosion of weathering steel.

10.2 Rust Analysis by X-ray Diffraction (XRD)

10.2.1 Quantitative Measurement of Rust Composition

Quantitative measurement of rust composition has been conducted by X-ray diffraction (XRD) using the internal standard method. Figure 10.1 summarizes the experimental procedure for this method. As explained in the figure, the rust for analysis is first mixed with the sample for internal standard substance, and the quantitative value is then obtained from the comparison of relative diffraction intensity of each rust composition with the calibration curve. "Rust Science Research Group" in the Japan Society of Corrosion Engineering has examined and modified this quantitative measurement method and finally showed the standard guidelines [10]. ZnO powder with diameter size of 0.2–0.3 μm is selected as the internal standard substance from the standpoint of mixing uniformity. Figure 10.2 presents the calibration curves for α-FeOOH rust and X-ray intensity ratio to internal standard substance, comparing ZnO powder with CaF_2 powder used as conventional internal standard substance. It is obvious that ZnO powder is much better than CaF_2 powder as internal standard substances. Figure 10.3 presents the example of the quantitative measurement of actual rust composition, showing the thickness loss of mild steel (JIS SM), 0.3Cu-0.2Ni-0.5Cr steel, 0.3Cu-0.2Ni steel, and 0.3Cu-0.2Ni-0.1Ti steel exposed at Kakogawa Works' quay with the addition of 5% NaCl spray once a week for one year as a function of the fraction of β-FeOOH rust. It is found that the order of chloride corrosion resistance is

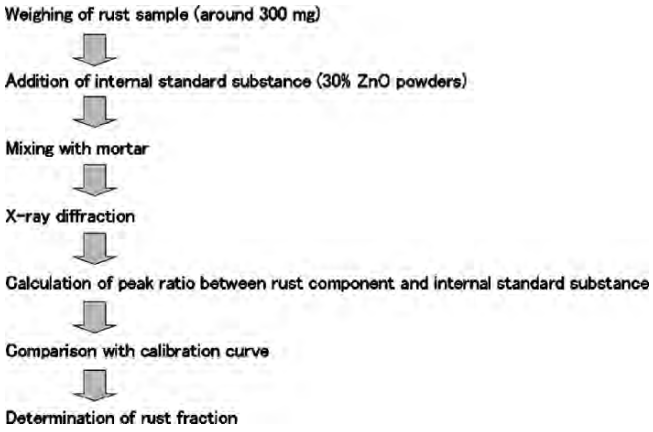

Fig. 10.1. Experimental procedure of quantitative measurements of rust composition

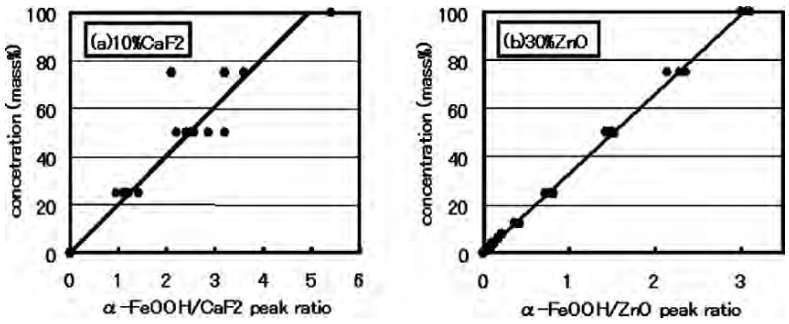

Fig. 10.2. Comparison of calibration curves of α-FeOOH rust and X-ray intensity ratio to internal standard substances. (**a**) CaF_2 powder used as conventional internal standard substance, (**b**) ZnO powder as recommended substance

0.3Cu-0.2Ni-0.1Ti steel >0.3Cu-0.2Ni steel >0.3Cu-0.2Ni-0.5Cr steel >mild steel (JIS SM), and the chloride corrosion resistance tends to increase with the decrease of the fraction of β-FeOOH rust. It indicates that Ti seems to be effective as an alloying element to improve corrosion resistance of Cu-Ni steel in chloride environments by decreasing the formation of β-FeOOH rust.

10.2.2 Analysis of Crystallite Size of Rust Particle

Crystallite size of rust particles can be estimated from the width at half height of the XRD peaks by using the Scherrer equation. It will be explained in detail in Sect.10.4.6.

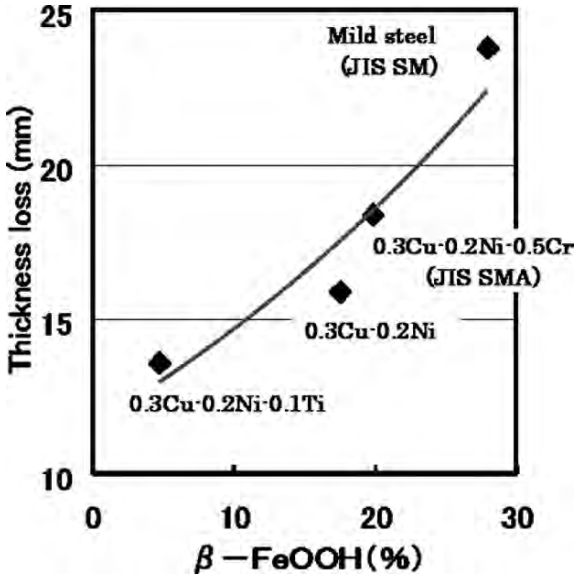

Fig. 10.3. Relation between thickness loss and fraction of β-FeOOH rust of unpainted steels exposed at Kakogawa Works' quay for one year (5%NaCl spray added once a week)

10.2.3 In-situ Observation of Oxidation and Reduction Processes of Iron Rusts by Synchrotron Radiation

A probe beam emitted from a synchrotron radiation facility is the ideal solution to rust studies because of its extensive wavelength range focused orientation (parallel beam), stability, and intense brightness [11, 12]. The world's most powerful SR facility is SPring-8 (Super Photon Ring, 8 GeV), in the Harima Science Park (Hyogo Prefecture, Japan), which entered operation in October 1997. It produces an extremely bright synchrotron radiation beam 10^8–10^{10} times more intense than a conventional laboratory X-ray source and 10^3 times more intense than the beam produced by Photon Factory (Tsukuba, Japan). SPring-8 can continuously emit X-rays covering an extensive range of energy (100 eV to a few hundred KeV; or 10–0.01 nm in terms of wavelength). Some examples of the SR studies we have conducted are reviewed below.

Since XRD patterns can be obtained in only a few minutes of exposure time using an ultra-bright synchrotron radiation (SR) beam, SR-XRD investigations of the structural modification of crystallite substances over a time scale of a few minutes to a few tens of minutes can obtain results not possible with a conventional laboratory XRD apparatus. The results reviewed below were used to evaluate changes in the crystal structure of iron surface rust in a chloride solution environment using an ultra-bright beam in Hutch B of the BL24XU beamline of SPring-8 [13]. The substrate was a high-purity

iron specimen (4N grade). The surface of this pure iron test piece was emery polished down to #200, and the X-ray beam was irradiated at a 1.2° angle of incidence with saturated NaCl aqueous solution supplied onto the test piece surface at 60 min intervals. Figure 10.4 depicts the experimental set-up. Figure 10.5 summarizes the observed $FeOOH/Fe_3O_4$ peak height ratio being low immediately after the application of the NaCl aqueous solution but using as the surface dried. The repetition of the variation pattern of $FeOOH/Fe_3O_4$ after each application of NaCl aqueous solution implies that the observed rusting behavior could be interpreted in terms of the electrochemical redox model proposed by U.R. Evans [14].

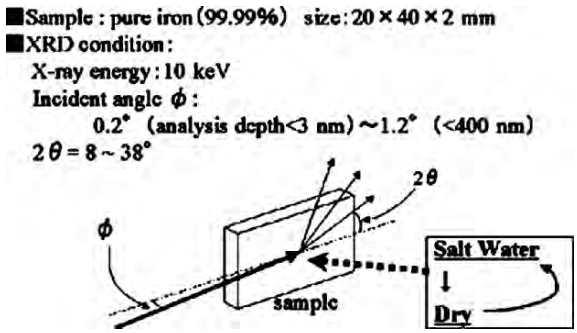

Fig. 10.4. Schematic set-up for in-situ observation of the iron rust formation process using an ultra-bright X-ray beam

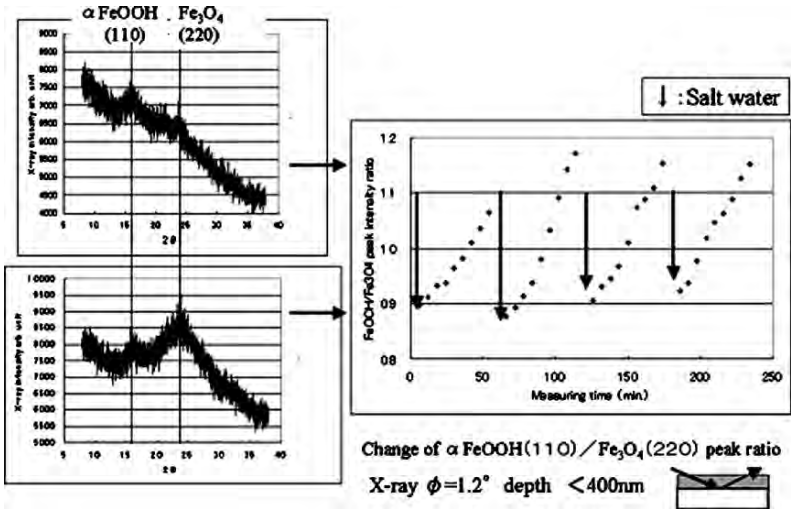

Fig. 10.5. Time change of $FeOOH/Fe_3O_4$ peak ratio intensity during cyclic wet/dry test using saturated NaCl aqueous solution

10.3 Rust Analysis by X-ray Adsorption Fine Structure (XAFS)

The X-ray adsorption fine structure (XAFS) technique is very effective for conducting atomic-scale structural characterization for rusts. Synchrotron radiation is the ideal probe beam for XAFS because of its intense brightness, extensive range of wavelength, and high stability. Unlike other conventional methods of structural analysis, XAFS is capable of analyzing the structure around a specific constituent atom in any state, including liquid and gas as well as crystalline or amorphous solids. Thus XAFS has an almost unlimited potential range of application and is considered to be very useful to corrosion researchers studying rusts [12, 15].

XAFS actually has two constituents: XANES (X-ray adsorption near edge structure) and EXAFS (extended X-ray adsorption fine structure). XANES covers the energy range from the adsorption edge of the selected element up to 50 eV higher than this, and EXAFS covers the energy range from this point up to 1200 eV. The XANES spectrum contains information concerning the valence number and electronic state of the selected elements; the EXAFS spectrum has information concerning the coordination number of the concerned atom and the distance from it to the neighboring atoms. The standard procedure for EXAFS spectrum analysis with reference to the absorption of the hypothetical atom in isolation involves determining the absorption initiation point by first order differentiation of the magnified XANES part, calibration of the EXAFS vibration function, and Fourier transformation to derive the radial distribution function around the concerned atom [15].

Iron rusts formed in an atmospheric environment can be in the form of α-FeOOH, β-FeOOH, γ-FeOOH, Fe_3O_4, or XRD-amorphous iron oxide. In recent research we identified Ti as an element that improves the corrosion resistance of steel in an atmospheric environment containing chloride [16]. Using XRD and a molecular-absorption technique, we proved that Ti would promote the formation of XRD-amorphous rust (favorable for rust densification) and the refinement of β-FeOOH (believed to be detrimental to rust stability). The aspects discussed below were elucidated by SR-XAFS analysis. The SR-XAFS study analyzed a β-FeOOH sample with and without Ti(IV) using the XAFS apparatus of BL16B2 in SPring-8 at an accelerating voltage of 8.0 GeV for investigation of short range structure of the products. α-FeOOH and γ-FeOOH with and without Ti(IV) were also investigated for comparison. X-ray absorption spectra at the Fe K-edge (7713 eV) were taken at transmission mode using a Si (111) crystal. The radial distribution functions obtained from EXAFS on these rust products at Ti/Fe=0 and 0.1 are shown in Fig. 10.6. The function of the product without Ti(IV) represented by a solid line possesses two strong peaks at radial distances (R) of 0.1–0.35 nm that are assigned respectively to Fe-O and Fe-Fe for edge sharing of octahedrons. In the case of the product at Ti/Fe=0.1 shown by a dashed line the peak at R=0.2-0.35 nm markedly diminishes, especially in β-FeOOH, while

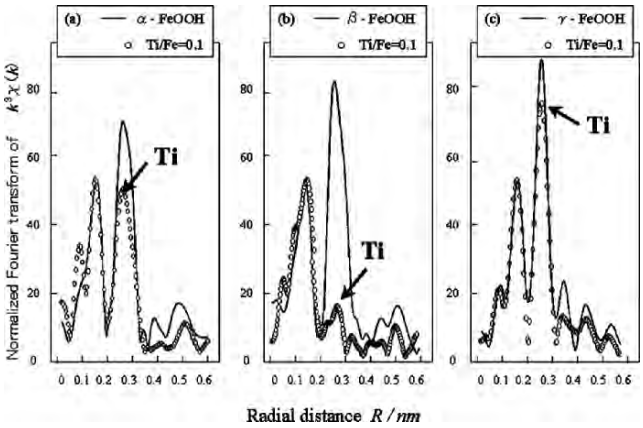

Fig. 10.6. Radial distribution functions around Fe in each FeOOH with and without Ti. (**a**) α-FeOOH, (**b**) β-FeOOH, (**c**) γ-FeOOH

the intensity of the Fe-O peak at R=0.1–0.15 nm does not differ from the same peak of the product without Ti(IV). In case of β-FeOOH, the Fe-Fe peak of corner-sharing octahedrons appears as a shoulder of the Fe-Fe peak at R=0.27 nm for the product without Ti(IV). This finding is indicative of a marked effect of Ti(IV) on the short range structure of β-FeOOH, i.e., the nearest octahedrons of Fe(III) are steeply decreased by doping with Ti(IV). As will be mentioned later, the amounts of Ti(IV) incorporated in the formed particles (Ti/Fe=1.0) is ten times that of the starting solution (Ti/Fe=0.1). This Ti/Fe ratio of 0.1 means that the octahedrons of Fe(III) in the particles are almost surrounded by those of Ti(IV), supporting homogeneous distribution of Fe(III) and Ti(IV) in the particles. The peak (Fe-O) at R=0.14 nm possesses a shoulder in the short distance side around R=0.09 nm. This shoulder becomes distinct with doping of Ti(IV), which can be ascribed to the Fe-O coordinate bond between hydration water and Fe(III) [9]. Figure 10.7 shows the XANES spectra around Ti K-absorption edge for TiO_2 standard samples (rutil, anatase) and Ti-doped α-FeOOH, β-FeOOH and γ-FeOOH. From the comparison of spectrum curves with TiO_2 samples, the chemical state of Ti in each FeOOH rusts seems to be close to that of TiO_2 of rutil type. The electronic state of β-FeOOH rust was evaluated by a DV-Xα calculation based from the pre-edge peaks shown around X-ray energy from 4.96–4.98 eV, and it was concluded that Ti atoms are substituted from Fe atoms in the octahedron network units.

10.4 Approach of Artificial Rust Synthesis

10.4.1 Background of the Approach

The corrosion of steels starts with the formation of $Fe(OH)_2$ through the reaction between Fe^{2+} and OH^- produced by an electrochemical process.

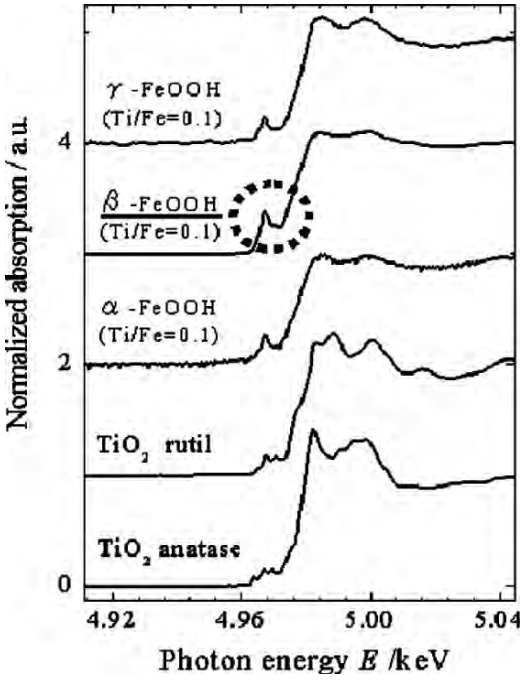

Fig. 10.7. XANES spectra around Ti *K-absorption* edge for TiO_2 standard samples (rutil, anatase) and Ti-doped α-FeOOH, β-FeOOH and γ-FeOOH

Depending on the specific conditions, the $Fe(OH)_2$ thus formed undergoes different reactions and is converted by further oxidation to α-, β-, or γ-FeOOH, Fe_3O_4, or X-ray amorphous iron oxide. The rust particles range in size from nanometers to micrometers. These rust particles are agglomerated into a rust layer. The structure, compactness, and permeability of molecules and ions of the rust layer are dependent on the structure and morphology of the rust particles as well as on their agglomeration state. Iron oxide particles can be synthesized from aqueous solutions containing Fe ions, but the process by which they are formed is by no means simple, and several aspects are not well understood. For the moment, the formation process of iron oxide fine particles in aqueous solution is considered to be as follows [17]. Primary particles of a few nm diameter are formed through the agglomeration of multi-nuclei complex ions generated from the hydrolysis of Fe ion. These primary particle agglomerations join together to form larger particles and are crystallized by ripening. Since the processes of particle agglomeration are sensitive to such factors as pH, anionic species, temperature, and solution concentration, the composition and structure of the particles vary depending on the formation condition. During the atmospheric corrosion of steels, water phase is believed to be formed in the pores of the rust layer by capillary condensation when the relative humidity (RH) exceeds 40%. The water phase formed causes subsequent rust particle formation like the rust particle formation that occurs in

bulk aqueous solution. This model process is corroborated by the fact that the composition and structure of the rust deposited on weathering steel surfaces are dependent on the environmental conditions, for example, dense protective rust layers consisting of refined particles tend to form in inland rural environments with a low density of airborne salt particles, whereas coarse-grained non-protective rust layers are formed in coastal atmospheres with a high density of airborne salt particles [18]. Small proportions of alloying elements such as Cr, Cu, Ni, and Ti are added to weathering steel to improve its corrosion resistance in the atmosphere. These alloying elements promote the formation of the protective rust layers that account for the good corrosion resistance of weathering steel in air. For example, alloyed Cu contributes to the refinement of the rust particles, thereby improving the adhesion of the rust layer to the steel substrate surface [19]. Okada et al. claimed that the retardation of corrosion realized by simultaneous alloying with Cu, Cr, and P resulted from the formation of stable XRD-amorphous spinel oxide which homogeneously covers the bottom layer of rust [20]. Yamashita et al. analyzed rust layers deposited on weathering steel surfaces during periods of atmospheric exposure ranging from 0.5 to 26 years [21]. They concluded that the rust particles deposited on weathering steel were refined by alloying with Cu and Cr, and were either α-FeOOH or Cr(III)-substituted α-FeOOH. According to Kamimura and Stratman, retarding the cathodic reaction was the major role of Cr alloyed to weathering steel [22]. It is also acknowledged that Ni-alloyed steel has superior corrosion resistance in an environment containing Cl^- [23]. Nakayama et al. reportedly developed Ti-alloyed weathering steel with high corrosion resistance in atmospheres containing Cl^- [5]. Nonetheless, there is still no systematic understanding of the role of alloying elements in improving the weathering performance of steel, and especially of the influence of alloying element on the process of rust formation.

As was pointed out above, a rust layer deposited on a steel surface is actually an agglomeration of particles of various Fe oxides. Thus, in order to understand the mechanism by which any particular alloying element enhances corrosion resistance, one must first of all analyze its influence on rust composition and structure. Then on the basis of the information so obtained, one may interpret the observed evidence pertaining to rust layers deposited on weathering steel surfaces in field atmospheric-exposure tests. In other words, in order to identify the role of an alloying element, we must not only analyze the rust deposited in the field exposure test but also synthesize the concerned rust component in the laboratory in the presence of the specific alloying constituent. There have been several research studies of the influence of various metal ions on the composition and structure of Fe oxides from the perspective of soil science and mineralogy as well as of material science. Very little work in this line, however, has concentrated exclusively on rust characterization, with the exception of the studies by Inouye and co-workers on α-FeOOH [24], β-FeOOH [25], and γ-FeOOH [26].

In light of this, the author et al. singled out four alloying elements that are known to improve the corrosion resistance of weathering steel, and investigated the influence Ti(IV), Cr(III), Cu(II), and Ni(II) on the structure of representative rust constituents, including α-FeOOH [27–29], β-FeOOH [9, 30], γ-FeOOH [31], Fe_3O_4 [31–33], and amorphous Fe oxide particles [34,35]. This chapter thoroughly reviews the findings to develop a systematic understanding of the mechanism whereby the currently employing elements improve the corrosion resistance of weathering steels. A guideline to be followed in searching for new alloying elements that can further enhance the corrosion resistance of weathering steel or low alloying steel is proposed.

10.4.2 Synthesis of Rust Particles

The rust particles of α- and β-FeOOH, and XRD-amorphous oxide were prepared by hydrolysis of ferric solutions and those of γ-FeOOH and Fe_3O_4 were obtained by air-oxidation of ferrous solutions. The starting solutions of ferrous or ferric salts contain Ti(IV), Cr(III), Cu(II), and Ni(II) at varied metal/Fe atomic ratios. These metal ions were selected taking account of alloying metals of weathering steel as described above. The detailed preparation methods are described in the literatures [27–35].

10.4.3 Particle Morphology

The compactness of rust layers is related to morphology of rust particles, because pores are formed in rust layers and their sizes depend on the morphology of the particles. Therefore, the shape and size of the rust particles are very important for estimating the compactness of rust layers concerned with corrosion resistance of steel. The influences of Ti(IV), Cr(III), Cu(II), and Ni(II) on the morphology of rust particles are described below. The α-FeOOH particles formed without the metal ions had an elongated sheet shape with about 50×500 nm size. The addition of Ni(II) did not induce any significant morphological change. In contrast, the addition of Ti(IV), Cr(III), and Cu(II) resulted in the formation of irregular agglomerations refined α-FeOOH particles. The rust particles formed with a high Ti/Fe of 0.1 yielded denser agglomerations of fine particles. The rust particles also became minute by the increased Cu(II) addition, but not by the increased Ni(II) addition. Figure 10.8 presents TEM pictures of β-FeOOH particles formed with different metal ions. The addition of Ti(IV) to a Ti/Fe atomic ratio of 0.1 led to the agglomeration of minute particles, but no such morphological modification was induced by adding the rest of the metal ions to metal/Fe atomic ratio of 0.1. Such refinement of β-FeOOH particles was realized only with Ti(IV) among the examined metal ions. The γ-FeOOH rusts formed without the additives had an elongated thin-flake geometry. The addition of Cu(II), Ni(II) or Cr(III) made the particles smaller, while the addition of Ti(IV) caused no marked morphological change of the particles. In the case of Fe_3O_4, the

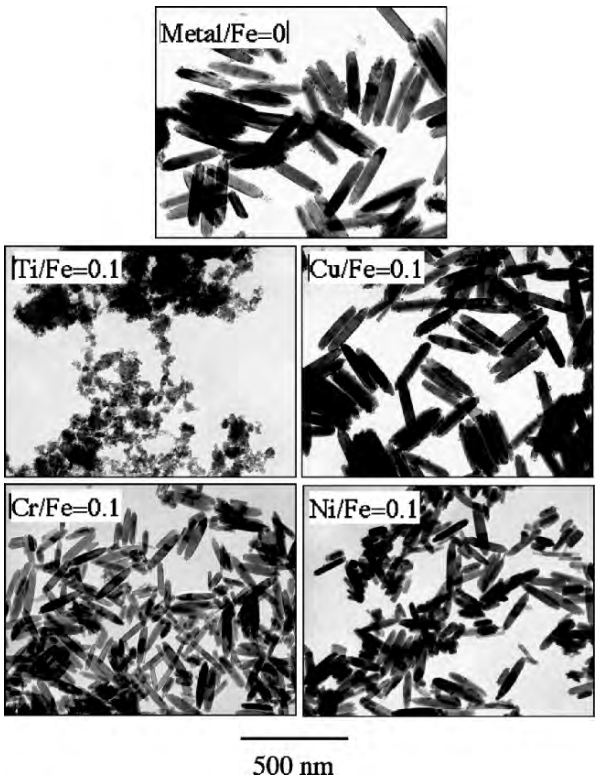

Fig. 10.8. TEM pictures of β-FeOOH rusts formed with Ti(IV), Cr(III), Cu(II), and Ni(II) at metal/Fe=0.1

addition of Ti(IV) showed little influence on particle morphology. The addition of Cu(II) and Cr(III) decreased particle size, while that of Ni(II) led to coarsening. All the XRD amorphous rust particles formed with or without the additive metal ions are strongly aggregated. The size of fine particles composing the agglomerates was difficult to estimate from the TEM pictures, so the mean particle size D (nm) was determined from specific surface area S (m^2/g) using the relation

$$D = 6/(dS)$$

where density d was assumed to be 3.8 g/cm^3. The D values of the particles formed with metal/(Fe+metal) = 0 and 0.8 in atomic ratio were 4.1 nm for the rust formed without the additives, 3.4 nm for Ti(IV), 6.7 nm for Cr(III), 4.2 nm for Cu(II), and 5.9 nm for Ni(II). All of these amorphous particles were identified as nano-sized particles.

10.4.4 Specific Surface Area

Since the rust particle geometry was irregular, with the exception of the β-FeOOH particles, it was not easy to discuss quantitatively the particle size of rusts. Instead, specific surface area (S) was employed as the representative parameter for particle dimensions. Figure 10.9 plots the obtained S of α-FeOOH against metal/Fe atomic ratio in the starting solution. The S increased with the rising metal/Fe ratio on adding metal ions. The increase of S was especially significant with the addition of Cu(II). These results indicated that the addition of the metal ions reduced the particle size of rusts and the effect of Cu(II) was most remarkable. Figure 10.10 plots S of β-FeOOH as a function of metal/Fe ratio of the starting solution. Only the addition of Cu(II) steeply increased S of the rust while those of the other metal ions essentially did not change S. In the cases of γ-FeOOH and Fe_3O_4, the addition of all the metal ions increased S of these rusts though it depends on the kind of metal ions. XRD-amorphous rust showed high S values of ca. 200–400 m^2/g, because these rusts were nano particles as mentioned above. The addition of Cr(III) or Ni(II) decreased S while that of Ti(IV) slightly increased S and that of Cu(II) did not vary it.

10.4.5 XRD

The composition and crystallinity of the rusts were investigated by powder XRD. Figure 10.11 displays the XRD patterns of the rusts formed in the

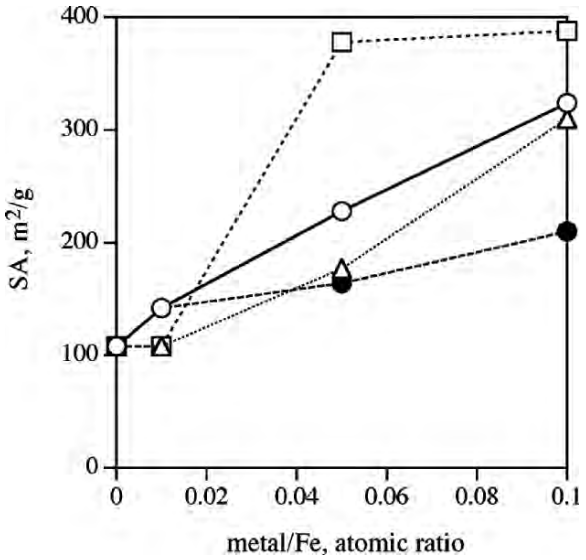

Fig. 10.9. Specific surface area (SA) of α-FeOOH rusts formed with Ti(IV) [*open circles*], Cr(III) [*triangles*], Cu(II) [*squares*], and Ni(II) [*filled circles*]

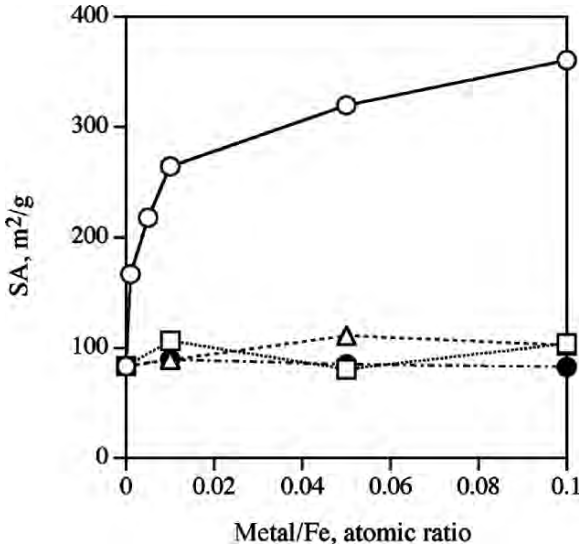

Fig. 10.10. Specific surface area (SA) of β-FeOOH rusts formed with Ti(IV) [*open circles*], Cr(III) [*triangles*], Cu(II) [*squares*], and Ni(II) [*filled circles*]

presence of Cu(II). The diffraction peaks of α-FeOOH were weakened by increasing Cu/Fe ratios in the starting solution and disappeared at Cu/Fe=0.1. This clearly shows that the addition of Cu(II) reduced the crystallinity of α-FeOOH rust to inhibit the crystallization at Cu/Fe=0.1. The addition of the other metal ions lowered the α-FeOOH peaks but not markedly compared to the case of Cu(II). The crystallinity of β-FeOOH rust was significantly reduced by adding a little Ti(IV) and the formation of β-FeOOH was completely inhibited at Ti/Fe = 0.05. On the other hand, the decline of the peak intensity of the β-FeOOH rust was not so drastic with Cr(III), Ni(II), and Cu(II). Thus, Ti(IV) showed the greatest interference to crystallization of β-FeOOH. The crystallization of γ-FeOOH rust was interfered with by the addition of metal ions other than Ti(IV) and was completely inhibited on adding Cr(III) at Cr/Fe = 0.03, Cu(II) at Cu/Fe = 0.05, and Ni(II) at Ni/Fe = 0.1. The addition of Ti(IV) slightly improved the crystallinity of γ-FeOOH. In the case of Fe_3O_4, the rust particles were less crystallized with increasing metal/Fe ratio of each metal ion. At a high Ni/Fe ratio of 0.1 the Fe_3O_4 rust was not formed. XRD patterns of XRD-amorphous rusts had no peaks when they were taken using CuKa radiation from a sealed XRD tube at 15 kV and 30 mA. Figure 10.12 shows the XRD patterns of the amorphous rusts taken by the more powerful rotating-type cathode X-ray tube operated at 40 kV and 120 mA. The rust formed without the additive metal ions showed only two broad peaks. With increasing Ti/Fe ratio the broad peaks become more broad, indicating the depression of crystallinity with Ti(IV). The observed broad peaks suggested that the Fe(O, OH, OH_2) octahedron formed sheet

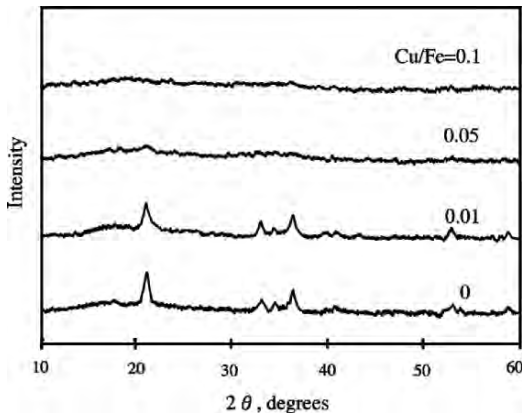

Fig. 10.11. XRD patterns of α-FeOOH rusts formed with Cu(II)

geometry by forming bonds at the edges. It was concluded that the amorphous rust consisted of agglomerated fine sheets of this constitution [36]. In fact, two such broad peaks reportedly emerged from ferrihydrite [37, 38].

10.4.6 Crystallite Size

As reviewed above, the crystallinity of rusts was influenced by the addition of metal ions in different ways, varying with kinds of rust and metal ion. For quantitative comparison of the effect of metal ion on crystallite size of the rust particles, we measured the width at half height of the XRD peaks so as to estimate the crystallite size using the Scherrer equation. Figure 10.13 shows the crystallite size (L) of α-FeOOH rust obtained using the (110) peak of α-FeOOH. The L of the rust was not much changed on adding Ti(IV) or Cr(III). On the other hand, the addition of Cu(II) and Ni(II) decreased L, especially markedly in the case of Cu(II). The case of β-FeOOH rust is shown in Fig. 10.14. The addition of Ti(IV) drastically reduced L of the β-FeOOH rust while that of the other metal ions decreased it a little, though L of the rust at Cu/Fe=0.05 increased. L values of γ-FeOOH, Fe_3O_4, and XRD-amorphous rusts were lowered by the addition of all the metal ions except for the γ-FeOOH-Ti(IV) system where L slightly increased with increase of Ti/Fe.

10.4.7 Comparison of Effects of Metal Ions on Particle Size and Crystallinity of Rusts

As described above, the effects of the examined metal ions on crystallinity and specific surface area differed from one metal to another. The effects of individual metal ion were compared in order to elucidate the functions of metal ions in corrosion resistance of weathering steel and confirm the most potential alloying metal out of the examined metal ions.

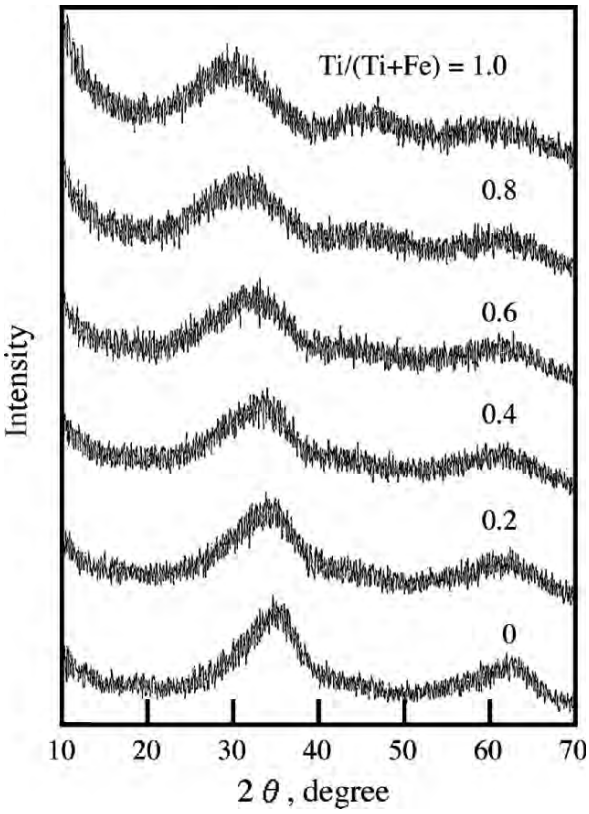

Fig. 10.12. XRD patterns of XRD-amorphous rusts formed with Ti(IV)

(1) Influence on Crystallinity

The index (L–Lo)/Lo was employed to compare the influence of the metal ions on crystallinity. In this index, Lo refers to the crystallite size at metal/Fe = 0, and L to the size at metal/Fe = 0.05 for crystalline rusts or at metal/(Fe + metal) = 0.05 for XRD amorphous rusts. Figure 10.15 summarizes the evaluated results. The index (L–Lo)/Lo was positive for the sytems of α-FeOOH-Ti, α-FeOOH-Cr, β-FeOOH-Cu, and γ-FeOOH-Ti, indicating improved crystallinity. In contrast, the indexes of the other systems were negative, indicating lowered crystallinity. The decline in crystallinity was significant for the β-FeOOH-Ti, γ-FeOOH-Cu, and γ-FeOOH-Ni systems. The greatest crystallinity fall was identified as Cu(II) for α-FeOOH, Ti(IV) for β-FeOOH, Cu(II) and Ni(II) for γ-FeOOH, and Ni(II) for Fe_3O_4. There was no metal ion with a very intense effect on crystallinity of all the rusts. Since the Lo at metal/Fe = 0 varies considerably from one type of rust to another, direct comparison of the effect of any metal ions on different rust types is of no significance.

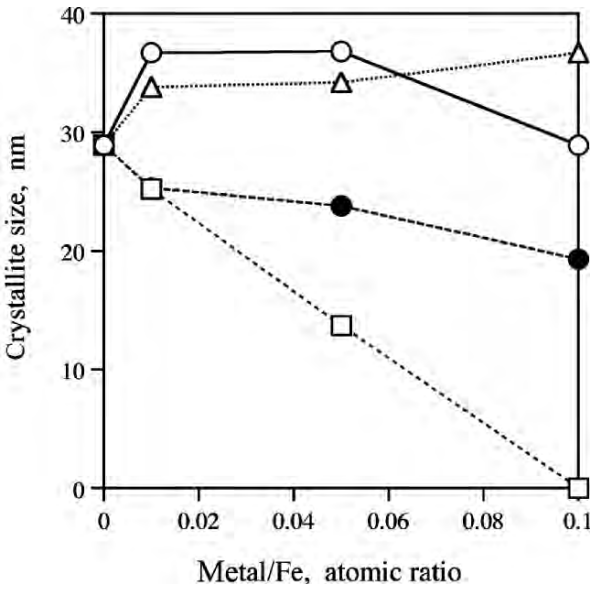

Fig. 10.13. Crystallite sizes of α-FeOOH rusts formed with Ti(IV) [*open circles*], Cr(III) [*triangles*], Cu(II) [*squares*], and Ni(II) [*filled circles*] at varied metal/Fe ratios in starting solution

(2) Influence of Particle Size

Specific surface area is a parameter that represents particle size of rust. So, this parameter was used to compare the particles added with metal ions. Figure 10.16 summarizes the results. In the figure, So refers to the specific area of the rust particles with no additive metal ion, and S to that of the rust particles at metal/Fe = 0.05 for the crystalline rusts or at metal/(Fe+metal) = 0.2 for the XRD amorphous rusts. The parameter (S–So)/So was positive except for the systems of β-FeOOH-Cu and XRD amorphous rusts with Cr(III) and Ni(II) though these systems showed slightly negative. This suggested that there was a general trend of depression of rust particle size, that is, increase of specific surface area, with the addition of metal ions for every type of rust examined. The decrease of particle size was especially significant in the α-FeOOH-Cu, β-FeOOH-Ti, Fe_3O_4-Ni systems. Needless to say, similarly to the case of crystallinity, it would be meaningless to compare the effectiveness of any given metal ion to decrease the particle size among different types of rusts.

(3) Incorporation of Metal Ions into Rusts

The influence of metal ions is considered to be caused by incorporation of the metal ions; the incorporated metal ion into rust crystal changes the crystal

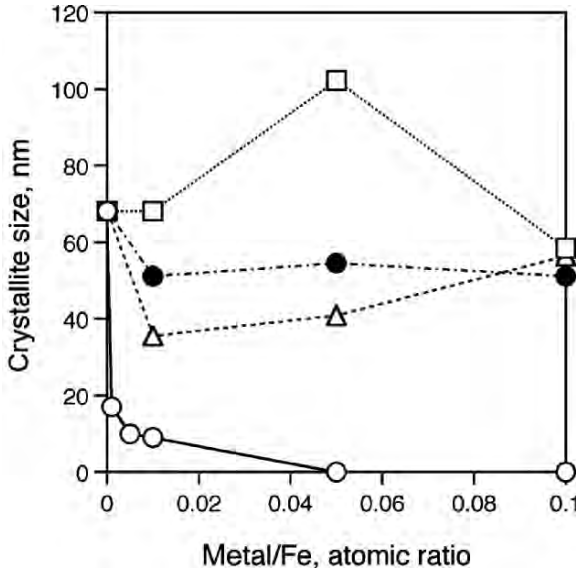

Fig. 10.14. Crystallite sizes of β-FeOOH rusts formed with Ti(IV) [*open circles*], Cr(III) [*triangles*], Cu(II) [*squares*], and Ni(II) [*filled circles*] at varied metal/Fe ratios in starting solution

structure according to radius and valence of the metal ions. The incorporation of the examined metal ions into the rust particles was investigated by ICP-AES. Apart from a few cases, most of the metal ions added in the starting solutions were contained in the formed rust particles. Figure 10.17 plots the metal content of β-FeOOH rusts against that of the starting solution. Different from the other rusts, the metal/Fe ratio in the β-FeOOH rust was far lower than in the starting solutions for every examined metal ion except for Ti(IV). The metal ions added in the starting solutions were not incorporated in the rust particles and remained in the solution after the reaction. The large incorporation of Ti(IV) was ascribed to its high hydrolysis constant. Ti(IV) is easily hydrolyzed to produce H^+, leading to a low pH of 1.55 that is not favorable for β-FeOOH formation.

10.4.8 Comprehensive Comparison of Effects of Metal Ions

To consider the mechanism of corrosion resistance of low alloy steel, the effects of metal ions on the formation of different types of rusts are comprehensively compared in Table 10.1 based on the results obtained. The squares in this table refer to the situation of lowered crystallinity and decreased particle size, suggesting the formation of a dense rust layer. The open circles represent the enhanced extent of lowered crystallinity and decreased particle size leading to the formation of a high protective rust layer. The filled circles show the situation of improved crystallinity and particle growth of rusts, indicating that the

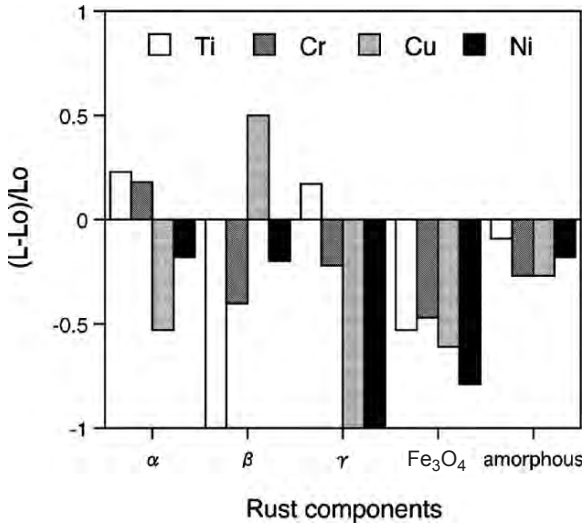

Fig. 10.15. Comparison of (L–Lo)/Lo of different rusts formed with Ti(IV), Cr(III), Cu(II), and Ni(II)

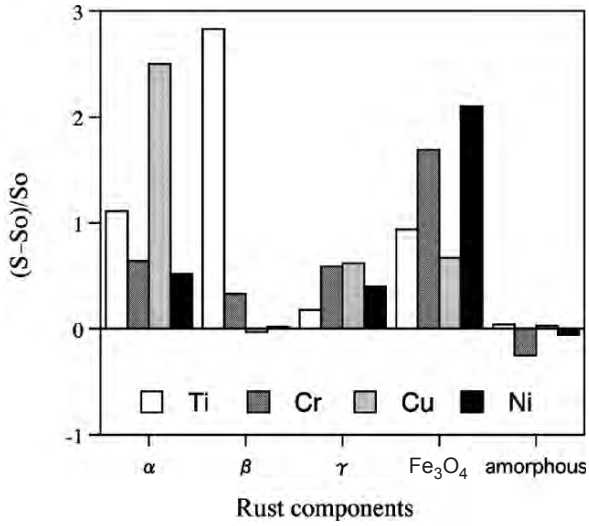

Fig. 10.16. Comparison of (S–So)/So of different rusts formed with Ti(IV), Cr(III), Cu(II), and Ni(II)

formation of dense protective rust was retarded. The triangles indicate the insignificant influence of metal ion addition on rust formation. Since the XRD amorphous rusts inherently had nano-sized particles with no additives, the effect of the added metal ions failed to emerge clearly. Thus, XRD-amorphous rusts may be excluded from the discussion that follows about the effects of

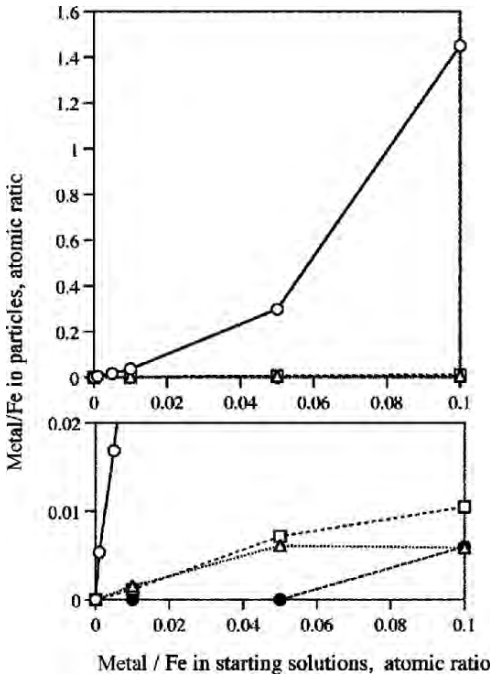

Fig. 10.17. Plots of metal/Fe ratios in β-FeOOH rust particles formed with Ti(IV) [*open circles*], Cr(III) [*triangles*], Cu(II) [*squares*], and Ni(II) [*filled circles*] against those starting solutions

each metal ion on the structure of rusts. However, amorphous rust is a main product of corrosion and is considered to pertain intimately to the structure and nature of the rust layer, though the details remain uncertain. Only Ti(IV) decreased the particle size of the XRD-amorphous rust and Cr(III) most increased it. Generally, the metal ions examined contributed to the refinement of rust particle size except in a few cases. It is noteworthy that Cu(II) effectively reduced the particle size and crystallinty of the α-FeOOH rust and only Ti(IV) inhibited the β-FeOOH formation. Further, the crystallization of the γ-FeOOH rust was markedly interfered with by Cr(III), Cu(III) or Ni(II), and the particle growth of Fe_3O_4 rust was much retarded by Ni(II).

10.4.9 Mechanism for Emergence of Corrosion Resistance

The role of alloying metals in corrosion resistance of low alloying steels can be discussed on the basis of the aforementioned results. The addition of all the examined metal ions retarded the crystallization and particle growth of the rust constituents, suggesting that alloying metals contribute to the formation of dense protective rust layers. Since the major constituents of the

Table 10.1. Comprehensive comparison of effects of metal ions on crystallinity and particle size of rusts

Rust		Cu(II)	Cr(III)	Ni(II)	Ti(IV)
α-FeOOH	Crystallinity	□	△	□	□
	Particle size	□	□	□	□
β-FeOOH	Crystallinity	△	□	□	◯
	Particle size	△	△	△	◯
γ-FeOOH	Crystallinity	◯	◯	◯	△
	Particle size	□	□	□	△
Fe_3O_4	Crystallinity	□	□	□	◯
	Particle size	□	□	□	□
X-ray amorphous	Crystallinity	□	□	□	□
	Particle size	△	●	●	□

open circles; marked fall, *squares*; fall, *triangles*; unchanged, *filled circles*; rise

steel rust which form in a Cl-free environment are α- and γ-FeOOH, and Fe_3O_4, it is really reasonable that the usual weathering steels are alloyed with Cu, Cr, and Ni, because alloying with these metals interferes with the crystallization and particle growth of the rusts to form dense protective rust layers. On the other hand, β-FeOOH and Fe_3O_4 formed from β-FeOOH by the Evans process are the major components in an environment containing Cl^-. Alloying with Ti would enhance the corrosion resistance of steel because it retards the formation of β-FeOOH rust. Additional alloying with Ni and Cu would further reinforce the corrosion resistance obtained by alloying with Ti, because Ni(II) and Cu(II) compensate the weak point of Ti (IV) by inhibiting the crystallization and particle growth of γ-FeOOH rusts. In fact, a new type of weathering steel alloyed with Cu, Ni, and Ti has performed satisfactorily in a coastal atmosphere and under an accelerated salt spray exposure test [5].

References

1. T. Nakayama: J. Soc. Mat. Sci., Japan, **50**, 542 (2001) (in Japanese).
2. Public Works Research Institute, Kozai Club, and Japan Association of Steel Bridge construction,"Report of Joint Research on the Application of Weathering Steels to Bridges (XX)"(1003) (in Japanese).
3. M. Nambu: J. Miner. Perol. Econ. Geal. **59**, 143 (1968).
4. T. Yokoi, S. Takeuchi, H. Shirasawa, T. Nakayama: *Proceedings of the International Symposium on Plant Aging and Life*, JSCE and NACE, Sapporo(1995).
5. T. Nakayama, F. Yuse, T. Kan, M. Sakai, K. Ohe: CAMP-ISIJ, **11**, 454 (1998) (in Japanese).
6. T. Nakayama, F. Yuse, H. Kawano, K. Ohe, K. Abe, and M. Sakai: R&D Kobe Steel Engineering Reports, **51**, 29 (2001) (in Japanese).
7. K. Shiotani, T. Nakayama, H. Kihira, H. Miyuki, M. Takemura, F. Kawabata, K. Abe, T. Kusunoki, Y. Watanabe, and K. Matsui: *Proceedings of JSCE*

132ed Symposium of SABI[RUST] Chemistry on the Phase-III *toward Realizing Minimum Maintenance Bridge Conception*, 73 (2001).
8. M. Yamashita, K. Asami, T. Ishikawa, T. Otsuka, K. Tamura, and T. Misawa: *Proceedings of JSCE 132ed Symposium of SABI[RUST] Chemistry on the Phase*-III *toward Realizing Minimum Maintenance Bridge Conception*, 93 (2001).
9. T. Ishikawa, R. Katoh, A. Yasukawa, K. Kandori, T. Nakayama, and F. Yuse: Corrosion Sci, **43**, 1727 (2001).
10. T. Nakayama, H. Kihira, K. Shiotani, H. Miyuki, M. Takemura, M. Yamashita, and T. Nishimura: *Proceedings of JSCE 132ed Symposium of SABI[RUST] Chemistry on the Phase-III toward Realizing Minimum Maintenance Bridge Conception*, 65 (2001).
11. H. Winick: *Properties of Synchrotron Radiation*, ed. by H. Winick and D. Doniach, "Synchrotron Radiation Research", Plenum, New York, 11 (1979).
12. T. Nakayama: Shikizai (Japan Society of Color Materials), **73**, p.22 (2000).
13. T. Yasunaga, T. Nakayama, T. Miyashita, and K. Arai: *Proc.* 49th *Japan Conf. Materials and Environments*, JSCE, p. 11 (2002).
14. T. Misawa: Zairyo-to-Kankyo, **50**, 538 (2001).
15. Y. Udagawa: *XAFS (X-ray Absorption Fine Structure), Measurement Methods Series* published by Jpn. Spectroscopic Soc., p. 23 (1993).
16. T. Nakayama, F. Yuse and T. Ishikawa: ESCCD 2001, p. 201 (2001).
17. T. Ishikawa: Zairyo-to-Kankyo (Corros. Eng.), **46**, 411 (1997).
18. T. Ishikawa, M. Kumagai, A. Yasukawa and K. Kandori: Corrosion, **57**, 346 (2001).
19. N. Masuko and Y. Hisamatu: *Boshoku-Gijutu (Corros. Eng.)*, **17**, 17 (1967).
20. H. Okada, Y. Hosoi, K. Yukawa and H. Naito: Tetusto-to-Hagane, **55**, 355 (1969).
21. M. Yamashita, H. Miyuki, H. Nagano and T. Misawa: Zairyo-to-Kankyo (Corros. Eng.), **43**, 26 (1994).
22. T. Kamimura and M. Stratmann: Corros. Sci., **43**, 429 (2001).
23. A. Usami, M. Yamamoto, H. Mabuchi, K. Kutsurin, T. Tsuzuki, K. Tanabe, and S. Inoue: Zairyou-to-Purosesu, **9**, 482 (1996).
24. K. Inouye, S. Ishii, K. Kaneko and T. Ishikawa: Z. anorg. allg. Chem., **391**, 86 (1972).
25. K. Inouye, K. Imamura, K. Kaneko and T. Ishikawa: Bull. Chem. Sco. Jpn., **47**, 743 (1974).
26. K. Inouye, K. Ichimura, K. Kaneko and T. Ishikawa: Corros. Sci., **16**, 507 (1976).
27. T. Ishikawa, A. Nagashima, and K. Kandori: J. Mater. Sci., **26**, 6231 (2001).
28. T. Ishikawa, H. Yamashita, A. Yasukawa, K. Kandori, T. Nakayama and F. Yuse: J. Mater. Chem., **10**, 543 (2000).
29. T. Ishikawa, N. Motoyoshi, A. Yasukawa, K. Kandori, T. Nakayama and F. Yuse: Zairyo-to-Kankyo (Corros. Eng.), **50**, 155 (2001).
30. T. Ishikawa, T. Motoki, R. Katoh, A. Yasukawa, K. Kandori, T. Nakayama and F. Yuse: J. Colloid Interface Sci., **250**, 74 (2002).
31. T. Ishikawa, M. Kumagai, A. Yasukawa, K. Kandori, T. Nakayama and F. Yuse: Corros. Sci., **44**, 1073 (2002).
32. T. Ishikawa, H. Nakazaki, A. Yasukawa, K. Kandori, and M. Seto: Mater. Res. Bull., **33**, 1609 (1998).

33. T. Ishikawa, H. Nakazaki, A. Yasukawa, K. Kandori, and F. Yuse: Corros. Sci., **41**, 1665 (1999).
34. T. Ishikawa, T. Ueno, A. Yasukawa, K. Kandori, T. Nakayama and T. Tsubota: J. Mater. Chem., **12**, 2416 (2002).
35. T. Ishikawa, T. Ueno, A. Yasukawa, K. Kandori, T. Nakayama and T. Tsubota: Corros. Sci., **45**, 1037 (2003).
36. W. Feitknecht, R. Giovanoli, W. Michaelis, M. Müller: Helv. Chim. Acta, **56**, 2647 (1973).
37. F. W. Chukhrov, B. B. Zvyagin, G. Gorshkov, L. P. Yermilova and V. V. Balashova: Intl. Geol. Rev., **16**, 1131 (1973).
38. U. Schwertmann and W. R. Fisher: Geoderma, **10**, 237 (1973).

11 Various Scale Analyses to Create Functioning Corrosion Products

Masao Kimura, Tadashi Mizoguchi, Hiroshi Kihira, Michio Kaneko

11.1 Introduction

Since corrosion is a set of complicated phenomena consisting of electrochemical, colloid chemical, and other physico-chemical processes regarding substances and energies, structural analytical approaches are useful to elucidate these mechanisms. In this chapter, authors will explain recent advancements in this field of study.

Figure 11.1 shows a schematic illustration of corrosion on an iron surface in the atmosphere, which is modified from one proposed elsewhere [1]. On an atomic-scale (c.a. <1 nm), iron and metallic elements added in steel form cations that are coordinated by six water molecules in an acidic solution [2] such as $[Fe(OH_2)_6]^{2+}$ shown in Fig. 11.1(a). In a neutral solution, metal cations react with OH^-, O_2, and H_2O, resulting in formation of hydroxocations as exemplified in terms of $[Fe(OH)_x(OH_2)_{6-x}]^{(3-x)+}$. On a colloidal-scale (c.a. 1–100 nm), polymerization of these octahedra leads to formation of fine particles of hydroxides, oxyhydroxides, or oxides. These particles grow into grains or layers through a long period of aging processes affected by repetition of wet and dry cycles (Fig.11.1(b)). Reaction conditions (concentration, acidity, temperature, nature of the anions, etc.) have a strong influence on the structural or morphological changes of poly-octahedra during corrosion. Knowing changes in various-scale structures and morphology will provides us with information on reaction mechanisms, which may become clues to innovate novel corrosion control techniques.

In Sect. 11.2, structural aspects of corrosion products are discussed. An important structural viewpoint, "polymerization of $Fe(O,OH)_6$ octahedra", is emphasized in order to understand evolution of corrosion products. Based on these insights, two important strategies for preventing corrosion are proposed in Sect. 11.3: i.e. (I) resisting acidification near the solution/metal interface: "*pH-strategy*", and (II) shielding the interface against environments: "*shielding-strategy*". In Sect. 11.4, advanced structural analytical approaches are described: i.e. (A) in situ observation of reactions near the solution/metal interface using synchrotron radiation, and (B) quantitative evaluation of nano-scale structures of corrosion products using Mössbauer spectroscopy.

In order to create more elaborated tactics for developing materials, three various-scale analytical approaches will be discussed from Sect. 11.5 to

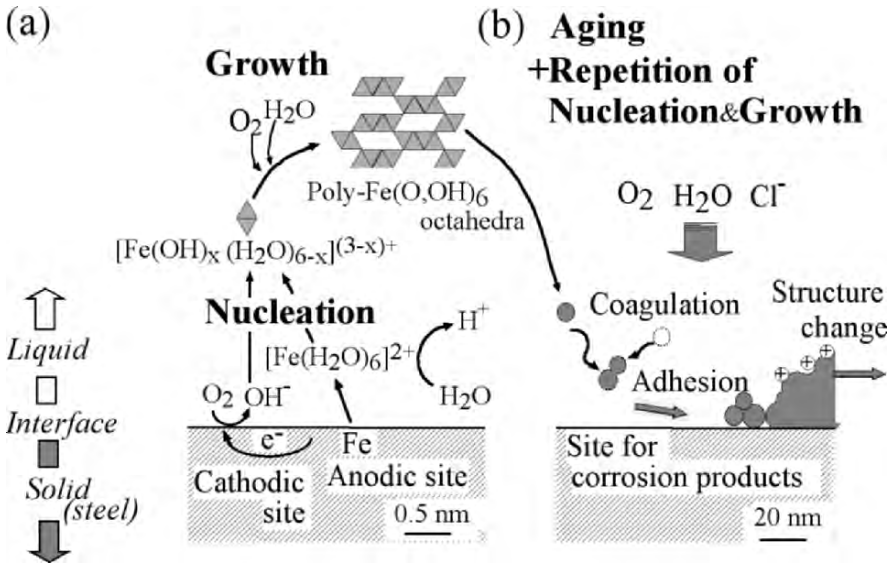

Fig. 11.1. Scheme of corrosion on iron surface in the atmosphere: (**a**) atomic-scale reactions in an initial wet cycle, (**b**) colloidal-scale reactions during repetition of wet and dry cycles for a long period. *Triangle pairs* represent an $M(O, OH)_6$ octahedron

Sect. 11.7: i.e. localized corrosion in stainless steel, rusting of conventional weathering steel, and atmospheric corrosion in advanced weathering steel, respectively. Lastly, further possibilities for developments of anti-corrosion materials based on the various-scale analyses will be discussed in Sect. 11.8.

11.2 Various Scale Analyses for Structures of Corrosion Products

11.2.1 Ideal Structures of Iron Oxyhydroxides and Oxides

There are two ways of expressing ideal crystal structures of iron oxyhydroxides or oxides [3]: i.e. linkage model as in Fig. 11.2 and ball model as in Fig. 11.3. The former is convenient to see whole skeleton structures of various compounds as linkage of $Fe(O, OH)_6$ octahedral and/or $Fe(O, OH)_4$ tetrahedral units. The latter is more realistic than the former so that it is useful to consider the surface or spatial functions to occur on each product.

11.2.2 Formation Process of Corrosion Products

When corroded, metallic elements added to steel form cations, which are coordinated by six water molecules in acidic solution. In higher pH solutions, metal cations form hydroxo-cations [2]. These same skeleton units of $M(O, OH)_6$ (M = a central metal) octahedra are connected either by olation or oxolation in the following ways [4]:

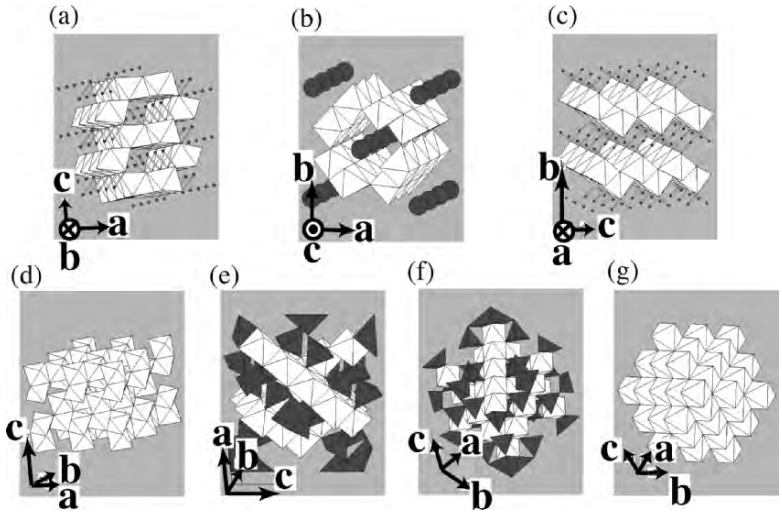

Fig. 11.2. Linkage models for atomic structures of oxides and oxyhydroxides typically found in rust formed on steel surface. Atomic structures are shown by a combination of $Fe(O,OH)_6$ octahedra representing (**a**) α-FeOOH, (**b**) β-FeOOH, (**c**) γ-FeOOH, (**d**) α-Fe_2O_3, (**e**) γ-Fe_2O_3, (**f**) Fe_3O_4, and (**g**)FeO. *Gray spheres* in (b) represent chloride ions. The structure models in (e) and (f) also include tetrahedra of FeO_4, which are shown gray for clarity. These drawings are produced with ATOMS (Shape Software) using structural data of the Inorganic Crystal Structure Database (NIST and FIZ KARLSRUHE)

$$\text{Olation}: \quad -M-OH+\ -M-OH_2 \rightarrow -M-OH-M-+H_2O \quad (11.1)$$

$$\text{Oxolation}: \quad -M-OH+\ -M-OH \rightarrow -M-O-M-+H_2O \quad (11.2)$$

This is how oxyhydroxides or oxides grow. Possible formation model of α-FeOOH is illustrated in Fig. 11.4 [4].

As shown in Fig.11.1, the formation process of solid particles from ions can be visualized by three steps: i.e. (I) nucleation, (II) growth, and (III) aging [1]. Nucleation corresponds to the first step of precursor condensation and solid formation. Then the growth process follows, where $M(O,OH)_6$ octahedra units as cations or smaller sized growing nuclei accumulate to form larger particles basically by diffusion.

Coagulation and adhesion processes ensue to generate corrosion products, which undergo aging processes leading the system to stability. In aging processes, modification of particles may occur in phenomena such as increase in particle size, change in crystal type, change in morphology, etc. [4]

Resulting from these complicated processes, corrosion products are generally classified as coarse and fine grains, both of which are composed of crystallites and inter-crystallites as shown in Fig. 11.5. The structures in the former are similar to those of ideal crystals as shown in Fig. 11.2, while in the latter, linkage of $M(O,OH)_6$ octahedra is disordered. This type of disorder may be caused by existence of defects and/or different sizes of $M(O,OH)_6$

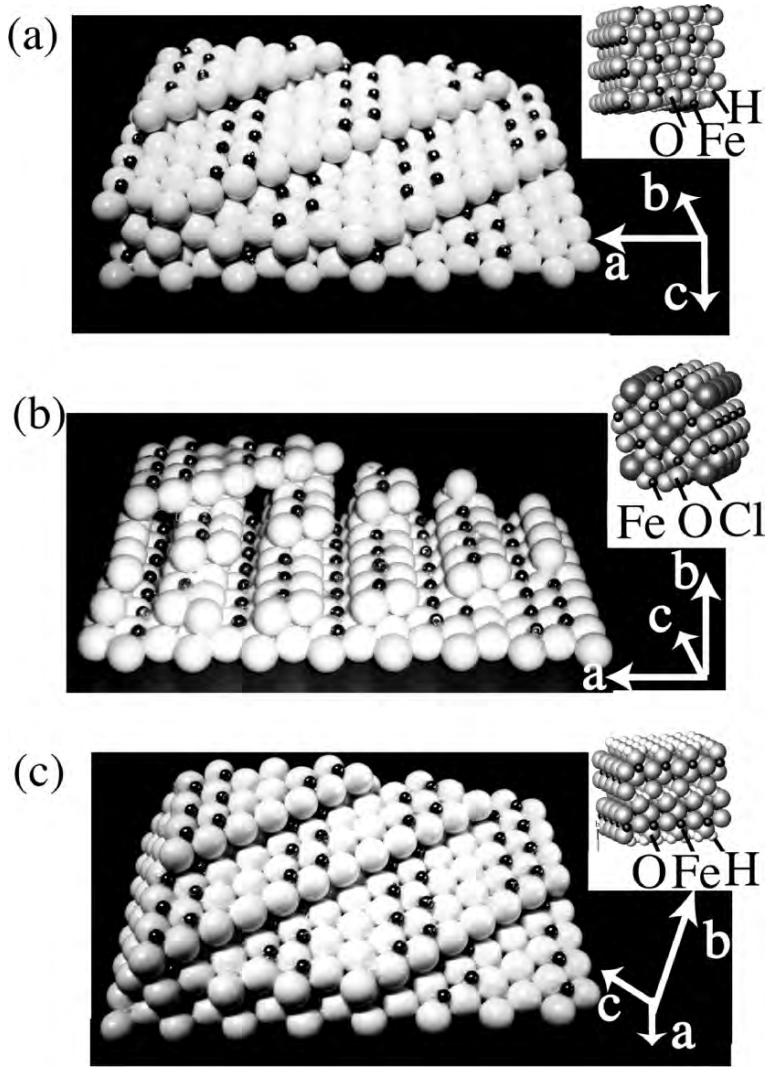

Fig. 11.3. Ball models for atomic structures of (**a**) α-FeOOH, (**b**) β-FeOOH, and (**c**) γ-FeOOH, where stacking of oxygen (*large white*) and iron (*small black*) is emphasized. *Inserts* show atomic structures where crystals and their crystallographic directions are identical to those of Fig. 11.2 (**a**)–(**c**). *Large gray spheres* show oxygen; *large dark*, chloride ions; *small black*, iron ions; and *small white*, hydrogen ions, respectively. The size of hydrogen is enlarged by five times for clarity. The ball models shown here were hand made by Ms. S. Takakura

Fig. 11.4. Possible formation processes of α-FeOOH from iron ions after [4]

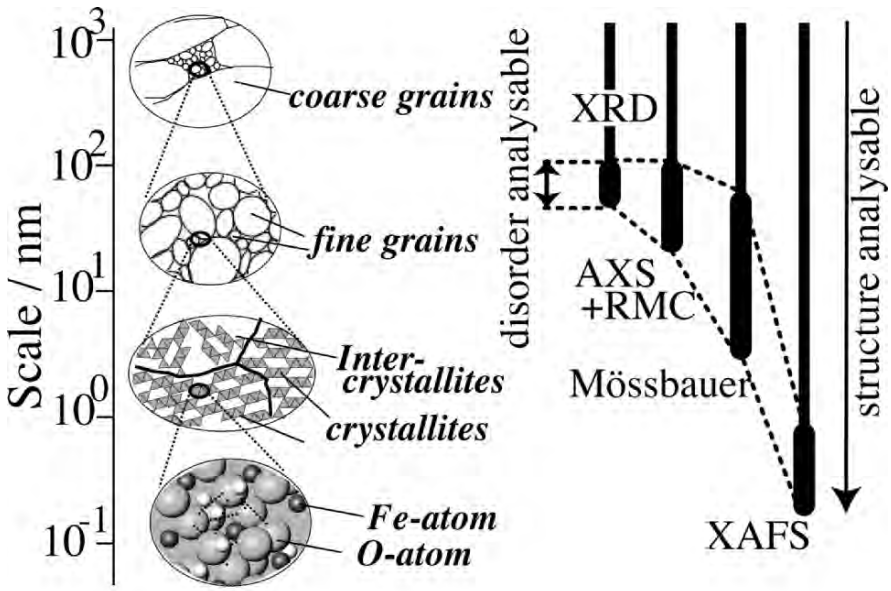

Fig. 11.5. Schematic illustration of structures for corrosion product on various scales. Corrosion products are generally classified as coarse and fine grains, both of which are composed of crystallites and inter-crystallites. They are made of $M(O, OH)_6$ octahedra, which are symbolized by triangle pairs. Various scale analytical-approaches are shown in terms of X-ray diffraction (XRD), combination of anomalous X-ray scattering (AXS) and reverse Monte-Carlo simulation (RMC), Mössbauer spectroscopy, and X-ray absorption fine structure (XAFS). Atomic structures can be investigated by these techniques in regions shown by *bars*. Disorder can be detected in the regions indicated by *thick bars*

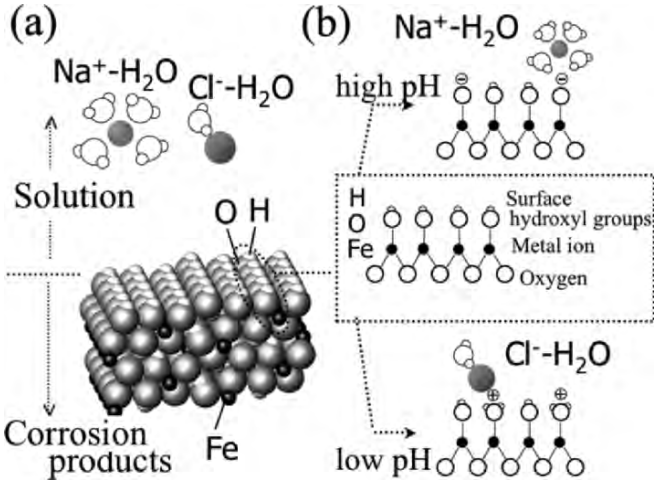

Fig. 11.6. Schematic portrayal on surface atomic structure of α-FeOOH in an aquatic solution (**a**), and its change due to different acidity (**b**). Hydrogen ions are enlarged five times for clarity

octahedra made of additional elements. In order to characterize structures of corrosion products, we need various scale analytical-approaches that are sensitive to different structural correlation lengths as imaged in Fig. 11.5.

11.2.3 Surface of Corrosion Products in an Aquatic Media

When exposed to environments containing water, metal oxyhydroxides or oxides are covered with so-called surface hydroxyl (-OH) groups. Figure 11.6 shows schematic models of an atomic structure of α-FeOOH surface in an aquatic media; in a solution with low pH, the surface hydroxyl groups change into -OH_2^+, resulting in the formation of a positively charged surface. In a solution with high pH, the surface hydroxyl groups change into -O^-, resulting in the formation of a negatively charged surface. The tendency of the surface charging largely depends on the type of compounds and its surface state, which can be evaluated by so-called point of zero charge i.e. pH_{pzc}.

Since pH_{pzc} of α-FeOOH is c.a. 7.7 [5], its surface is charged positively when wet with neutral water. Now we consider atmospheric corrosion of mild steel in high air-born salinity conditions. When rust becomes wet and corrosion progresses, the pH of wet rust is lowered by the hydrolysis of the metal cations. Then, the surface hydroxyl groups of the rust (e.g. α-FeOOH) change into -OH_2^+ [5]. When the rust dries, some of the surface hydroxyl groups change into $\text{-OH}_2^+ \cdot \text{Cl}^-$, which becomes the source of hydrochloric acid to decrease pH when the rust becomes wet again. If the steel/rust interface becomes wet and acidic, corrosion of the steel is accelerated. Thus, the accumulation of chlorides in the inner rust causes a vicious cycle against the durability of steel members.

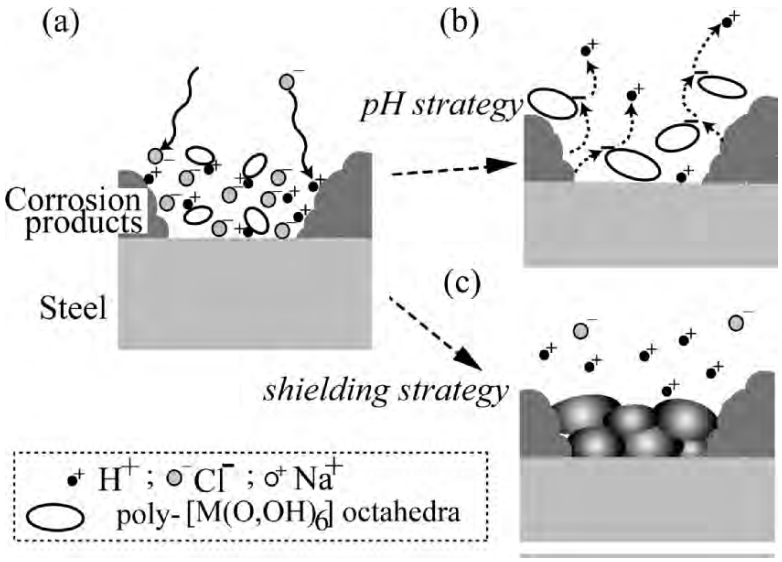

Fig. 11.7. Schematic illustration of mild steel corrosion. (**a**) Spontaneous situation: concentration of metal and hydrogen ions near the solution/metal interface are high due to hydrolysis. *Ovals* represent $M(O,OH)_6$ octahedra such as $[Fe(OH)_x(OH_2)_{6-x}]^{(3-x)+}$. Some -OH groups of them may change into $-OH_2{}^+$. (**b**) Improved situation by "*pH-strategy*": resisting acidification near the interface by negatively-charged poly-$M(O,OH)_6$ octahedra. (**c**) Improved situation by "*shielding-strategy*": shielding the interface against environments by protective layers

11.3 Strategies for Preventing Corrosion

11.3.1 Resisting Acidification Near the Solution/Metal Interface: "*pH-strategy*"

Corrosion rate of steel in an aquatic solution depends on pH. The corrosion rates of mild steel in air-saturated HCl-NaOH solution as function of pH are reported in [6,7]. In a region of pH<4, the corrosion rate increases acutely as pH decreases. In a region of pH = c.a. 4–10, the corrosion rate is independent of pH because of passive film formation. Thus keeping pH high is one of the essential strategies against corrosion.

However, due to hydrolysis of metallic ions, pH tends to decrease when corrosion progresses. This trend is prominent at the solution/metal interface, since concentrations of cations are high. To achieve electrical neutrality, chloride ions are accumulated near the interfacial region to spur the vicious cycle of corrosion acceleration (Fig. 11.7 (a)).

The first strategy for preventing corrosion is resisting acidification near the solution/metal interface, which we call "*pH-strategy*". The simplest tactics for this is to carry hydrogen ions away from the interface to the bulk solution

instead of having chloride ions approach toward the interface (Fig. 11.7 (b)). This can be achieved by controlling the state of poly-$M(O,OH)_6$ octahedra; acidification is suppressed by stable large negatively-charged poly-$M(O,OH)_6$ octahedra near the interface. As the state of poly-$M(O,OH)_6$ octahedra largely depends on many factors such as pH, co-existing species in the solution, electrochemical potential, etc., in situ observation is essential to elucidate the structures of ions near the interface.

11.3.2 Shielding the Interface against Environments: "*shielding-strategy*"

In atmospheric corrosion, a steel surface is always covered with a layer composed of hydroxides and/or oxyhydroxides. This layer changes the corrosion conditions at the interface such as concentrations of ions, oxygen, time of wetness, acidity, etc. The corrosion rate will be reduced when the layer acts as a barrier against environments. Thus, the second strategy for preventing corrosion is shielding the solution/metal interface against environments, namely "shielding-strategy". Barrier properties of rust depend on its various-scale structures and morphology which can be optimized by controlling the corrosion process. This may be designed by use of analytical results obtained through in situ observation of the reactions, and by quantitative evaluation of nano-scale structures of corrosion products.

11.4 Analytical Techniques of Corrosion on Various Scales

11.4.1 In situ Observation of Reactions near the Solution/Metal Interface using Synchrotron Radiation

X-ray-based techniques have many merits for in situ observation of reactions near the solution/metal interface during corrosion with wet and dry cycles. X-rays can penetrate into the interface through air containing oxygen and moisture, even through a thin water film into the interface. Much advanced application of X-ray analyses became possible by synchrotron radiation (SR): an intense and forward-focused beam of radiation that is emitted when the path of an electron traveling almost at the speed of light is bent by a magnetic field [8].

In order to characterize structures of corrosion products in various scales as imaged in Fig. 11.5, we utilized various analytical approaches that are sensitive to three structural-correlation lengths ξ: i.e. (1) ξ >50 nm (long-range order: LRO), (2) ξ ∼1–50 nm (middle-range order: MRO), and (3) ξ <1 nm (short-range order: SRO).

(1) In situ Observation of LRO Structures

Conventional X-ray diffraction (XRD) techniques can detect detailed structural information in terms of LRO. XRD technique has been widely applied to in situ observation of reactions during wet and dry cycles [9–12].

In order to observe structural changes in corrosion products that are located at various distances ($d(z)$) from the interface, an in situ analytical system combining an electrochemical cell with X-ray diffractometer that can manage grazing-incident X-ray scattering (GIXS) and surface (or *evanescent*) scattering [13–15] was developed [12]. This feature allows us to control the penetration depth ($l_{\text{x-ray}}$) of the X-ray beam in two ranges: i.e. $l_{\text{x-ray}} \sim 0.5 - 10$ μm by GIXS, and $l_{\text{x-ray}} \sim 0.1 - 10$ nm by surface scattering, by controlling both the energy of X-ray beam and the incident angle (α_{i}) of the X-ray beam relative to the specimen surface. In both X-ray geometries, we measured scattering intensities using a two-dimensional detector so-called image plate as well as a conventional scintillation detector. This enables us to measure diffraction intensities in a wide range of reciprocal lattices in a relatively short time, even in the case when grains are preferentially orientated.

(2) Analytical Approach to MRO Structure

Structural information in terms of MRO (c.a. 1–50 nm) is important to consider the polymerization of M(O, OH)_6 octahedra as in Fig. 11.4. However, it is difficult to determine MRO structures by conventional XRD, since crystallographic information of Fe-Fe, Fe-O and O-O correlation is mixed and averaged. Furthermore, conventional XRD gives broad peaks when grain size is smaller than c.a. 50 nm, which is often found in corrosion products. Thus additional analytical approaches are necessary to determine MRO structures.

One outcome was achieved by a combination of Anomalous X-ray Scattering (AXS) [16,17] and Reverse Monte-Carlo simulation (RMC) [18]. Crystallographic information of Fe-Fe, Fe-O and O-O correlation can be separated by measuring scattering intensities with different X-ray energies near the absorption edge of Fe. This technique successfully revealed atomic-scale structure of liquids [19–21]. This technique was also applied to quantitative analysis of nano-scale structure of Fe(O, OH)_6 octahedra in rust [9, 22, 23]. In this approach, we can obtain radial distribution function (RDF) of each element: i.e. RDF for Fe-Fe, Fe-O and O-O pairs, while we obtain a correlation that is mixed and averaged over all elements of Fe, O, and H in conventional XRD. Once RDF is obtained for each pair, the atomic structure in terms of MRO can be determined using RMC, which visualizes the atomic configurations based on RDF.

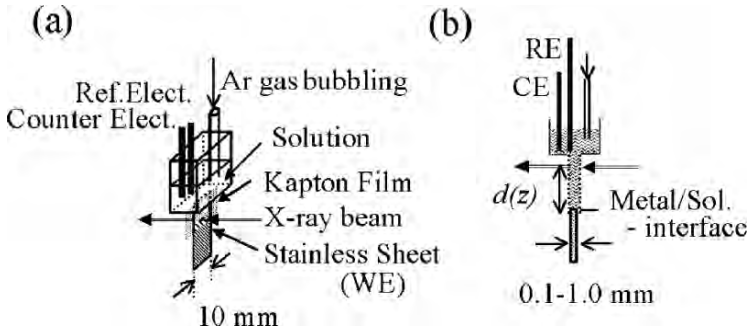

Fig. 11.8. Schematic illustration for a deviced electrochemical model pit for in situ XAFS measurements. (**a**) Perspective, and (**b**) side views

(3) Analytical Approach to SRO Structure

In XAFS, oscillatory modulation near an X-ray absorption edge of a specific element of a specimen provides information in terms of ligand coordination around the absorbing atom both in solid and solution [24]. We can determine the distance between the centered atom and the neighboring ligands, the number of ligands, and the stereographic arrangement of ligands. Therefore XAFS is useful for in situ observation of SRO with correlation range of less than 1 nm as in Fig. 11.5 during wet and dry cycles. XAFS has been widely used to study rust-formation [9, 12, 25–29].

In order to observe change in SRO structures during corrosion by XAFS, two types of electrochemical cells were devised. One is for simulating atmospheric corrosion [12]. A block specimen could be kept in a horizontal position, over which a solution film could form. XAFS spectra were measured in a reflection geometry by monitoring fluorescence using a solid state detector with 19-elements [30]. The other is for simulating localized corrosion as in Fig. 11.8. SRO structures of ions in a solution near the metal/solution interface were in situ observed [26,31,32]. A sheet of stainless steel and a reservoir containing various types of solution are joined together by a flat box made of transparent film. A typical size of box is about 0.1 mm in thickness and 10 mm in width. An X-ray beam passes through the film box containing the solution at different distances from the metal/solution interface: *d(z)*. XAFS measurements were performed in a transparent geometry, while the electrochemical potential of the metal sheet was controlled.

11.4.2 Mössbauer Spectroscopy

Each Fe^{3+} ion has a spin magnetic moment of 5 Bohr magnetons due to five 3d electrons in Fe^{3+}. The spin magnetic moments of Fe^{3+} ions coupled by super-exchange interaction give the characteristic Fe^{3+} Néel temperatures for the different phases of FeOOH. In the three phases of FeOOH in rust, the spin

magnetic moments are coupled as anti-ferromagnetic state below Fe^{3+}Néel temperatures: i.e. $T_N^{\alpha} = 403$K, $T_N^{\beta} = 280$K and $T_N^{\gamma} = 73$K, respectively. Rust on the advanced weathering steel with the addition of 3 mass% Ni [33, 34] also contains a ferri-magnetic spinel phase of $T_N^{S} = 860$K. Since the super-exchange interactions through O^{2-} ions are rather short ranged, the magnetic properties can be determined uniquely as the number of atoms at the surface of crystalline grains is much less than that inside the grains. Therefore this method is applicable even to substances with very fine crystalline grains.

In the anti-ferromagnetic state, spin magnetic moment of each Fe^{3+} ion aligns in the easy direction of the crystals by magneto-crystalline anisotropy which is determined by the crystal symmetry. The uniaxial anisotropy energy can be written as

$$E_A = K_u V(1 - \cos^2\theta) \tag{11.3}$$

where V is the volume of a grain, θ is the angle between a spin direction and the easy axis, and K_u is the uniaxial anisotropy constant, e.g. $K_u = 10^3$ J/m^3 for α-FeOOH [35].

Above the Fe^{3+} Néel temperature in paramagnetic state, each spin fluctuates randomly and the sub-lattice magnetization is vanishing. Up to the Néel temperature the sub-lattice magnetization of the anti-ferromagnet fluctuates along the easy axis, i.e. $\theta = 0$ or π. According to the mean field theory, their average volume decreases with increasing temperature. It is essential, however, to take into account that fine grains of an anti-ferromagnet become super-paramagnetic even below the Néel temperature when the thermal energy exceeds the potential barrier of E_A in Eq. (11.3), i.e. $K_u V$ at $\theta = \pi/2$. The characteristic transition probability over the potential maximum, $K_u V$, at temperature T is given as the inverse of the relaxation time, τ, which is derived as [36]

$$\tau = \tau_0 \sqrt{\frac{K_u V}{k_B T}} \exp\left[-\frac{K_u V}{k_B T}\right]. \tag{11.4}$$

Due to the hyper-fine interaction between electron spins and nuclear spins, Fe nuclei experience a large hyper-fine field, e.g. 502kOe and 450 kOe in α-FeOOH and γ-FeOOH, respectively at low temperatures. ^{57}Fe nuclear level is split by this hyper-fine field into 2 and 4 Zeeman levels for ground (I = 1/2) and excited states (I = 3/2), respectively, resulting in six resonant absorption lines by dipolar transition whose energies are $(h/2\pi)\omega_j$ (j = 1,2,...6) in the Mössbauer spectrum. Mössbauer spectroscopy is a nuclear γ-ray (14.4 keV for ^{57}Fe) resonant absorption with the recoilless transitions of nuclei embedded in a solid lattice with a natural line width of 4.2×10^{-8} eV.

The hyper-fine field is proportional to the sub-lattice magnetization that disappears above the Néel temperature. Thus doublet absorption lines with quadrupole splitting are observed. The detailed temperature dependence of

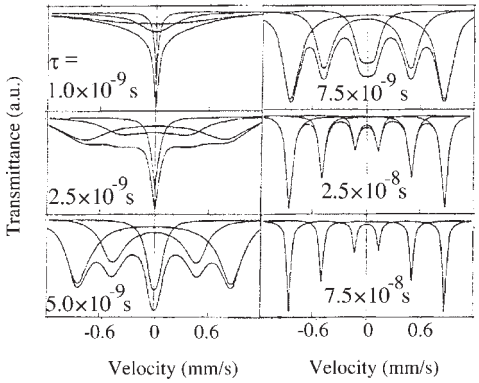

Fig. 11.9. Mössbauer absorption spectra calculated for various relaxation times, τ

Mössbauer spectra, which are quite different below and above the Néel temperature, is useful information to identify the phases with different T_{N}.

In reality, fruitful discussion becomes available if one analyses the rather complex data of Mössbauer spectroscopy due to the super-paramagnetic relaxation phenomena. Electron spins flip within the super paramagnetic relaxation time, τ which is determined by the ratio of the anisotropy energy, $K_{\mathrm{u}}V$ and thermal energy, $k_{\mathrm{B}}T$, as described in Eq. (11.4). The former is proportional to the volume, V, of each fine grain in which the spins of Fe^{3+} are exchange coupled. Mössbauer spectra are affected by the relaxation effect when $1/\tau$ becomes larger than the difference of transition frequency of ^{57}Fe nuclei in the hyperfine field, i.e.,

$$(\omega_{7-j} - \omega_j)\tau < 1, \qquad (\mathrm{j} = 1, 2, 3) \tag{11.5}$$

so that we calculate the absorption spectra, $S_{\mathrm{cal}}(\omega, V, T)$ according to the relaxation theory of resonance as shown in Fig. 11.9 [37]. The observed Mössbauer resonant absorption spectrum $S_{\mathrm{obs}}(\omega, V, T)$ at temperature T is the weighted sum of the convolution of calculated spectrum of each phase with the distribution, $f_k(V)$, of fine grains volume in the phase k, whose fractions are x_k, as follows:

$$S_{obs}(\omega, T) = \sum_k x_k \int f_k(V) S_k^{cal}(\omega, T, V) dV \tag{11.6}$$

where $k = \alpha$-, β-, γ-FeOOH or spinel phase. Now our final goal is to get not only the fractions of different phases, x_k, but also the fine grains volume distribution of each phase, $f_k(V)$, in the real rust.

11.5 Establishing *pH-strategy* through Analyses of Localized Corrosion on Stainless Steel

11.5.1 Localized Corrosion of Stainless Steel

Due to the strong nature of passive film formation, stainless steel is known as one of the high corrosion resistance metals. However, in environments containing chloride or bromide ions, stainless steel is apt to corrode in specific areas. This is called localized corrosion in which pitting and crevice corrosion are typical forms. The process depends upon numerous factors such as species in the solution, pH, temperature, electrochemical potential, properties of passive film, inclusion in the metal, surface morphologies, etc.

Within the actively corroding zone such as pits in the metal undergoing localized corrosion, pH becomes low due to the hydrolysis of accumulated metal cations:

$$\mathrm{M^{n+}} + n\mathrm{H_2O} \rightarrow \mathrm{M(OH)_n} + n\mathrm{H^+} \tag{11.7}$$

Since it is most likely that $\mathrm{H^+}$ ion is adsorbed on $\mathrm{M(O,OH)_6}$ octahedra to form positively charged colloidal substances, mobility of $\mathrm{Cl^-}$ ions become higher than that of $\mathrm{H^+}$. Thus accumulation of chloride ions ensues inside a locally corroding part. Therefore, it is very intriguing to observe the concentration and the state of ions near the solution/metal interface within a model pit.

11.5.2 Concentration of Metal Cations inside a Locally Corroding Part

Several approaches have been attempted for in situ observation of a locally corroding part [38,39]. Concentrations inside pits were investigated by X-ray fluorescence measurements using an in situ microprobe technique [38], in which the composition and thickness of the salt layer were successfully determined.

Structures as well as concentrations of metal anions inside model pits were observed in situ by the method discussed in Sect. 11.4.1 (C) [26,31,32]. In situ XAFS spectra were measured for model pits using sheets of Fe-18%Cr-12%Ni-2%Mo, of which potential was kept at $E = 0.8\ V_{\mathrm{sat.Ag/AgCl}}$ vs. a saturated Ag/AgCl reference electrode in a solution of 1M LiBr. Since there is ohmic drop in the model pit, the potential at the interface is estimated to be c.a. $-0.1\ V_{\mathrm{sat.Ag/AgCl}}$. This condition corresponds to an active dissolution region with no passive film at the interface with the dissolution rate maintained constant; in other words, this simulates a so-called stable pit. The results have shown that concentrations of both $\mathrm{Cr^{3+}}$ and $\mathrm{Br^-}$ ions, determined by the amount of absorption at Cr K- and Br K-edges, respectively, decrease linearly as the distance from the solution/metal interface ($d(z)$) increases as in Fig.11.10 (a).

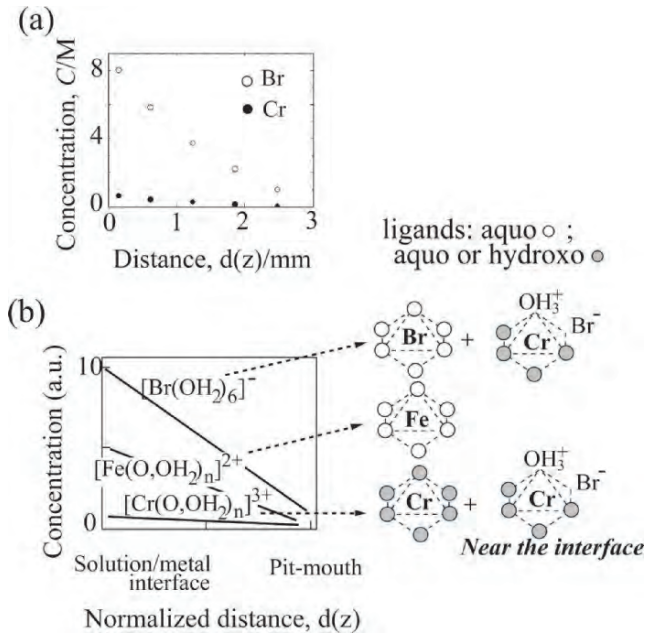

Fig. 11.10. Dependence of concentration on *d(z)* for (**a**) chromium and bromine inside a pit with a depth of 2.7 mm. (**b**) Schematic illustration of concentration dependence of ions on *d(z)* and possible structure models of them. *White and gray spheres* represent aquo and aquo/hydroxyo ligands around a centered ion

XAFS spectra at different positions *d(z)* were analyzed in order to determine the structures around Cr^{3+} and Br^{-}. As in Fig.11.10 (b), these analyses have shown that chromium and bromide ions are surrounded by c.a. six oxygen atoms in a region far from the interface, suggesting that these ions are hydrated, or that some chromium ions may form a hydroxo complex. In contrast, in a region near the interface it was shown that some of chromium ions are directly bound to bromide ions, which indicates the formation of Cr^{3+}- Br^{-}-H_2O complex (cf. Fig.11.10 (b)). This result is intriguing, since the following complex formations are indicated:

$$Cr^{3+} + 6H_2O \rightarrow Cr(OH)_3(H_2O)_3 + 3H^+ \tag{11.8}$$

$$Cr(OH)_3(H_2O)_3 + 3H^+ + Br^- \rightarrow CrBr(OH)_2(H_2O)_3 + 2H^+ + H_2O \tag{11.9}$$

Nevertheless both reactions decrease pH.

11.5.3 Formation of Poly-Mo(O, OH)$_6$ Octahedra

It is known that molybdenum is an element to improve pitting resistance. There have been numerous studies devoted to elucidating the effects of

molybdenum on the pitting susceptibility of stainless steels: i.e. improving the resistance of the passive film against breakdown [40,41], enhancing repassivation characteristics [42], reducing the active dissolution rate of the bare metal inside the pits [43, 44], etc. States of molybdenum in sulfuric acid are measured in situ by a channel flow double electrode [45], in which it was reported that $Mo(V)_{sol}$ was detected in the passive region, and that both $Mo(V)_{sol}$ and $Mo(VI)_{sol}$ were detected in the transpassive region. However, little information has been acquired on the structure of Mo ions near the interface.

As discussed in Sect. 11.5.1, pH inside pits tends to be low. Concentrated chloride ions stabilize the growth of pits, resulting in further decreases in pH. In order to break this vicious cycle and prevent pitting, measures to resist acidification near the solution/metal interface are important. The mechanism to prevent pitting by molybdenum addition was investigated, having an eye to *pH-strategy* [26, 31, 32].

Structures of ions, including molybdenum, in model pits were observed in situ by the technique as discussed in Sect. 11.4.1(C) [26, 31, 32]. In situ XAFS spectra were measured for a model pit using sheets of Fe-18%Cr-20% Ni-5%Mo, which was kept at E = 1.6 $V_{sat.Ag/AgCl}$ in solutions of 2 M LiBr and LiCl. The estimated potential at the interface is c.a. 0.7 $V_{sat.Ag/AgCl}$ after ohmic drop correction. The pitting potentials of the ferritic Fe-18%Cr-x%Mo alloys are reported to increase largely with the Mo content in chloride solutions, but slightly in bromide solutions [46]. Thus comparison of molybdenum states in LiBr and LiCl will give us intriguing information.

In both solutions, the concentrations of molybdenum ions inside the model pit decrease almost linearly as the distance *d(z)* increases. In both solutions, energies of Mo K-edge are located almost at the same position for 2 M solution of Na_2MoO_4, which indicates that the valence of molybdenum ion is $Mo(VI)_{sol}$.

Each XAFS spectrum at a different distance *d(z)* was analyzed to determine the structure of molybdenum ions. Figure 11.11 (a) shows the Fourier transforms of XAFS spectra at the Mo-K edge obtained by in situ measurements in 2 M LiBr. These spectra in Fig. 11.11 (a) correspond to radial distribution functions (RDF) around molybdenum atoms. Near the pit mouth (i.e. far from the interface, c.a. $d(z) = 3.0$ mm) molybdenum forms molybdate ions in terms of $[MoO_2(OH_2)_4]^{2-}$; i.e. molybdenum atoms are coordinated by two oxygen and four water molecules [47]. However, near the interface, molybdenum forms a complex with bromide ions such as $[MoBr_mO_n(OH_2)_{6-m-n}]^{x-}$ as shown by strong peaks near R = 0.22 nm, also found in RDF of $MoBr_3$. Though the intensity of these peaks decreases as the distance *d(z)* increases, they are observed even near the pit mouth ($d(z) = 3.0$ mm).

Completely different results were obtained in 2 M LiCl. In a wide range from near the pit mouth to the interface, RDF spectra in 2 M LiCl showed clear peaks in a region R = 0.13 − 0.17 nm, corresponding to the Mo-O interatomic distance that indicates MoO_6 octahedra (cf. Fig. 11.11 (c)). Near the

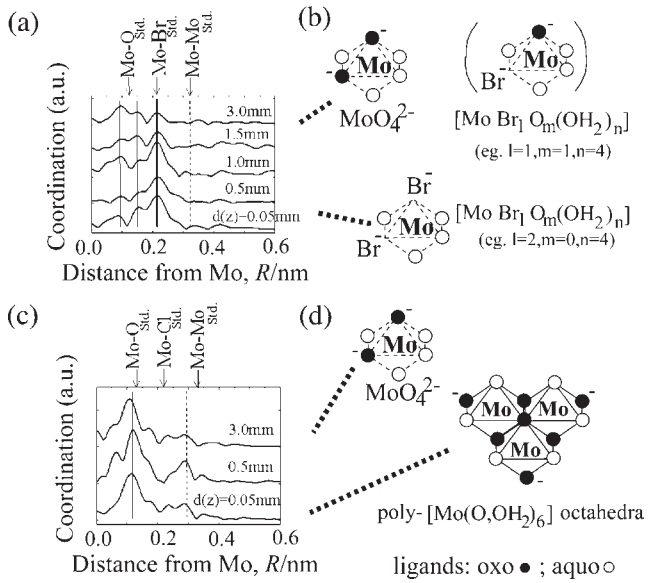

Fig. 11.11. Fourier transforms of XAFS spectra at Mo-edge ((**a**), (**c**)) together with schematic illustrations for interpreted existing states of $Mo(O, OH)_6$ octahedra ((**b**), (**d**), respectively) in LiBr and LiCl. *Arrows* at the top of (a) and (**c**) show atomic distance of Mo-O, Mo-Br, and Mo-Mo found in reference materials. *Thin, thick and dashed lines* correspond to peak positions for atomic distance of Mo-O, Mo-Br, and Mo-Mo, respectively

interface, other peaks were clearly found in the region R=0.25 − 0.35 nm, corresponding to the inter-atomic distance between two molybdenum atoms located in centers of neighboring two-MoO_6 octahedra. Intensity of peaks corresponding to the Mo-Mo correlation, decreases as *d(z)* increases. These results show that molybdenum forms $[MoO_2(OH_2)_4]^{2-}$ near the pit mouth, and poly-$Mo(O, OH_2)_6$ octahedra near the interface (cf. Fig. 11.11 (d)). These different results are probably obtained because of the difference in affinities in terms of Mo-Br and Mo-Cl.

Polymerization of the $[MoBr_mO_n(OH_2)_{6-m-n}]^{x-}$ is hard to achieve, since olation and/or oxolation (Eqs. (11.1) and (11.2)) are interfered with. In contrast, polymerization of $Mo(O, OH_2)_6$ octahedra can progress to form negatively-charged large poly-$M(O, OH)_6$ octahedra (cf. Fig. 11.7 (d)) near the interface in LiCl. Diffusion rates of the large poly-$M(O, OH)_6$ octahedra are much lower than those of hydrogen ions. Consequently hydrogen ions diffuse away from the interface out to the pit mouth. This may lead to an increase in pH to facilitate re-passivation. Concrete view of the poly-$Mo(O, OH_2)_6$ octahedra structure is left as an issue for further discussion.

Table 11.1. Chemical compositions of mild, conventional weathering, and advanced weathering steels

Specimen	Chemical composition (mass%)						
	C	Si	Mn	P	Cr	Cu	Ni
Mild steel	0.16	0.50	1.50	0.025	···	···	···
Conventional weathering steel	0.10	0.42	1.54	0.004	0.52	0.30	0.32
Advanced weathering steel	0.05	0.04	1.02	0.008	···	0.40	3.03

11.6 Establishing *shielding-strategy* through Analyses of Protective Rust on Weathering Steel

11.6.1 Protective Rust on Weathering Steel

Reducing the maintenance cost of infrastructures is a challenge in corrosion protection. Repeatedly adding coatings is easy, but the life cycle maintenance cost (LCC) eventually accumulates after a long service period. Low alloy steels with atmospheric-corrosion resistance that do not need painting, were first commercialized in the 1960s [48], and these are now called weathering steel. In a relatively mild environment, weathering steel with a typical composition of Fe-0.4Cu-0.8Cr mass% is durable due to the formation of protective rust [9, 10, 37, 48–54].

11.6.2 Polymerization of $Fe(O, OH)_6$ Octahedra through Wet and Dry Cycles

Changes in various scale structures during wet and dry cycles on the surface of weathering and mild steels, as in Table 11.1, were investigated by in situ observation of XAFS and XRD, with an eye to the polymerization of $M(O, OH)_6$ octahedra [9, 10].

After six months corrosion at an urban area, chromium was involved in polymerized $Fe(O, OH)_6$ octahedra in the rust on weathering steel. Chromium does not simply substitute the site for iron as indicated in previous work [55], but occupies a different site from $Fe(O, OH)_6$ octahedra. The atomic-correlation of Cr-Fe(Cr) in the rust is 12% smaller than that of Fe-Fe in α-FeOOH, which is also confirmed by other studies [27]. Copper formed CuO_x polyhedra with a different structure from $Fe(O, OH)_6$ octahedra in the rust. These results showed that addition of chromium and copper results in formation of $Cr(O, OH)_x$ and CuO_x polyhedra having different sizes and structures from $Fe(O, OH)_6$ octahedra. These may work as heterogeneous nucleation sites in the polymerization processes of $M(O, OH)_6$ octahedra.

The aging process follows the nucleation and growth process. Figure 11.12 shows the MRO structures of corrosion products formed on weathering steel: (a) after 2 week in seawater, and (b) after 31 year in a semi-rural atmosphere.

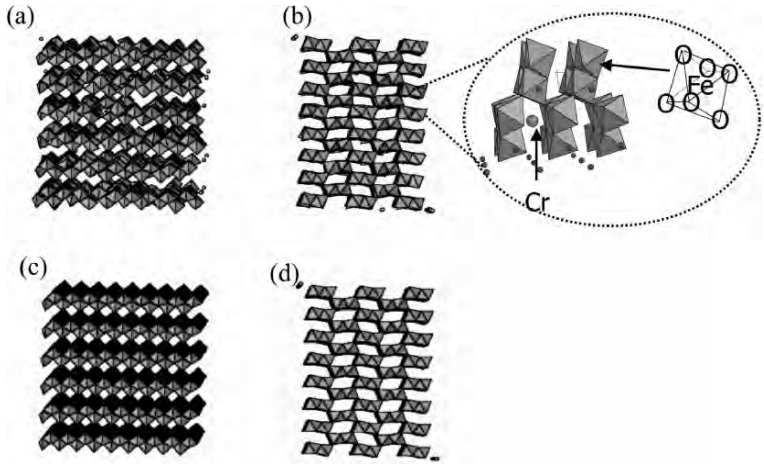

Fig. 11.12. The structures of corrosion products formed on weathering steel: (**a**) after 2 week in seawater, and (**b**) after 31 year in a semi-rural atmosphere. Ideal structures of crystal γ-FeOOH and α-FeOOH are also shown in (**c**) and (**d**) as references, respectively

Though the MRO structure of the specimen (a) has some similarity to that of crystalline γ-FeOOH, the linkage of $\mathrm{Fe(O,OH)_6}$ octahedra is largely disordered. In contrast to this, the MRO structure of the specimen (b) is similar to that of crystalline α-FeOOH and the linkage of $\mathrm{Fe(O,OH)_6}$ octahedra is well ordered. These results show that disordered linkage of $\mathrm{Fe(O,OH)_6}$ octahedra in products formed at an early stage of corrosion transforms into a more stable structure through the aging process. This transformation in inter-crystalline region as shown in Fig. 11.5 is indicative of the phenomena in which so-called X-ray amorphous rust [49] gradually changes into XRD detectable α-FeOOH phase [52] through long term aging process.

Differences in evolution of $\mathrm{M(O,OH)_6}$ octahedra through the polymerization reaction, are summarized and illustrated in Fig. 11.13, where the $\mathrm{Fe(O,OH)_6}$ octahedra are symbolized by triangle pairs for simplicity. Additional elements change the polymerization reaction, resulting in various-scale structures of rust formed after a long time.

11.6.3 Various Scale Analyses for Structures of Protective Rust

The effects of additional elements on structures of rust on various scales were investigated using conventional weathering and mild steels as in Table 11.1, which were exposed for 31 years in a semi-rural area.

XRD results indicate that both rusts consist of α- and γ-FeOOH with grain size less than c.a. 27 nm (c.a. 10×10^3 nm^3). The diffraction peaks of α-FeOOH in rust on weathering steel is composed of two broad peaks with different widths, indicating that the grain-size distribution has two peaks around $d = 10$ nm (c.a. 0.5×10^3 nm^3) and $d = 30$ nm (c.a. 14×10^3 nm^3) [9].

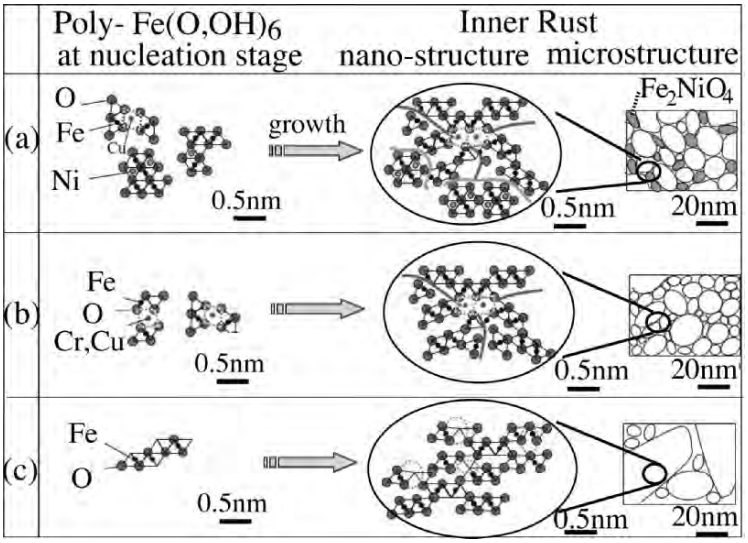

Fig. 11.13. Schematic diagram of evolution of the $Fe(O, OH)_6$ octahedra in rust formed on (**a**) advanced weathering, (**b**) conventional weathering, and (**c**) mild steels

Nano structure analysis by transmission electron microscopy (TEM) also showed that the rust is composed of fine grains around 27 nm (c.a. 10×10^3 nm^3) with ambiguous boundaries.

Quantitative analysis of fine grains distribution of the rust was carried out by Mössbauer spectroscopy as discussed in Sect. 11.4.2. Figure 11.14 (a), (c) shows examples of the absorption spectra for α-FeOOH in the rusts. The spectra of major components of α-FeOOH (85 mol%) in the rusts were obtained by subtracting those of paramagnetic γ-FeOOH phase (15 mol%) at each temperature from the original data. One can find differences between them at intermediate temperatures, e.g. 60 K and 100 K, which are caused by different distributions of fine grain sizes through super-paramagnetic relaxation.

Detailed analyses of the spectra have shown the volume distribution histogram of α-FeOOH grains in the rusts as shown in Fig. 11.15. The calculated spectra (Fig. 11.14 (b), (d)) based on the assumed distribution fit well with the observed ones (Fig. 11.14 (a), (c)). The main α-FeOOH phase for both of them consists of fine grains whose volume is distributed mostly below 3×10^4 nm^3. There is, however, quite an interesting difference between the rusts on the mild and weathering steels. In the former, the rust fine grains volume distribution is clearly separated into two regions, i.e. there is a missing region between $3\sim 7\times 10^3$ nm^3, while in the latter fine grains distribution is continuous without any missing region. The volume fraction of rust on the weathering steel in the large region is much smaller (47%) than that of the rust on the mild steel (83%).

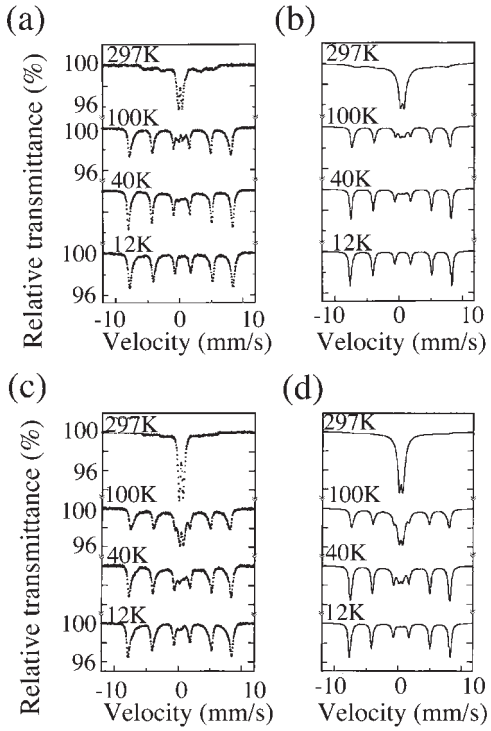

Fig. 11.14. Extracted Mössbauer spectra of α-FeOOH in rusts measured for (**a**) mild, and (**c**) conventional weathering steels after 31 year exposure to a semi-rural atmosphere. Also shown are calculated ones: (**b**) for the former and (**d**) for the latter steels using the assumed volume distribution histogram for α-FeOOH grains

The continuous distribution of fine grains volume is necessary in order to make a densely packed protective inner layer on the weathering steel. This is essential to understand why the rust on weathering steel produced in the atmosphere is protective. Rust on steel exposed to the atmosphere has been aged after successive periodic wet and dry cycles over several decades, during which nuclei of $Fe(O,OH)_6$ octahedra get together to form variously sized particles followed by dissolution and precipitation processes, resulting in slow growth to form a densely packed protective rust layer.

Now we consider why the characteristic morphology is realized in the protective layer of rust on the weathering steel. It should be noted that small amounts of additional elements, e.g. 0.3 mass% of Cu and 0.5 mass% of Cr, play an important role as heterogenous nucleation sites such as $Cr(O,OH)_6$ or CuO_x polyhedra in aqueous solution in wet cycles at the initial stage of the polymerization of $Fe(O,OH)_6$ octahedra. During growth of fine grains, they are repelled out of the crystallites of FeOOH phase due to the local violation of charge balance and the difference in solubility, creating recycling nucleation

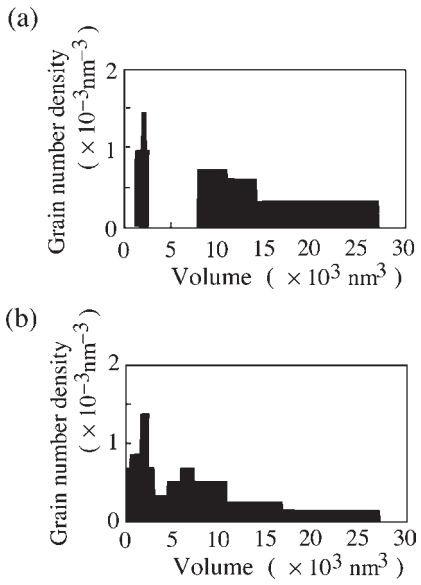

Fig. 11.15. The best-fitted volume distribution, $f_\alpha(V)$, of α-FeOOH in rust (**a**) on the mild and (**b**) on the conventional weathering steels

sites for new grains. Overwhelming nucleation sites with relatively slow grain growth in the atmospheric circumstances make a variety of volumes of grains. The number of grains increases with repetition of wet and dry cycles so long as there is room to make new grains until they become densely packed with stress to produce the protective rust layer against further corrosion of steel (cf. Figs. 11.5 and 11.13).

Differences between the fine grain volume distributions of rust on mild steel and that on weathering steel must be a key to support the above interpretation. Fine grains in a small volume size region (53%) found in the rust on weathering steel may be surrounded tightly by other grains which suppress supply of $Fe(O, OH)_6$ octahedra for further grain growth. Fine grains in a large volume size region (83%) of the rust on mild steel seem to have free gap space where aqueous solution with aggressive ions can enter, thereby corroding steel interface. Then after a long period, such as 31 years, the grain volume distribution shifts to the larger side, leaving the missing region, say, among fine grains since growth of grains preferentially occurs. While in rust of weathering steel, heterogeneous nucleation sites always make new grains simultaneously with growth of old grains, resulting in continuous grain volume distribution.

It should be noted that the analytical approach using Mössbauer spectroscopy is based on the fundamental assumption that the rust consists of intrinsic magnetic crystallites which have definite Néel temperature and magneto-crystalline anisotropy in each phase. Success in obtaining the

temperature independent fine grains volume distribution for each phase seems to support the following picture; i.e. although they are recognized to contain a so-called X-ray amorphous phase, atomic structure in the aged rust on weathering steel is as in Fig. 11.5, and is entirely different from silicate glass or metallic glass where disordered arrangement is continuous without any grain boundary.

11.7 Combination of *pH*- and *shielding-strategies* through Analyses of Protective Rust on Advanced Weathering Steel

11.7.1 Advanced Weathering Steel

Protective rust forms on conventional weathering steel when it is exposed to a mild environment. However, the protective rust does not form on the surface of conventional weathering steel under severe conditions where the amount of airborne salinity is higher than the limit of, say, c.a. 0.05 $mg/dm^2/day$ in Japan. So-called "advanced weathering steel", containing 3.0 mass% Ni and 0.4 mass% Cu as in Table 11.1, has been developed to increase anti-air-borne salinity properties [33, 34], for which applicability limits are shown by a method reported elsewhere [56].

11.7.2 Polymerization of $(Fe, Ni)(O, OH)_6$ Octahedra through Wet and Dry Cycles

Changes in various scale structures during wet and dry cycles on the surface of advanced weathering steel as in Table 11.1 were investigated by in situ observation of XAFS and XRD with an eye to the polymerization of $M(O, OH)_6$ octahedra [12, 57]. In situ XRD showed that dissolved ferrous ions form $Fe(OH)_2$ in wet conditions with seawater and that $Fe(OH)_2$ transforms into γ-FeOOH and Fe_3O_4 in air in the transition from a wet to a dry state. In situ XAFS showed that nickel atoms substitute iron atoms in FeO_6 octahedral sites in Fe_3O_4 to form Fe_2NiO_4. Fe_2NiO_4, which formed in the first wet cycle, remained in the following dry cycle in the case of advanced weathering steel. The stabilization of Fe_3O_4 is unique compared to conventional weathering steel, where Fe_3O_4 was easily oxidized to form α- and/or γ-FeOOH in a dry cycle in the case of conventional weathering steel [58, 59].

Formation of $(Fe, Ni)O_6$ octahedra and CuO_x polyhedra affects the properties of rust drastically. First, $(Fe, Ni)O_6$ octahedra and CuO_x polyhedra provide heterogeneous sites for the nucleation of $Fe(O, OH)_6$ octahedra, resulting in formation of protective rust composed of fine grains even in high airborne salinity conditions (cf. Fig. 11.13). Second, formation of $(Fe, Ni)O_6$ octahedra changes the ion-exchanging properties of rust from anion to cation selective.

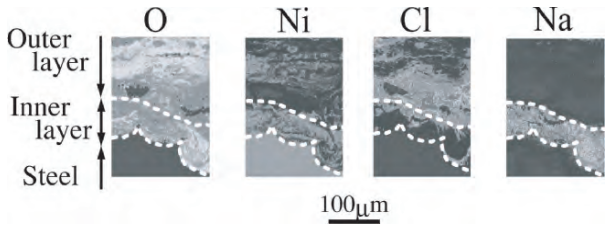

Fig. 11.16. Compositional mapping of the cross-section of rust formed on the advanced weathering steel after nine year exposure to a coastal atmosphere. The *gray scale* shows compositions of O, Ni, Na and Cl measured by an electron-probe micro analyzer (EPMA); the higher the concentration, the lighter the gray scale. *Broken white lines* indicate layer boundaries

11.7.3 Formation of Cation-exchanging Poly-$(Fe, Ni)(O, OH)_6$

The reported values of point of zero charge (pH_{pzc}) are: $pH_{pzc}(Fe_3O_4)$ = 5.8 [60] and $pH_{pzc}(\alpha\text{-FeOOH})$ = 7.7 [5]. $pH_{pzc}(Fe_2NiO_4)$ was estimated by calculating the energy of hydrogen ion adsorption in water using the density functional theory, which showed that $pH_{pzc}(Fe_2NiO_4)$ is much closer to $pH_{pzc}(Fe_3O_4)$ than to $pH_{pzc}(\alpha\text{-FeOOH})$. Thus, the surface of stabilized Fe_3O_4, namely Fe_2NiO_4, in the inner layer becomes more negative than FeOOH, to accumulate positive sodium ions instead of negative chloride ions. In other words, the hydroxyl (-OH) groups on the surface of the inner rust of advanced weathering steel change into $-O^-$ during wet periods (cf. Fig. 11.6). Then the rust dries, these form $-O^- \cdot Na^+$ to accumulate sodium ions. In the next wet process, an increase in pH could occur because they generate NaOH. The higher pH makes the surface charge of colloidal rust particles more negative to collect more positive sodium ions, which facilitates passivation of the advanced weathering steel.

This various-scale mechanism really changes macroscopic structures of rust. Figure 11.16 shows compositional mapping of the cross-section of rust formed on the advanced weathering steel after nine year exposure in a coastal area. The rust is composed of inner and outer layers, where the concentrations of Ni and Na are higher in the former, while Cl is accumulated in the latter [12, 33, 57].

Mass fraction estimated by XRD measurements was about 70, 10, 10, and 10% for α-FeOOH, β-FeOOH, γ-FeOOH and spinel (Fe_2NiO_4 or Fe_3O_4), respectively for the inner layer. Fraction of the Fe_2NiO_4 phase was detected quantitatively with SQUID (super-conducting quantum interference device) magnetometer as it is ferromagnetic. Extrapolating observed magnetization at 7 K in varying fields up to 7 T, the spontaneous magnetization of spinel phase was obtained. Atomic fraction of spinel phase is estimated to be 10–14% in the inner layer of the rust as listed in Table 11.2 [61].

Table 11.2. Atomic fraction of Fe in different phases, i.e. α-, β-, γ-FeOOH and spinel (Fe_3O_4 + Fe_2NiO_4), in rusts formed on advanced weathering steel after nine year exposure to a coastal atmosphere

Phase	S-in	U-in	S-out	U-out
α-FeOOH	0.69	0.67	0.74	0.67
β-FeOOH	0.10	0.14	0.10	0.15
γ-FeOOH	0.08	0.06	0.06	0.04
Spinel	0.13	0.13	0.10	0.14

11.7.4 Various Scale Analyses of the Rust on the Advanced Weathering Steel

The rust formed on advanced weathering steel after nine year exposure to a coastal atmosphere was investigated by Mössbauer spectroscopy. Rusts exposed under different conditions, i.e. under-shade horizontal (U) and out-of-shade vertical (S) facing to sea, were prepared from inner (in) and outer (out) parts of rust layers. Thus these conditions were designated as U-in, U-out, S-in and S-out, respectively. The former exposure condition (U) is more severe than the latter (S) as wet periods are longer. In the latter, there are also chances of periodic cleaning by rain followed by quicker drying.

Fractions of, x_α, x_β and x_γ, and volume distributions of $f_\alpha(V)$, $f_\beta(V)$ and $f_\gamma(V)$ of each specimen were determined by Mössbauer spectroscopy in a similar procedure to that described in Sect. 11.6.3 [61]. Extensive development in the analytical process was required to determine all of $f_\alpha(V)$, $f_\beta(V)$ and $f_\gamma(V)$. Two assumptions were made for calculation: i.e. (1) $f_\alpha(V)$ is composed of two peaks of Gaussian, and (2) $f_\beta(V)$ has the same shape as $f_\alpha(V)$. These assumptions are expected to be reasonable considering the results of conventional weathering steel as discussed in Sect. 11.6.3. Determined fractions of Fe ions in different phases, i.e. α-, β-, γ-FeOOH and Fe_2NiO_4 in the rust were obtained as listed in Table 11.2. The largest uncertainty of 3% may be included in the fraction of β-FeOOH.

More than 48 observed Mössbauer spectra at different temperatures for four samples can be reasonably reproduced with temperature independent volume distribution functions as shown in Fig. 11.17. Among the grains of α-FeOOH and β-FeOOH in the inner layer of the rust, S-in and U-in show continuous distribution of volume in the region less than 3×10^4 nm^3 with 4∼8% of an order of magnitude smaller grains of γ-FeOOH. It is also found that the distribution tends to separate into two peaks for under-shade conditions, which is indicative of less protectiveness of the inner rust than that in the out-of-shade condition.

We clearly found that the fine grains volume distribution function, $f_\gamma(V)$, for γ-FeOOH is quite different from that in α- and β-phases. This is interesting for considering the ageing of the rust. It was said qualitatively that

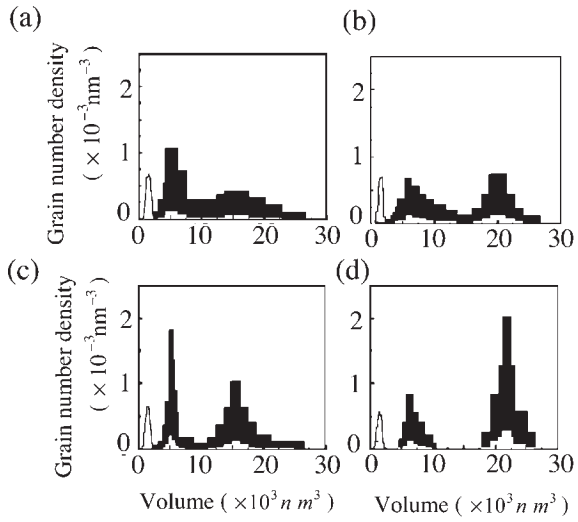

Fig. 11.17. The fine grains volume distribution, $f_j(V)$, of the inner and the outer layers of rust formed on advanced weathering steel after nine year exposure to a coastal atmosphere, (**a**) S-in, (**b**) U-in, (**c**) S-out, and (**d**) U-out: *black* for $f_\alpha(V) + f_{spinel}(V)$, *white* for $f_\beta(V)$, and *gray* for $f_\gamma(V)$

γ-FeOOH is the first precipitate from aqueous solutions as colloidal rust particles, which will gradually be transformed into the more stable α-FeOOH phase during long periods at ambient temperature. We found that 4∼8% of Fe in the rust remained in γ-FeOOH phase as very fine grains, which were most reluctant to transform as they could not get appreciable gain of bulk free energy compared to the surface energy.

It would be interesting to speculate the stage of separation between γ-FeOOH phase and α-FeOOH phase. If one calculates the size of spherical particles which contains the same number of $Fe(O, OH)_6$ octahedra inside and at the surface of the sphere, about 480 $Fe(O, OH)_6$ octahedra in the sphere are estimated. At the surface they have freedom to expand outside but inside they are rather tightly condensed. This critical sphere size would be one of the standards for minimum crystallite size because 240 $Fe(O, OH)_6$ octahedra is enough to distinguish the atomic arrangement of both γ-FeOOH and α-FeOOH phases. Typical grain volume of γ-FeOOH phase in rust on advanced weathering steel after nine years exposure contains about 80,000 $Fe(O, OH)_6$ octahedra, which is about 170 times larger than the standard size for minimum crystallite.

11.8 Summary

In this chapter, various scale analyses of pitting and atmospheric corrosion were implemented by (A) in situ observation of reactions near the solution/metal

interface using synchrotron radiation, and (B) Mössbauer spectroscopy. Polymerization of $M(O,OH)_6$ (M=metal) octahedra [4], which may be expressed as evolution of the $Fe(O,OH)_6$ network as elsewhere [9,10], is a quite important and useful concept to understand corrosion mechanisms. The combination of this concept with recent advances in the fields of analytical methods provides the opportunity to "see" corrosion reactions under real environments on various scales.

Applying presently proposed various scale analytical techniques, authors have been trying to develop further anti-corrosion steels by controlling corrosion products with functions with an eye to $M(O,OH)_6$-octahedra continuum. At this moment two major strategies have been posted: i.e. (1) controlling the interfacial pH: "*pH-strategy*" and (2) shielding the interface against environments: "shielding-strategy". In the former arguments, various scale observation of ion states in a solution near the interface gave a lot of information on the effects of alloying elements on controlling the function of poly-$M(O,OH)_6$. In the latter, various scale analyses of structure and morphology of rust during wet and dry cycles elucidated the process of nucleation, growth, and aging in terms of poly-$M(O,OH)_6$ octahedra. Designing corrosion products having an eye to $M(O,OH)_6$ octahedra in terms of their structure and functions is one of the recently established fields of study. Further investigations by various scale analyses will give us useful guidelines to innovate more functioning materials and technologies.

We thank Drs. Y. Waseda, T. Okada, T. Ishikawa, and M. Hashimoto for helpful discussion. We thank Drs. M. Saito, Y. Ishii, and Mr. N. Ohta for experimental support. We thank Drs. M. Hashimoto, S. Ito, N. Okumura and M. Hibi for their encouragement in the research. We thank Drs. T. Matsushita, M. Nomura, M. Tanaka, T. Mori and Y. Kitajima for supporting the synchrotron experiments at Photon Factory, KEK, in Japan.

References

1. H. Kihira: *Electrical Phenomena at Interfaces, Fundamentals, Measurements and Applications. 2nd ed.*, ed. H. Ohshima and K. Furusawa (Macel Dekker, Inc., New York, 1998), pp. 429-440.
2. G. Licheri and G. Pinna: *Proc. of EXAFS and Near Edge Structure*, Frascati, Italy, 1982 (Springer-Verlag), pp. 240-247.
3. R. M. Cornell and U. Schwertmann: *The Iron Oxides*, 2nd ed. (Wiley-VCH GmbH & Co. KGaA, Weinheim, 2003).
4. J.-P. Jolviet: *Metal Oxide Chemistry and Synthesis* (John Wiley & Sons Ltd, West Sussex, England, 2000).
5. W. Stumm and J. J. Morgan: *Aquatic Chemistry*, 3rd ed. (John Wiley & Sons, Inc., New York, 1996), pp. 533-549.
6. W. Whiman, R. Russell and V. Altieri: *Ind. Eng. Chem.*, **16**, 665 (1924).
7. N. Sato: *Petrotech*, **4**, 461 (1981).
8. P. A. Montano and H. Oyanagi: *MRS bulletin*, **24**, 13-16 (1999).

9. M. Kimura, T. Suzuki, G. Shigesato, M. Saito, S. Suzuki, H. Kihira, K. Tanabe and Y. Waseda: *J. Japan Inst. Metals*, **66**, 166-175 (2002).
10. M. Kimura, T. Suzuki, H. Shigesato, H. Kihira and S. Suzuki: *ISIJ International*, **42**, 1534-1540 (2002).
11. M. Yamashita, H. Konishi, T. Kozakura, J. Mizuki and H. Uchida: *Mater. Trans.*, **46**, 1004-1009 (2005).
12. M. Kimura, H. Kihira, N. Ohta, M. Hashimoto and T. Senuma: *Corros. Sci.*, **47**, 2499-2509 (2005).
13. W. C. Marra, P. Eisenberger and A. Y. Cho: J. Appl. Phys., **50**, 6927-6933 (1979).
14. H. Dosch: *Critical Phenomena at Surfaces and Interfaces* (Springer-Verlag, Berlin Heideberg, 1992).
15. M. Kimura, A. Acosta, H. Fujioka and M. Oshima: J. Appl. Phys., **93**, 2034-2040 (2003).
16. Y. Waseda: *Novel Application of Anomalous X-ray Scattering for Structural Characterization of Disordered Materials* (Springer-Verlag, Heidelberg, 1984).
17. Y. Waseda: *Anomalous X-ray Scattering for Materials Characterization* (Springer-Verlag, Berlin, 2002).
18. R. L. Mcgreevy and L. Pusztai: Mol. Simulation, **1**, 359-367 (1988).
19. M. Saito, C. K. Park, K. Omote, K. Sugiyama and Y. Waseda J. Phys. Soc. Japan, **66**, 633-640 (1997).
20. S. Kang, C. Park, M. Saito and Y. Waseda: Mater. Trans. JIM, **40**, 552 (1999).
21. Y. Waseda, S. Kang, K. Sugiyama, M. Kimura and M. Saito: J. Phys. Cond. Matter., **A195**, 12-17 (2000).
22. S. Suzuki, M. Saito, M. Kimura, T. Suzuki, H. Kihira and Y. Waseda: ISIJ International, **43**, 366-372 (2003).
23. S. Suzuki, Y. Takahashi, M. Saito, M. Kusakabe, T. Kamimura, H. Miyuki and Y. Waseda: Corros. Sci., **47**, 1271-1284 (2005).
24. B. K. Teo: *EXAFS: Basic Principles and Data Analysis* (Springer, Berlin, 1986).
25. S. Suzuki, T. Suzuki, M. Kimura, Y. Takagi, K. Shinoda, K. Tohji and Y. Waseda: J. Appl. Surf. Sci., **169-200**, 109-112 (2001).
26. M. Kimura, M. Kaneko and N. Ohta: ISIJ International, **42**, 1398-1402 (2002).
27. M. Yamashita, H. Konishi, J. Mizuki and H. Uchida: Mater. Trans. JIM, **45**, 1920-1924 (2004).
28. S. Suzuki, Y. Takahashi, T. Kamimura, H. Miyuki, K. Shinoda, K. Tohji and Y. Waseda: Corros. Sci., **46**, 1751-1763 (2004).
29. H. Konishi, M. Yamashita, H. Uchida and J. Mizuki: Mater. Trans., **46**, 337-341 (2005).
30. M. Nomura and A. Koyama: *X-ray Absorption Fine Structure*, edited by S. S. Hasnain, Ellis Horwood, London, (1991), p.667.
31. M. Kimura, M. Kaneko and T. Suzuki: J. Synchrotron Rad., **8**, 487-489 (2001).
32. M. Kimura and M. Kaneko: *Proc. of Electrochemical Soc. Int. Symp.*, Honolulu, **2004-19**, 273-288 (2004).
33. H. Kihira, A. Usami, K. Tanabe, M. Ito, G. Shigesato, Y. Tomita, T. Kusunoki, T. Tsuzuki, S. Ito and T. Murata: *Proc. of Electrochemical Soc. Int. Symp.*, Honolulu, 1999, Vol.99-26 (The Electrochemical Soc. Inc.), pp. 127-136.
34. H. Kihira, S. Ito, T. Mizoguchi, T. Murata, A. Usami and K. Tanabe: Zairyo-to-Kankyo, **49**, 30-40 (2000).

35. T. Shinjo: J. Phys. Soc. Japan, **21**, 917 (1966).
36. W. F. Brown, Jr.: Phys. Rev., **130**, 1677-1682 (1963).
37. T. Okada, Y. Ishii, T. Mizoguchi, I. Tamura, Y. Kobayashi, Y. Takagi, S. Suzuki, H. Kihira, M. Itoh, A. Usami, K. Tanabe and K. Masuda: *Jpn. J. Appl. Phys.*, **39**, 3382-3391 (2000).
38. H. S. Isaacs, J. H. Cho, M. L. Rivers and S. R. Sutton: J. Electrochem. Soc., **142**, 1111-1118 (1995).
39. H. S. Isaacs: *Synchrotron Techniques in Interfacial Electrochemistry*, ed. C. A. Melendres and A. Tadjenddine (Kluwer Academic Publishers, Netherland, 1994), pp. 199-214.
40. K. Sugimoto and Y. Sawada: Corros. Sci., **17**, 425-445 (1977).
41. Z. Szklarska-Smialowska: *Pitting corrosion of metals* (National Association of Corrosion Engineers, Houston, 1986), pp. 145-157.
42. H. Ogawa, H. Omata, I. Itoh and H. Okada: Corrosion, **34**, 52-60 (1978).
43. R. C. Newman: Corros. Sci., **25**, 331-339 (1985).
44. R. C. Newman: Corros. Sci., **25**, 341-350 (1985).
45. M. Itagaki, T. Suzuki and K. Watanabe: Electrochemica Acta, **42**, 1081-1086 (1997).
46. M. Kaneko and H. S. Isaacs: Corros. Sci., **44**, 1825-1834 (2002).
47. K. Shinoda, E. Matsubara, M. Saito, Y. Waseda, T. Hirato and Y. Awakura: Z. Naturforsch, **52 a**, 855-862 (1997).
48. C. B. Larabee and S. K. Coburn: *Proc. of Int. Congress on Metallic Corrosion*, London, U.K., 1962, pp. 276-285.
49. H. Okada, Y. Hosoi, K. Yukawa and H. Naito: J. Iron Steel Inst. Japan (TETSU-TO-HAGANE), **55**, 355-365 (1969).
50. T. Misawa, K. Asami, K. Hashimoto and S. Shimodaira: Corros. Sci., **14**, 279-289 (1974).
51. H. Kihira, S. Ito and T. Murata: Corros. Sci., **31**, 383-388 (1990).
52. M. Yamashita, H. Miyuki, Y. Matsuda, H. Nagano and T. Misawa: Corros. Sci., **36**, 283-299 (1994).
53. T. Kamimura, S. Nasu, T. Tazaki, K. Kuzushita and S. Morimoto: Mater. Trans. JIM, **41**, 1208-1215 (2000).
54. S. Nasu, T. Kamimura and T. Tazaki: Hyperfine Interactions, **193/140**, 175-182 (2002).
55. M. Yamashita, H. Miyuki, H. Nagano and T. Misawa: J. Iron Steel Inst. Japan (TETSU-TO-HAGANE), **83**, 448-453 (1997).
56. H. Kihira, T. Senuma, M. Tanaka, K. Nishioka, Y. Fujii and Y. Sakata: Corros. Sci., **47**, 2377-2390 (2005).
57. M. Kimura, H. Kihira, M. Nomura and Y. Kitajima: *Proc. of Electrochemical Soc. Int. Symp.*, Honolulu, 2004, Vol. 2004-14, pp. 133-142.
58. U. R. Evans and C. A. J. Taylor: Corros. Sci., **12**, 227-246 (1972).
59. M. Stratmann: Ber. Bunsenges. Phys. Chem. **94**, 626-639 (1990).
60. M. Sakashita and N. Sato: Boshoku-Gijyutsuu(Corros. Eng.), **28**, 450-461 (1979).
61. T. Mizoguchi, Y. Ishii, T. Okada, M. Kimura and H. Kihira: Corros. Sci. **47**, 2477-2491 (2005).

12 Mössbauer Spectroscopic Study on Rust Formed on Steel Surfaces

Takayuki Kamimura, Saburo Nasu

12.1 Introduction

Weathering steel containing a small amount of Cr, Cu, Ni and P has been widely noticed from the viewpoint of a reduction in maintenance cost of steel structures. This steel is standardized as G 3114 in Japanese Industrial Standards [1] and A588 in American Society for Testing and Materials [2]. It is widely accepted that it forms a protective rust (corrosion products) layer, which is dense and adherent to steel, during long term exposure to the atmosphere. This protective rust layer reduces the corrosion rate of steel. Because of this beneficial property, the weathering steel has been used for many steel structures on land such as bridges.

Figure 12.1 shows the corrosion loss curves of weathering steel and mild steel (plain carbon steel) exposed in a moderate industrial environment. The corrosion loss for the weathering steel is less than half that for the mild steel. The enhanced corrosion resistance of weathering steels is achieved by alloying with a combination of elements. This beneficial alloying effect has been known for several decades. Numerous studies have shown that weathering steels can form a protective rust layer that seals out the atmosphere and retards further corrosion. This is in contrast to other steels that form coarse, flaky and porous oxides that allow the atmosphere to continue penetrating the steel.

Because of the protectiveness of the rust layer formed on weathering steels, it has been investigated by means of various techniques like the X-ray diffraction technique (XRD), Electron Probe Microanalyzer (EPMA), IR spectroscopy, Raman spectroscopy, ^{57}Fe Mössbauer spectroscopy, Transmission Electron Microscope (TEM) and X-ray Absorption Fine Structure (XAFS) to elucidate the mechanism of its superior weatherability [3–23]. It is well known that the rust is composed mainly of ferric oxyhydroxides (FeOOH) and an X-ray amorphous substance, which gives no clear peaks in X-ray diffraction patterns. It is reported that different structures of oxyhydroxides such as α-FeOOH, β-FeOOH and γ-FeOOH are formed, and in some cases spinel type of iron oxides such as magnetite (Fe_3O_4) are contained in the rust layer depending on environmental conditions; the exposure positions (vertical or horizontal), time of wetness, gases contained in the atmosphere such as SO_2 gas, and airborne salt and deicing salt particles. It is of great interest that the remarkable influence of additional alloying element is only observed with

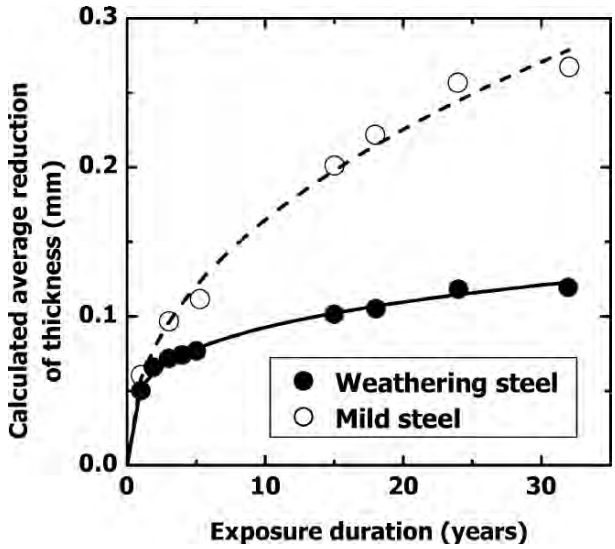

Fig. 12.1. Corrosion loss curves of weathering steel and mild steel exposed in a moderate industrial environment

repeated wetting and drying of the samples [24–26]. The typical condition for atmospheric corrosion is alternating wetting and drying of the metal surface, which result from temperature fluctuation between day and night as well as weather changes. If the surface is always kept wet or if the sample is immersed in a neutral electrolyte, the corrosion rates of pure iron and low-alloy steel are nearly the same [27]. Therefore, it is of importance to elucidate the fine structure of rust for comprehending the origin of the protectiveness of rust, and corrosion behavior of steel during the wet and dry cyclic condition as well. From these perspectives, various techniques have been applied recently for analyzing the rust layer formed on steel, and its fine structure has been progressively demonstrated. One of the powerful techniques is "Mössbauer spectroscopy", and important information of rust has been reported together with results from other complementary techniques [13, 14, 16, 18, 28–32]. In this chapter, we first present a brief overview of the importance understanding the role of rust on corrosion during the wet and dry cyclic condition. Second, we make a brief description of ^{57}Fe Mössbauer spectroscopy. Finally we discuss the results from ^{57}Fe Mössbauer measurements for the rust formed on steel surface exposed for a long term.

12.2 Importance of Rust in Corrosion Process of Steel During Wet and Dry Cyclic Conditions

In general, the corrosion of steel in the neutral condition proceeds by the coupled reaction of anodic oxidation (dissolution) of iron (Eq. 12.1) and cathodic

reduction of oxygen (Eq. 12.2), and both reactions are equivalent. Since a little oxygen dissolves in aqueous solution, the rate of the iron dissolution is determined by the diffusion limited O_2 reduction, that is, the oxygen diffusion to the surface is the rate-determining step:

$$\mathrm{Fe} \rightarrow \mathrm{Fe}^{2+} + 2\mathrm{e}^{-}(\text{anodic reaction}) \tag{12.1}$$

$$\frac{1}{2}\mathrm{O}_2 + \mathrm{H}_2\mathrm{O} + 2\mathrm{e}^{-} \rightarrow 2\mathrm{OH}^{-}(\text{cathodic reaction}) \tag{12.2}$$

If the concentration of dissolved oxygen is quite low, the corrosion is suppressed because of the suppression of the reaction at Eq. (12.2). In the presence of the chemical species (oxidant), which can play a role in the reaction at Eq. (12.2), the corrosion is accelerated. For instance, the reason why steel easily dissolves in the low pH solution accompanying H_2 gas evolution is that the cathodic reaction is the reduction reaction of H^+ (Eq. 12.3), which exists voluminously in low pH solution, not the reaction at Eq. (12.2):

$$2\mathrm{H}^{+} + 2\mathrm{e}^{-} \rightarrow \mathrm{H}_2(\text{cathodic reaction}) \tag{12.3}$$

When the electrolyte is very thin on the steel surface, the corrosion can be accelerated because of the increase in the oxygen supply to the surface. The electrochemical properties of metals covered by thin electrolyte films are different from those in bulk electrolytes mainly for the following reasons [33]:

(1) The transport of electroactive species from the gas phase like O_2 is very fast and may even be controlled by the transport through the phase-boundary electrolyte/gas.
(2) The activity of ion [e.g. pH] in the electrolyte layer is not constant but may vary drastically as the reaction proceeds.
(3) During corrosion, metal cations are formed which quickly reach the limit of solubility in the thin electrolyte layer and therefore may form passivating films on the top of the metal surface.

Evans [34–36] developed an electrochemical model for the atmospheric corrosion of iron (Evans model). He postulated that in a period of high water content within the pore structure of the rust the anodic dissolution of iron is balanced by the cathodic reaction of Fe(III)-oxides in the rust layer. In this model, rust plays the role of oxidant:

$$\begin{cases} \mathrm{Fe} \rightarrow \mathrm{Fe}^{2+} + 2\mathrm{e} & (12.4) \\ \mathrm{Fe}^{2+} + 8\mathrm{FeOOH} + 2\mathrm{e} \rightarrow \mathrm{Fe}_3\mathrm{O}_4 + 4\mathrm{H}_2\mathrm{O} & (12.5) \end{cases}$$

$$\text{Re-oxidation of rust: } \mathrm{Fe}_3\mathrm{O}_4 + \frac{3}{4}\mathrm{O}_2 + \frac{9}{2}\mathrm{H}_2\mathrm{O} \rightarrow 9\mathrm{FeOOH} \tag{12.6}$$

Subsequently, Stratmann's [37–44] group has reported a series of electrochemical study for the atmospheric corrosion of iron [35, 45–47]. Figure 12.2

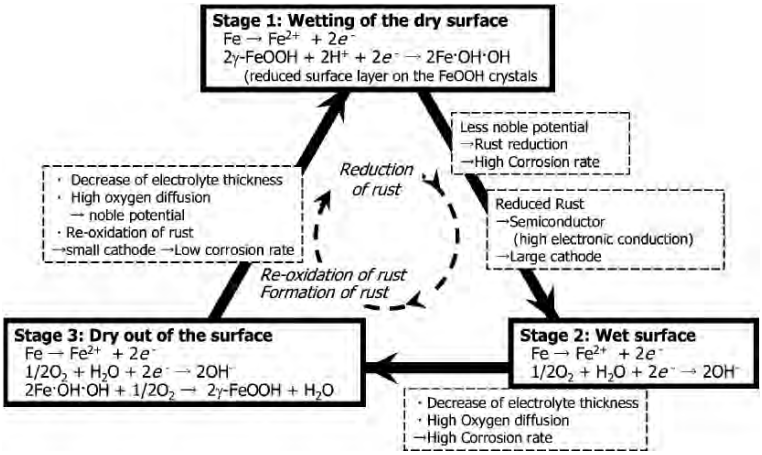

Fig. 12.2. Schematic diagram of the corrosion during wet and dry cyclic condition

shows the schematic diagram of corrosion during wet and dry cyclic conditions. During wetting, the rust is reduced, that is, the rust works as oxidant. Anodic reaction of iron dissolution is balanced by the reduction of rust; in particular, γ-FeOOH is reduced to the Fe^{2+}-doped intermediate expressed as $Fe \cdot OH \cdot OH$ [39]. During the reduction, Fe^{2+} species are created within the lattice of the γ-FeOOH [38, 39], therefore increasing the conductivity of the n-type semiconducting oxide [48]:

$$\gamma\text{−FeOOH} + H^+ + e^- \rightarrow Fe \cdot OH \cdot OH \tag{12.7}$$

The reduced intermediate is a reduced surface layer on the γ-FeOOH. During the wet stage after wetting, the oxygen can be reduced on that surface, and oxygen reduction current is almost constant. During the drying stage, in which the electrolyte thickness decreases, the oxygen reduction on the reduced surface of the γ-FeOOH increases because of the decrease of the diffusion path. The reduced surface of the γ-FeOOH acts as a large cathode and therefore the corrosion accelerates. The above model can explain the propounded phenomenon that the electrolyte thickness is related to the corrosion rate [49]. When the above mechanism of corrosion during the wet and dry cyclic condition is taken into account, it can be presumed that the characteristics of the rust formed can affect the corrosion process, and the alloying elements added to weathering steel can affect the characteristics of the rust such as the reduction behavior and electron conductivity [19, 44, 50]. The protective rust layer is formed through the above corrosion process, and therefore the initial corrosion process will also be highly correlated to the characteristics of the rust layer. Since the rust is not only a result but also a cause, the detailed investigation of the rust layer formed on steel is of great importance to elucidate the mechanism of the atmospheric corrosion of steel.

12.3 Mössbauer Spectroscopy

Mössbauer spectroscopy is based on the recoilless nuclear resonance absorption of γ-rays, known as the Mössbauer effect discovered by R. L. Mössbauer in 1958. A nucleus has its characteristic energy level. When nuclear transition follows from one to another lower level with γ-ray emission, the energy of emission is equal to the difference in the energy of these two levels. Since the energy of the γ-ray is large, the emitting atom is recoiled and moves in the opposite direction of the γ-ray with a recoil velocity. From the conservation law of energy and momentum, the energy of the emitted γ-ray becomes smaller than the difference in the energy of two nuclear levels. If there is a probability for the nucleus to emit or absorb the γ-ray without any phonon excitation, it is possible for the atom to emit (or absorb) γ-rays without recoiling at all. This is the Mössbauer effect.

The Mössbauer effect provides a means of studying the local atomic environment around the nuclei. The interactions between the nucleus and the atomic electrons depend strongly on the electronic, chemical and magnetic state of the atom. Information from these hyperfine interactions is provided by the hyperfine parameter, which can be determined experimentally from the shift and split of the absorption in a Mössbauer spectrum. Mössbauer effect cannot be observed for all atoms. One of the representative Mössbauer nuclei is ^{57}Fe. The most abundant isotope of iron contains 30 neutrons, yielding ^{56}Fe, but ^{54}Fe, ^{57}Fe and ^{58}Fe are also naturally occurring and therefore the average atomic mass is 55.847 when considering their abundance ratio of 91.7%, 5.8%, 2.17%, and 0.3%, respectively. Among these, the ^{57}Fe is used as a probe nucleus for Mössbauer spectroscopy, and it is naturally contained in iron, which we see every day. The width of γ-ray emitted from the first excited state (14.4 KeV) of the ^{57}Fe nucleus is very narrow of the order of 10^{-9} eV, and the energy gap difference due to the chemical state among absorbing atoms varies by a magnitude of about 10^{-7} eV. Therefore, the Mössbauer spectroscopy makes it possible to investigate the small change in the hyperfine structure. In conventional Mössbauer spectroscopy, ^{57}Co in Rh matrix is used as a γ-ray source. The source is moved oscillatory with a small velocity in order to modulate the γ-ray energy by the Doppler effect. Spectra are commonly plotted as percent transmission (vertical axis) vs source velocity (horizontal axis), which corresponds to energy. In the case of ^{57}Fe, 1 mm/s of Doppler velocity corresponds to 4.803×10^{-8} eV, and Mössbauer spectroscopy can detect the change of 0.1 mm/s, which corresponds to approximately 5×10^{-9} eV.

The representative information obtained from Mössbauer spectroscopy is as follows:

(1) Oxidation state (valence): $Fe^{2+}, Fe^{3+}, Fe^{4+}$, etc.
(2) Magnetic property: paramagnetism, ferromagnetism, antiferromagnetism, ferrimagnetism, etc.

(3) Chemical property: electric state around Fe atom, especially electric field gradient at nucleus caused by its own electrons and surrounding electronic states.
(4) Crystallographic property: bound state of Fe atom in the lattice.

The above information can be obtained from the following parameters obtained by analyzing the spectra [51–53]:

(1) Isomer shift (IS, δ): This can be obtained from the position of the absorbing peak and the center of spectrum gravity. The peak position is defined by the difference in the electron density at the nucleus between the source and absorber, and therefore is directly related to the number of s-electrons. s-Electron wave function is affected by the number of $3d$ electrons, and IS value is directly related to the valence of Fe, $Fe^{2+}(3d^6)$ and $Fe^{3+}(3d^5)$.
(2) Magnetic dipole splitting (H_{int}): Interaction of the dipole moment of the nucleus with the magnetic field at the nucleus causes a splitting of the nuclear energy levels by nuclear Zeeman effect, resulting in six peaks. The separation of peaks 1 and 6 is proportional to the magnitude of the hyperfine magnetic field. Contributions to the hyperfine magnetic field at the nucleus consist of (1) core polarization due to its own magnetic $3d$ electrons, (2) orbital magnetic moments, (3) conduction electron polarization, and (4) the dipole fields due to the neighboring magnetic ions.
(3) Quadrupole splitting (QS, ΔEq): Splitting of the energy levels is caused by interaction between the nuclear quadrupolar moment and an electric field gradient at the nucleus, and depends on the valence and spin state of the Fe atom, as well as the coordination and degree of distortion of the crystallographic site.

Other parameters such as full-width at half-maximum (FWHM) and recoil-free fraction (f) can be extracted from the spectrum. The above parameters can be used to identify the chemical and magnetic phases present in the sample like a fingerprint. Table 12.1 shows the Mössbauer parameters of the representative iron oxyhydroxides and iron oxides [20, 54–57], which are observed as the composition of the corrosion products formed on steel surface. The area of the obtained spectrum is proportional to the number of nuclei in the thin film approximation, and therefore the quantitative analysis can be performed for the species in the samples if each recoil-free fraction f of species, which correspond to the constant of proportionality, is known. Moreover, the advantage of the application of Mössbauer spectroscopy to the corrosion products of steel is that it can identify the poorly crystalline or fine particles which give no clear peaks by the ordinary X-ray diffraction method. Mössbauer spectra of the corrosion products formed on steel show, in general, the superposition of several spectra, and therefore a complex figure. Since the magnetic transition temperature of each constituent of the corrosion products varies, we can separate and identify them by measuring the spectra at

Table 12.1. Mössbauer parameters of representative iron oxyhydroxides and iron oxides, which are observed as the composition of the corrosion products formed on steel surface

	Temp. (K)	IS (mm/s)	ΔEq (mm/s)	Hint (T)		Transition temp. (K)	Ref.
Geothite	<400	0.37	0.48	–	Fe^{3+}	$T_N = 385 - 395$	20
α-FeOOH	298	0.36	−0.26	37.8	Fe^{3+}		20
	77	0.48	−0.25	49.9	Fe^{3+}		20
	5	0.48	−0.25	50.3	Fe^{3+}		20
	4.2	0.8	−0.25	50.6	Fe^{3+}		20
Akaganéite	300	0.38	1.01	–		$T_N = 280 - 290$	20
β-FeOOH		0.38	0.66	–			
		0.38	0.41	–			
	295	0.38	0.55				54
		0.37	0.95				
	77	0.47	−0.81	45.1			20
		0.49	−0.19	46.3			
		0.5	−0.05	47.8			
	5	0.46	−0.83	46.8			20
		0.47	−0.23	47.5			
		0.47	−0.06	48.8			
	4.2	0.49	−0.02	48.9			54
		0.49	−0.24	47.8			
		0.49	−0.81	47.3			
Lepidocrocite	300	0.37	0.62	–	Fe^{3+}	$T_N = 50 - 60$	20
γ-FeOOH	294	0.37	0.53	–			54
	77	0.48	0.64	–			20
	10	0.49	0.08	45.6			20
	4.2	0.47	0.02	45.8			54
	4.2	0.25	0.02	45.4			54

Continued on next page

Table 12.1. *Continued*

	Temp. (K)	IS (mm/s)	ΔEq (mm/s)	Hint (T)		Transition temp. (K)	Ref.
$Fe(OH)_2$	300	1.28	3.07	–	Fe^{2+}	$T_N = 31 - 33$	57
		1.05	2.98	–	Fe^{2+}		54
	4.6	1.31	3.07	19.5	Fe^{2+}		57
	4.2	1.1	3.06	20	Fe^{2}		54
Magnetite	300	0.27	0.00	49	Fe^{3+} A site	T_v(Vervey)=	55
Fe_3O_4		0.67	0.00	45	$Fe^{2.5+}$ B site	$118 - 122$	
	295	0.26	$<\mid 0.02 \mid$	49	Fe^{3+} A site	T_c=850	54
		0.67	0.00	46	$Fe^{2.5+}$ B site		
	78	0.48	−0.03	50.6	Fe^{3+} A site		56
		0.58	−0.03	51.4	Fe^{3+} B site		
		0.66	0.10	48.6	Fe^{3+} B site		
		0.90	−0.51	47.1	Fe^{2+} B site		
		1.04	2.30	36.5	Fe^{2+} B site		
	4.2	0.20	−0.03	51.2	Fe^{3+} A site		
		0.43	−0.18	53.2	Fe^{3+} B site		
		0.55	0.07	50.5	Fe^{3+} B site		
		0.80	−0.71	48.9	Fe^{2+} B site		
		0.75	2.03	36.5	Fe^{2+} B site		
Maghemite	300	0.29	0.01	50	Fe^{3+}	$T_c = 820 - 986$	55
γ-Fe_2O_3	300	0.23	$<\mid 0.02 \mid$	50	Fe^{3+}		54
		0.35		50	Fe^{3+}		
	4.2	0.40	$<\mid 0.02 \mid$	52			
		0.48	$<\mid 0.02 \mid$	53			

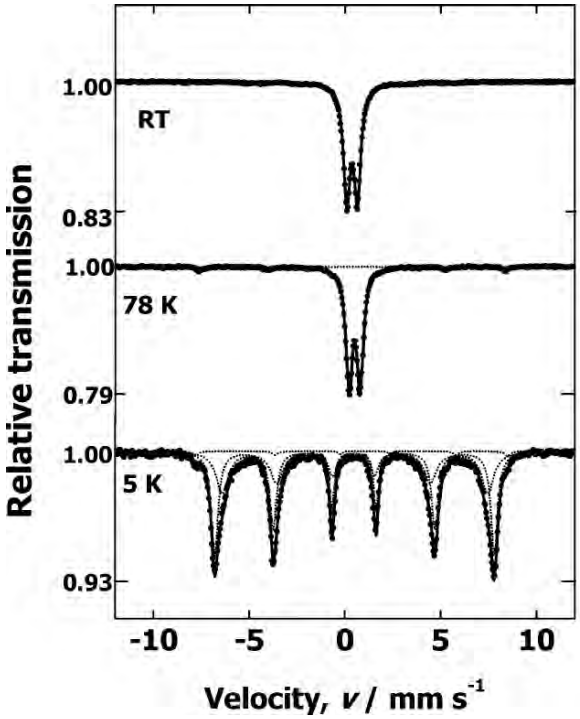

Fig. 12.3. Mössbauer spectra of γ-FeOOH (reagent)

different temperatures. Furthermore, the measurement at lower temperature is of importance for analyzing the corrosion products, which will be described later. The spectra of γ-FeOOH, which is commercially available, are given in Fig. 12.3, as representative data [20]. This was identified as single-phase of γ-FeOOH by the ordinary X-ray diffraction method. The room temperature spectrum showed mainly an intense quadrupole-split doublet. Since the Néel temperature of γ-FeOOH is lower than the 77 K of liquid nitrogen shown in Table. 12.1, the doublet is expected to be observed even at 78 K. However, the magnetically split sextet was superposed on the doublet for the spectra at 78 K, which can be interpreted as the contribution from the magnetically ordered α-FeOOH. For the spectra at 5 K, the central doublet completely vanished, and the magnetically split sextet only was observed. This magnetically split-component is divided into two sextets with strong and weak intensities by computer fitting. From the Mössbauer parameter obtained by analyzing the spectra, the week sextet was assigned to α-FeOOH. Therefore, it is concluded that the doublet obtained at RT contained a small amount of α-FeOOH. The Néel temperature of α-FeOOH is approximately 400 K, which is much higher than RT, and therefore these results indicate evidence of the existence of superparamagnetic small particles of α-FeOOH. The measurement

at the lower temperature of 5 K can detect the spectra of static state without the thermal motion of the magnetic moment, which means that the particle size effect is ignored. Therefore, Mössbauer spectroscopy can identify the small particles, which give no clear peaks in X-ray diffraction patterns, and have a great advantage for analyzing the corrosion products, whose particle size is widely distributed [13, 14, 18].

12.4 Investigation of Rust Formed on Weathering Steel and Mild Steel

The results of analyses of rust formed on weathering and mild steels are presented [13, 18]. As mentioned previously, the corrosion products are affected by the atmospheric conditions, the exposure positions (vertical or horizontal), time of wetness, gases contained in the atmosphere such as SO_2 gas, and airborne salt and deicing salt particles. Therefore, the definition of the exposure conditions is important. In the present study, plates of mild steel and weathering steel ($60 \times 100 \times 4$ mm^3) were exposed at Amagasaki, Japan at an angle of 30° facing south (shelterless condition), as shown in Fig. 12.4, for 15 years and 32 years, respectively. This site, located approximately 5 km inland from the coast but having less than 0.01 mdd (mg/dm^2/day) deposition rate of chlorides, is considered as an industrial region. The chemical composition of the steels used for the exposure test is listed in Table 12.2.

The cross-sectional observation of the rust layer is given in Fig. 12.5. For the mild steel, big cracks reaching the steel substrate were clearly observed, whereas no crack was observed for the weathering steel, indicating the dense, homogeneous, adherent and tight condition. Furthermore, the enrichment of Cu and Cr in the inner rust layer was observed by EPMA (data not shown here) [13], and it can be said that this enrichment can affect the protectiveness

Fig. 12.4. Example of outdoor exposure test. The plates tested are insulated with ceramic insulators

Table 12.2. Chemical composition of the steels tested (mass%)

	C	Si	Mn	P	S	Cu	Ni	Cr
Mild steel	0.12	0.32	1.47	0.023	0.004	0.01	0.02	0.04
Weathering steel	0.10	0.50	0.50	0.018	0.014	0.55	0.53	0.91

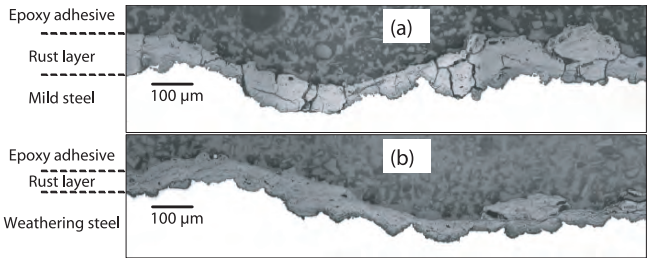

Fig. 12.5. Cross-section of the rust formed on mild steel for 15 years (**a**) and weathering steel exposed for 32 years (**b**) by optical microscope

of the rust layer. These agree with the typical results for the protective rust layer formed on weathering steel reported previously. It has been pointed out that the protective rust layer comprises double layer structures of inner and outer layers, and the inner layer, which is composed of X-ray amorphous substance, exhibits the protectiveness [3, 4, 6, 9, 58]. It is therefore important whether the X-ray amorphous substance is an intrinsic amorphous phase or not.

The ^{57}Fe Mössbauer spectra obtained from powdered specimens scraped from the inner rust are given in Fig. 12.6. The velocity scale is relative to α-Fe at 300 K. The spectra observed at 5 K are rather sharp and involve superposition of the well distinguishable sextets. This result leads to evidence that there is no amorphous phase in the rust layer, because Mössbauer spectra of amorphous magnetic substances should show a broad distribution of the hyperfine magnetic fields. One of the sextets is due to α-Fe having a magnetic hyperfine field $H_{int} = 33$ T (tesla) at room temperature, which was contaminated during the scraping of the rust. The spectra observed at 5 K except α-Fe were analyzed into two sextet spectra by a least-square-fit; one is due to α-FeOOH having $H_{int} = 50$ T, and the other is due to γ-FeOOH having $H_{int} = 45$ T. The spectrum at RT shows a superposition of an intense quadrupole-split doublet and a magnetically split-sextet. This magnetically split-component is divided into two sextets with weak and strong intensity. The latter sextet is clearly due to α-Fe having a magnetic hyperfine field $H_{int} = 33$ T at room temperature, as mentioned above. This strong doublet should assigned to γ-FeOOH, because the Néel temperature of α-FeOOH is much higher than 78 K. However, for the spectrum at 78 K, which is higher than the Néel temperature of γ-FeOOH, the intensity of the central doublet decreased and the intensities of the sextet lines increased. These results suggest that the

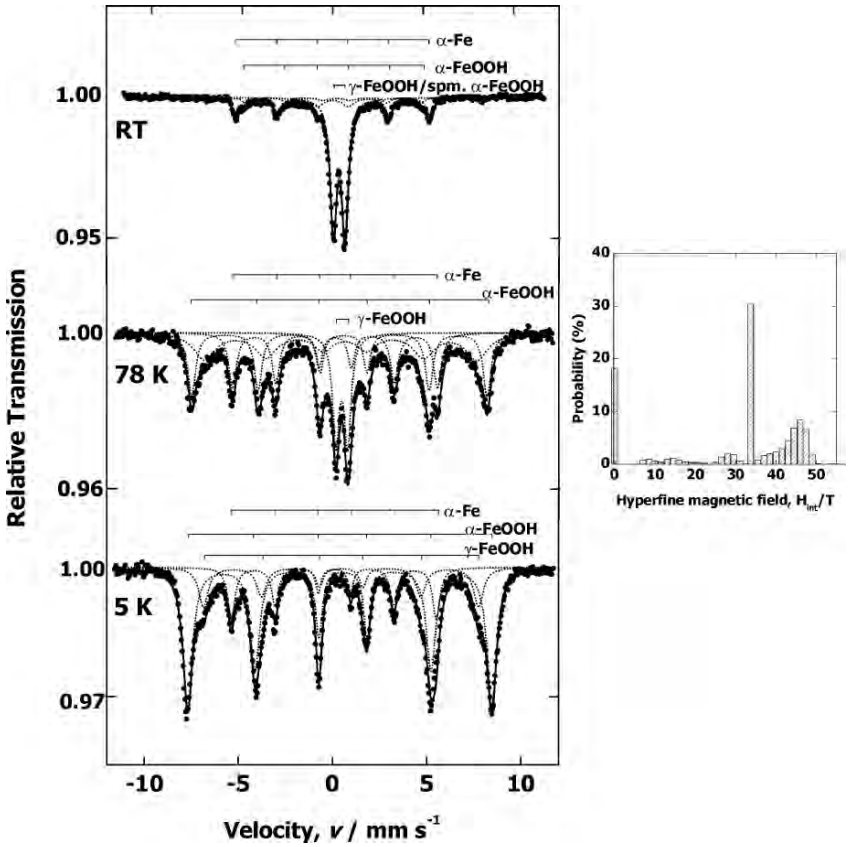

Fig. 12.6. Typical transmission Mössbauer spectra of the inner rust formed on weathering steel exposed for 32 years. The velocity is relative to α-Fe at room temperature. *Right*: hyperfine magnetic field distributions used to fit the spectra on the left

central paramagnetic component at 78 K may be due to the paramagnetic γ-FeOOH whose Néel temperature is reported to be 73 K [59] or 35 K [60] and also due to the superparamagnetic α-FeOOH whose Néel temperature is much higher than 78 K. This result is significant and leads to evidence of the existence of superparamagnetic small particles in the rust layer. It should be noted that the component showing a doublet at RT contains a considerable amount of superparamagnetic α-FeOOH (expressed as spm. α-FeOOH in the figure) which exhibits a paramagnetic doublet due to the rapid fluctuation of the total magnetic moments of the small particle, whereas the Néel temperature of α-FeOOH is above RT. The appearance of superparamagnetism is the result of the reduction of the relaxation time of the thermal motion of the magnetic moment to less than the period of Lamor procession motion. Superparamagnetism is a phenomenon that ferromagnetic or antiferromagnetic or ferrimagnetic materials exhibit, a behavior similar to paramagnetism

except that instead of each individual atom being independently influenced by an external magnetic field, the magnetic moment of the entire crystallite tends to align with the magnetic field at temperatures below the Curie or the Néel temperature. Therefore, materials showing superparamagnetism exhibit their original ferromagnetism or antiferromagnetism or ferrimagnetism only when the temperature is decreased or the external magnetic field is applied.

The example of the results from the distribution analysis of the hyperfine magnetic field at 78 K is given on the right in Fig. 12.6. The distribution of the hyperfine magnetic field corresponds to the distribution of the particle size. This figure indicates that the particle size of α-FeOOH in the rust is widely distributed. The central doublet obtained at 78 K cannot be clearly identified because it may contain smaller particles, which show superparamagnetism even at 78 K. Further measurements at lower temperature are needed to confirm that the superparamagnetic fluctuation of the magnetic moments is negligible. For the spectra at 5 K the central doublet completely vanished, which implies that the superparamagnetic fluctuations of magnetic moments in nano-scaled particles of hydroxides become static at 5 K. From the spectra observed at 5 K, it is possible that the accurate identification and quantitative determination of the rust composition can be performed. It is concluded from the above Mössbauer spectroscopic study that, the X-ray amorphous substance in the rust layer formed on the weathering steel, which gives no peaks in X-ray diffraction pattern, is mainly α-FeOOH showing superparamagnetism owing to its small particle size.

Figure 12.7 shows the ^{57}Fe Mössbauer spectra obtained from powdered samples scraped from the inner rust formed on the mild steel exposed for 15 years in an industrial environment, together with the results from the distribution analysis of the hyperfine magnetic field at RT and 78 K at the right of the figures, respectively. The spectra obtained were different from that for the weathering steels. The room temperature spectrum of the inner rust shows a superposition of an intense quadrupole-split doublet and a magnetically split-sextet. In addition, another broad sextet was observed, which has a large full-width at half-maximum (FWHM) and does not show the sharp spectrum. This sextet having a large hyperfine field of approximately 50 T was never observed for the rust formed on the weathering steels. From the hyperfine parameters of this spectra at low temperature, it can be assigned to $Fe_{3-\delta}O_4$ ($0 < \delta < 1/3$, $\delta = 1/3$ corresponds to γ-Fe_2O_3.), which cannot be identified by the ordinary X-ray diffraction method. Since the spectra from Fe(II+III) at B-site in Fe_3O_4 were not observed at RT as shown in Fig. 12.6, δ is thought to be mainly close to 1/3 (corresponding to γ-Fe_2O_3) and it is probable that the rust contains $Fe_{3-\delta}O_4$ having various values ($0 < \delta < 1/3$). This may result in the broad spectrum and widely distributed hyperfine magnetic field at RT, shown in Fig. 12.7 on right hand side. It is therefore concluded that the difference in the rust composition between weathering steel and mild steel is the formation of $Fe_{3-\delta}O_4$ in the rust formed on mild steel exposed for a long term. That is, the added elements of Cu, Cr and Ni in

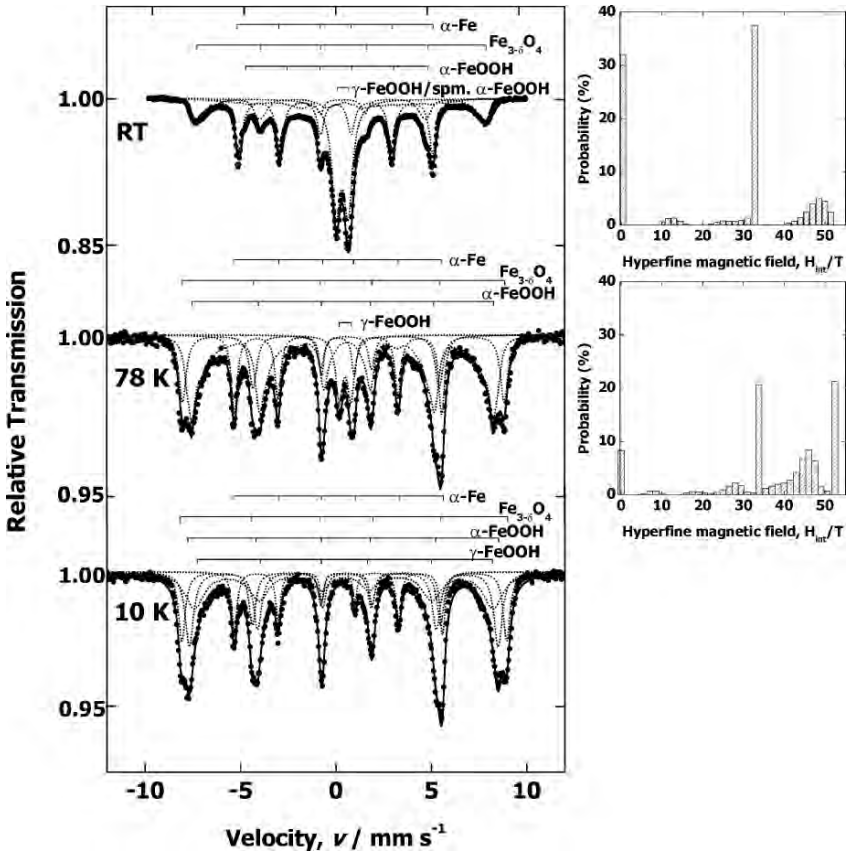

Fig. 12.7. Typical transmission Mössbauer spectra of the inner rust formed on mild steel exposed for 15 years. The velocity is relative to α-Fe at room temperature. *Right*: hyperfine magnetic fíeld distributions used to fit the spectra on the left

the weathering steel can suppress the formation of Fe_3O_4. However, since the composition of the rust is influenced by the environment as mentioned above, it should be noted that the rust formed on weathering steel does not always contain Fe_3O_4. This tendency was already observed for the rust formed on the steel exposed for a short term [61, 62]. Furthermore, it is also reported that the existence of Cr can suppress the formation of Fe_3O_4 in the initial wet and dry cyclic condition [19]. The formation process of Fe_3O_4 is still unclear, and how the formation of Fe_3O_4 is related to the corrosion and the protectiveness of the rust layer, which will be issues for the future. As described above, Mössbauer spectroscopy can identify the rust having ultra-fine particles, and even a small amount contained in the rust layer as well. Recently, it was reported that the mass fraction of α-FeOOH including ultra-fine particles increases with an increase of the exposure duration, and the increased tendency

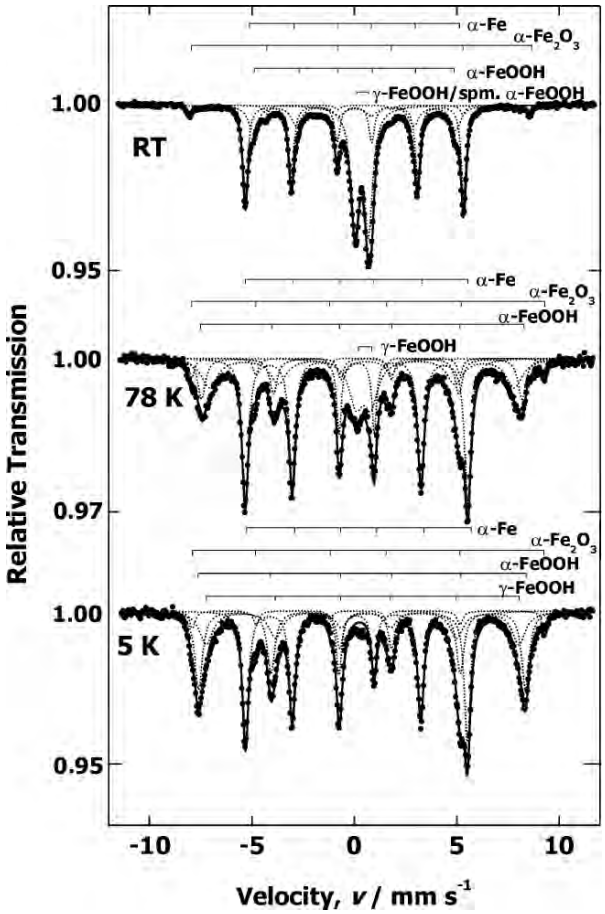

Fig. 12.8. Mössbauer spectra of the rust formed on weathering steel coated with a surface pretreatment promoting protective rust formation exposed for a few years. The velocity is relative to α-Fe at room temperature. α-Fe_2O_3 is not rust but pigment in the treatment

of the mass fraction of α-FeOOH has a linear-relationship to the logarithm of the exposure duration [31, 62]. Therefore, the corrosion rate of the weathering steels can be closely related to the mass fraction of α-FeOOH [63], and α-FeOOH must play an important role in the formation of the protective rust layer. Furthermore it becomes a powerful technique for the investigation of a small amount of rust formed on weathering steel coated with a surface pretreatment promoting protective rust formation [64, 65], as shown in Fig. 12.8. The result clearly indicates that α-FeOOH is preferentially formed on weathering steel exposed for a few years.

12.5 Summary

Mössbauer spectroscopy is a powerful tool for analyzing the rust formed on steel surface, and it is expected that it clarifies the nature of the rust, together with the discussion of the results by other complementary techniques. Mössbauer spectroscopy has different nondestructive methods to conversion electron Mössbauer spectroscopy (CEMS), and conversion X-rays Mössbauer spectroscopy (CXMS) [66, 67]. The analytical depth for CEMS is approximately 50 nm, and for CXMS is 10–20 μm, and therefore they can be applied for the in-situ investigation of the initial rust formation process. Mössbauer spectroscopy will be increasingly used in order to elucidate the atmospheric corrosion mechanism in consideration of the electrochemical process in future.

References

1. *Hot-rolled atmospheric corrosion resisting steels for welded structure* (Japanese Industrial Standards Committee) JIS G 3114, (1987).
2. ASTM Standard A588, *Standard Specification for High-Strength Low-Alloy Structural Steel with 50 ksi [345 MPa] Minimum Yield Point to 4-in. [100-mm] Thick* (ASTM International, West Conshohocken, PA) (2002).
3. H. Okada, Y. Hosoi, K. Yukawa, H. Naito: Trans. ASM, **62**, 278 (1969).
4. H. Okada, Y. Hosoi, H. Naito: Corrosion, **26**, 429 (1970).
5. T. Misawa, M. Yamashita, Y. Matsuda, H. Miyuki, H. Nagano: J. Iron Steel Inst. Jpn, **79**, 69 (1993).
6. T. Misawa, K. Asami, K. Hashimoto, S. Shimodaira: Corros., Sci., **14**, 279 (1974).
7. J. T. Keiser, C. W. Brown, R. H. Heidersbach: Corros. Sci., **23**, 251 (1983).
8. M. Yamashita, H. Miyuki, T. Matsuda, H. Nagano, T. Misawa: Corros. Sci., **36**, 283 (1994).
9. H. Okada: J. Soc. Mater. Sci. Japan, **17**, 705 (1968).
10. H. Kihira, S. Ito, T. Murata: Corros. Sci., **31**, 383 (1990).
11. K. Asami, M. Kikuchi: Corros. Sci., **45**, 2671 (2003).
12. J. T. Keiser, C. W. Brown: Corros. Sci., **23**, 251 (1983).
13. T. Kamimura, S. Nasu: Materials Transactions, *JIM*, **41**, 1208 (2000).
14. T. Okada, Y. Ishii, T. Mizoguchi, I. Tamura, Y. Kobayashi, Y. Takagi, S. Suzuki, H. Kihira, M. Itou, A. Usami, K. Tanabe, K. Masuda: Jpn. J. Appl. Phys., **39**, 3382 (2000).
15. S. J. Oh, D. C. Cook, H. E. Townsned: Corros. Sci., **41**, 1687 (1999).
16. D. C. Cook, R. Balasubramanian, S. J. Oh, M. Yamashita: Hyp. Interact., **122**, 59 (1999).
17. S. J. Oh, D. C. Cook: J. Korean Phy. Soc., **36**, 106 (2000).
18. T. Kamimura, S. Nasu, T. Tazaki, K. Kuzushita, S. Morimoto: Materials Transactions, **43**, 694 (2002).
19. T. Kamimura, S. Nasu, T. Segi, T. Tazaki, S. Morimoto, H. Miyuki: Corros. Sci., **45**, 1863 (2003).
20. S. Nasu, T. Kamimura, T. Tazaki: Hyperfine Interactions, **139-140**, 175 (2002).

21. M. Kimura, T. Suzuki, G. Shigesato, H. Kihira, S. Suzuki: ISIJ International, **42**, 1534 (2002).
22. S. Suzuki, Y. Takahashi, T. Kamimura, H. Miyuki, K. Shinoda, K. Tohji, Y. Waseda: Corros. Sci., **46**, 1751 (2004).
23. H. Konishi, M. Yamashita, H. Uchida, J. Mizuki: Mater. Trans., **46**, 337 (2005).
24. M. Pourbaix: Corros. Sci., **12**, 161 (1972).
25. M. Pourbaix: Corros. Sci., **14**, 25 (1974).
26. H. Schwitter and H. Boehni: J. Electrochem. Soc., **127**, 15 (1980).
27. K. Bohnenkamp: Tribune du CEBEDEAU, **324**, 1 (1970).
28. M. Yamashita, T. Misawa, H. E. Townsend, D. C. Cook: J. Jpn. Inst. Metal, **64**, 77 (2000).
29. M. Yamashita, T. Misawa, S. J. Oh, R. Balasubramanian, D. C. Cook: Zairyo-to-Kankyo, **49**, 82 (2000).
30. J. F. Marco, M. Gracia, J. R. Gancedo, M. A. Martín-Luengo, G. Joseph: Corros. Sci., **42**, 753 (2000).
31. T. Kamimura, T. Doi, T. Tazaki, K. Kuzushita, S. Morimoto, S. Nasu: *Proc. 2nd Int. Conf. on Environment Sensitive Cracking and Corrosion Damage*, 190-196 (2001).
32. S. Music, G. P. Santana, G. Šmit, V. K. Garg: Journal of Alloys and Compounds., **278**, 291 (1998).
33. M. Stratmann, H. Streckel: Ber. Bunsenges. Phys. Chem., **92**, 1244 (1988).
34. U. R. Evans: Corros. Sci., **9**, 813 (1969).
35. U. R. Evans, C.A. Tayler: Corros. Sci., **12**, 227 (1972).
36. U. R. Evans: Nature, **206**, 980 (1965).
37. M. Stratmann: Ber. Bunsenges. Phys. Chem., **94**, 626-630 (1990).
38. M. Stratmann, K. Hoffmann: Corros. Sci., **29**, 1329 (1989).
39. M. Stratmann, K. Bohnenkamp, H.-J. Engell: Corros. Sci., **23**, 969 (1983).
40. M. Stratmann, K. Bohnenkamp, T. Ramchandran: Corros. Sci., **27**, 905 (1987).
41. M. Stratmann, K. Bohnenkamp, H.-J. Engell: Welkstoffe und Korrosion, **34**, 604 (1983).
42. M. Stratmann, J. Müller: Corros. Sci., **36**, 327 (1994).
43. M. Stratmann, H. Streckel: Corros. Sci., **30**, 697 (1990).
44. T. Kamimura, M. Stratmann: Corros. Sci., **43**, 429 (2001).
45. A. Kuch: Corros. Sci., **28**, 221 (1988).
46. I. Suzuki, Y. Hisamatsu, N. Masuko: J. Electrochem. Soc., **127**, 2210 (1980).
47. I. Suzuki, N. Masuko, Y. Hisamatsu: Corros. Engineering Japan, **23**, 141 (1974).
48. J. W. Schultz, S. Mohr, M. M. Lohrengel: J. Electroanal. Chem., **154**, 57 (1983).
49. N. D. Tomachov: Corrosion, **20**, 7t (1964).
50. M. Schneider, M. Stratmann: Ber. Bunsen. Phy. Chem., **96**, 1731 (1992).
51. S. Nasu: Mater. Sci. Tech., **71**, 952 (2001).
52. S. Nasu: J. High Pressure Inst. Jpn., **34** , 39 (1996).
53. S. Nasu: Materia Japan, **39**, 563 (2000).
54. R. M. Cornell, U. Schwertmann, *The Iron Oxides*, (Wiely-VCH GmbH & Co. KGaA. 1996).

55. K. Wada: *Master's thesis* Osaka University, (1993).
56. C. M. Srivastava, S. N. Shringi, M. V. Babu: Phys. Stat. Sol. (a), **65**, 731 (1981).
57. T. Tazaki: *Master's thesis* Osaka University, (2002).
58. H. Okada, Y. Hosoi, K. Yukawa, H. Naito: J. Iron Steel Inst. Jpn., **55**, 355 (1969).
59. C. E. Johnson: J. Phys. C(Solid St. Phys.), **2**, 1996 (1969).
60. Ph. Bauer, J. M. Génin, D. Rezel: Hyperfine Interactions, **28**, 757 (1986).
61. T. Kamimura, S. Nasu, T. Segi, S. Morimoto: *Proc. 49th Japan Conf. Materials and Environments* (JSCE, A-103S 2002).
62. T. Kamimura, S. Nasu, T. Segi, S. Morimoto: *Proc, 13th Asian-Pacific Corrosion Control Conference* CD086 (2003).
63. T. Kamimura, M. Yamashita, H. Uchida, H. Miyuki: J. Jpn. Inst. Metals, **65**, 922 (2001).
64. H. Kishikawa, H. Miyuki, S. Hara, M. Kamiya, M. Yamashita: The Sumitomo Search, **60**, 20 (1998).
65. H. Miyuki, T. Kamimura, T. Doi, M. Yamashita, T. Misawa: Materia Japan, **41**, 39 (2002).
66. K. Nomura, M. Tasaka , Y. Ujihira: Corrosion, **44**, 133 (1988).
67. T. Kamimura, S. Nasu, T. Tazaki: *Proceedings of JSCE Materials and Environments* 2000, 2000B-102, (2000).

Index